

# Probing Quarkonium Production in Jets Using Effective Field Theories

by

Reginald Alexander Bain

Department of Physics  
Duke University

Date: \_\_\_\_\_

Approved:

---

Thomas Mehen, Supervisor

---

Ayana Arce

---

Kate Scholberg

---

Harold Baranger

---

Joshua Socolar

Dissertation submitted in partial fulfillment of the requirements for the degree of  
Doctor of Philosophy in the Department of Physics  
in the Graduate School of Duke University  
2017

ABSTRACT

Probing Quarkonium Production in Jets Using Effective Field  
Theories

by

Reginald Alexander Bain

Department of Physics  
Duke University

Date: \_\_\_\_\_

Approved:

---

Thomas Mehen, Supervisor

---

Ayana Arce

---

Kate Scholberg

---

Harold Baranger

---

Joshua Socolar

An abstract of a dissertation submitted in partial fulfillment of the requirements for  
the degree of Doctor of Philosophy in the Department of Physics  
in the Graduate School of Duke University  
2017

Copyright © 2017 by Reginald Alexander Bain  
All rights reserved except the rights granted by the  
Creative Commons Attribution-Noncommercial Licence

# Abstract

While bound states of heavy quarks  $Q\bar{Q}$  called *quarkonia* have been studied for nearly a half-century, their production is still not well understood. We examine how techniques from Effective Field Theories (EFTs) of the strong force can be used to probe the production of the  $J/\psi(c\bar{c})$ . The focus will be to study how quarkonia are produced in *jets*, highly-collimated sprays of hadrons ubiquitous at particle colliders. We review the study of quarkonium production using Non-relativistic QCD (NRQCD) and the study of jet substructure observables using the Soft-Collinear Effective Theory (SCET). The concept of Fragmenting Jet Functions (FJF), which describe a hadron's energy distribution inside a jet of measured substructure, is extended to jets where the angularity is measured or where the transverse momenta of a hadron relative to the jet axis is measured. Predictions of the energy distribution of  $J/\psi$  in jets at the LHC using FJFs are compared with the latest LHCb data using various extractions of the non-perturbative NRQCD long-distance-matrix-elements (LDMEs) in the literature. These distributions are also calculated using a modification of the PYTHIA Monte Carlo, which is shown to have an unphysical model of quarkonium production and gives results consistent with our FJF calculations. Our predictions of the energy of  $J/\psi$  produced in jets fit the data much better than default Monte Carlo results. We also demonstrate that LDMEs extracted from high transverse momentum data do a better job at predicting the LHCb measurements.

To my parents, for their unending sacrifice, patience, and faith in me.

# Contents

<b>Abstract</b>	<b>iv</b>
<b>List of Tables</b>	<b>x</b>
<b>List of Figures</b>	<b>xi</b>
<b>List of Abbreviations and Symbols</b>	<b>xix</b>
<b>Acknowledgements</b>	<b>xxiii</b>
<b>1 Introduction</b>	<b>1</b>
1.1 Quantum Chromodynamics . . . . .	2
1.2 Effective Field Theories (EFT) . . . . .	6
1.2.1 What is an EFT? . . . . .	6
1.2.2 Factorization of Observables . . . . .	8
1.2.3 Constructing Effective Theories . . . . .	9
1.2.4 Resummation of Logarithms . . . . .	12
1.3 Outline of this Work . . . . .	14
<b>2 Quarkonium Production</b>	<b>16</b>
2.1 Introduction & Brief History of Quarkonium . . . . .	16
2.2 Spectroscopy and Basic Properties . . . . .	19
2.3 Models of Quarkonium Production . . . . .	22
2.3.1 Potential Models for Charmonia . . . . .	22
2.3.2 Sources of Quarkonium Production . . . . .	23

2.3.3	The Color Singlet Model . . . . .	24
2.4	NRQCD — A Modern Theory of Quarkonium Production & Decay . . . . .	31
2.4.1	Lagrangian of NRQCD . . . . .	31
2.4.2	NRQCD Factorization . . . . .	34
2.4.3	Power Counting & Selection Rules . . . . .	35
2.4.4	Leading Power NRQCD . . . . .	37
2.4.5	Fragmentation Functions at $\alpha_s(2m_c)$ . . . . .	39
2.5	The Polarization Puzzle . . . . .	42
2.5.1	Calculating Quarkonium Polarization . . . . .	42
2.5.2	Predictions & Measurements of Quarkonium Polarization . . . . .	45
2.6	Going Forward . . . . .	49
<b>3</b>	<b>Jets: Nature’s High-Energy Conical Laboratory</b>	<b>52</b>
3.1	Introduction . . . . .	52
3.2	Origins of Jet Physics . . . . .	53
3.3	Jet Algorithms & Jet Substructure . . . . .	55
3.3.1	Jet Algorithms . . . . .	55
3.3.2	Jet Substructure . . . . .	58
3.4	Soft-Collinear Effective Theory . . . . .	61
3.4.1	Introduction . . . . .	61
3.4.2	Light Cone Coordinates . . . . .	62
3.4.3	Momentum Regions in SCET . . . . .	62
3.4.4	Label Momentum Formalism . . . . .	65
3.4.5	Leading-Order SCET Lagrangian . . . . .	67
3.4.6	Factorization in SCET . . . . .	68

<b>4</b>	<b>Fragmenting Jet Functions: Introduction &amp; Developments</b>	<b>76</b>
4.1	Introduction . . . . .	76
4.1.1	Fragmentation Functions . . . . .	77
4.1.2	Fragmentation with a Cut on Thrust . . . . .	78
4.2	Basic Properties of the FJF . . . . .	80
4.2.1	Origin of the FJF . . . . .	80
4.2.2	Sum Rules . . . . .	82
4.2.3	FJFs in the Literature . . . . .	82
4.3	Operator Definitions of FJFs . . . . .	83
4.3.1	Calculating Renormalized FFs & FJFs at One-loop. . . . .	86
4.3.2	Anomalous Dimensions of the FJF . . . . .	87
4.4	Angularity Dependent FJFs . . . . .	87
4.4.1	Angularity in Light-Cone Coordinates . . . . .	87
4.4.2	Defining the Angularity FJF . . . . .	88
4.4.3	One-Loop Calculation of Matching Coefficients . . . . .	90
4.4.4	Summary of Perturbative Results . . . . .	95
4.5	Transverse Momentum Dependent FJFs (TMDFJF) . . . . .	97
4.5.1	TMDs & Collinear-Soft Modes . . . . .	97
4.5.2	Definition & Factorization . . . . .	99
4.5.3	Perturbative Calculation of TMD Matching Coefficients . . . . .	103
4.5.4	Summary of Collinear Perturbative Results . . . . .	106
4.5.5	Perturbative Calculation of Collinear-Soft Function . . . . .	107
4.6	Alternative Definition of TMDFJF . . . . .	109
<b>5</b>	<b>Applications to Quarkonia in Jets with Comparisons to Monte Carlo &amp; Data</b>	<b>112</b>
5.1	Introduction . . . . .	112

5.2	<i>b</i> Quark to <i>B</i> Meson Fragmentation in $e^+e^- \rightarrow$ Dijets . . . . .	114
5.3	Gluon to $J/\psi$ Fragmentation in $e^+e^- \rightarrow$ 3 Jets . . . . .	123
5.4	Applications of the TMDFJF to Quarkonium Production . . . . .	134
5.5	FJF/PYTHIA Predictions vs. LHCb Data on $J/\psi$ Production . . . . .	143
5.5.1	Method 1: GFIP for LHCb . . . . .	144
5.5.2	Method 2: FJF for LHCb . . . . .	146
5.5.3	Comments on Uncertainties . . . . .	147
5.5.4	Comparisons of GFIP, FJFs, & Data . . . . .	149
<b>6</b>	<b>Conclusions</b>	<b>151</b>
<b>A</b>	<b>Velocity Scaling in NRQCD</b>	<b>154</b>
<b>B</b>	<b>Symmetries of Leading Order SCET Lagrangian</b>	<b>158</b>
<b>C</b>	<b>Renormalization Group &amp; Rapidity Renormalization Group Techniques</b>	<b>160</b>
C.1	RGE for Unmeasured Functions . . . . .	161
C.2	RGE for Measured Functions . . . . .	164
C.3	RGE + RRGE for TMD Functions . . . . .	164
<b>D</b>	<b>Plus-functions and Profile Functions</b>	<b>167</b>
D.1	Plus-Functions . . . . .	167
D.2	Profile Functions . . . . .	169
	<b>Biography</b>	<b>183</b>

# List of Tables

2.1	We consider three sets of LDMEs for NRQCD production mechanisms, listed here in units of $\text{GeV}^3$ .	46
5.1	The characteristic scales of each piece of the factorization theorem shown in Eq. (5.1). The scales minimize potentially large logarithms in each function.	120
5.2	Characteristic scales of the different functions in the factorization theorem.	138
5.3	Results of fits of the function $\log(f_\omega(z))$ shown in Fig. 5.12 to the function $C_0 \exp(-z C_1)$ .	143
5.4	We consider three sets of LDMEs for NRQCD production mechanisms, listed here in units of $\text{GeV}^3$ .	146
C.1	Orders of the matching calculation, non-cusp anomalous dimensions, cusp anomalous dimensions, and QCD $\beta$ -function needed for various fixed order calculations and logarithmic resummation orders. Adapted from Refs. [1, 2].	163
C.2	Values of the cusp and non-cup parts of the anomalous dimensions for the collinear and collinear-soft functions.	166

# List of Figures

1.1	The Large Hadron Collider (LHC), a 14 TeV center-of-mass energy proton-proton collider in Geneva, Switzerland. Image courtesy of <a href="https://home.cern/topics/large-hadron-collider">https://home.cern/topics/large-hadron-collider</a> . . . . .	2
1.2	The elementary particles described by the Standard Model of Particle Physics (SM). . . . .	3
1.3	The running of the strong coupling $\alpha_s(Q)$ as shown in Ref.[3] where the focus was extracting the strong coupling from 3-jet differential cross-sections as a function of the 3-jet invariant mass and the 3 jets with the highest transverse momenta are selected. The plot also shows previous measurements of $\alpha_s$ and compares the 3-jet extraction with world averages of the coupling. . . . .	6
1.4	The Drell-Yan process can be factorized into PDFs for each incoming hadron and a partonic-cross section of the form $d\hat{\sigma}(ab \rightarrow l^+l^-)$ which can be calculated in perturbation theory. . . . .	8
1.5	An example of how a full theory tree-level process is matched onto a tree-level EFT process for the $D^0 \rightarrow K^- \pi^+$ example at the quark level described in the text. A one-loop matching procedure would involve additional diagrams that connect quark lines with a gluon. . . . .	11
2.1	Original plot of the BNL group's $J/\psi$ mass peak at 3.1 GeV. Image taken from Ref. [4]. . . . .	17
2.2	(Left) Computer reconstruction of the decay of the $\psi(2S) \rightarrow J/\psi \pi^+ \pi^-$ at the Mark 1 detector at the SPEAR experiment (shown on right). Courtesy SLAC National Accelerator Laboratory at <a href="http://www.slac.stanford.edu/vault">http://www.slac.stanford.edu/vault</a> . . . . .	18

2.3	The spectrum of experimentally established charmonium ( $c\bar{c}$ ) states. Levels are organized horizontally according to their $J^{PC}$ and vertically according to their mass. The $J/\psi$ is the $^3S_1$ singlet charmonium state. Several hadronic transitions between charmonium states are also shown such as the $\psi(2S) \rightarrow \pi^+\pi^- J/\psi$ process. Graphic is a courtesy of Ref. [5]. . . . .	21
2.4	Flux-tube visualization of a potential model for the strong force. . . .	23
2.5	The diagrams contributing to $gg \rightarrow J/\psi g$ or any other $^3S_1^{[1]}$ charmonium state at LO in the CSM. The double line denotes the charmonium state and $c \leftrightarrow \bar{c}$ would require switching the directions of each fermion arrow. . . . .	26
2.6	Plots from Ref. [6] using data from Ref. [7] which show the LO CSM predictions for the $J/\psi$ (a) and $\psi'$ (b) production rates. Both diagrams show that these predictions (as described in the text) under-predict experimental observations by orders of magnitude. This helped to motivate the study of fragmentation contributions at high transverse momenta. . . . .	27
2.7	This shows a fragmentation diagram that contributes to $\eta_c(^1S_0^{[1]})$ production at $\mathcal{O}(\alpha_s^4)$ . Although higher order in the coupling than LO contributions in the CSM, in the limit that $p_T \gg m_c$ , this diagram can be shown to be enhanced by $p_T^2/m_c^2$ . At high $p_T$ this enhancement compensates for the $\alpha_s$ suppression. . . . .	28
2.8	Inclusive cross-section for inclusive $J/\psi$ (Left) and $\psi(2S)$ (right) production at the Tevatron at $\sqrt{s} = 1.8$ TeV [8]. The cross-sections are for direct $J/\psi$ ( $\psi(2S)$ ) production and are differential in $p_T$ and for central rapidities $ \eta  < 0.6$ . Both plots show that both the LO CSM and LO CSM + fragmentation predictions are orders of magnitude below the data. With the addition of color-octet production mechanisms, both the $J/\psi$ and $\psi(2S)$ predictions from NRQCD are in near perfect agreement with the data. . . . .	30
2.9	Example of diagrams for (a) LO non-fragmentation contributions and (b) fragmentation contributions to $J/\psi$ production. The relevant scalings in the coupling and transverse momenta are shown, emphasizing that, while suppressed by orders of $\alpha_s$ , fragmentation diagrams are enhanced by powers of the $p_T$ for very high transverse momenta. . . .	37

2.10	Basic fragmentation diagrams for the ${}^3S_1^{[8]}$ , ${}^1S_0^{[8]}$ , ${}^3P_J^{[8]}$ , and ${}^3S_1^{[1]}$ NRQCD production mechanisms for $J/\psi$ that are most important in the leading power approximation of NRQCD. The scalings of each mode with the expansion parameters $\alpha_s$ and $v$ are also shown in each case. . . .	38
2.11	Figure from Ref. [9] showing CDF data for prompt $\psi'$ production and theoretical predictions of the total LO CSM contributions (dotted curves), the CSM + fragmentation contributions (dashed curves) and the ${}^3S_1^{[8]}$ color-octet fragmentation contribution (solid curve). Theoretical predictions match CDF data quite well, which motivates the use of NRQCD to describe quarkonium hadroproduction at high $p_T$ , specifically because of its inclusion of intermediate color-octet states.	39
2.12	Plot showing the polar anisotropy parameter $\alpha = \lambda_\theta = (\sigma_T - 2\sigma_L)/(\sigma_T + 2\sigma_L)$ resulting from fits of the angular distribution of di-muons in direct $\psi'$ production (a) and prompt $J/\psi$ production (b) (in $p\bar{p} \rightarrow J/\psi(\rightarrow \mu^+\mu^-) + X$ events) to the distribution $1 + \alpha \cos^2(\theta)$ as a function of the transverse momentum $p_T$ where $\theta$ is the angle between the $\mu^+$ 3-momentum in the $J/\psi$ rest frame and the $J/\psi$ 3-momentum in the lab frame. This shows significant disagreement between theoretical predictions of [10] and Tevatron data [11]. . . . .	40
2.13	This plot, adapted from Ref. [12], shows the fragmentation functions in leading power NRQCD plotted as a function of $z$ , the fraction of the fragmenting parton's energy carried by the hadron. The curves are normalized (by multiplying the functions by numbers) such that all of the curves fit on the same plot. . . . .	41
2.14	The polarization of $J/\psi$ is studied using the angular distribution of decays to $l^+l^-$ . This figure from Ref. [13] shows a coordinate system for measuring this distribution. The polarization axis is chosen to be along $z$ according to several conventions which are shown in Fig 2.15.	43
2.15	The three conventions for defining the polarization axis: HX — helicity frame, GJ — Gottfried-Jackson frame, CS — Collins-Soper frame. In this figure taken from Ref. [13], $b_1$ and $b_2$ represent the directions of the incoming beams and $Q$ the direction of the quarkonium. . . . .	44
2.16	The polarization of $J/\psi$ is studied using the angular distribution of decays to $l^+l^-$ . Knowing the eigenvalues of $J'_z$ along the axis of production, basic properties of angular momentum can be used to show that polarization can be expressed in terms of eigenstates of $z$ a polarization axis fixed by one of the conventions described in the text. This figure is adapted from Ref. [13]. . . . .	45

2.17	A sample of 2 (out of 28) plots that show the global fits performed in Refs. [14, 15] of NLO NRQCD predictions (shown as CS+CO,NLO). The plots show that the data clearly favor the inclusion of the color-singlet and color-octet modes predicted at NLO in NRQCD over LO NRQCD and the color-singlet model (shown as CS, LO and CS, NLO) at both leading and next-to-leading order. . . . .	47
2.18	A comparison of LHCb data [16] for prompt $J/\psi$ production of the polarization observable $\lambda_\theta$ with $k_T$ factorization (modification of CSM; shown in diagonal magenta lines) [15] and three different NLO NRQCD predictions as a function of $p_T(J/\psi)$ for the LHCb rapidity range of $2.5 < y < 4$ . The blue diagonal lines (NRQCD(1)) are based on global fits of Ref. [15], the red vertical lines (NRQCD(2)) on fits of Ref. [17], and the green hatched pattern (NRQCD(3)) on a high- $p_T$ fit from Ref. [18, 19]. We do not consider the fits of Ref. [17] or from the $k_T$ factorization approach in this work. . . . .	48
2.19	Cross-sections as a function of $p_T$ for the two LDME extractions in Ref. [18]. Darker bands (NLO Total I) show predictions that use the fits shown in Table 5.4 for the simultaneous fit of the LDMEs to the polarization and $p_T$ for specifically $p_T > 7$ GeV data from CDF and CMS. The lighter bands show show upper and lower bounds of fits that fix $\mathcal{O}(^1S_0^{[8]}) = 0$ and $\mathcal{O}(^3S_1^{[8]}) = \mathcal{O}(^3P_J^{[8]}) = 0$ as the upper and lower bounds, respectively. The top and bottom figures show comparisons with ATLAS (left) [20] and CMS (right) [21] data. . . . .	49
2.20	Comparison from Ref. [22] of analytic predictions using NLO NRQCD + LP factorization for the anisotropy parameter $\lambda_\theta = (\sigma_T - 2\sigma_L)/(\sigma_T + 2\sigma_L)$ with data from (a) CDF Run I [11] and CDF Run II [23] and (b) CMS data [24]. Again, $\sigma_T(\sigma_L)$ is the cross-section for transversely (longitudinally) polarized production of the $J/\psi$ . . . . .	50
2.21	Polar anisotropy parameter $\lambda_\theta = (d\sigma_T - 2d\sigma_L)/(d\sigma_T + 2d\sigma_L)$ for $J/\psi$ production using LDMEs from fits performed in Ref. [18] compared with data from CDF Run I [25] and Run II [26]. This plot also shows the individual contributions of each NRQCD production mechanism to the overall polarization. This makes the cancelation of the transverse components of the $^3P_J^{[8]}$ and $^3S_1^{[8]}$ components at high $p_T$ visible. . . .	51
3.1	Displays of 2-jet (a) and 3-jet (b) events as shown in Ref. [27, 28]. . .	54

3.2	This figure from Ref. [29] shows how two jet algorithms, the SIS-Cone [30] and anti- $k_T$ algorithms, behave when applied to the same event. Highlighted areas represent jets in the space of the azimuthal angle $\phi$ , rapidity $y$ , and transverse momentum $p_T$ with cone size parameter $R = 1$ . $f$ is the so-called overlap parameter and is defined in [30]. . . . .	57
3.3	An illustration of two characteristic values of the thrust parameter $\tau = 1 - T$ showing (a) pencil-like dijets for $\tau \sim 0$ and (b) isotropic final state with 0 jets. . . . .	58
3.4	Diagram (a) shows a sample $e^+e^-$ cross-section differential in the angularity $\tau_a$ for different values of $a$ with $a < 1$ . Diagram (b) illustrates the jet-shape observable as a fraction of transverse energy within a cone of radius $r$ within a larger jet of radius parameter $R$ with total soft radiation $\Lambda_S$ falling outside of the jets. . . . .	60
3.5	This diagram shows a dijet event divided into two hemispheres $a$ and $b$ with two light-cone directions $n^\mu$ and $\bar{n}^\mu$ . The SCET degrees of freedom are color-coded. Collinear radiation is shown in blue within the jet boundary and ultra-soft radiation is shown in green. The underlying hard interaction is shown in red. . . . .	63
3.6	Modes of SCET <sub>I</sub> (a) and SCET <sub>+</sub> (b) plotted on curves of constant virtuality $p^2$ of the hard, collinear, collinear-soft, and ultra-soft modes. The relevant power counting parameter $\lambda$ is shown in each case. In (b), the diagonal line represents a line of constant rapidity representing the boundary of a jet of radius parameter $R$ . . . . .	64
4.1	The information encoded in the fragmentation function as defined in Eq. (4.1) where the $d\hat{\sigma}_i$ describes the short-distance partonic process and the right hand side of the diagram, encoded by the $D_{i \rightarrow h}$ , describes the non-perturbative hadronization of the parton. . . . .	78
4.2	This plot [31] shows simulated results from Pythia for thrust distributions for selected 2-pion pairs at the $\Upsilon(4S)$ resonance of $\sqrt{s} = 10.58$ GeV. Shown are $e^+e^- \rightarrow B^+B^-$ (open diamonds), $e^+e^- \rightarrow B^0\bar{B}^0$ (open circles), $e^+e^- \rightarrow c\bar{c}$ events (full triangles), and $e^+e^- \rightarrow q\bar{q}$ for light-quarks $q \in u, d, s$ (full squares). The plot is normalized to the total number of events in all channels and the vertical green line shows the thrust cut $T > 0.8$ . . . . .	79

4.3	The information encoded in the fragmenting jet function as originally defined for measured jet invariant mass $\mathcal{G}(s, z, \mu)$ . A parton $i$ perturbatively splits off quarks/gluons and becomes a jet of invariant mass $s$ . The initial splittings are large angle/high virtuality and are described perturbatively by the $\mathcal{J}_{ij}(s, z, \mu)$ . At lower parton virtualities, the non-perturbative effects become important, at which point the emissions are described by the FFs, $D_{i \rightarrow h}(z/x, \mu)$ . . . . .	80
4.4	Feynman diagrams that give non-scaleless contributions to the quark FJF at NLO in $\alpha_s$ . Diagram (b) also has a mirror image that is not explicitly shown. . . . .	85
4.5	Non-scaleless diagrams that contribute to the gluon FJF at NLO. Again, diagram (b) has a mirror image that is not explicitly drawn above. . . . .	85
4.6	We consider $1 \rightarrow 2$ splittings at NLO with the momenta shown. A delta function then provides the measurement of the invariant mass, angularity, etc. . . . .	89
4.7	Real gluon emission diagrams that contribute to the collinear-soft function $S_C^i(\mathbf{p}_\perp, z, \mu, \nu)$ at $\mathcal{O}(\alpha_s)$ . The gluons passing through the shaded oval indicate they are contained within the phase-space of the jet. . . . .	107
5.1	The $z$ distributions for $d\sigma(\tau_0, z)$ at $\tau_0 = (1.5, 2.0, 2.5) \times 10^{-3}$ for analytic calculations with theoretical uncertainties (from varying the scale $\mu$ up and down by a factor of 2) are shown in green. Monte Carlo simulations using Madgraph + PYTHIA and Madgraph + Herwig are shown as black and red lines, respectively. . . . .	119
5.2	Analytic results for the $z$ distributions of $d\sigma(\tau_0, z)$ at $\tau_0 = (1.5, 2.0, 2.5) \times 10^{-3}$ . The orange curve is calculated using characteristic scale for the measured jet function does not depend on $z$ whereas the green curve uses a scale that does depend on $z$ (as in Fig. 5.1). . . . .	122
5.3	Angularity distributions of $d\sigma(\tau_a, z)$ for $a = 0$ at $z = 0.4, 0.6, 0.8$ . Analytic results are shown as green bands. Monte Carlo results are shown as black lines for Madgraph + PYTHIA and red lines for Madgraph + Herwig. . . . .	123
5.4	Angularity distributions of $d\sigma(\tau_a, z)$ for $a = 0$ at $z = 0, 1, 0.3, 0.5, 0.7$ . Analytic calculations are shown as red (green) bands for the ${}^3S_1^{(8)}$ ( ${}^1S_0^{(8)}$ ) production mechanisms. Results from Madgraph + PYTHIA are shown as red (green) dashed lines for the same mechanisms. . . .	126

5.5	Angular distributions of $d\sigma(\tau_a, z)$ for $a = +1/2, 0, -1/2, -1$ at $z = 0.5$ . Analytic calculations are shown as red (green) solid lines for the ${}^3S_1^{(8)}$ ( ${}^1S_0^{(8)}$ ) production mechanisms. Results from Madgraph + PYTHIA are shown as red (green) dashed lines for the same mechanisms.	127
5.6	A diagrammatic representation of how default PYTHIA handles the showering of octet-onia states, via gluon emissions from a $c\bar{c}$ state with probability $2P_{qq}(z)$ . This creates an energy distribution that is, ultimately, much harder than analytic calculations due to the structure of $P_{qq}$ splitting function.	129
5.7	A diagrammatic representation of how gluon-fragmentation-improved-PYTHIA (GFIP) handles the showering and hadronization of quarkonium states, by mimicing our analytic picture of the evolution and fragmentation of a gluon. A hard-scale gluon is showered down by PYTHIA to the scale $\sim 2m_c$ . The final state gluon energy distribution is then convolved with the leading-power NRQCD gluon FFs.	131
5.8	$z$ distributions of $d\sigma(\tau_a, z)$ for NLL' analytic calculations (colored bands), PYTHIA (colored dashed lines), and GFIP (solid black lines) for fixed values of $\tau_0 = (4, 5, 6) \times 10^{-3}$ .	132
5.9	The TMDFJF as a function of the $p_\perp$ of the $J/\psi$ for the ${}^3S_1^{[1]}, {}^3S_1^{[8]}, {}^1S_0^{[8]}, {}^3P_J^{[8]}$ production mechanisms for jet energies $E_J = 100$ GeV. Theoretical uncertainties are calculated by varying the renormalization scales by factors of 1/2 and 2.	139
5.10	The TMDFJF as a function of the $p_\perp$ of the $J/\psi$ for the ${}^3S_1^{[1]}, {}^3S_1^{[8]}, {}^1S_0^{[8]}, {}^3P_J^{[8]}$ production mechanisms where the jet energies $E_J = 500$ GeV. Theoretical uncertainties are calculated by varying the renormalization scales by factors of 1/2 and 2.	140
5.11	The TMDFJF as a function of the $z$ of the $J/\psi$ for the ${}^3S_1^{[1]}, {}^3S_1^{[8]}, {}^1S_0^{[8]}, {}^3P_J^{[8]}$ production mechanisms, with $p_\perp = 10$ GeV for $E_J = 100$ and 500 GeV. Theoretical uncertainties are calculated by varying the renormalization scales by factors of 1/2 and 2.	141
5.12	The quantity $f_\omega^{J/\psi}(z)$ (as defined in the text) as a function of $z$ relative to the jet axis for each NRQCD production mechanism where the jet has $E_J = \omega/2 = 100$ GeV (left) and 500 GeV (right). The $J/\psi$ is restricted to have $p_\perp \in [5, 20]$ GeV in the 100 GeV jet and $p_\perp \in [5, 60]$ GeV in the 500 GeV jet.	142

5.13	Differential cross section for prompt $J/\psi$ production within jets as a function of $z(J/\psi)$ , the fraction of the jet's transverse momentum carried by the $J/\psi$ produced within it as shown in Ref. [32]. The distribution is normalized such that the total sum of the bin heights is 1. The plot also shows a leading-order NRQCD-based prediction from PYTHIA as well as a breakdown of the PYTHIA contributions into single and double parton scattering contributions. . . . .	144
5.14	PYTHIA predictions for $c$ quark and gluon $z$ distributions (where $z$ is the fraction of the energy of the parton initiating the jet) after showering to the scale $2m_c$ . . . . .	145
5.15	Predicted $z(J/\psi)$ distribution using GFIP (gray) and FJF (red) for the three choices of LDME in Table 5.4 and the LHCb measurements of $z(J/\psi)$ . . . . .	148
A.1	Relevant pieces of the NRQCD Lagrangian with estimates of their scaling in the power counting parameter $v$ as seen in [33]. . . . .	155
A.2	Estimates of values of relevant scales in NRQCD for charmonium where $v_{c\bar{c}} \sim 0.3$ as seen in [33]. . . . .	156
B.1	Visualization of re-parameterizations of the of the light-cone directions $n$ and $\bar{n}$ via RPI <sub>I</sub> (a) and RPI <sub>II</sub> (b). Along with RPI <sub>III</sub> , which can be thought of as boosts, these transformations are an important symmetry of $\mathcal{L}_{\text{SCET}}$ . . . . .	159
D.1	Profile functions for $\mu_S^{PF}(\tau_0)$ and $\mu_J^{PF}(\tau_0)$ , the $\tau_0$ -dependent renormalization scales that we use in the scale variations of our measured soft function and measured jet function. Also shown are traditional scale variations done by varying $\mu$ by $\pm 50\%$ . . . . .	170

# List of Abbreviations and Symbols

## Symbols

$\Lambda_{\text{QCD}}$	The scale at which QCD becomes non-perturbative. Usually assumed to be $\approx 500$ MeV.
$Q\bar{Q}$	A heavy quark-antiquark pair such as $c\bar{c}$ or $b\bar{b}$ .
$\mathcal{Q}$	A real quarkonium state with physical quantum numbers.
${}^{2S+1}L_J^{[c]}$	Spectroscopic notation used to classify quarkonium states where $L$ and $S$ are the orbital and spin angular momenta, respectively and $J = L + S$ . $[c]$ is either $[1]$ for color-singlet states or $[8]$ for color-octet states.
$X$	Symbol used to represent inclusive set of particles.
$\mathbf{p}_\perp$	A transverse momentum relative to a jet axis.
$p_T$	A transverse momentum relative to a beam axis.
$\tau_a$	The angularity, a family of jet-substructure observables parameterized by $a < 1$ .
$H$	Generally refers to a hard function in context of SCET. Calculated via square of matching coefficients.
$S$	Generally a soft function or ultra-soft function, describing cross-talk radiation between jets in SCET.
$J$	Generally a jet function, describing highly boosted radiation collinear to some jet axis in SCET.
$\otimes$	Additive convolution $g \otimes F = \int dx dy F(x)g(y)\delta(z - (x + y))$ .
$\bullet$	Multiplicative convolution $g \otimes F = \int dx dy F(x)g(y)\delta(z - (xy))$ .
$R_{\mathcal{Q}}(0)$	A radial wave-function for the quarkonium state $\mathcal{Q}$ evaluated at the origin.

b	The Fourier conjugate of the transverse momentum $p_{\perp}$ that is sometimes called the impact parameter in the literature.
$\mathcal{G}_i^j(s, z, \mu)$	The fragmenting jet function for measured invariant mass of a jet $s$ . This parameter can be replaced with other measurements of observables.
$\mathcal{J}_{ij}$	Perturbatively calculable matching coefficients of fragmenting jet functions onto fragmentation functions.
$\lambda_{\theta}$	Polar anisotropy parameter. Calculated using amplitudes for producing hadrons in certain polarization state.

## Abbreviations

LHC	Large Hadron Collider. The 14 TeV $pp$ collider at CERN in Geneva, Switzerland. Currently, the most powerful particle accelerator in the world.
CM	Center-of-mass frame.
SM	Standard Model of Particle Physics
BSM	Beyond-the-standard-model physics.
QFT	Quantum Field Theory, a relativistic generalization of quantum mechanics that is the main theoretical tool of particle physics.
QED	Quantum Electrodynamics, the well-established quantum theory of relativistic electromagnetic interactions.
QCD	Quantum Chromodynamics, the modern theory of the strong nuclear force.
EFT	Effective Field Theory. Generally derived from a parent full theory, EFTs focus on particular degrees of freedom in a problem to make high-precision calculations much easier.
CKM	Cabibbo-Kobayashi-Maskawa matrix. Contains strengths of couplings of different quark flavors in weak decays.
NRQCD	Non-relativistic QCD. The state-of-the-art EFT for describing the phenomenology of heavy quarkonium.
LDME	Long Distance Matrix Element. In NRQCD, these describe the non-perturbative long-distance evolution of $Q\bar{Q}$ states into physical quarkonium states $\mathcal{Q}$ .

BNL	Brookhaven-National Laboratory.
ATLAS	A Toroidal LHC Apparatus, an experiment at the LHC.
CMS	Compact Muon Solenoid, a competing experiment at the LHC with ATLAS.
SLAC	Stanford-Linear-Accelerator-Center.
SPEAR	Stanford Positron Electron Accelerating Ring, a 4 GeV $e^+e^-$ collider built in 1972.
JADE	Japan, Deutschland, and England, an international collaboration established in 1977.
CDF	The Collider-Detector at Fermilab. An experiment that collided $p\bar{p}$ pairs at the Tevatron.
FCNC	Flavor changing neutral currents. Weak decays mediated by neutral $Z^0$ bosons that do not preserve quark flavor.
GIM	Glashow-Iliopoulos-Maiani mechanism that explains the suppression of FCNCs via a symmetry between lepton and quark families.
CSM	Color-singlet model. One of the first attempts at a theory of quarkonium production. Was shown to have significant, unrecconcilable flaws.
SCET	Soft-Collinear Effective Theory. The modern EFT used to describe jet physics at high-energy colliders. Ideal for studying jet production processes.
PDF	Parton Distribution Functions. These describe the distribution of momenta of partons within a hadron.
FF	Fragmentation Functions. They describe the probability of partons fragmenting into hadrons (or partons) with a certain momentum fraction.
FJF	Fragmenting Jet Functions. These are used to describe particular hadrons created inside of a jet of certain properties.
TMD	Transverse Momentum Dependent.
TMDFJF	Transverse Momentum Dependent Fragmenting Jet Function. Generalizes FJF to observables dependent upon a hadron's angle with a particular jet axis.

RGE	Renormalization Group Equations. These describe the evolution of various probability functions (usually in a factorization theorem for a cross-section) with the renormalization scale $\mu$ .
RRGE	Rapidity Renormalization Group Equations.
DGLAP	Dokshitzer-Gribov-Lipatov-Altarelli-Parisi equations. The names given to the RGEs for which the evolution kernel are the QCD splitting functions $P_{ij}$ .
GFIP	Gluon-fragmentation-improved-PYTHIA. A modification of the PYTHIA Monte Carlo that aims to properly implement gluon fragmentation to $J/\psi$ .
LO/NLO	Leading order and next to leading order. Generally used to describe fixed-order perturbative calculations in some coupling.
LL/NLL	Leading and next-to-leading logarithmic order, which describe the powers of large logarithms resummed using RG techniques.
IR	Infrared-red, generally referring to divergences appearing in the small energy/momentum limit.
UV	Ultra-violet, generally referring to divergences appearing in the large energy/momentum limit.
IRC	Infrared-Collinear-Safety, which describes a property where an observable (in our case a jet algorithm) is safe in both the collinear and IR limits.
LP	Leading-power. This is generally used to describe an EFT where only terms at lowest order in some power counting parameter are considered.

# Acknowledgements

Without the support of many wonderful individuals, my goal of obtaining a Ph.D. in physics would have never been realized. I must first thank my father, Reg, for fostering my interest in physics when I was barely old enough to say the word “proton” and to my mother, Erin, for instilling in me the focus, drive, and discipline that pursuing a career in science requires. I must also thank Milind Purohit of the University of South Carolina for giving me a chance to get involved in particle physics research while still in high school. Additionally, I must thank my thesis advisor, Tom Mehen, for being a fantastic mentor and collaborator. Tom has always offered his time for discussions and is an endless source of creative research ideas. I thank all of my collaborators, including Yiannis Makris, Lin Dai, Andrew Hornig, and Adam Leibovich, from whom I have learned a great deal about physics and who were quite fun to work with. I thank my brothers, Connor, Quentin, and Ian as well as Douglas Brown, Garrett Barkley, and Jim Talbert for being great sources of encouragement. I must also acknowledge the generous financial support of the National Science Foundation Graduate Research Fellowship program, the Dept. of Energy Office of Science, and Los Alamos National Laboratory. Finally, I want to thank Sarah Evans for her positivity, thoughtfulness, and unwavering support for all of my endeavors.

# 1

## Introduction

Experiments at the Large Hadron Collider (LHC), shown in Fig. 1.1 aim to answer a number fundamental questions in physics. What is the origin of mass? Do extra dimensions of space exist? What is the nature of dark matter? Can the theories of the strong and electro-weak forces be described by an underlying Grand-Unified-Theory? While many of the exciting discoveries that may be made at the LHC involve the search for new particles, this thesis will focus on uncovering the origins of an old one. The  $J/\psi$  was discovered nearly a half-century ago in 1974, providing the first experimental evidence of a 4th *charm* quark and confirming several key predictions of the evolving theory of the strong force, Quantum Chromodynamics (QCD). Although its discovery was a major milestone for particle physics, as we will discuss in Chapter 2, its production is, ironically, still not well-understood. This thesis develops a new formalism with which to study how  $J/\psi$  are produced at the extreme conditions of the LHC. In this introduction, we will briefly review the basic ideas of the Standard Model and the theory of QCD. We will then discuss the essential ideas of resummation and effective theories, two approaches to quantum field theoretic calculations which will be important for a proper understanding of



FIGURE 1.1: The Large Hadron Collider (LHC), a 14 TeV center-of-mass energy proton-proton collider in Geneva, Switzerland. Image courtesy of <https://home.cern/topics/large-hadron-collider>.

later chapters.

## 1.1 Quantum Chromodynamics

Our knowledge of elementary particle physics is encapsulated by the Standard Model (SM). The SM describes the quantum behavior of the electromagnetic force and strong and weak nuclear forces through the interaction of the elementary particles shown in Fig. 1.2. The elementary particles fall into two general categories: fermions, particles with half-integer spin that obey Fermi-Dirac statistics and bosons, integer-spin particles that obey Bose-Einstein statistics. Fermions can then be divided into leptons, elementary particles such as the electron and its corresponding neutrino, and quarks such as the up and down. Quarks and leptons bind together to form atoms, the building blocks of everyday matter. Atomic nuclei consist of protons and neutrons, which are made of combinations of up and down quarks. Bosons are divided into vector bosons, particles such as the photon and gluon whose exchange mediates forces, and scalar bosons which include the recently discovered Higgs, which is responsible for giving particles mass. Each elementary particle carries a set of

# The Standard Model of Particle Physics

Fermions			Bosons		
Mass	2.3 MeV	1.275 GeV	173.07 GeV	0 eV	125.09 GeV
Charge	2/3	2/3	2/3	0	0
Spin	1/2	1/2	1/2	1	0
	$u$ up	$c$ charm	$t$ top	$\gamma$ photon	$H$ Higgs
Quarks	4.8 MeV -1/3 1/2	95 MeV -1/3 1/2	4.18 GeV -1/3 1/2	0 eV 0 1	Scalar Bosons
	$d$ down	$s$ strange	$b$ bottom	$g$ gluon	
	0.511 MeV -1 1/2	105.67 MeV -1 1/2	1.7768 GeV -1 1/2	80.39 GeV 0 1	
Leptons	$e$ electron	$\mu$ muon	$\tau$ tau	$W^\pm$ W boson	Vector Bosons
	$\nu^e$ electron neutrino	$\nu^\mu$ muon neutrino	$\nu^\tau$ tau neutrino	$Z^0$ Z boson	
	<2.2 eV 0 1/2	<1.7 MeV 0 1/2	<15.5 MeV 0 1/2	91.19 GeV 0 1	

FIGURE 1.2: The elementary particles described by the Standard Model of Particle Physics (SM).

intrinsic properties which are described by their quantum numbers, some of which are shown in Fig. 1.2.

This work will largely focus on how quarks (specifically the charm quark) and gluons interact via the strong force as described by QCD. The stem *chromo* in QCD refers to a special quantum number held by quarks and gluons (the vector boson or force carrier particle of the strong force) called color. Each quark (anti-quark) carries one of three colors (anti-colors) which include red ( $r$ ), blue ( $b$ ), and green ( $g$ ), and each gluon carries some linear combination of color and anti-color such as  $(r\bar{b} + b\bar{r})/\sqrt{2}$ . Quarks and gluons form bound states called hadrons. Hadrons are

further divided into mesons, bound states whose quantum numbers can be formed by  $q\bar{q}$  pairs, and baryons, whose quantum numbers are determined by combinations of  $qqq$  or  $\bar{q}\bar{q}\bar{q}$ . In recent years, more exotic quark states such as the tetraquark and pentaquark have also been observed [34].

The Lagrangian of QCD is given by

$$\mathcal{L}_{\text{QCD}} = \sum_f \bar{q}_i (i\not{D}_{ij} - m_f \delta_{ij}) q_j - \frac{1}{4} G_{\mu\nu}^a G_a^{\mu\nu}, \quad (1.1)$$

where  $\sum_f$  is a sum over quark flavors (up, down, etc.),  $m_f$  is the quark mass,  $i, j$  represent indices in color-space,  $\delta_{ij}$  is a Kronecker delta in color-space, and  $a$  is an index of the adjoint representation of the Lie group  $SU(3)$  (for color-space). The gauge covariant derivative is given by

$$\not{D}_{ij} = \gamma^\mu (\partial_\mu \delta_{ij} + i g_s T_{ij}^a A_\mu^a), \quad (1.2)$$

where  $g_s$  is the strong coupling constant, the matrices  $T^a$  are generators of  $SU(3)$  and  $A_\mu^a$  is the gauge field (the gluon). The gauge field strength tensor is given by

$$G_{\mu\nu}^a = \partial_\mu A_\nu^a - \partial_\nu A_\mu^a - g_s f_{abc} A_\mu^b A_\nu^c \quad (1.3)$$

where  $f_{abc}$  are the structure constants of  $SU(3)$  defined via the commutation relation

$$[T_a, T_b] = i f_{abc} T_c. \quad (1.4)$$

A key feature of QCD lies in the nature of its coupling constant, which in perturbative calculations is generally expressed via  $\alpha_s = g_s^2/4\pi$ . In quantum field theory (QFT), coupling constants run with the renormalization scale  $\mu$ . This scale is generally chosen to be the dominant scale in the process such as the momentum transfer in a collision. By studying the basic interactions of quarks and gluons at one-loop, one can derive the QCD  $\beta$ -function, which describes the evolution of the coupling with

$\mu$ . The  $\beta$ -function is written as

$$\beta(\alpha_s) = \mu \frac{d\alpha_s}{d\mu} = -2\alpha_s \left[ \left( \frac{\alpha_s}{4\pi} \right) \left( \frac{11}{3}N_C - \frac{2}{3}N_f \right) + \mathcal{O}(\alpha_s^2) + \dots \right], \quad (1.5)$$

where  $N_C$  is the number of colors and  $N_F$  is the number of quark flavors. At this order, the  $\beta$ -function can be solved using separation of variables for the coupling as a function of the energy scale  $\mu \sim Q$

$$\frac{1}{\alpha_s(Q^2)} = \frac{1}{\alpha_s(Q_0^2)} + \frac{\beta_0}{4\pi} \log \left( \frac{Q^2}{Q_0^2} \right), \quad (1.6)$$

where  $\beta_0 = 11C_A - 2N_F/3$  where  $C_A = N = 3$  and where  $\alpha_s(Q^2)$  and  $\alpha_s(Q_0^2)$  are the coupling at two energy scales  $Q$  and  $Q_0$ . This coupling will vary widely and perturbation theory in  $\alpha_s$  will only be reliable when  $\alpha_s \ll 1$ . Let us define the scale at which the coupling is infinite as  $\Lambda_{\text{QCD}}$  and choose this as our starting scale  $Q_0 = \Lambda_{\text{QCD}}$ <sup>1</sup>

$$\alpha_s(\Lambda_{\text{QCD}}) = \infty \implies 1/\alpha_s(\Lambda_{\text{QCD}}) = 0 \implies \alpha_s(Q^2) = \frac{4\pi}{\beta_0 \log(Q^2/\Lambda_{\text{QCD}}^2)}. \quad (1.7)$$

The evolution of  $\alpha_s(Q^2)$  is shown in Fig. 1.3. For  $Q \gg \Lambda_{\text{QCD}}$ , QCD is perturbative and the coupling  $\alpha_s(Q^2)$  decreases with increasing  $Q^2$ . This phenomenon is called **asymptotic freedom** and says that at energies well above  $\Lambda_{\text{QCD}} \sim 0.5$  GeV, quarks and gluons are quasi-free particles. In this context, we often refer to quarks, anti-quarks, and gluons collectively as **partons**. The key consequence of asymptotic freedom is that at the extremely high energies of modern colliders, the perturbative expansion of QCD should have greater and greater accuracy. At energies below  $\Lambda_{\text{QCD}}$ , QCD is non-perturbative and the coupling becomes large. As we will discuss in Chapter 3, at these scales, partons exhibit **confinement** and are trapped in colorless

<sup>1</sup> The choice of  $\alpha_s(\Lambda_{\text{QCD}}) = \infty$  was for simplicity as one could just as easily pick  $\alpha_s(\Lambda_{\text{QCD}}) = 1$  or any other value that would not be suitable for a perturbative expansion.

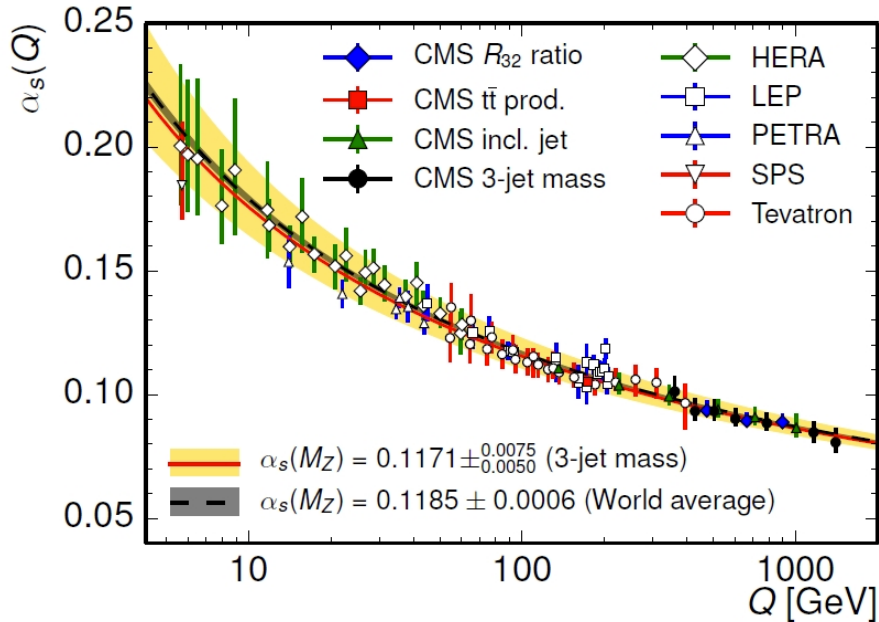


FIGURE 1.3: The running of the strong coupling  $\alpha_s(Q)$  as shown in Ref.[3] where the focus was extracting the strong coupling from 3-jet differential cross-sections as a function of the 3-jet invariant mass and the 3 jets with the highest transverse momenta are selected. The plot also shows previous measurements of  $\alpha_s$  and compares the 3-jet extraction with world averages of the coupling.

hadrons. This means that hadrons look like fundamental particles in scattering processes.

Much of this work is built upon the idea that high precision calculations of scattering cross-sections and decay rates can be made tractable through the use of **Effective Field Theories (EFTs)**. The concept of an EFT is quite simple: calculations in QCD can be made computationally simpler by removing degrees of freedom that are far above the energy scale of the physics one is interested in studying.

## 1.2 Effective Field Theories (EFT)

### 1.2.1 What is an EFT?

The computational complexity of QCD is often immense. This makes QCD ill-suited for many practical calculations of interesting phenomena. In practice, physicists

adopt effective approaches that focus on the dynamics of certain degrees of freedom in a particular energy regime. In introductory classical mechanics, calculations of everyday falling objects can be made simple by working under the assumption that the force of gravity on an object from the earth is constant. This is done by saying that, relative to the size and distance travelled of ordinary falling objects, the surface of the earth can be approximated as an infinite flat plane.

In the multipole expansion in classical electrodynamics, calculations of the electrostatic potential can be made simpler in the limit that  $r \gg s$  where  $s$  is the size of the distribution and  $r$  is the distance from the charge distribution at which the potential is calculated. By expanding the potential in  $s/r \ll 1$ , the distribution can be approximated as a point of charge  $Q$  at lowest order in the expansion. Corrections can then be systematically included as powers of  $\mathcal{O}(s^n/r^n)$  which contain finer details of the structure of the charge distribution. These terms containing successive powers of  $s/r$ , the **power counting** parameter, are referred to as the point charge ( $\mathcal{O}(1)$ ) term, the dipole moment ( $\mathcal{O}(s/r)$ ), quadrupole moment ( $\mathcal{O}(s^2/r^2)$ ), and so forth.

EFTs refer to effective descriptions of physics at particular energy/length scales as applied to QFTs such as QCD. This work will focus on two specific EFTs:

1. **Non-relativistic Quantum Chromodynamics (NRQCD)** — A well-established EFT which describes heavy mesons such as quarkonia (e.g.  $J/\psi(c\bar{c})$ ,  $\Upsilon(b\bar{b})$ , etc.) as non-relativistic bound states. We discuss NRQCD in depth in Chapter 2.
2. **Soft-Collinear Effective Theory (SCET)** — An EFT developed in the last 15 years that we will use to describe **jets**, tightly collimated sprays of highly boosted particles found in many events at high energy colliders. We introduce SCET in Chapter 3.

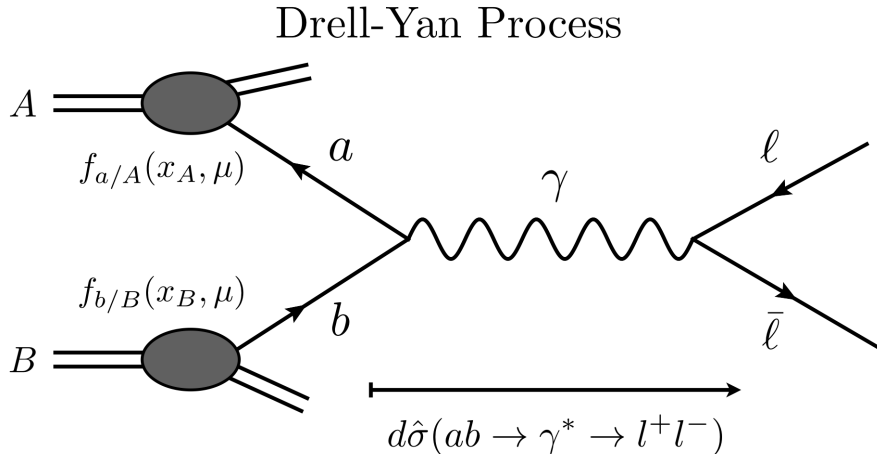


FIGURE 1.4: The Drell-Yan process can be factorized into PDFs for each incoming hadron and a partonic-cross section of the form  $d\hat{\sigma}(ab \rightarrow l^+l^-)$  which can be calculated in perturbation theory.

We will now briefly discuss three important concepts in EFT calculations: the factorization of observables, the basics of constructing an EFT, and the resummation of potentially large logarithms using renormalization group equations (RGE).

### 1.2.2 Factorization of Observables

The concept of **factorization** is fundamental to most applications of QCD. Observables such as cross-sections are said to factorize if they can be calculated as a product or convolution of perturbatively calculable functions and universal non-perturbative pieces. The term universal here implies that the function is independent of the process and can thus be used in other related calculations. Factorization theorems also separate observables into functions describing physics at several well-separated energy scales. An example of a well-known factorization theorem in high-energy physics is the hard-scattering of hadrons in the Drell-Yan process  $A+B \rightarrow l^+ + l^- + X$  where  $A$  and  $B$  are hadrons,  $l^+, l^-$  are leptons, and  $X$  represents any other leptons/hadrons. Fig. 1.4 shows this process at lowest order. Ref. [35] proved that the cross-section

can be written (to all orders in perturbation theory) as

$$\frac{d\sigma(AB \rightarrow \ell^+\ell^-X)}{dQ^2dy} = \sum_{a,b} \int dx_A dx_B f_{a/A}(x_A, \mu) f_{b/B}(x_B, \mu) \frac{d\hat{\sigma}(ab \rightarrow \ell^+\ell^-X)}{dQ^2dy}, \quad (1.8)$$

where  $f_{a/A}(x_A, \mu)$  and  $f_{b/B}(x_B, \mu)$  are parton distribution functions (PDF) which give the density of the parton  $a(b)$  with momentum fractions  $x_A(x_B)$  of the hadrons  $A(B)$ . The  $d\hat{\sigma}/dQ^2dy$  is the partonic cross-section differential in the invariant mass  $Q^2$  of the  $\ell^+\ell^-$  pair and the rapidity  $y$  of the lepton pair. This partonic cross-section is calculable in perturbative QCD and governs high-energy scale physics. The PDFs are universal non-perturbative functions describing low-energy fluctuations that must be extracted from experiment. The factorization scale  $\mu$  essentially separates the high and low energy regimes and is chosen to be of the order of the hard scale  $Q$  in order to minimize potentially large logarithms. All-orders factorization theorems in QCD are complex and have only been rigorously proven in a small number of cases. We will see how factorization theorems play a key role in EFTs in the following sections.

### 1.2.3 Constructing Effective Theories

Perturbative calculations of processes that contain several different physical scales (such as particle masses, momentum cut-offs, etc.)  $\mu_1, \mu_2, \dots$  inevitably involve logarithms of ratios of these scales  $\log(\mu_1/\mu_2), \dots$ . In certain regions of phase space, these physical scales may be widely separated  $\mu_1 \ll \mu_2$ , causing these logarithms to become large. Let us consider the example of the weak decay of  $D^0 \rightarrow K^- + \pi^+$ . At the partonic level, this process looks like  $(c\bar{u}) \rightarrow (s\bar{u}) + (u\bar{d})$  where the  $\bar{u}$  acts as a spectator quark. The lowest order amplitude for this process can be written as

$$\begin{aligned} \mathcal{M}(c \rightarrow su\bar{d}) &= \left(\frac{g_2}{\sqrt{2}}\right)^2 V_{cs}V_{ud}^* \frac{1}{k^2 - m_W^2} \left(g^{\mu\nu} - \frac{k^\mu k^\nu}{m_W^2}\right) \\ &\times [\bar{u}(p_s)\gamma_\mu P_L u(p_c)] [\bar{u}(p_u)\gamma_\nu P_L v(p_{\bar{d}})], \end{aligned} \quad (1.9)$$

where  $g_2$  is the weak coupling constant,  $p_{c,s,u,\bar{d}}$  are quark external momenta,  $V_{ij}$  are elements of the CKM matrix,  $k_\mu$  is the exchanged 4-momentum,  $m_W$  is the mass of the  $W$ -boson, and  $u, v, \bar{u}, \bar{v}$  are Dirac spinors. To make calculations simpler, we can work in the limit that  $k^2 \ll m_W^2$  since the final state quarks need to be within bound states. This allows us to expand the propagator by writing the propagator as  $-1/m_W^2(1 + \mathcal{O}(k^2/m_W^2))$  yielding

$$\mathcal{M}(c \rightarrow s u \bar{d}) \approx -\frac{4G_F}{\sqrt{2}} V_{cs} V_{ud}^* [\bar{u}(p_s) \gamma_\mu P_L u(p_c)] [\bar{u}(p_u) \gamma_\nu P_L v(p_{\bar{d}})], \quad (1.10)$$

where  $G_F/\sqrt{2} = g_2^2/(8m_W^2)$  is the so-called Fermi constant. By expanding the propagator, we have removed the  $W$ -boson as a degree of freedom from the theory, replacing it with a four-fermion interaction. This amplitude can be calculated in a simpler version of the full weak theory where tree-level diagrams are replaced with four-point interactions from an effective theory of the weak force as shown in Fig. 1.5. High-energy degrees of freedom are removed and an EFT is established through a procedure called **matching**.

The Lagrangian of this EFT is first constructed by considering the most general  $\mathcal{L}^{\text{EFT}}$  whose terms satisfy basic desired symmetries. This will take the form

$$\mathcal{L}^{\text{EFT}} = -\frac{4G_F}{\sqrt{2}} V_{cs} V_{ud}^* \sum_j C_j(\mu) \mathcal{O}_j^{\text{EFT}}(\mu), \quad (1.11)$$

where in this case there will be 2 such 4-quark operators,  $\mathcal{O}_j^{\text{EFT}}$ , and  $C_j(\mu)$  are perturbatively calculable coefficients that describe physics at the scale  $m_W$ . These coefficients for each of the terms in the EFT Lagrangian are extracted through a **matching calculation**. This procedure involves comparing calculations of the same physical quantity in the full theory and EFT. At tree-level, this matching is trivial (see Fig. 1.5) and yields coefficients of 1. At one-loop level, the matching calculation involves diagrams containing single gluons connecting the external quark lines and

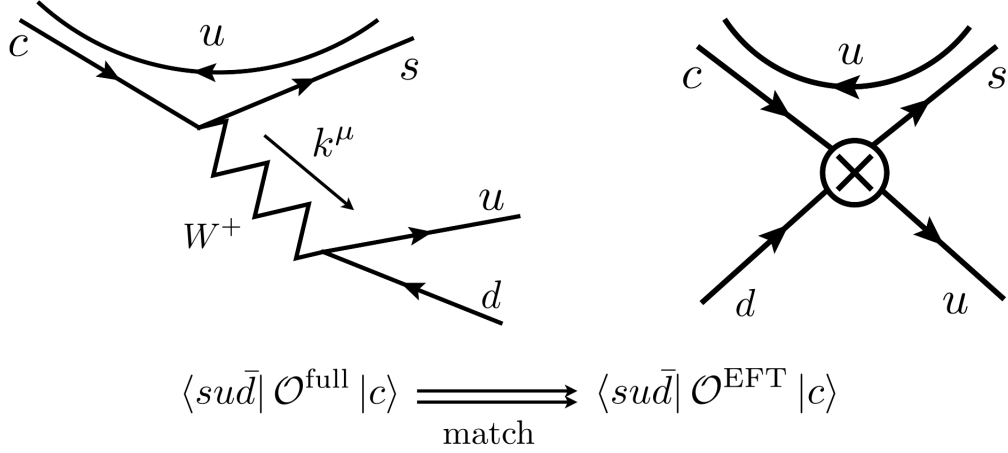


FIGURE 1.5: An example of how a full theory tree-level process is matched onto a tree-level EFT process for the  $D^0 \rightarrow K^- \pi^+$  example at the quark level described in the text. A one-loop matching procedure would involve additional diagrams that connect quark lines with a gluon.

looks, schematically, like

$$\begin{aligned}
 \langle sud\bar{d} | \mathcal{L}^{\text{full}} | c \rangle^{(1)} &= \langle sud\bar{d} | \mathcal{L}^{\text{EFT}} | c \rangle^{(1)} \\
 &= \sum_j \left[ C_j^{(0)}(\mu) \langle sud\bar{d} | \mathcal{O}_j^{(1)}(\mu) | c \rangle + C_j^{(1)}(\mu) \langle sud\bar{d} | \mathcal{O}_j^{(0)}(\mu) | c \rangle \right], \quad (1.12)
 \end{aligned}$$

where (0) and (1) denote leading-order (LO) and next-to-leading-order (NLO) contributions, respectively. The matching coefficients in this case look like  $C_j(\mu) = 1 + \mathcal{O}[\alpha_s(m_W)]$ . Having written down an effective Lagrangian and performed the matching at a given order in  $\alpha_s$ , we now have the essential elements needed for constructing an EFT.

### 1.2.4 Resummation of Logarithms

The matrix element  $\langle s\bar{u}\bar{d} | \mathcal{L}^{\text{full}} | c \rangle$  can ultimately be written in the following schematic form

$$\begin{aligned} \langle f | i\mathcal{L}^{\text{full}} | i \rangle &\sim 1 + \alpha_s L + \alpha_s^2 L^2 + \alpha_s^3 L^3 + \dots \\ &+ \alpha_s + \alpha_s^2 L + \alpha_s^3 L^2 + \dots \\ &+ \alpha_s^2 + \alpha_s^3 L + \dots \end{aligned} \quad (1.13)$$

where one can show that  $L \sim \log(m_W^2/m_c^2)$  where  $m_c$  is the charm quark mass. Since  $m_c \ll m_W$ , powers of the logarithms,  $L$ , are generally large enough such that  $L \sim 1/\alpha_s$ .<sup>2</sup> Thus, powers of  $\alpha_s^n L^m \sim \alpha_s^{n-m}$  become increasingly important and can spoil perturbation theory. However, higher powers of these logarithms can be included without performing the full calculation at  $n$ -loops through the use of RGEs.

RGEs can be used to **resum** these logarithms in a simple but powerful way. In the full theory, the matrix elements contain powers of  $L$ , a logarithm of a ratio of scales. Thus no single choice of the renormalization scale  $\mu$  will minimize all of the large logarithms. However, in our EFT formalism, matrix elements of the full theory are factorized via

$$\langle s\bar{u}\bar{d} | i\mathcal{L}^{\text{EFT}} | c \rangle = C_j(\mu) \langle s\bar{u}\bar{d} | \mathcal{O}_j^{\text{EFT}}(\mu) | c \rangle \quad (1.14)$$

$$= \left( 1 + \alpha_s \log\left(\frac{m_W^2}{\mu^2}\right) + \dots \right) \left( 1 + \alpha_s \log\left(\frac{\mu^2}{m_c^2}\right) + \dots \right). \quad (1.15)$$

The logarithms  $L$  have now been factorized into two separate logarithms that are independently minimized by the choices of  $\mu = m_W$  in the coefficients  $C_j(\mu)$  and  $\mu = m_c$  in the matrix elements of  $\mathcal{O}_j^{\text{EFT}}(\mu)$ . We can simultaneously resum powers of both of these logarithms using RGEs. In the one-loop calculation, the UV poles in the EFT can be used to derive RGEs for the  $C_j(\mu)$  coefficients

$$\mu \frac{d}{d\mu} C_j(\mu) = \gamma_{ji}^C C_i(\mu), \quad (1.16)$$

---

<sup>2</sup> Here, the external momentum  $p_c$  has been put on-shell.

where, as shown in Appendix C,  $\gamma_{ji}$  is the coefficient's **anomalous dimension** which is in this case a  $2 \times 2$  matrix calculated to a given order in perturbation theory.<sup>3</sup> Let us ignore the indices  $i, j$  for the purpose of clarity. Solving this RGE then yields an equation of the form

$$C(\mu) = \exp \left[ \int_{\alpha_s(\mu)}^{\alpha_s(m_W)} \frac{d\alpha}{\beta(\alpha_s)} \gamma^C(\alpha_s) \right] C(m_W) = U_F(\mu, m_W, \gamma^C) C(m_W), \quad (1.17)$$

where  $C(\mu)$  and  $C(m_W)$  are coefficients evaluated at two different scales. This describes the evolution of the coefficients from the scale at which their logs are minimized down to an arbitrary scale  $\mu$ , which can ultimately be set to  $\mu = m_c$ . In our EFT where we have essentially interpreted  $m_W = \infty$ , this running down to the scale  $m_c$  resums large logarithms of  $m_W^2/m_c^2$ . If the anomalous dimensions are calculated at lowest order, we can see explicitly how these logarithms are resummed by expanding the evolution kernel

$$U_F(\mu, m_W, \gamma^C) \sim 1 + \alpha_s L + \alpha_s^2 L^2 + \alpha_s^3 L^3 + \dots, \quad (1.18)$$

This shows that the logarithms of the form  $\alpha_s^n L^m$  for  $n = m$ , corresponding to the first row of Eq. (1.13), have been included without doing an  $n$ -loop calculation. This is called leading-logarithmic (LL) resummation and it requires that the anomalous dimension and QCD beta function be known to 1-loop order. Higher orders of resummation would include additional rows of Eq (1.13). The second and third rows, for example, shows the form of logs that would be included in next-to-leading-logarithmic (NLL) and next-to-next-to-leading-logarithmic (NNLL) resummation. Each subsequent row includes terms of order  $\alpha_s^n L^m$  where  $m = n, n - 1, n - 2, \dots$ . In Appendix C, Table C.1 contains additional details on the ingredients needed for various fixed order and resummed calculations.

<sup>3</sup> Anomalous dimensions are a feature of quantum theories that deal with the scaling dependence of Green's functions in the theory on the renormalization scale,  $\mu$ .

### 1.3 Outline of this Work

The remainder of this thesis will focus on the use of EFTs to study the production of the  $J/\psi$  in jets in  $e^+e^-$  and  $pp$  collisions. In Chapter 2, the history of quarkonium production theory is reviewed and the basic elements of NRQCD are discussed. In Chapter 3, we introduce the physics of jets and comment on how jet substructure is studied both analytically and experimentally. We then introduce SCET, a modern EFT used for calculating jet processes. Chapters 1, 2, and 3 cover background material that is important for understanding later chapters of this thesis. Chapters 4 and 5 then present the original results of the author with collaborators, much of which is published in Refs. [36–38].

Chapter 4 first reviews the Fragmenting Jet Function (FJF) formalism, which describes the energy distribution of a hadron produced within a jet where the substructure of that jet is measured. The formalism is extended to jets where the angularity (a jet substructure observable to be defined in Chapter 3) of the jet containing an identified hadron is measured in Section 4.4. FJFs are then extended to jets where the transverse momentum of a hadron in the jet relative to the jet axis is measured in Section 4.5. In both of these cases, one-loop perturbative calculations of matching coefficients of the FJFs onto traditional fragmentation functions (FFs) are performed.

In Chapter 5, the FJF formalism is applied to the study of  $J/\psi$  production. Using the perturbative results calculated in Section 4.4, a phenomenological FF extracted from  $e^+e^-$  for  $B$  mesons, and NRQCD FFs for  $J/\psi$ , we calculate resummed cross-sections for the production of these hadrons in jets where the angularity of the jet is measured. These analytic results are then compared with Monte Carlo simulations. While the  $B$  meson calculations are consistent with Monte Carlo predictions, the energy distributions for the  $J/\psi$  are not. A way to reconcile the discrepancy between

analytic and Monte Carlo results using a modification of the PYTHIA Monte Carlo is introduced, which has important implications for future quarkonium production calculations. The FJFs for jets that contain a hadron whose transverse momentum relative to the jet axis is measured are shown to be able to discriminate between different ways quarkonia are produced. Finally, we show that analytic results using the FJF formalism are consistent with recent measurements from the LHCb experiment, performing much better than state-of-the-art Monte Carlo simulations.

Appendix A discusses important scales and power counting rules in NRQCD. Appendix B then comments on key symmetries of the SCET Lagrangian. In Appendix C, renormalization group equations for different classes of functions are derived. Finally, Appendix D outlines properties of plus-distributions and profile functions, which were used in the calculations of Chapters 4 and 5.

## Quarkonium Production

### 2.1 Introduction & Brief History of Quarkonium

Quarkonia are quark-antiquark pairs bound together by the strong force. Studies of quarkonia typically focus on  $c\bar{c}$ , known as charmonium, and  $b\bar{b}$ , known as bottomonium. The large masses of the  $c, b$  quarks relative to the light quarks  $u, d, s$  make these heavy quarkonia (notated as  $Q\bar{Q}$ ) particularly interesting systems to study. As is discussed in Section 2.4 and Appendix A, heavy quarkonia are characterized by a number of scales, some of which are perturbative, and some of which are non-perturbative. For example, while the mass of a charm quark is large  $\sim 1.5$  GeV (a perturbative scale where  $\alpha_s \approx 0.35$ ), other relevant scales such the radial excitations of a charmonium state can scale as  $\sim 0.5$  GeV (a non-perturbative scale  $\sim \Lambda_{\text{QCD}}$  where  $\alpha_s \approx 0.7$ ).

A wide spectrum of both charmonium and bottomonium states have been observed experimentally and studied extensively. Ironically, although their discovery was one of the earliest triumphs of the quark model and of QCD, the production of quarkonia is still not well understood. In this chapter, we will first review the history

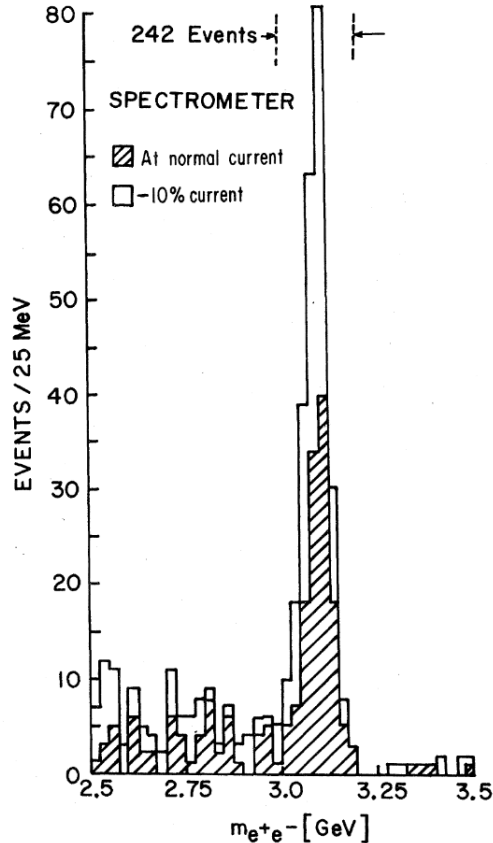


FIGURE 2.1: Original plot of the BNL group’s  $J/\psi$  mass peak at 3.1 GeV. Image taken from Ref. [4].

of quarkonium physics and introduce the basic spectroscopy of charmonium states. We will then discuss how our picture of the mechanisms of quarkonium production has evolved from the earliest models to the modern theory of non-relativistic QCD (NRQCD). Reviews of NRQCD can be found in Refs. [33, 39, 40].

The first experimental evidence of quarkonia was seen in 1974 with the discovery of the  $J/\psi$ , a charmonium state with mass 3.1 GeV (e.g. Fig. 2.1) and the same  $J^{PC} = 1^{--}$  quantum numbers as a photon. The  $J/\psi$  was found nearly simultaneously in decays to  $e^+e^-$  by Ting et al. [4] at Brookhaven National Laboratory’s Alternating Gradient Synchrotron and to  $\mu^+\mu^-$  by Richter et al. [41] at SLAC’s SPEAR experiment, hence the particle’s peculiar two-symbol name. Ting’s group

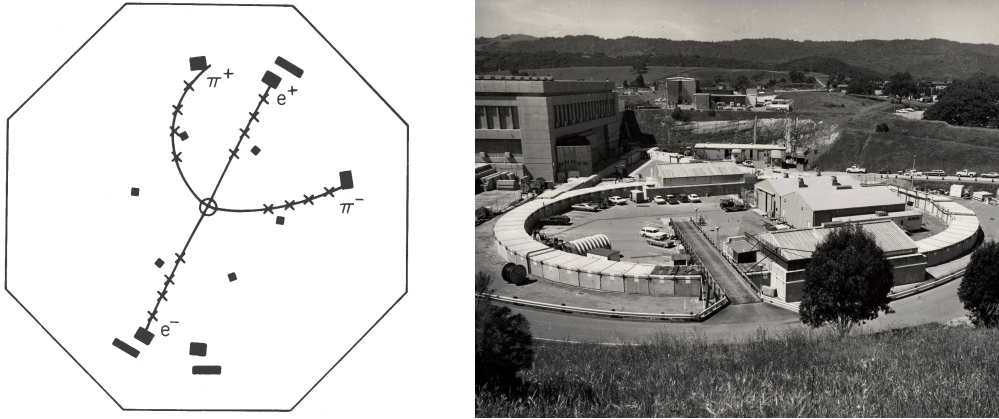


FIGURE 2.2: (Left) Computer reconstruction of the decay of the  $\psi(2S) \rightarrow J/\psi\pi^+\pi^-$  at the Mark 1 detector at the SPEAR experiment (shown on right). Courtesy SLAC National Accelerator Laboratory at <http://www.slac.stanford.edu/vault>.

named the new particle  $J$  supposedly because of its close resemblance to the Chinese character for Ting's name, while Richter's group named the state  $\psi$  for the shape of the decays shown in Fig. 2.2.

The discovery of the  $J/\psi$  was a major victory for the nascent form of what we now know as QCD. Followed just 10 days later by the discovery of the  $\psi(2S)$ , another resonant state of charmonium, the  $J/\psi$  discovery kicked off the so-called November Revolution. The  $J/\psi$  provided the most compelling evidence yet of the existence of the charm quark, which had been proposed 10 years earlier by Bjorken and Glashow in Ref. [42]. At the time, the charm quark was needed to confirm a number of theoretical phenomena including the GIM mechanism [43]. Proposed in 1970 by Glashow-Iliopoulos-Maiani, the GIM mechanism described a theory of weak interactions where flavor-changing neutral currents were highly suppressed. Flavor-changing neutral currents (FCNC) are weak interactions mediated by  $Z^0$  bosons that do not preserve flavor. This occurs, for example when an interaction converts  $s \rightarrow u$  in the decays of  $K_L \rightarrow \mu^+\mu^-$ . While these decays are highly suppressed<sup>1</sup>, before

<sup>1</sup> The branching fraction  $\text{Br}[K_L \rightarrow \mu^+\mu^-] = (6.84 \pm 0.11) \times 10^{-9}$  according to Ref. [44].

the proposal of the charm quark, this suppression was not predicted by the theory. The GIM mechanism restored a lepton-quark symmetry through the introduction of a 4th quark with a charge of  $2/3$ . This symmetry naturally suppresses contributions from FCNCs.

The first “open flavor” charmed particles (i.e. particles with one charm quark and one light antiquark) were then found in 1976, with the discovery of the 1865 MeV  $D^0(c\bar{u})$  (via decays to  $K\pi$ ) and eventually the  $D^\pm(c\bar{d}, \bar{c}d)$ . As all of these new particles could be predicted in the quark model proposed in the early 1960’s by Gell-Mann [45] and Zweig [46], their existence provided strong support for the idea that quarks are dynamical physical objects as opposed to merely a way to interpret a curious symmetry amongst particle masses and spins.

Just a few years later, in 1977, experimentalists at Fermilab [47] discovered the  $\Upsilon$ , a  $b\bar{b}$  bound state with a mass of around 9.5 GeV. This provided evidence for the bottom quark, the fifth quark overall and first in a third generation of quarks.<sup>2</sup> The  $\Upsilon(2S)$  was discovered shortly thereafter [49] and was the first of many additional  $b\bar{b}$  states that could be predicted by the quark model. Interestingly, the discovery of  $\Upsilon(2S)$  was published in the same issue of Physical Review Letters as Ref. [50], in which Steven Weinberg and George Sterman defined the modern concept of jets in QCD.

## 2.2 Spectroscopy and Basic Properties

Bound states of  $c\bar{c}$  were predicted to form a spectrum analogous to that of positronium ( $e^+e^-$  bound states), hence the name charmonium first proposed by Appelquist, et al., in Ref. [51]. Quarkonia are categorized according to their spin and angular momentum quantum numbers in spectroscopic notation of the form  $n^{2S+1}L_J$  where  $n$

---

<sup>2</sup> This kept intact the symmetry between quarks and leptons, as the bottom matched with the  $\tau$  lepton, which had been discovered in 1975 [48].

is the principal quantum number,  $S$  is the spin,  $L$  is the orbital angular momentum, and  $\vec{J} = \vec{L} + \vec{S}$  is the total angular momentum. Quarkonia are also often classified according to their  $J^{PC}$  quantum numbers, in which the parity is  $P = (-1)^{L+1}$  and the charge conjugation parity is  $C = (-1)^{L+S}$ .

There are a number of basic transitions/decays of charmonia. Above  $\sqrt{s} = 3.74$  GeV, charmonia are kinematically allowed to decay to  $D\bar{D}$  meson pairs ( $m_{D\bar{D}} = 3.74$  GeV). Below this  $D\bar{D}$  threshold, all of the charmonium states predicted by QCD have been observed experimentally. These particles tend to have very small widths and decay via electromagnetic/strong interactions to charged leptons/light hadrons and transition to lower mass quarkonium states. One example is the decay  $\psi(2S) \rightarrow J/\psi(1S)\pi^+\pi^-$ , a transition to a lower charmonium state which accounts for 33.6% of the total branching fraction  $Br[\psi(2S)]$ . Above the  $D\bar{D}$  threshold, charmonia generally have larger decay widths and decay predominantly to open-flavor hadrons via strong interactions. An example of such a decay is  $\psi(4160) \rightarrow D\bar{D}$ , where the particle is named for its mass of 4160 MeV. Bottomonia have similar properties, including a corresponding  $B\bar{B}$  threshold at  $\sqrt{s} = 10.56$  GeV.

Our focus going forward will be on the  $J/\psi$ , a  $n = 1$  S-wave charmonium state. Not only was the  $J/\psi$  the first quarkonium state discovered, but it also has properties that make it particularly interesting and easy to study experimentally. The  $J/\psi$  has a branching fraction to leptons that is orders of magnitude higher than other hadrons. Consider the ratio of the branching fractions of leptonic decays of the  $J/\psi$  and  $\phi(1020)$  meson

$$\frac{\text{Br}[J/\psi \rightarrow \mu^+\mu^-]}{\text{Br}[\phi \rightarrow \mu^+\mu^-]} \approx 20 \times 10^3. \quad (2.1)$$

There are several key reasons for this enhancement. Decays to open-heavy-flavor such as  $J/\psi \rightarrow D^0\bar{D}^0$  (in analogy to the  $\phi \rightarrow K^+K^-$  process for strangeness) are not allowed kinematically because it lies below the  $D\bar{D}$  threshold with  $m_{J/\psi}(3.1 \text{ GeV}) <$



$J/\psi \rightarrow ggg \rightarrow 3$  pions is thus the lowest order allowed hadronic decay of the  $J/\psi$ . This process is higher order in the coupling  $\alpha_s$ , which at high energies such as the scale  $2m_c$  (the only physical scale present in this tree level diagram), is small.

Thus, while many mesons have small branching fractions to leptons, the  $J/\psi$  has a combination of properties that make it decay to  $\mu^+\mu^-$  comparatively quite often. This makes the  $J/\psi$  particularly easy to observe experimentally. Modern detectors contain chambers designed specifically to measure the kinematics of muons, which generally have a clear signal (the signature is often distinguishable by eye). Thus, the kinematics of the dimuon pairs decaying specifically from  $J/\psi$  are easy to reconstruct. Additionally, the low mass  $m_{J/\psi} = 3.1$  GeV allows us to easily produce  $J/\psi$  with high transverse momentum. In this region,  $\alpha_s$  is small and our perturbative QCD techniques are reliable.

## 2.3 Models of Quarkonium Production

### 2.3.1 Potential Models for Charmonia

A potential model of charmonium is appealing for its simplicity and similarity with positronium. Based on the qualitative features of QCD we make the ansatz

$$V(r) \sim -C_F \frac{\alpha_s}{r} + kr. \quad (2.2)$$

At short distances, this potential looks like a Coulomb potential where  $C_F$  is a color-factor associated with the color configuration of the  $c\bar{c}$ . If the quark-antiquark pairs are in a color-octet state, one can show (by considering a basic  $q\bar{q}$  interaction in QCD) that  $C_F = -1/6$ . If they are in a color-singlet state then  $C_F = 4/3$ . Thus, only the color-singlet case yields an attractive short-range potential. This is consistent with experiment, since we always observe particles that are color-singlets.

As  $r \rightarrow \infty$ , the potential is linear in  $r$  and becomes extremely large, on the order of  $\Lambda_{\text{QCD}}$  at a distance of 1 fm. The potential is consistent with the flux tube

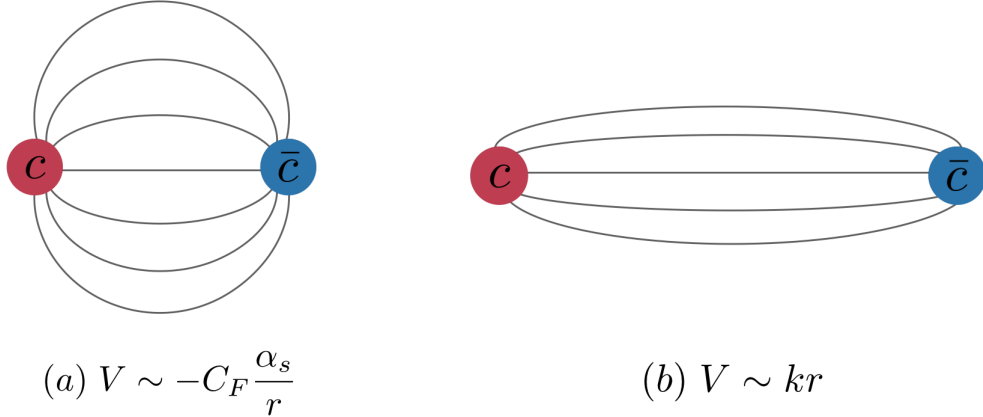


FIGURE 2.4: Flux-tube visualization of a potential model for the strong force.

model shown in Fig. 2.4 with constant string tension (energy density)  $k$ . At short-distances perturbation theory is valid and at long-distances, where the model exhibits confinement, perturbation theory breaks down.

This static potential can be supplemented with relativistic corrections to account for fine and hyperfine splittings of different spin states. This includes the  $^1S_0$  and  $^3S_1$  charmonium states (the  $\eta_c$  and  $J/\psi$ ) and the splittings of different  $\chi_c$  P-wave states shown in Fig. 2.2. Ref. [52] used a potential model to predict the masses of various charmonia and bottomonia and found, especially for states below the  $D\bar{D}$  threshold, fairly accurate results. Their predicted mass of  $m_{J/\psi} = 3.096$  GeV and  $m_{\Upsilon} = 9.460$  GeV are within 0.03% and 0.003% of the PDG [44] masses, respectively. However, potential models are purely phenomenological and begin to break down for the higher mass states. Additionally, we seek a theory that can be derived from the QCD Lagrangian.

### 2.3.2 Sources of Quarkonium Production

Quarkonia can be produced in a variety of ways which can be separated into several categories:

- **Non-prompt** — Non-prompt sources include decays from  $B$  mesons such as

$B^\pm \rightarrow J/\psi + K^+$ ,  $B^\pm \rightarrow \psi(2S) + K^+$ , or  $B_s^0 \rightarrow J/\psi + \phi$ , etc.

- **Prompt** — These are decays that are not from  $B$  mesons. This category is further divided into **feed-down** and **direct** contributions (see below).
- **Feed-down** — These contributions include  $J/\psi$  produced from decays from higher charmonium states such as  $\chi_{c0} \rightarrow \gamma J/\psi$ .
- **Direct** — These modes will be our primary concern in this work. They involve a variety of processes such as, at the partonic level,  $gg \rightarrow J/\psi g$  and are generally the source of production we refer to when studying calculations of quarkonium production using the models we describe below.

We do not consider non-prompt sources of  $J/\psi$  in this work. While  $B$ -meson decays to  $J/\psi$  become extremely prevalent at high transverse momenta (e.g., Ref. [53]), these decays can generally be separated from prompt sources of  $J/\psi$  production in experimental analyses. Because of their relatively long lifetime, detectors can tag  $J/\psi$  decaying from  $B$  mesons by identifying displaced decay vertices.

### 2.3.3 The Color Singlet Model

Inspired by the concept of QCD factorization and in analogy with positronium, the Color-Singlet Model (CSM) is perhaps the most intuitive way to approach calculating quarkonium production cross-sections and decay rates. The CSM describes the production of quarkonia as the perturbative creation of a heavy  $Q\bar{Q}$  state that has the same angular momentum and color quantum numbers as the  $J/\psi$ , namely  $^3S_1^{[1]}$ .<sup>4</sup>

This model relies on several basic ideas

1. **Factorization** — Quarkonium production observables can be factorized into two pieces: the creation of a heavy  $Q\bar{Q}$  pair at short-distance scales and the

<sup>4</sup> We have switched notation slightly here, dropping the principle quantum number (which is 1 here) and adding a color-quantum number where [1] denotes a color-singlet state and [8] denotes a color-octet state.

non-perturbative binding of this  $Q\bar{Q}$  pair into a physical quarkonium bound state. The former is calculable in perturbation theory and the second is a universal piece to ultimately be extracted from experiments.

2. **Static approximation** — The  $Q\bar{Q}$  pair is created at roughly threshold energy ( $p \approx 0$ ) and their relative velocity  $v$  is very small. Large relative velocities would disallow the  $Q\bar{Q}$  to form a bound state.
3. **Quantum Numbers** — The  $Q\bar{Q}$  pair must be in the physical color state of the quarkonium. This configuration remains the same through even non-perturbative stages of production.

The formula for inclusive production of  $J/\psi$  in the CSM can ultimately be written in the following schematic form

$$\sigma_{\text{CSM}}(ij \rightarrow J/\psi + X) \sim \hat{\sigma}(ij \rightarrow c\bar{c} [{}^3S_1^{[1]}]) \times |R_{J/\psi}(0)|^2, \quad (2.3)$$

where  $\hat{\sigma}$  is the partonic cross-section for  $c\bar{c}$  production at threshold in the color-singlet state and  $|R_{J/\psi}(0)|^2$  is the square of the radial wave-function of the  $c\bar{c}$  pair. This wave-function can be thought of as the probability that the  $c\bar{c}$  pair will collapse to  $r = 0$  to form a  $J/\psi$ . In order to calculate the partonic cross-section for  $J/\psi$  production at hadron colliders at LO, one must calculate the CSM diagrams of the form shown in Fig. 2.5. An appealing feature of the CSM is that only one phenomenological parameter, the radial wave-function at the origin, is needed to calculate  $J/\psi$  production. These radial wave-functions can be readily extracted from measurements of quarkonium decays. A formula analogous to Eq. (2.3) can be used to calculate the decay rate of the  $J/\psi$  into light hadrons or leptons.

For other charmonium excitations, Eq. (2.3) can be generalized to

$$\sigma_{\text{CSM}}(ij \rightarrow \mathcal{Q} [{}^{2S+1}L_J^{[1]}] + X) \sim \hat{\sigma}(ij \rightarrow Q\bar{Q} [{}^{2S+1}L_J^{[1]}]) \times \left| \frac{d^L R_{J/\psi}(0)}{dr^L} \right|^2, \quad (2.4)$$

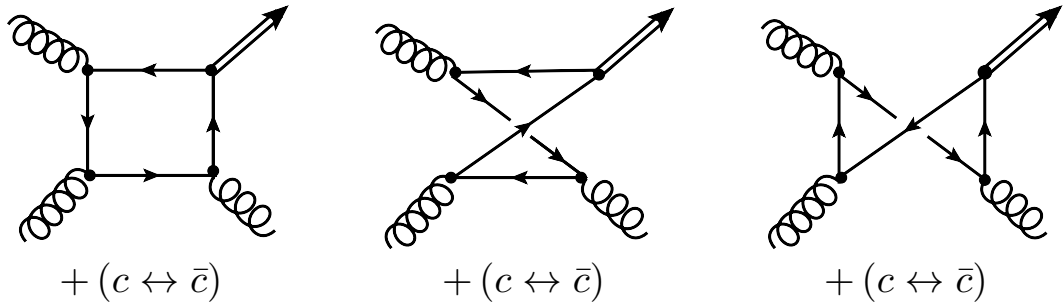


FIGURE 2.5: The diagrams contributing to  $gg \rightarrow J/\psi g$  or any other  ${}^3S_1^{[1]}$  charmonium state at LO in the CSM. The double line denotes the charmonium state and  $c \leftrightarrow \bar{c}$  would require switching the directions of each fermion arrow.

where derivatives of the spatial wave-function at the origin are needed for  $P$  –  $wave$  quarkonia states such as the  $\chi_{cJ}$ . Despite its simplicity, the CSM ultimately was proven to be grossly inaccurate by the CDF experiment in the 1990’s (e.g. Fig. 2.6). Experimentalists found that predictions of the prompt  $J/\psi$  and  $\psi(2S)$  (also called the  $\psi'$ ) production rates by the LO CSM were orders of magnitude below observed rates [6, 7]. This is referred to as the  $\psi'$  anomaly.

Further attempts were made to reconcile the CSM with measurements at hadron colliders by including contributions from **fragmentation** mechanisms. Diagrams for fragmentation mechanisms have the property that a single “cut” can be made on a parton such that one side of the cut is a partonic scattering process while the other side consists of a parton of virtuality order  $(2m_c)^2$ . Fig. 2.7 shows an example of a gluon fragmentation mechanism for the production of  $\eta_c$ , a  ${}^1S_0^{[1]}$  charmonium state. Relative to the leading order  $\eta_c$  production diagrams which scale as  $\mathcal{O}(\alpha_s^3)$ , this diagram scales as  $\mathcal{O}(\alpha_s^4)$ . Ref. [54] showed that, while fragmentation diagrams such as Fig. 2.7 are suppressed by orders of  $\alpha_s$ , at extremely high transverse momentum,  $p_T$ , they are enhanced by relative order  $p_T^2/m_c^2$ . At high enough values of  $p_T$ , this factor can easily overcome the relative  $\mathcal{O}(\alpha_s)$  suppression. Ref. [54] found similar

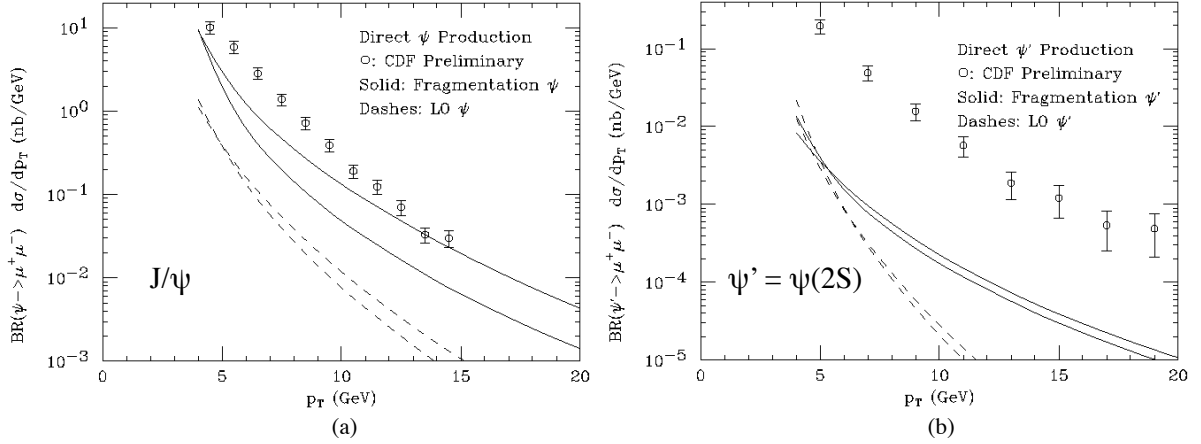


FIGURE 2.6: Plots from Ref. [6] using data from Ref. [7] which show the LO CSM predictions for the  $J/\psi$  (a) and  $\psi'$  (b) production rates. Both diagrams show that these predictions (as described in the text) under-predict experimental observations by orders of magnitude. This helped to motivate the study of fragmentation contributions at high transverse momenta.

results for gluon fragmentation to  $J/\psi$  diagrams.

Diagrams contributing to fragmentation are, generally, at least one higher order in  $\alpha_s$  than the lowest order non-fragmentation diagrams. However, Ref. [54] showed that for  $S$ -wave quarkonia such as the  $\eta_c$  and  $J/\psi$ , gluon fragmentation contributions were enhanced by a factor of  $p_T^2/m_Q^2$  in the limit that  $p_T \gg m_Q$ . Fragmentation contributions from gluon fragmentation to  $P$ -wave quarkonia were then calculated in Ref. [55]. In the large- $p_T$  regime where fragmentation dominates, Ref. [54] also showed that the cross-section for quarkonium production factorizes via

$$d\sigma[A + B \rightarrow \mathcal{Q} + X](p_T) = \int dx \sum_i d\hat{\sigma}[A + B \rightarrow i + X](p_T/x) \times D_{i \rightarrow \mathcal{Q}}(x, \mu), \quad (2.5)$$

where  $\mathcal{Q}$  is a quarkonium state,  $i$  is a parton type and  $x$  is the fraction of  $i$ 's momentum carried by  $\mathcal{Q}$ . The factor  $\hat{\sigma}_i$  is the partonic cross-section for, in Fig. 2.7, the scattering of  $gg \rightarrow gg$ , and  $D_{i \rightarrow \mathcal{Q}}$  is a Fragmentation Function (FF). The FF describes the fragmentation of the gluon into the a  $\mathcal{Q} = {}^1S_0^{[1]}$  quarkonium state and

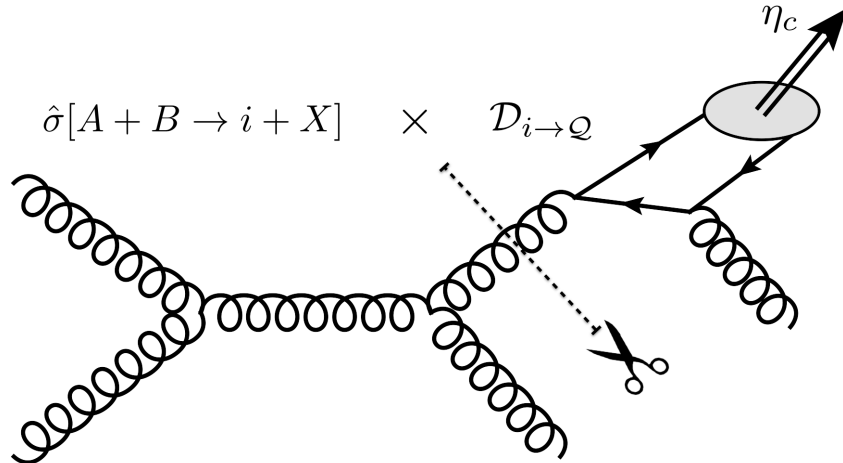


FIGURE 2.7: This shows a fragmentation diagram that contributes to  $\eta_c(^1S_0^{[1]})$  production at  $\mathcal{O}(\alpha_s^4)$ . Although higher order in the coupling than LO contributions in the CSM, in the limit that  $p_T \gg m_c$ , this diagram can be shown to be enhanced by  $p_T^2/m_c^2$ . At high  $p_T$  this enhancement compensates for the  $\alpha_s$  suppression.

is interpreted as the probability that the  $\eta_c$  carries a fraction  $x$  of the gluon's momentum. Additionally, Ref. [54] showed that FFs could be calculated perturbatively at the quark mass scale  $\mu = 2m_c$ . Potentially large logarithms of  $p_T/m_c$  appearing in the FFs could then be resummed by solving the DGLAP (Dokshitzer-Gribov-Lipatov-Altarelli-Parisi) equations [56]; the renormalization group equations for FFs given by

$$\mu \frac{\partial}{\partial \mu} D_{i \rightarrow \mathcal{Q}}(z, \mu) = \sum_j \int_z^1 \frac{dx}{x} \tilde{P}_{ji}(z/x, \mu) D_{j \rightarrow \mathcal{Q}}(x, \mu), \quad (2.6)$$

where  $\tilde{P}_{ji}(x, \mu)$  are the QCD splitting functions originally derived in Ref. [56]. These functions give the probability for a parton  $i$  to fragment into a parton  $j$  that carries a fraction  $x$  of its longitudinal momentum. At leading order in  $\alpha_s$  they can be

expressed as

$$\begin{aligned}
\tilde{P}_{qq}(x) &= C_F \left( \frac{1+x^2}{(1-x)_+} + \frac{3}{2} \delta(1-x) \right), \\
\tilde{P}_{gq}(x) &= T_R \left( \frac{1+(1-x)^2}{x} \right), \\
\tilde{P}_{qg}(x) &= C_F (x^2 + (1-x)^2), \\
\tilde{P}_{gg}(x) &= C_A \left( \frac{2(1-x+x^2)^2}{x(1-x)_+} + \frac{\beta_0}{2C_A} \delta(1-x) \right), \tag{2.7}
\end{aligned}$$

where  $\beta_0$  was defined in Eq. (1.6),  $C_F = 4/3$ ,  $T_R = 1/2$ ,  $C_A = 3$  and the  $qq$  and  $gq$  channels make use of plus-distributions, which are defined in Appendix D. Both FFs and splitting functions will be discussed in much more detail in Chapter 4.

Thus, at high  $p_T$ , quarkonia production could be factorized into three stages. Consider the production of  $\eta_c$  ( $^1S_0^{[1]}$  charmonium) as shown in Fig. 2.7. In this simpler case, the required pieces of production are: the partonic cross-section for  $gg \rightarrow gg^*$  where the virtual gluon is not far off-shell, the gluon propagator  $\sim 1/q^2$ , and the FF for  $g \rightarrow \eta_c g$ . Ref. [54] calculated each of the FFs for the singlet  $S$ -wave quarkonia. For the  $\eta_c$ , they found

$$D_{g \rightarrow \eta_c} = \frac{1}{3\pi} \alpha_s (2m_c)^2 \frac{|R_{\eta_c}(0)|^2}{(2m_c)^3} (3z - 2z^2 + 2(1-z) \log(1-z)) \tag{2.8}$$

where  $R_{\eta_c}(0)$  is the radial wave-function at the origin to be extracted from decay processes and, at this scale,  $\alpha_s(2m_c) \approx 0.26$ .

Calculations of the fragmentation contributions to prompt  $J/\psi$  production at the Tevatron were calculated in Ref. [6, 57] and are shown as solid lines in Fig. 2.6. The inclusion of fragmentation modes improved the shape of the  $p_T$  spectrum as compared to Tevatron data. However, when experimentalists isolated direct production, the LO CSM + fragmentation predictions for the  $J/\psi$  production rate were roughly 30 times lower than observed rates. For the  $\psi'$ , this disagreement was even worse.

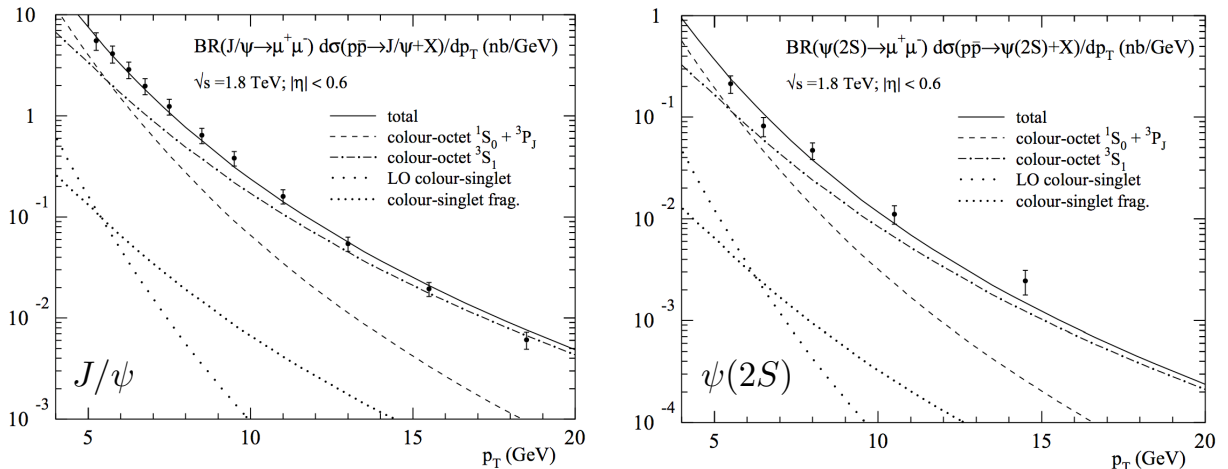


FIGURE 2.8: Inclusive cross-section for inclusive  $J/\psi$  (Left) and  $\psi(2S)$  (right) production at the Tevatron at  $\sqrt{s} = 1.8$  TeV [8]. The cross-sections are for direct  $J/\psi$  ( $\psi(2S)$ ) production and are differential in  $p_T$  and for central rapidities  $|\eta| < 0.6$ . Both plots show that both the LO CSM and LO CSM + fragmentation predictions are orders of magnitude below the data. With the addition of color-octet production mechanisms, both the  $J/\psi$  and  $\psi(2S)$  predictions from NRQCD are in near perfect agreement with the data.

Additionally, the CSM was found to yield uncanceled infrared (IR) divergences in the production cross-sections and decay rates of  $P$ -wave quarkonia. Consider the cross-section for inclusive  $\chi_{cJ}$  production

$$d\sigma_{\text{CSM}}(\chi_{cJ} + X) \sim d\hat{\sigma}(Q\bar{Q} \left[ {}^3P_J^{[1]} \right] + X) |R'_{\chi_{cJ}}(0)|^2. \quad (2.9)$$

At NLO, this factorization is spoiled by logarithmic IR divergences coming from soft gluon emissions at  $\mathcal{O}(\alpha_s^3)$  in the short-distance piece  $d\hat{\sigma}$  [58, 59]. At this point, the CSM could be conclusively declared as unable to describe quarkonium production and decay in modern high-energy hadron colliders.

## 2.4 NRQCD — A Modern Theory of Quarkonium Production & Decay

### 2.4.1 Lagrangian of NRQCD

In order to deal with the problems of the CSM, Ref. [60] developed Non-Relativistic Quantum Chromodynamics (NRQCD), which was based on the idea that a  $Q\bar{Q}$  pair could be treated as a non-relativistic, Schrodinger-like approximation of a QCD bound state. This formalism provided a natural cancellation of the IR divergences in the  $P$ -waves and provided the first model of quarkonium production directly derivable from full QCD. NRQCD has since become the standard theoretical approach to calculating quarkonium production and decay. In this section, we will outline the theoretical foundations of the NRQCD factorization approach as developed in Ref. [60].

Quarkonium production involves several distinct energy scales: the mass  $M$ , the typical momentum  $Mv$ , and the typical kinetic energy  $Mv^2$  of the heavy  $Q\bar{Q}$  pair. NRQCD factorization is built upon the idea that quarkonia are produced first by the perturbative creation of a heavy  $Q\bar{Q}$  over short-distances of order  $\sim 1/M$ . These  $Q\bar{Q}$  pairs then undergo a non-perturbative transition into physical quarkonia over long-distances of order  $\sim 1/(Mv)$  and larger. The scale  $Mv^2$  then represents the order of radial and/or orbital angular momentum excitations. As long as the scales satisfy  $Mv^2 \ll Mv \ll M$ , these stages should be factorizable. For typical charmonia/bottomonia, these scales can indeed be shown to be well-separated. This is discussed in more detail in Appendix A. The average relative velocity of a  $c\bar{c}$  charmonium state is  $v_c \approx 0.3$  and for a  $b\bar{b}$  bottomonium state is  $v_b \approx 0.1$  [33].

The presence of these well-separated scales motivates the construction of an EFT that is a simultaneous expansion of QCD in  $\alpha_s$  and the relative velocity  $v$ . By considering the relativistic behavior of heavy quarks only as power corrections, the

Lagrangian of this theory should describe the low-energy sector of QCD for heavy quarks. This theory should also maintain several of the key symmetries of full QCD such as  $SU(3)$  gauge symmetry, rotational symmetry<sup>5</sup>, and discrete symmetries such as parity  $P$  and charge-conjugation  $C$  symmetry. Additionally, the theory should conserve the numbers of heavy quarks and anti-quarks (so-called heavy quark phase symmetry). The most general Lagrangian satisfying these symmetries was shown in Ref. [60] to be

$$\mathcal{L}_{\text{NRQCD}} = \mathcal{L}_{\text{light}} + \mathcal{L}_{\text{heavy}} + \delta\mathcal{L}, \quad (2.10)$$

where the gluons and  $N_f$  flavors of light quarks are described by the usual relativistic QCD Lagrangian shown in Eq. (1.1) for  $m_u = m_d = m_s = 0$  and

$$\mathcal{L}_{\text{heavy}} = \psi^\dagger \left( iD_0 + \frac{\mathbf{D}^2}{2M} \right) \psi + \chi^\dagger \left( iD_0 - \frac{\mathbf{D}^2}{2M} \right) \chi + \delta\mathcal{L}. \quad (2.11)$$

In Eq. (2.11),  $\psi$  and  $\chi$  are heavy quark and anti-quark spinor fields, respectively. With  $\delta\mathcal{L} \rightarrow 0$ , this Lagrangian is the minimal form of NRQCD and contains a heavy quark spin symmetry. Thus, this form of  $\mathcal{L}_{\text{NRQCD}}$  can describe splittings between radial excitations of quarkonium (such as the  $J/\psi \leftrightarrow \psi'$ ) and between orbital angular momentum excitations (such as the  $J/\psi \leftrightarrow \chi_{cJ}$ ) but not between spin excitations (such as  $\eta_c \leftrightarrow J/\psi$ ). Thus  $\mathcal{L}_{\text{light}} + \mathcal{L}_{\text{heavy}}$  describes the light quarks according to ordinary QCD and heavy quarks/anti-quarks according to a Schrodinger field theory.

The term  $\delta\mathcal{L}$  contains the LO contributions of relativistic effects on the heavy

---

<sup>5</sup> Full Lorentz symmetry will not be manifest in the non-relativistic limit, but is recoverable via corrections in powers of  $v$ .

quarks and is given by

$$\begin{aligned}
\delta\mathcal{L} = & \frac{c_1}{8M^3} (\psi^\dagger(\mathbf{D}^2)^2\psi - \chi^\dagger(\mathbf{D}^2)^2\chi) \\
& + \frac{c_2}{8M^2} (\psi^\dagger(\mathbf{D} \cdot g\mathbf{E} - g\mathbf{E} \cdot \mathbf{D})\psi + \chi^\dagger(\mathbf{D} \cdot g\mathbf{E} - g\mathbf{E} \cdot \mathbf{D})\chi) \\
& + \frac{c_3}{8M^2} (\psi^\dagger(i\mathbf{D} \times g\mathbf{E} - g\mathbf{E} \times i\mathbf{D}) \cdot \boldsymbol{\sigma}\psi + \chi^\dagger(i\mathbf{D} \times g\mathbf{E} - g\mathbf{E} \times i\mathbf{D}) \cdot \boldsymbol{\sigma}\chi) \\
& + \frac{c_4}{2M} (\psi^\dagger(g\mathbf{B} \cdot \boldsymbol{\sigma})\psi - \chi^\dagger(g\mathbf{B} \cdot \boldsymbol{\sigma})\chi),
\end{aligned} \tag{2.12}$$

where the  $c_i = 1 + \mathcal{O}(\alpha_s)$  are dimensionless coefficients that are sensitive to high-energy (short-distance) physics and can be found through matching scattering amplitudes in NRQCD with the corresponding expressions in full QCD. The terms  $\mathbf{E} = G^{0i}$  and  $\mathbf{B} = \frac{1}{2}\epsilon^{ijk}G^{jk}$  are the chromo-electric and chromo-magnetic components of  $G^{\mu\nu}$ . We note that the heavy quark spin symmetry of the minimum NRQCD Lagrangian is now broken by  $\boldsymbol{\sigma}$  dependent terms. In taking the non-relativistic limit, we effectively removed effects occurring at length scales of  $1/M$ .<sup>6</sup> Thus, in order to reproduce the effects of creation/annihilation of pairs  $Q\bar{Q}$ , we can explicitly include local 4-fermion operators in  $\delta\mathcal{L}$  of the form

$$\delta\mathcal{L}_{4\text{-fermion}} = \sum_n \frac{f_i}{M^{d_n-4}} \mathcal{O}_n \quad \text{where} \quad \mathcal{O}_n = \psi^\dagger \mathcal{K}'_n \chi \chi^\dagger \mathcal{K}_n \psi, \tag{2.13}$$

where  $f_i$  are perturbatively calculable functions of  $\alpha_s(2m_c)$  and  $\mathcal{K}_n, \mathcal{K}'_n$  are products of combinations of a spin matrix (1 or  $\boldsymbol{\sigma}$ ), color matrix (1 or  $T^a$ ), and/or a polynomial in the covariant derivative,  $\mathbf{D}$ . Each  $\mathcal{O}_n$  is a creation/annihilation operator for a  $Q\bar{Q}$  pair. It creates a  $Q\bar{Q}$  pair in a color and angular-momentum state dictated

<sup>6</sup> Integrating out higher scales ultimately means that the operators in  $\delta\mathcal{L}$  will carry a dependence on  $\mu$ , the renormalization scale or ultraviolet cutoff of NRQCD. Each matching coefficient  $c_i(\mu)$  should then depend on  $\mu$  in such a way that exactly cancels the  $\mu$  dependence of the operators. While the evolution of these matrix elements can be considered, the logarithms associated with this dependence are not generally considered when studying quarkonium production at high  $p_T$ , where logarithms of  $p_T/m_Q$  are more important.

by the form of  $\mathcal{K}'_n$  after annihilating a  $Q\bar{Q}$  pair in a state with quantum numbers given by  $\mathcal{K}_n$ . Each operator must respect the symmetries of the NRQCD Lagrangian described above and should have a  $1/M^{d_n-4}$  mass scaling where  $d_n$  is the dimension of the operator  $\mathcal{O}_n$  is introduced in order to make the coefficients  $f_n$  dimensionless.

#### 2.4.2 NRQCD Factorization

Having constructed a Lagrangian for NRQCD, we can now more clearly describe its picture of quarkonium production. Ref. [60] showed that the cross-section for the inclusive production of quarkonium can be written schematically in the following factorized form

$$d\sigma(\mathcal{Q} + X) = \sum_n d\hat{\sigma}(Q\bar{Q}[n] + X) \times \langle \mathcal{O}^{\mathcal{Q}}[n] \rangle, \quad (2.14)$$

where  $n \equiv {}^{2S+1}L_J^{[1,8]}$  describes the quantum numbers of the heavy  $Q\bar{Q}$  pair. Here  $d\hat{\sigma}$  is a short-distance, perturbatively calculable cross-section for the creation of a  $Q\bar{Q}$  in the state  $n$  and  $\langle \mathcal{O}^{\mathcal{Q}}[n] \rangle$  are long-distance-matrix-elements (LDMEs) that describe the non-perturbative hadronization of the  $Q\bar{Q}$  pair into a physical quarkonium state  $\mathcal{Q}$ . By inserting a projection operator onto the quarkonium state  $\mathcal{P}_{\mathcal{Q}}$  into our expression for  $\mathcal{O}_n$  above, the LDMEs can ultimately be shown to take the form

$$\langle \mathcal{O}^{\mathcal{Q}}[n] \rangle \equiv \sum_{X,\lambda} \langle 0 | \chi^\dagger \mathcal{K}_m | \mathcal{Q}(\lambda) + X \rangle \langle \mathcal{Q}(\lambda) + X | \chi^\dagger \mathcal{K}_n \psi | 0 \rangle \quad (2.15)$$

$$\text{where } \mathcal{P}_{\mathcal{Q}} = \sum_{X,\lambda} | \mathcal{Q}(\lambda) + X \rangle \langle \mathcal{Q}(\lambda) + X |, \quad (2.16)$$

where  $\sum_{X,\lambda}$  is a sum over the possible other hadrons,  $X$ , in the final state and  $\lambda$  is the possible polarization states of the quarkonium  $\mathcal{Q}$ .

NRQCD describes quarkonium production as the perturbative formation of a  $Q\bar{Q}$  pair in a state  $n$  where there is no requirement that  $n$  match the quantum numbers of the physical quarkonium state  $\mathcal{Q}$  as was the case in the CSM. The theory

assumes that soft gluons at nonperturbative energy scales  $\leq Mv$  are emitted that change the quantum numbers of the intermediate  $Q\bar{Q}$  pair as it transitions into  $\mathcal{Q}$ . The scaling of these transitions is dictated by the multipole expansion in the velocity  $v$ . These soft gluon effects are accounted for in the LDMEs, each of which carries a scaling in  $v$ . Derivations of the NRQCD factorization theorem rely on standard factorization methods in full QCD as well as the separation of the scales  $Mv^2 \ll Mv \ll M$ . Factorization of production cross-sections in NRQCD has, however, not been rigorously proven to all-orders in  $\alpha_s$ .

### 2.4.3 Power Counting & Selection Rules

Power counting in NRQCD dictates the order in the  $v$  expansion at which intermediate  $Q\bar{Q}$  states contribute to the production of a given quarkonium state  $\mathcal{Q}$ . In Appendix A, we explain how writing the NRQCD Lagrangian explicitly in terms of the vector potential  $\mathbf{A}$  by working in the Coulomb gauge  $\nabla \cdot \mathbf{A} = 0$  makes the power counting in  $v$  manifest. The possible Fock states of a quarkonium state  $\mathcal{Q}$  have the schematic form

$$|\mathcal{Q}\rangle = \psi_{Q\bar{Q}}^{\mathcal{Q}} |Q\bar{Q}\rangle + \psi_{Q\bar{Q}g}^{\mathcal{Q}} |Q\bar{Q}g\rangle + \dots, \quad (2.17)$$

where the dominant Fock state is the color-singlet  $Q\bar{Q}_{[{}^{2S+1}L_J^{[1]}]}$  state (where the quantum numbers depend on the the quarkonium state being studied) and higher Fock states contain dynamical gluons. Each higher Fock state is suppressed by orders of  $\alpha_s$  and  $v$ . The probability associated with each Fock state is then dictated by their coupling with the dominant  $Q\bar{Q}$  state through transitions described by the terms of the Lagrangian. Two such such transitions are

1. **Chromo-electric Transitions** — These come from Lagrangian terms such as  $\psi^\dagger (ig\mathbf{A} \cdot \nabla)\psi$ . Transitions between, for example,  $|Q\bar{Q}g\rangle$  and  $|Q\bar{Q}\rangle$  Fock states involve selection rules  $\Delta L = \pm 1$  and  $\Delta S = 0$ . These transitions change

the color state from color-singlet to color-octet and from color-octet to either color-octet or color-singlet.

2. **Chromo-magnetic Transitions** — These transitions are associated with terms such as  $\psi^\dagger(\nabla \times g\mathbf{A}) \cdot \boldsymbol{\sigma}\psi$ . They break heavy quark spin symmetry, have selection rules  $\Delta L = 0$  and  $\Delta S = \pm 1$  between Fock states, and have the same rules for color quantum numbers as the chromo-electric case.

Using these basic transitions, the LDMEs can be shown to have the following scaling in  $v$

$$\langle \mathcal{O}^{\mathcal{Q}}[{}^{2S+1}L_J^{[1,8]}] \rangle \sim v^{3+2L+2E+4M}, \quad (2.18)$$

where  $E$  and  $M$  represent the minimum number of chromo-electric and chromo-magnetic transitions needed for the transition of  $Q\bar{Q}[{}^{2S+1}L_J^{[1,8]}]$  to the quantum numbers of  $\mathcal{Q}$ . For  $J/\psi$ , the dominant Fock state is  $\langle \mathcal{O}^{J/\psi}[{}^3S_1^{[1]}] \rangle \sim v^3$  and the leading order color-octet states such as  $\langle \mathcal{O}^{J/\psi}[{}^3S_1^{[8]}] \rangle$  scale as  $v^7$ .

Recall that, in the CSM, IR divergences in calculations of  $\chi_{cJ}$  production were left unregulated (recall Eq. (2.9)). NRQCD naturally provides a solution to this problem by including both color-singlet and color-octet intermediate states. At LO in the  $v$  expansion of NRQCD, two terms contribute to inclusive  $\chi_{cJ}$  production

$$\begin{aligned} d\sigma(\chi_{cJ} + X) &\sim \hat{\sigma}(Q\bar{Q}[{}^3P_J^{[1]}] + X) \times \langle \mathcal{O}^{\chi_{cJ}}[{}^3P_J^{[1]}] \rangle \\ &+ \hat{\sigma}(Q\bar{Q}[{}^3S_1^{[8]}] + X) \times \langle \mathcal{O}^{\chi_{cJ}}[{}^3S_1^{[8]}] \rangle. \end{aligned} \quad (2.19)$$

NRQCD dictates that both of these terms scale as  $\sim v^5$ , since  $Q\bar{Q}[{}^3S_1^{[8]}]$  can be reached from the dominant  $\chi_{cJ}$  through a single chromo-electric transition. In the calculation of  $\chi_{cJ}$  decays, the IR singularities of the color-octet piece match those of the  ${}^3P_J^{[1]}$  state as shown in Ref. [60].

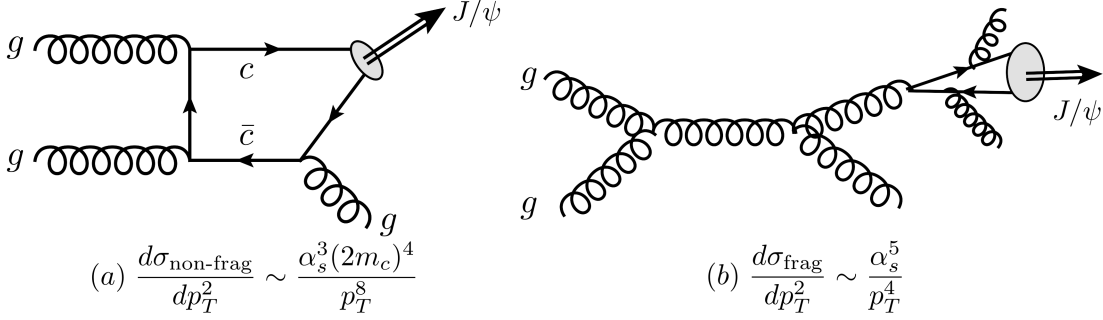


FIGURE 2.9: Example of diagrams for (a) LO non-fragmentation contributions and (b) fragmentation contributions to  $J/\psi$  production. The relevant scalings in the coupling and transverse momenta are shown, emphasizing that, while suppressed by orders of  $\alpha_s$ , fragmentation diagrams are enhanced by powers of the  $p_T$  for very high transverse momenta.

#### 2.4.4 Leading Power NRQCD

Recall from our discussion of the CSM that, at high transverse momenta, fragmentation contributions dominate the production of quarkonia. For  $S$ -wave quarkonia such as the  $J/\psi$  and  $\psi(2S)$  where  $p_T \gg m_c$ , the leading CSM contribution scales as  $d\sigma/dp_T^2 \sim \alpha_s^3(2m_c)^4/p_T^8$  [54]. As shown in Fig. 2.4.4, fragmentation modes are higher order in  $\alpha_s$  but are enhanced by factors of the  $p_T$ . This motivates the use of **leading-power factorization** (LP), which considers contributions to quarkonium production organized in powers of  $1/p_T^2$ . Applying LP factorization to the short-distance piece of the NRQCD factorization formula in Eq. (2.14) yields

$$d\hat{\sigma}(Q\bar{Q}[n] + X) = \sum_i d\hat{\sigma}(i + X) \bullet D_{i \rightarrow Q\bar{Q}[n]}(z), \quad (2.20)$$

where the sum is over parton species,  $D_{i \rightarrow Q\bar{Q}[n]}$  are single parton FFs into heavy  $Q\bar{Q}$  pairs in the intermediate color and angular momentum state  $n$ , and  $\bullet$  represents a convolution in the momentum fraction  $z$  carried by  $Q\bar{Q}$ . The newly factorized short-distance piece  $\hat{\sigma}(i + X)$  is now completely independent of the intermediate  $Q\bar{Q}[n]$  state. In this formalism, NRQCD power counting dictates that the leading contri-

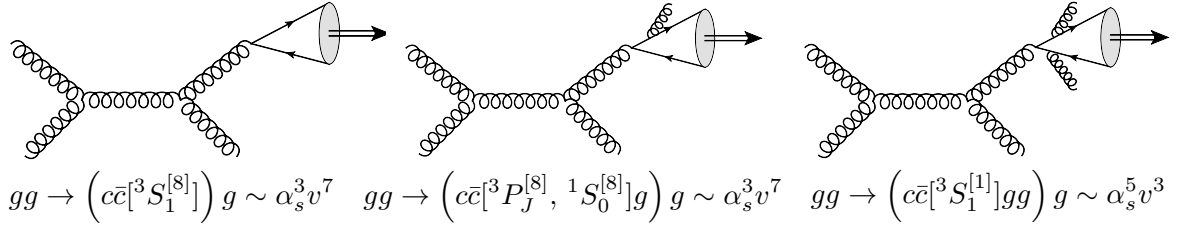


FIGURE 2.10: Basic fragmentation diagrams for the  ${}^3S_1^{[8]}$ ,  ${}^1S_0^{[8]}$ ,  ${}^3P_J^{[8]}$ , and  ${}^3S_1^{[1]}$  NRQCD production mechanisms for  $J/\psi$  that are most important in the leading power approximation of NRQCD. The scalings of each mode with the expansion parameters  $\alpha_s$  and  $v$  are also shown in each case.

Contributions will be the  $\langle \mathcal{O}^{J/\psi}({}^3S_1^{[8]}) \rangle$ ,  $\langle \mathcal{O}^{J/\psi}({}^3P_J^{[8]}) \rangle$ ,  $\langle \mathcal{O}^{J/\psi}({}^1S_0^{[8]}) \rangle$ ,  $\langle \mathcal{O}^{J/\psi}({}^3S_1^{[1]}) \rangle$  mechanisms. Note that, going forward, we refer to these mechanisms colloquially as the **NRQCD production mechanisms** or the **LDMEs** for  $J/\psi$ . Diagrammatic representations and relevant scaling are shown in Fig. 2.10. Color-octet contributions are suppressed by relative order  $v^4$  but are enhanced by relative orders of  $p_T$  and, in the case of the  ${}^3S_1^{[8]}$  for example, by relative order  $1/\alpha_s^2$ .

The LP factorization approach allows us to compute fragmentation contributions beyond fixed order. By solving the leading-order DGLAP equations for the FFs for each of the  $J/\psi$  LDMEs listed above, we can include contributions to the FFs from leading logarithms of the form  $\log(p_T^2/(2m_c)^2)$  to all orders in  $\alpha_s$ . This RG evolution will play an important role when we calculate quarkonium production in jets in Chapters 4 and 5. The first calculation of these fragmentation contributions to  $J/\psi$  production was performed in Ref. [9] where the authors extracted the  $\langle \mathcal{O}^{\psi'}({}^3S_1^{[8]}) \rangle$  LDME from CDF data for prompt  $\psi'$ . Their results were a significant improvement from the LO CSM predictions as can be seen in Fig. 2.11. A more complete calculation of the color-octet fragmentation contributions was then performed in Refs. [61, 62]. The authors provided the first NRQCD calculations of the  $P$ -wave fragmentation contributions to  $J/\psi$  as well as contributions to  $\chi_{cJ}$  and  $\Upsilon$  production.

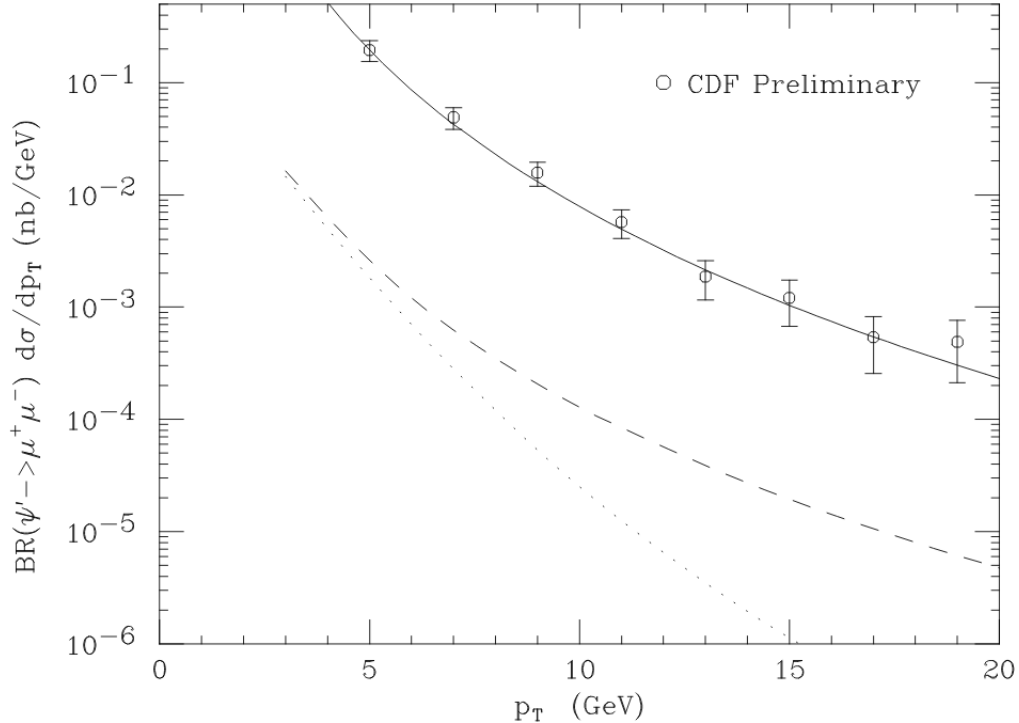


FIGURE 2.11: Figure from Ref. [9] showing CDF data for prompt  $\psi'$  production and theoretical predictions of the total LO CSM contributions (dotted curves), the CSM + fragmentation contributions (dashed curves) and the  ${}^3S_1^{[8]}$  color-octet fragmentation contribution (solid curve). Theoretical predictions match CDF data quite well, which motivates the use of NRQCD to describe quarkonium hadroproduction at high  $p_T$ , specifically because of its inclusion of intermediate color-octet states.

The ability of these calculations to predict the  $p_T$  spectrum of quarkonia at the Tevatron gave the NRQCD community hope that the addition of color-octet mechanisms might finally provide a robust prediction of  $J/\psi$  and  $\psi'$  production. The prevailing sentiment of the community was that the CSM was incomplete and that the dominant source of  $S$ -wave quarkonia at high  $p_T$  came from  $g \rightarrow Q\bar{Q}[{}^3S_1^{[8]}]$  fragmentation.

#### 2.4.5 Fragmentation Functions at $\alpha_s(2m_c)$

At this point, we can present the analytic expressions for the leading power NRQCD FFs as first calculated in Ref. [63, 64]. Each FF is calculated at the scale  $\mu = 2m_c$  and

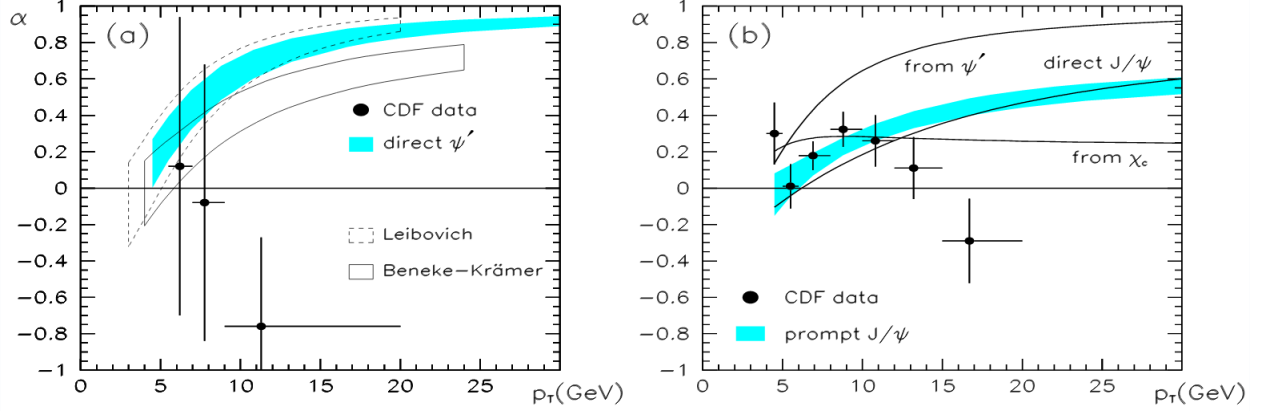


FIGURE 2.12: Plot showing the polar anisotropy parameter  $\alpha = \lambda_\theta = (\sigma_T - 2\sigma_L)/(\sigma_T + 2\sigma_L)$  resulting from fits of the angular distribution of di-muons in direct  $\psi'$  production (a) and prompt  $J/\psi$  production (b) (in  $p\bar{p} \rightarrow J/\psi(\rightarrow \mu^+\mu^-) + X$  events) to the distribution  $1 + \alpha \cos^2(\theta)$  as a function of the transverse momentum  $p_T$  where  $\theta$  is the angle between the  $\mu^+$  3-momentum in the  $J/\psi$  rest frame and the  $J/\psi$  3-momentum in the lab frame. This shows significant disagreement between theoretical predictions of [10] and Tevatron data [11].

will, in subsequent chapters, be evolved using the LO DGLAP evolution equations in Eq. (2.6) to a higher energy scale. The FFs are presented in a form consistent with Ref. [12]

$$\begin{aligned}
D_{g \rightarrow J/\psi}^{3S_1^{[8]}}(z, 2m_c) &= \frac{\pi\alpha_s(2m_c)}{24m_c^3} \langle \mathcal{O}^{J/\psi}(3S_1^{[8]}) \rangle \delta(1-z), \\
D_{g \rightarrow J/\psi}^{1S_0^{[8]}}(z, 2m_c) &= \frac{5\alpha_s^2(2m_c)}{96m_c^3} \langle \mathcal{O}^{J/\psi}(1S_0^{[8]}) \rangle (3z - 2z^2 + 2(1-z) \log(1-z)), \\
D_{g \rightarrow J/\psi}^{3P_J^{[8]}}(z, 2m_c) &= \frac{5\alpha_s^2(2m_c)}{12m_c^5} \langle \mathcal{O}^{J/\psi}(3P_J^{[8]}) \rangle, \\
&\left( \frac{1}{6} \delta(1-z) + \left[ \frac{1}{1-z} \right]_+ \frac{13-7z}{4} \log(1-z) - \frac{(1-2z)(8-5z)}{8} \right),
\end{aligned} \tag{2.21}$$

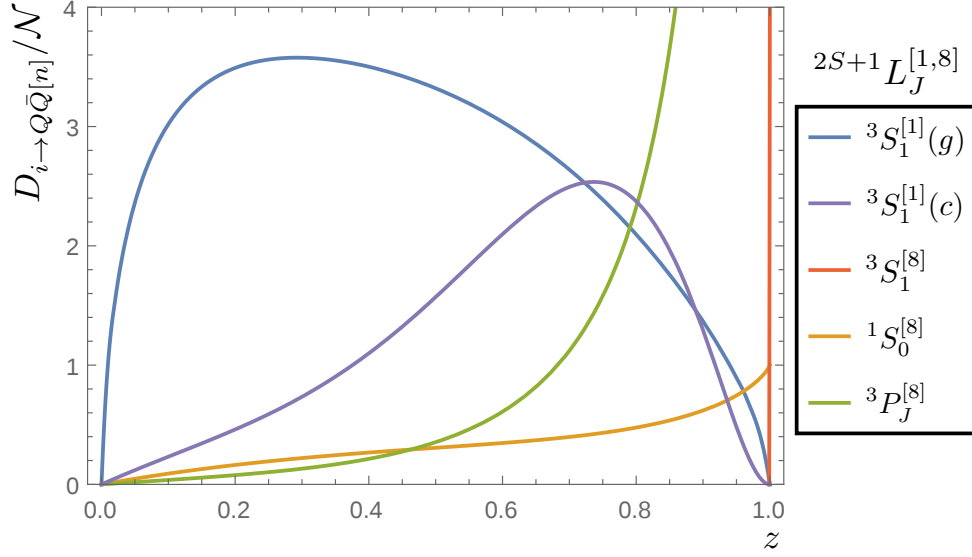


FIGURE 2.13: This plot, adapted from Ref. [12], shows the fragmentation functions in leading power NRQCD plotted as a function of  $z$ , the fraction of the fragmenting parton's energy carried by the hadron. The curves are normalized (by multiplying the functions by numbers) such that all of the curves fit on the same plot.

and

$$D_{g \rightarrow J/\psi}^{3S_1^{[1]}}(z, 2m_c) = \frac{5\alpha_s^3(2m_c)}{864\pi m_c^3} \langle \mathcal{O}^{J/\psi}(^3P_J^{[8]}) \rangle \int_0^z dr \int_{(r+z^2)/2z}^{(1+r)/2} dy \frac{1}{(1-y)^2(y-r)^2(y^2-r)^2} \\ \times \sum_{i=0}^2 z^i \left( f_i(r, y) + g_i(y) \frac{1+r-2y}{2(y-r)\sqrt{y^2-r}} \log \left( \frac{y-r+\sqrt{y^2-r}}{y-r-\sqrt{y^2-r}} \right) \right),$$

where the expressions  $f_i(r, y)$ ,  $g_i(r, y)$  are rather complicated polynomials of  $r \equiv (2m_c)^2/s$  and  $y \equiv p \cdot q/s$  and are given explicitly in Eq.(A10) in Ref. [12]. The integrals over  $r$  and  $y$  can only be performed numerically. Evaluated at  $2m_c$ , each of these functions is shown (using an interpolation for the singlet case) in Fig. 2.13. These functions will be used to calculate cross-sections for  $J/\psi$  produced in jets in Chapter 5.

## 2.5 The Polarization Puzzle

### 2.5.1 Calculating Quarkonium Polarization

A crucial test of NRQCD is to use the LDMEs extracted from the  $J/\psi$  ( $\psi'$ ) production cross-section to predict the polarization of the  $J/\psi$  ( $\psi'$ ). In this section, we outline how to calculate the polarization of these particles from the angular distribution of their decays to leptons.

Given a quantization axis  $\hat{z}$ , we say a particle is **unpolarized** when it has an equal probability  $1/(2J + 1)$  to be found in any of the possible  $J_z = -J, -(J - 1), \dots, +J$  eigenstates (where  $J$  is the total angular momentum). Otherwise, the particle is said to be **polarized**. The polarization of the  $J/\psi$  is interesting both theoretically and experimentally. Theoretically, polarization gives us insight into the  $J/\psi$ 's production, as it is dependent upon the underlying production mechanisms. Experimentally, proper predictions of polarization affect the uncertainty of measurements of the kinematic details (and thus the acceptance rates) of the decay products of the  $J/\psi$  in the detector [13].

The polarization of a  $J/\psi$  is measured by studying the geometry of  $J/\psi \rightarrow \mu^+ \mu^-$  decays. The intermediate state  $n$  of the  $Q\bar{Q}[n]$  pair is reflected in the angular distribution of the dimuon pair. In the rest-frame of the decaying  $J/\psi$ , a spherically symmetric dilepton angular distribution signals that the  $J/\psi$  is, on average, unpolarized, while an anisotropic distribution signals an underlying polarization.

Fig. 2.14 shows a coordinate system on which we can define the angular distribution of the dimuons. The polar angle  $\theta$  is defined to be between the  $l^+$  and a choice of polarization axis  $\hat{z}$ . The azimuthal angle  $\phi$  is measured with respect to the production plane — the plane containing the directions of the incident beams. There are three common choices for the polarization axis which are shown in Fig. 2.15: the Gottfried-Jackson frame [65] where  $\hat{z}$  is chosen along the direction of one of the

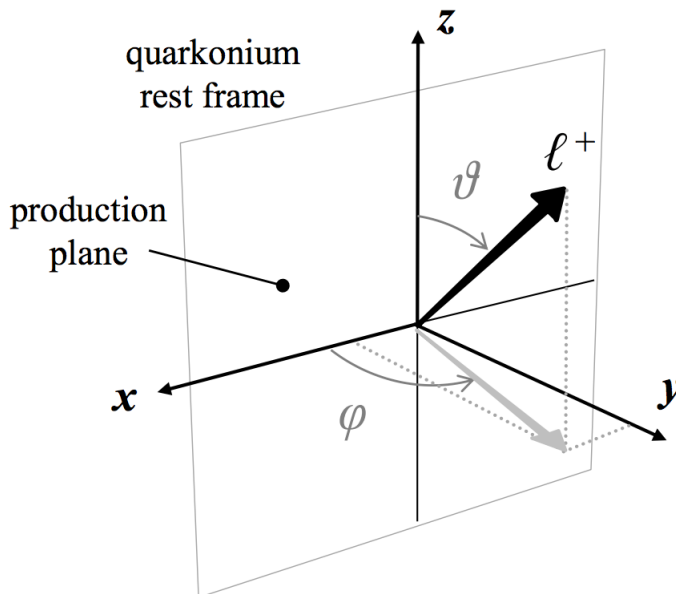


FIGURE 2.14: The polarization of  $J/\psi$  is studied using the angular distribution of decays to  $l^+l^-$ . This figure from Ref. [13] shows a coordinate system for measuring this distribution. The polarization axis is chosen to be along  $z$  according to several conventions which are shown in Fig 2.15.

beams, the Collins-Soper frame [66] where  $\hat{z}$  runs long the bi-sector of the acute angle between the two beams, and the helicity frame, where  $\hat{z}$  is chosen to be along the direction of the  $J/\psi$ 's momentum in the CM frame of the beams. We will work in the helicity frame. Transversely polarized  $J/\psi$  will have  $J_z = \pm 1$  where the spin of the particle aligns (anti-aligns) with its momentum. Longitudinally polarized  $J/\psi$  will have  $J_z = 0$ . Suppose that the  $J/\psi$  is in the angular momentum superposition state

$$|J/\psi; J = 1, m\rangle = a_{-1} |J/\psi; 1, -1\rangle + a_0 |J/\psi; 1, 0\rangle + a_{+1} |J/\psi; 1, +1\rangle, \quad (2.22)$$

where the total angular momentum  $J = 1$ ,  $m = -1, 0, +1$ , and the coefficients  $a_m$  are the probability amplitudes that the  $J/\psi$  will be in a given  $m$  state. In Fig. 2.16, the  $l^+l^-$  pair is produced in the  $J/\psi$  rest-frame along the  $z'$  axis and where  $J_{z'}$  is the projection of  $\pm 1$  onto  $z'$ .  $\theta$  and  $\phi$  are the polar and azimuthal angles between  $z'$  and the polarization axis  $z$ . Using rotation matrix techniques from quantum mechanics,

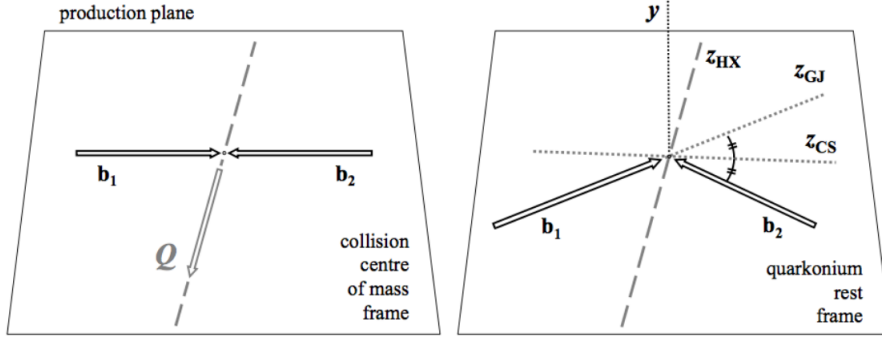


FIGURE 2.15: The three conventions for defining the polarization axis: HX — helicity frame, GJ — Gottfried-Jackson frame, CS — Collins-Soper frame. In this figure taken from Ref. [13],  $b_1$  and  $b_2$  represent the directions of the incoming beams and  $Q$  the direction of the quarkonium.

we can re-express the states in Eq. 2.22 as eigenstates of  $J_z$

$$|J, m'\rangle = \sum_{m=-J, \dots, +J} \mathcal{D}_{mm'}^{(J)}(\alpha, \beta, \gamma) |J, m\rangle, \quad (2.23)$$

where the Euler angles  $\alpha, \beta, \gamma$  will be  $\alpha = -\gamma = \phi$  and  $\beta = \theta$  such that

$$\mathcal{D}_{mm'}^{(J)}(\phi, \theta, -\phi) = e^{-i\phi(m-m')} d_{mm'}^{(J)}(\theta). \quad (2.24)$$

Here,  $d_{mm'}^{(J)}(\theta)$  are the reduced matrix elements (e.g.,  $d_{11}^{(1)} = (1 + \cos\theta)/2, \dots$ ). It can be shown (e.g., Ref. [13]) that the probability,  $W(\theta, \phi)$ , that a  $J/\psi$  decays into a  $l^+l^-$  pair with an angular distribution in  $\theta, \phi$  can be written as

$$W(\theta, \phi) \sim \frac{1}{3 + \lambda_\theta} (1 + \lambda_\theta \cos^2 \theta + \lambda_\phi \sin^2 \theta \cos 2\phi + \lambda_{\theta\phi} \sin 2\theta \cos \phi), \quad (2.25)$$

where for purely transverse (longitudinally) polarized distributions  $\lambda_\theta = +1(-1)$  and  $\lambda_\phi = \lambda_{\theta\phi} = 0$ . The symbol  $\lambda_\theta$  is the polar anisotropy parameter and can be expressed in terms of the probability amplitudes for the  $J/\psi$  to be in each  $J_z$  eigenstate as

$$\lambda_\theta = \frac{1 - 3|a_0|^2}{1 + |a_0|^2} \sim \frac{\sigma_T - 2\sigma_L}{\sigma_T + 2\sigma_L}. \quad (2.26)$$

Here,  $a_0$  is the probability amplitude of the  $J/\psi$  to be in the  $J_z = 0$  state and  $\sigma_T(\sigma_L)$  are the cross-sections for transversely (longitudinally) polarized  $J/\psi$ .

$J/\psi$  (COM frame)

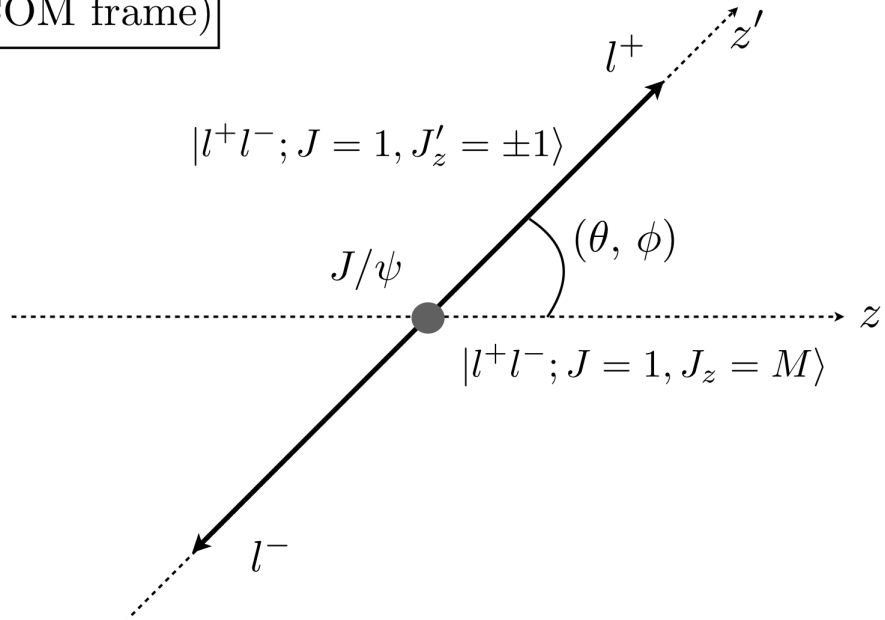


FIGURE 2.16: The polarization of  $J/\psi$  is studied using the angular distribution of decays to  $l^+l^-$ . Knowing the eigenvalues of  $J'_z$  along the axis of production, basic properties of angular momentum can be used to show that polarization can be expressed in terms of eigenstates of  $z$  a polarization axis fixed by one of the conventions described in the text. This figure is adapted from Ref. [13].

### 2.5.2 Predictions & Measurements of Quarkonium Polarization

Where NRQCD factorization holds, the LDMEs should be universal quantities. Ref. [67] showed that the dominance of the  $^3S_1^{[8]}$  mechanism meant that for large transverse momentum, nearly 100% of  $J/\psi$  and  $\psi'$  should be transversely polarized. Because this mechanism comes from the direct fragmentation of a single virtual gluon, as  $p_T$  is increased, this gluon gets closer and closer to being on its mass-shell. Gauge invariance dictates that gluons, which are massless, must always be transversely polarized. An intermediate  $Q\bar{Q}[^3S_1^{[8]}]$  becomes a physical color-singlet quarkonium state  $\mathcal{Q}$  via 2 chromo-electric transitions. Governed by an operator of the form  $\psi^\dagger(ig\mathbf{A} \cdot \nabla)\psi$ , chromo-electric transitions occur via soft gluon emissions and preserve the heavy quark spin symmetry. Thus, the resulting  $J/\psi$  or  $\psi'$  should

	$\langle \mathcal{O}^{J/\psi}(^3S_1^{[1]}) \rangle$ $\times \text{GeV}^3$	$\langle \mathcal{O}^{J/\psi}(^3S_1^{[8]}) \rangle$ $\times 10^{-2} \text{GeV}^3$	$\langle \mathcal{O}^{J/\psi}(^1S_0^{[8]}) \rangle$ $\times 10^{-2} \text{GeV}^3$	$\langle \mathcal{O}^{J/\psi}(^3P_0^{[8]}) \rangle / m_c^2$ $\times 10^{-2} \text{GeV}^3$
B & K [14, 15]	$1.32 \pm 0.20$	$0.224 \pm 0.59$	$4.97 \pm 0.44$	$-0.72 \pm 0.88$
Chao, et al. [18]	$1.16 \pm 0.20$	$0.30 \pm 0.12$	$8.9 \pm 0.98$	$0.56 \pm 0.21$
Bodwin et al. [22]	$1.32 \pm 0.20$	$1.1 \pm 1.0$	$9.9 \pm 2.2$	$0.49 \pm 0.44$

Table 2.1: We consider three sets of LDMEs for NRQCD production mechanisms, listed here in units of  $\text{GeV}^3$ .

be transversely polarized.

Fig. 2.12 shows that fixed order NRQCD predictions that the  $J/\psi$  and  $\psi'$  polarization is transverse at high- $p_T$  is obviously not correct. There are a number of possible theoretical uncertainties such as the uncertainty in the extraction of the LDMEs, higher order QCD effects that have been neglected in the calculation of the short-distance pieces, and higher order spin-symmetry violating terms in NRQCD. These cannot explain the drastic failure of the polarization prediction. This problem is known as the **polarization puzzle**.

There have been numerous extractions of the LDMEs since the publication of Ref. [10] in 1999. We will discuss three such extractions from Refs. [14, 15, 18, 22]. The results of each of these fits are presented in Table 2.1 and again in Table 5.4 for convenience in Chapter 5. In Refs. [14, 15], the authors performed fits using NLO fixed order calculations of direct  $J/\psi$  production that included both color-singlet and color-octet mechanisms to the world's data on  $J/\psi$  production. This included data from a wide variety of experiments and thus a wide variety of initial states including  $pp, p\bar{p}, \gamma\gamma, \gamma p, e^+e^-$ .

We note that Ref. [15] used  $1.32 \text{GeV}^3$  for the  $^3S_1^{[1]}$  LDME, which was extracted from the electromagnetic partial width  $\Gamma[J/\psi \rightarrow e^+e^-]$  in Ref. [68]. As can be seen in Fig. 2.17 (only LHCb and ATLAS are shown), the predictions of NLO NRQCD fit the data far better than CSM predictions, which under predicted the production

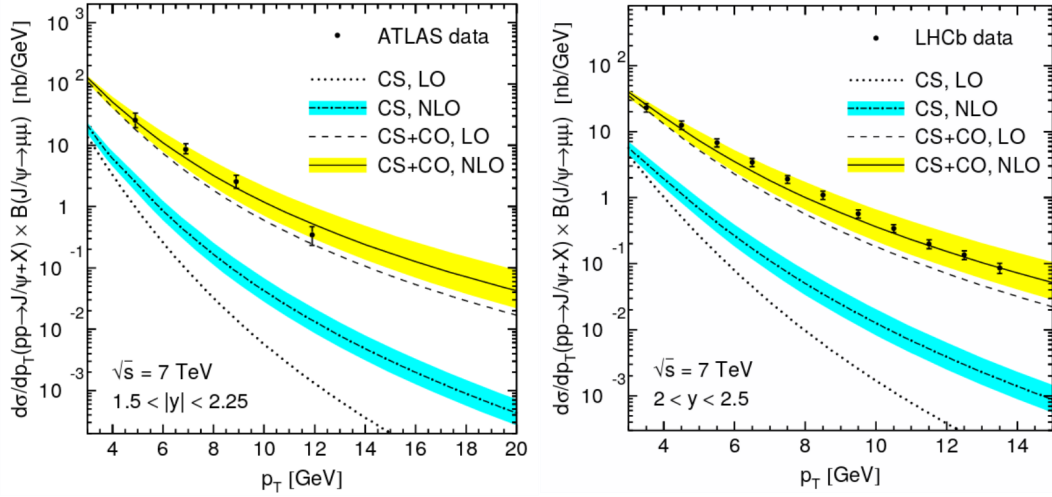


FIGURE 2.17: A sample of 2 (out of 28) plots that show the global fits performed in Refs. [14, 15] of NLO NRQCD predictions (shown as CS+CO,NLO). The plots show that the data clearly favor the inclusion of the color-singlet and color-octet modes predicted at NLO in NRQCD over LO NRQCD and the color-singlet model (shown as CS, LO and CS, NLO) at both leading and next-to-leading order.

rate an order of magnitude. Predictions of the  $J/\psi$  polarization using these fits are compared with LHCb data in Fig. 2.18, where they are drawn as blue diagonal lines. Similarly to the comparisons of NRQCD predictions with CDF data in Fig. 2.12, NRQCD with LDMEs extracted from the global fits of Ref. [15] predicts a strong transverse polarization at high  $p_T$ , which does not match the data. LHCb data from Ref. [16] shows unpolarized  $J/\psi$  with perhaps a slight longitudinal polarization at very high  $p_T$ .

In 2012, Ref. [18] performed an extraction of the LDMEs from a more restrictive data set using a fixed order NLO NRQCD calculation of prompt  $J/\psi$  production. Rather than fitting strictly to the  $p_T$  distribution, Ref. [18] performed a simultaneous fit of the LDMEs to both the  $p_T$  and polarization distributions for high  $p_T > 7$  GeV data at the Tevatron. Shown in Fig. 2.19, their predictions for direct  $J/\psi$  production also show good agreement in the  $p_T$  distributions. Their predictions for the polarization are shown in Fig. 2.18 as a green hatched pattern. While these fits

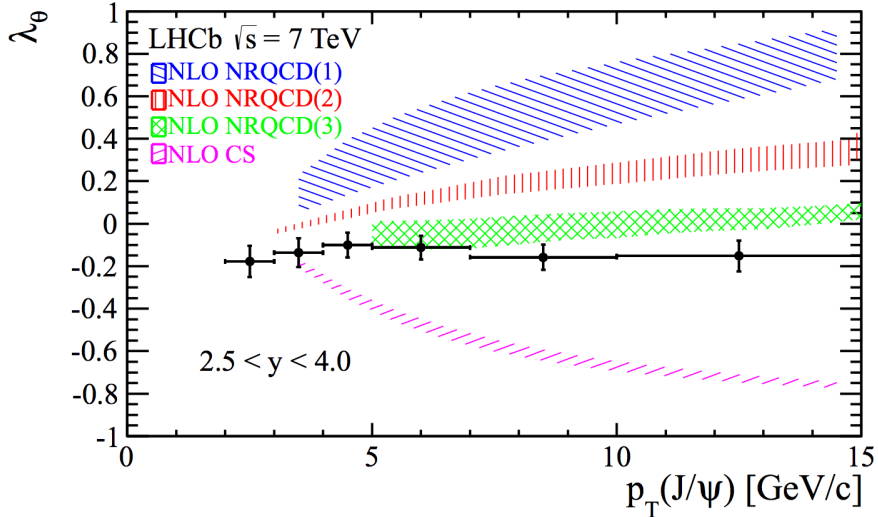


FIGURE 2.18: A comparison of LHCb data [16] for prompt  $J/\psi$  production of the polarization observable  $\lambda_\theta$  with  $k_T$  factorization (modification of CSM; shown in diagonal magenta lines) [15] and three different NLO NRQCD predictions as a function of  $p_T(J/\psi)$  for the LHCb rapidity range of  $2.5 < y < 4$ . The blue diagonal lines (NRQCD(1)) are based on global fits of Ref. [15], the red vertical lines (NRQCD(2)) on fits of Ref. [17], and the green hatched pattern (NRQCD(3)) on a high- $p_T$  fit from Ref. [18, 19]. We do not consider the fits of Ref. [17] or from the  $k_T$  factorization approach in this work.

do perform better than the polarization predictions of the global fits, they are still not within experimental errors at high  $p_T$ .

Finally, Ref. [22] performed a fit of the LDMEs to  $p_T > 10$  GeV data for prompt  $J/\psi$  production at both the Tevatron and the LHC. Their analytic prediction was based on NRQCD using the LP power factorization formalism described in the previous section. This approach allowed them to evolve the FFs from  $2m_c$  to  $m_T = \sqrt{p_T^2 + (2m_c)^2}$ , essentially the scale of the  $p_T$  of the  $J/\psi$ , resumming potentially large logarithms of  $p_T^2/(2m_c)^2$  at leading-logarithmic accuracy. They then made predictions of the polarization of  $J/\psi$  in direct production, which is compared against CDF and LHC data in Fig. 2.20. In both cases, their calculations of the polarization improved upon previous predictions, suggesting that the NLO + LP formalism provides a more accurate description of  $J/\psi$  production at high  $p_T$ .

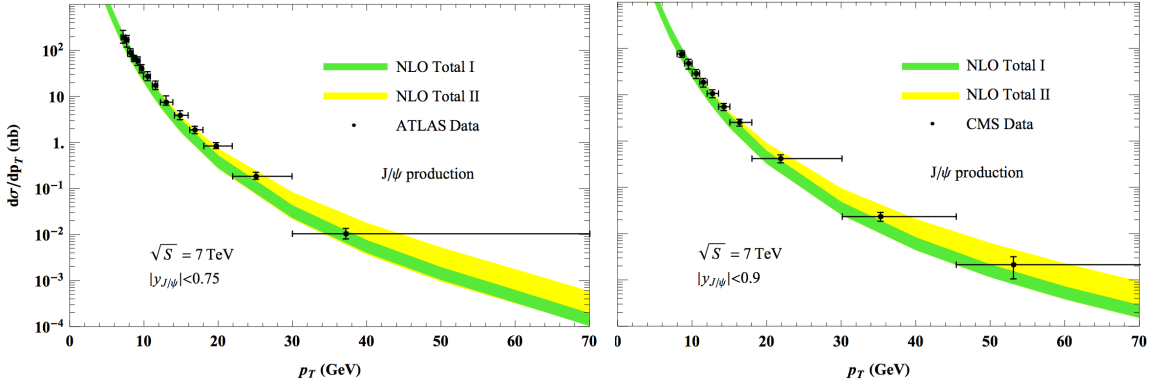


FIGURE 2.19: Cross-sections as a function of  $p_T$  for the two LDME extractions in Ref. [18]. Darker bands (NLO Total I) show predictions that use the fits shown in Table 5.4 for the simultaneous fit of the LDMEs to the polarization and  $p_T$  for specifically  $p_T > 7$  GeV data from CDF and CMS. The lighter bands show upper and lower bounds of fits that fix  $\mathcal{O}(^1S_0^{[8]}) = 0$  and  $\mathcal{O}(^3S_1^{[8]}) = \mathcal{O}(^3P_J^{[8]}) = 0$  as the upper and lower bounds, respectively. The top and bottom figures show comparisons with ATLAS (left) [20] and CMS (right) [21] data.

Ref. [18] and Ref. [22] predict polarization distributions that are much closer to the unpolarized data than the predictions of the global fits of Ref. [15]. Refs. [18, 22] enforce a cancellation of the  $^3S_1^{[8]}$  and  $^3P_J^{[8]}$  mechanisms. Fig. 2.21 shows individual contributions to the polarization parameter from each NRQCD production mechanism. As the  $^3S_1^{[8]}$  and  $^3P_J^{[8]}$  both have significant transverse components, their cancellation leaves the  $^1S_0^{[8]}$  mechanism, which largely mimics the data, as the main color-octet contribution at high  $p_T$ .

## 2.6 Going Forward

Ref. [18] and Ref. [22] showed improvements in the ability of NRQCD to predict the  $p_T$  distribution and polarization of the  $J/\psi$  in hadron collisions at high  $p_T$  over the global fits of Ref. [14]. They expose a more complex relationship amongst the contributions of the different NRQCD production mechanisms where the picture is not

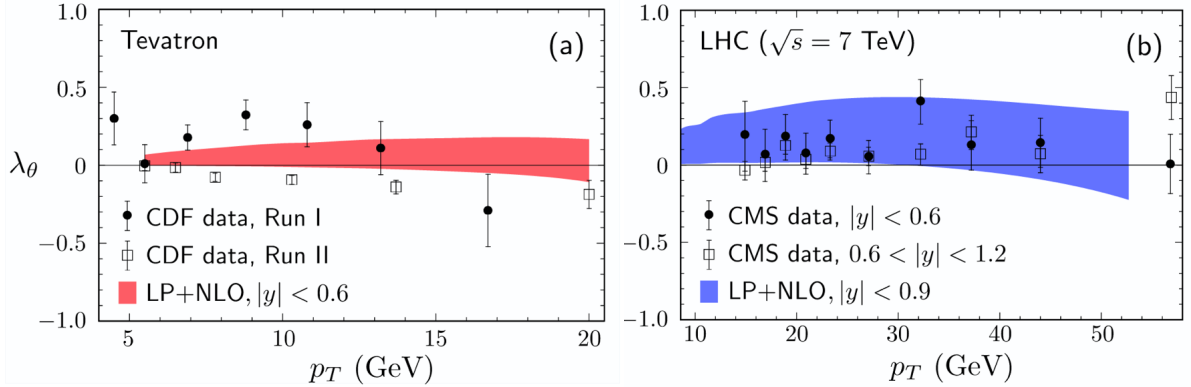


FIGURE 2.20: Comparison from Ref. [22] of analytic predictions using NLO NRQCD + LP factorization for the anisotropy parameter  $\lambda_\theta = (\sigma_T - 2\sigma_L)/(\sigma_T + 2\sigma_L)$  with data from (a) CDF Run I [11] and CDF Run II [23] and (b) CMS data [24]. Again,  $\sigma_T(\sigma_L)$  is the cross-section for transversely (longitudinally) polarized production of the  $J/\psi$ .

simply of a dominant  $^3S_1^{[8]}$  channel at high  $p_T$ . Ref. [22] also demonstrated the utility of the LP factorization formalism, which focuses on fragmentation contributions to  $J/\psi$  production.

However, significant differences between the three fits discussed above exposes an underlying tension in calculations of  $J/\psi$  production. The LDMEs, which describe the non-perturbative evolution of  $Q\bar{Q}[n]$  states into physical quarkonia, should be universal. Even amongst different fits to high  $p_T$  data, radically different results are found for the LDMEs. These imply different pictures of how quarkonia are produced and raises a number of intriguing questions: Do the velocity  $v$  or  $\alpha_s$  expansions in NRQCD have convergence issues? Does LP factorization break down at low transverse momentum?

Ref. [12] took on these questions and proposed alternative tests of NRQCD that focus on  $J/\psi$  produced within jets. They showed that recently developed jet substructure techniques can be harnessed to use jets as a laboratory in which to study quarkonium production in a regime where NRQCD factorization is reliable. In Chapter 3, we will discuss the fundamentals of jet physics and how jets provide a new

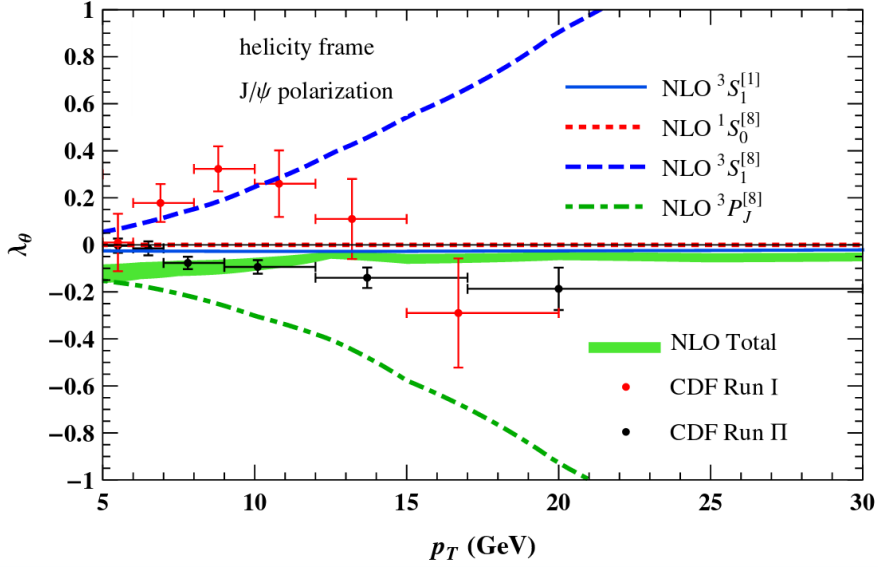


FIGURE 2.21: Polar anisotropy parameter  $\lambda_\theta = (d\sigma_T - 2d\sigma_L)/(d\sigma_T + 2d\sigma_L)$  for  $J/\psi$  production using LDMEs from fits performed in Ref. [18] compared with data from CDF Run I [25] and Run II [26]. This plot also shows the individual contributions of each NRQCD production mechanism to the overall polarization. This makes the cancelation of the transverse components of the  ${}^3P_J^{[8]}$  and  ${}^3S_1^{[8]}$  components at high  $p_T$  visible.

realm in which to extract information about the non-perturbative formation of the  $J/\psi$ .

# Jets: Nature's High-Energy Conical Laboratory

## 3.1 Introduction

Practically ubiquitous in high-energy particle collisions are highly collimated sprays of radiation called **jets**. Observed in detectors as clusters of particles in a restricted angular region, jets are one of the most fundamental predictions of QCD. A natural consequence of confinement, jets are important for a wide variety of reasons within both Standard Model (SM) and Beyond the Standard Model (BSM) physics. Jets are the source of large backgrounds to many interesting processes which motivates the development of methods by which to veto events containing jets. Jets also provide a laboratory in which to study the process of hadronization, providing a key bridge between partonic predictions and observables involving hadrons. Our goal is to understand how the substructure of jets, the distribution of the momenta of their constituent particles, can shed light on long outstanding puzzles in quarkonia production.

In this chapter, we first review the origins of jets in QCD and the history of jet-related discoveries. We give an overview of how jets are defined and introduce

observables that are used to classify their substructure. Finally, we explain how jets are studied using EFTs, focusing on the calculation of jet production cross-sections in Soft-Collinear Effective Theory (SCET). This introduction to SCET will be important in Chapter 4 when we discuss the FJF formalism. Using the FFs for  $J/\psi$  calculated in NRQCD, FJFs will allow us to calculate cross-sections for the production of quarkonia within jets where the substructure of the jet is measured.

### 3.2 Origins of Jet Physics

Due to asymptotic freedom, quarks and gluons behave as quasi-free particles at high-energies (short-distances). When these particles, which carry color, are created in high-energy collisions and reach a relative distance of  $\sim 1$  fm, they undergo the non-perturbative process of hadronization. Through the emission of gluons via bremsstrahlung radiation and their subsequent splittings into  $q\bar{q}$  pairs, these initially quasi-free particles ultimately result in the formation of many colorless hadrons.

In the discussion of the flux-tube model shown in Fig. 2.4, as the  $q\bar{q}$  move apart, the tension in the flux-tube causes it to break via the formation of a new  $q\bar{q}$  pair from the vacuum. Conservation of momenta and the IR structure (i.e., the soft and collinear limits) of the cross-section in QCD for jet production cause these jets to be highly collimated. Effects of confinement forces are soft compared to the high longitudinal momenta of the jet-initiating partons. Thus, the energies and angular distribution of these partons is reflected in the energies and angular distribution of the jets. This mapping between partons and hadronic jets makes the study of partons and the study of jets inseparable. Quark initiated jets were first observed at SPEAR [69, 70] at the Stanford Linear Accelerator Center (SLAC) in 1972 at  $\sqrt{s} \sim 4$  GeV, followed soon after by studies at the much higher energies of DORIS ( $\sqrt{s} \sim 5.6$  GeV) and PETRA ( $\sqrt{s} \sim 23.4$  GeV) at DESY in Hamburg, Germany. Refs. [71, 72] had previously predicted that the dominant source of hadron production in  $e^+e^-$

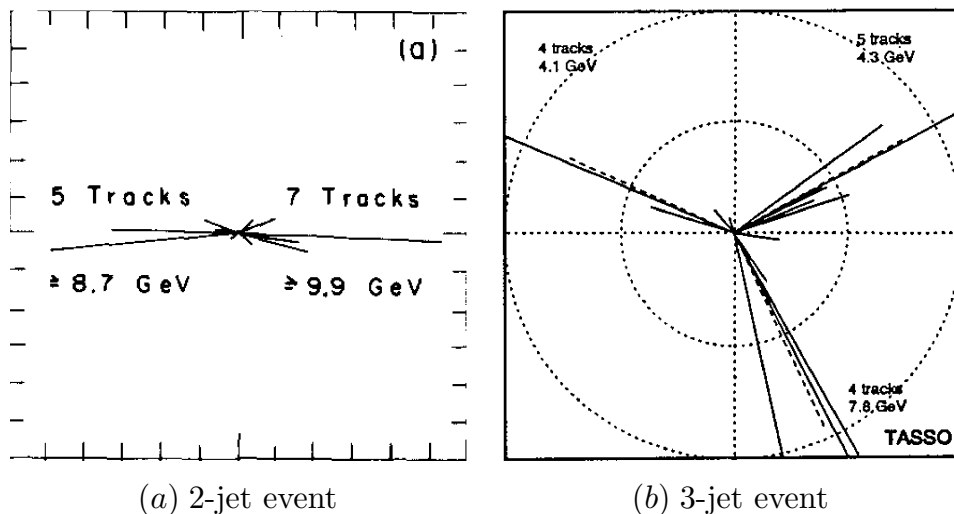


FIGURE 3.1: Displays of 2-jet (a) and 3-jet (b) events as shown in Ref. [27, 28].

annihilation should come from

$$e^+e^- \rightarrow q\bar{q} \rightarrow 2 \text{ jets.} \quad (3.1)$$

These events could be easily identified by looking at the angular distribution of the final state hadrons, which would have radiation accumulated on a central axis (back-to-back jets) instead of being isotropically distributed. It was also predicted in Ref. [73] that gluon-initiated jets could be definitively observed in the process

$$e^+e^- \rightarrow q\bar{q}g \rightarrow 3 \text{ jets,} \quad (3.2)$$

which was predicted to be the next-to-leading process for  $e^+e^- \rightarrow$  hadrons. Events with gluon jets could have a configuration where the three jets have approximately equal angular separation. This is often called the **Mercedes-Benz configuration**. The gluon jet would then be distinguishable from the quark jets by the larger amount of radiation present within its cone. In QCD, the probability of  $g \rightarrow gg$  splittings comes with a color-factor of  $C_A = 3$  while  $q \rightarrow qg$  splittings come with a color-factor of  $C_F = 4/3$  (see Eq. (2.7)), making  $g \rightarrow gg$  splittings more likely. Gluon jets, which

provided the first conclusive evidence of the existence of the gluon, were discovered at PETRA by several experiments in  $e^+e^-$  annihilation in 1979 in Refs. [28, 74–76].

The ability to identify and reconstruct jets is important to searches for new physics, as they are often large sources of background. In Higgs searches, for example,  $H \rightarrow W^+W^- \rightarrow l^+\nu l^-\bar{\nu}$  signals are subject to large backgrounds from  $t\bar{t} \rightarrow W^+W^-b\bar{b}$ . As discussed in Ref. [77], jet vetoes can be used to identify and cut events that contain jets that are emitted by  $b(\bar{b})$  quarks. Highly boosted  $b$  quarks often fragment into jets containing  $B$  mesons. This process of identifying the partonic origin of a jet based on its hadronic content is an example of tagging. There is also interest in developing techniques to separate jets produced by fragmenting quarks from jets produced by fragmenting gluons. This idea leads to the study of the detailed substructure of jets, which is the subject of the next section.

### 3.3 Jet Algorithms & Jet Substructure

#### 3.3.1 Jet Algorithms

Jets are defined in hadronic final states through jet algorithms and recombination schemes. Jet algorithms are simple sets of iterative rules for defining whether particles are close enough to be considered within the same jet. Recombination schemes then dictate how the four-momenta of the particles will be combined. Jet algorithms can be classified in two broad categories: cone algorithms, and sequential recombination algorithms.

The first modern jet definition was developed in 1977 by Sterman and Weinberg in Ref. [50]. A primitive type of cone algorithm, Sterman and Weinberg’s concept of a jet provided the first divergence-free analytic way to formally define dijet events in  $e^+e^-$  annihilation. Dijet events were classified as events where at least a fraction  $1 - \epsilon$  of the total event energy was contained within a cone of half-angle  $\delta$ . This provided the first consistent way to calculate dijet event cross-sections in perturbative QCD.

Modern cone algorithms use the concept of iterative cones where a final state particle is chosen as a seed particle,  $i$ , whose momentum is combined with all other particles  $j$  satisfying the condition that

$$\Delta R_{ij}^2 = (y_i - y_j)^2 + (\phi_i - \phi_j)^2 < R^2, \quad (3.3)$$

where  $R$  is a cone size parameter, and  $y_i, \phi_i$  are the rapidity and azimuthal angle of the  $i$ th particle defined via

$$y \equiv \frac{1}{2} \log \left( \frac{E + p_z}{E - p_z} \right) \quad \text{and} \quad \phi \equiv \tan^{-1} (p_y/p_x). \quad (3.4)$$

Here, all quantities are defined with reference to an axis  $\hat{z}$  along the incident beam line. The four-momenta of the particles satisfying the above condition are then summed and the seed  $i$  is iterated over all of the particles until a set of so-called stable cones is found. The stability condition ensures that the jets are insensitive to the addition of arbitrarily soft particles within or in-between jets or arbitrarily collinear emissions within jets, a condition called infrared-collinear (IRC) safety. The process of ensuring IRC safety is discussed in detail in Ref. [29].

Sequential recombination algorithms were first introduced by the JADE collaboration [78] with their JADE algorithm. A host of recombination algorithms such as the  $k_T$  [79], Cambridge/Aachen [80], and anti- $k_T$  [81] have since been developed, with the anti- $k_T$  being the most common algorithm used at modern hadron colliders. These algorithms mimic the undoing of QCD splittings via the following procedure

1. Define a distance metric  $d_{ij}$  to measure the angular separation between any two particles  $i, j$  and a metric  $d_{i,B}$  to measure the angular separation between each particle and the beam-line.
2. Calculate  $d_{ij}$  and  $d_{i,B}$  for all particles  $i, j$  in the event.

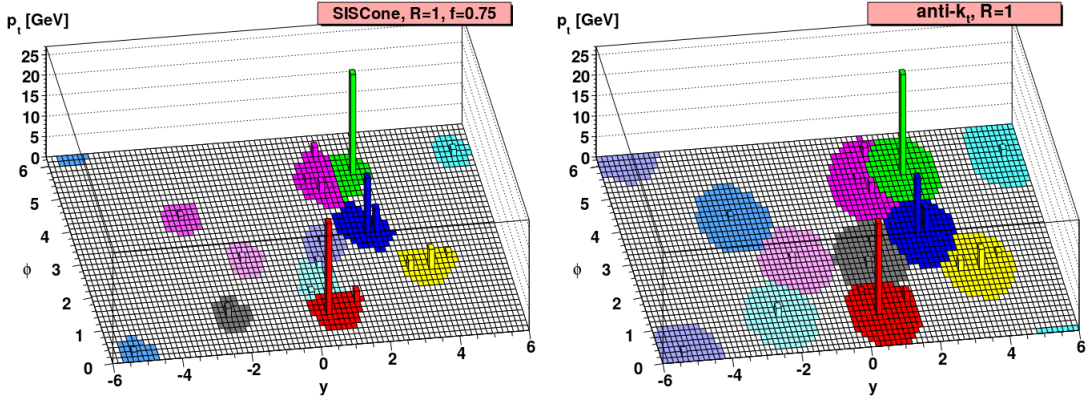


FIGURE 3.2: This figure from Ref. [29] shows how two jet algorithms, the SIS-Cone [30] and anti- $k_T$  algorithms, behave when applied to the same event. Highlighted areas represent jets in the space of the azimuthal angle  $\phi$ , rapidity  $y$ , and transverse momentum  $p_T$  with cone size parameter  $R = 1$ .  $f$  is the so-called overlap parameter and is defined in [30].

3. For each particle  $i$ , if for a given  $j$  you find  $d_{ij} < d_{iB}$ , combine the  $i$  and  $j$  four-momenta into a single track (called a pseudojet). Otherwise, declare that  $i$  is a jet by itself, remove it from the list of particles, and repeat step 1.
4. When no particles satisfying condition 3 are left, stop iterating.

Calculations in later chapters of this work will make use of cone and anti- $k_T$  algorithms. The anti- $k_T$  [81] is a specific case of the more general  $k_T$  algorithm and uses the following distance metrics

$$d_{ij} = \min(p_{Ti}^{2p}, p_{Tj}^{2p}) \frac{\Delta R_{ij}^2}{R^2}, \quad \text{where } d_{iB} = p_{Ti}^{2p}, \quad (3.5)$$

where  $p = -1$ ,  $p_{Ti}$  is the transverse momentum of the  $i$ th particle relative to the beam line, and  $\Delta R_{ij}$  and  $R$  are defined in Eq. (3.3). The subtleties of the divergence structure and implementation of these algorithms is discussed at length in Ref. [29].

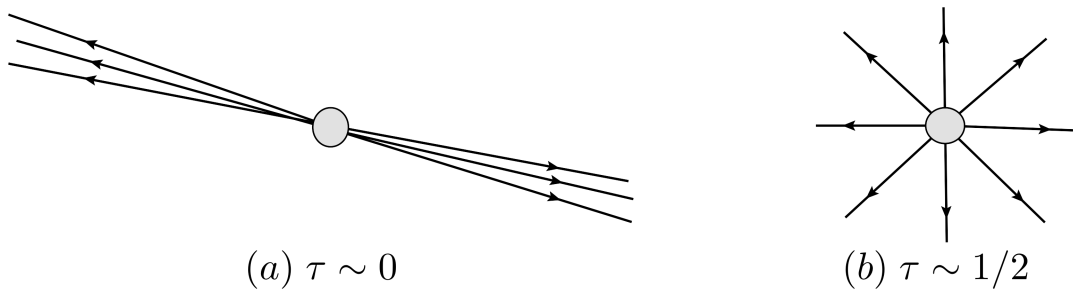


FIGURE 3.3: An illustration of two characteristic values of the thrust parameter  $\tau = 1 - T$  showing (a) pencil-like dijets for  $\tau \sim 0$  and (b) isotropic final state with 0 jets.

### 3.3.2 Jet Substructure

In addition to being able to identify and reconstruct jets, a quantitative understanding of a jet's substructure is also useful. **Jet substructure observables** are continuous variables that are weighted sums over the four-momenta of a jet's constituent particles. They are, in many cases, derivative of **event shapes**, well-established QCD observables (used largely in  $e^+e^-$  collisions) that allow us to study the geometric properties of the energy and momentum flow of the entire final state. Perhaps the most well-established event shape variable is **thrust**, which quantifies how much an event looks like a back-to-back dijet configuration. Originally defined in Ref. [82], thrust cross-sections have been calculated to N<sup>3</sup>LL accuracy [83], and have been used to extract the strong coupling  $\alpha_s$ . Thrust is defined as

$$T = \max_{\hat{n}} \frac{\sum_i |\hat{n} \cdot \vec{p}_i|}{\sum_i |\vec{p}_i|}. \quad (3.6)$$

Here,  $i$  runs over all of the final state particles in the event and  $\hat{n}$  is the jet axis that maximizes  $T$ , called the thrust axis. In practice, the quantity  $\tau \equiv 1 - T$  is more commonly used to characterize dijet events. This is because  $\tau \sim 0$  corresponds to an event with two back-to-back, highly-collimated, pencil-like jets and  $\tau \sim 1/2$  describes

a spherically symmetric distribution of final state particles. Fig. 4.2 illustrates these two thrust values. We will revisit calculations of thrust in our study of hadron production in jets in Chapter 4.

Jet substructure observables can be divided into several broad categories: observables that study the radial distribution of particles within a jet, those that focus on probing highly boosted decay kinematics, and those that aim to probe the color flow of events. Perhaps the simplest example of a jet substructure observable is the measurement of the invariant mass  $s$  of the jet which is given by

$$s = \left( \sum_{i \in J} p_i \right)^2. \quad (3.7)$$

Other jet-shape observables that study the radial distribution of particles include the aptly named jet-shape [84] and angularity [85]. The jet-shape observable measures how energy is distributed within a jet by taking ratios of the transverse energy contained within cones of radius  $r$  inside of a jet of size parameter  $R > r$ . The jet-shape can ultimately be expressed as  $E_r/E_R$ , the ratio of the energy in a jet of size  $R$  contained within an inner cone  $r$  such that at  $r = R$ , the jet-shape is 1. Angularities, denoted by  $\tau_a$  are a family of jet-shape observables calculated via a weighted sum over the transverse momentum of all of the particles within an jet, where the weighting is dictated by the value of a parameter  $a$

$$\tau_a \equiv \frac{1}{2E_J} \sum_{i \in J} |\mathbf{p}_\perp^i| e^{-\eta_i(1-a)}. \quad (3.8)$$

In this expression,  $E_J$  is the jet energy,  $\eta_i = \log(\tan(\theta/2))$  is the pseudorapidity of the particle  $i$  relative to the jet axis, the sum is over the particles in the jet, and  $-\infty < a < 2$ . Smaller values of  $a$  put more emphasis on contributions from particles closer to the edge of the jet. Additionally, as we will show in Chapter 4, angularities are directly related to the jet invariant mass when  $a = 0$  via  $\tau_0 = s/(2E_J)^2$ . Fig. 3.4(a)

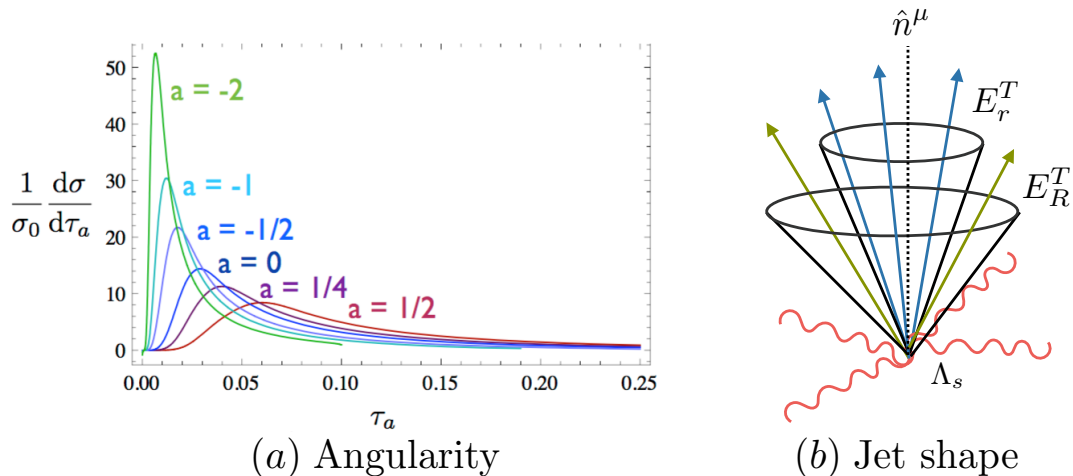


FIGURE 3.4: Diagram (a) shows a sample  $e^+e^-$  cross-section differential in the angularity  $\tau_a$  for different values of  $a$  with  $a < 1$ . Diagram (b) illustrates the jet-shape observable as a fraction of transverse energy within a cone of radius  $r$  within a larger jet of radius parameter  $R$  with total soft radiation  $\Lambda_S$  falling outside of the jets.

shows, roughly, how a cross-section differential in the angularity might depend on the parameter  $a$ . Fig. 3.4(b) shows a basic illustration of the jet-shape, where a cone of variable size  $r$  is drawn within a cone (or  $k_T$ ) type jet of radius  $R$  in order to measure how widely the jet’s radiation is distributed. Other jet substructure observables exist that focus on different aspects of a jet such as the kinematics of decays of its constituents [86] and the color-flow of particles within jets in an event [87]. These observables are not the focus of this work.

Jet substructure studies have a number of important applications, from discriminating between jets initiated by quarks vs. gluons, to tagging jets based on their hadronic content, to probing the very nature of hadronization. In the following section, we will discuss the EFT that is often used to calculate jet-substructure observables to high precision, which will be used heavily in Chapters 4 and 5.

## 3.4 Soft-Collinear Effective Theory

### 3.4.1 Introduction

Theoretical predictions of jet observables often involve multiple disparate energy scales. Consider the following hierarchy

$$E_J \approx Q \gg \sqrt{s} \gg \Lambda_{\text{QCD}}, \quad (3.9)$$

where  $s$  is the jet invariant mass. Since jets are made up of highly boosted particles, the energy of a jet is generally far greater than its invariant mass, which is turn much greater than the scale of non-perturbative physics,  $\Lambda_{\text{QCD}}$ . As we discussed in Chapter 1, calculations of QCD processes involve logarithms of ratios of the physical scales in the problem. These logarithms can often be so large as to cause a breakdown of perturbation theory. Renormalization group techniques can be used to resum these logarithms in a systematic way, drastically improving the accuracy of a calculation by including the most important terms at higher orders in  $\alpha_s$ . EFTs facilitate the resummation of different logarithms by making each function in a factorization theorem dependent upon a single physical scale.

Developed in Refs. [88–91], Soft-Collinear-Effective Theory (SCET) can be used to derive powerful factorization theorems for jet processes. SCET is an EFT that focuses on degrees of freedom that are soft and collinear with respect to light-like jet directions  $n$  in the presence of a much harder interaction.<sup>1</sup> Factorization theorems in SCET have been used to study event-shape distributions in, for example, Refs. [93–96] and jet substructure observables in Refs. [1, 85, 97]. In Ref. [1], the authors derived a factorization theorem in  $e^+e^- \rightarrow N$  jet events where the substructure of  $M \leq N$  of the jets was measured. Our goal in this section is to develop the SCET formalism necessary to understand the factorization of a general class of jet substructure observables  $\tau$  in  $e^+e^-$  annihilation.

<sup>1</sup> See Ref. [92] for a pedagogical introduction to SCET.

### 3.4.2 Light Cone Coordinates

A useful set of coordinates for describing the degrees of freedom on SCET can be constructed from light-like vectors  $n_i^\mu$  where  $n^2 = 0$  called **light-cone coordinates**.

We can construct a basis of light cone vectors  $n$  and  $\bar{n}$  using the properties that

$$n^2 = 0, \quad \bar{n}^2 = 0, \quad n \cdot \bar{n} = 2. \quad (3.10)$$

The simplest choice (up to re-parameterizations to be discussed later) for  $n$  and  $\bar{n}$  is

$$n^\mu = (1, 0, 0, 1) \quad \text{and} \quad \bar{n}^\mu = (1, 0, 0, -1). \quad (3.11)$$

We can then decompose any four-momentum  $p^\mu$  using the so-called Sudakov decomposition

$$p^\mu = \frac{n^\mu}{2} \bar{n} \cdot p + \frac{\bar{n}^\mu}{2} n \cdot p + p_\perp^\mu = (p^+, p^-, \mathbf{p}_\perp), \quad (3.12)$$

where  $p^+ = p_+ \equiv n \cdot p$ ,  $p^- = p_- \equiv \bar{n} \cdot p$ , the transverse momentum  $p_\perp^\mu = (0, 0, \mathbf{p}_\perp)$  can be expressed in Minkowski form,  $p_\perp^\mu$ , or Euclidean form,  $\mathbf{p}_\perp$ , and  $p_\perp^\mu p_{\perp,\mu} = -\mathbf{p}_\perp^2$ . The metric tensor  $g^{\mu,\nu}$ , using the  $(+, -, -, -)$  convention, can then be expressed as

$$g^{\mu\nu} = \frac{1}{2} n^\mu \bar{n}^\nu + \frac{1}{2} \bar{n}^\mu n^\nu + g_\perp^{\mu\nu} \quad \text{and} \quad \epsilon_\perp^{\mu\nu} = \frac{1}{2} \epsilon^{\mu\nu\alpha\beta} \bar{n}_\alpha n_\beta. \quad (3.13)$$

The square of the four-momentum,  $p_\mu$ , is

$$p^2 = p^+ p^- + p_\perp^2 = p^+ p^- - \mathbf{p}_\perp^2. \quad (3.14)$$

### 3.4.3 Momentum Regions in SCET

Fig. 3.5 shows an  $e^+e^- \rightarrow$  dijets event, which at lowest order in perturbation theory is initiated by  $e^+e^- \rightarrow \gamma^* \rightarrow q\bar{q}$ . One can divide the event into two hemispheres (a) and (b) and consider the two jet directions as  $\bar{n}^\mu$  and  $n^\mu$ . In both hemispheres the collinear particles are highly collimated but consist of many different hadrons. For

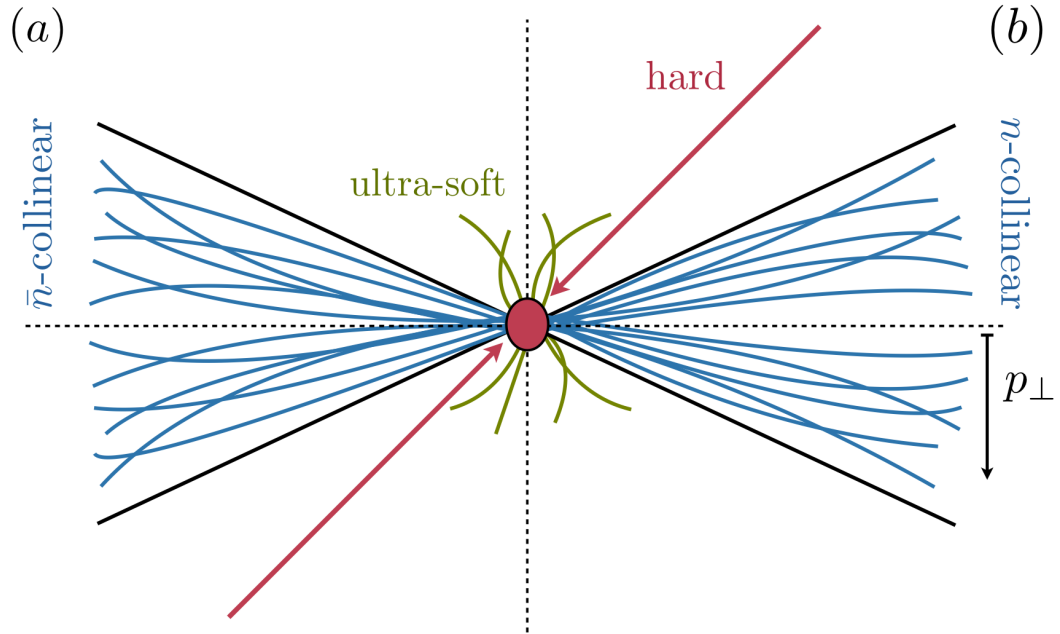


FIGURE 3.5: This diagram shows a dijet event divided into two hemispheres  $a$  and  $b$  with two light-cone directions  $n^\mu$  and  $\bar{n}^\mu$ . The SCET degrees of freedom are color-coded. Collinear radiation is shown in blue within the jet boundary and ultra-soft radiation is shown in green. The underlying hard interaction is shown in red.

a jet with particles whose large momentum component is  $p^-$ , we see the following scaling

$$\Lambda_{\text{QCD}} \ll p_T \ll p^- \approx Q, \quad (3.15)$$

where  $Q$  is the scale of the center-of-mass energy and  $\mathbf{p}_\perp$  is the scale of the transverse momenta of the particles in the jet. In this example, SCET describes three relevant degrees of freedom that live at each of these well-separated momentum scales. Often referred to as SCET **modes**, the momenta of these degrees of freedom scale according to

$$\begin{aligned} (1) \ n\text{-collinear} &\rightarrow p_n^\mu \sim Q(\lambda^2, 1, \lambda), \\ (2) \ \bar{n}\text{-collinear} &\rightarrow p_{\bar{n}}^\mu \sim Q(1, \lambda^2, \lambda), \\ (3) \ \text{ultra-soft} &\rightarrow p_{us} \sim Q(\lambda^2, \lambda^2, \lambda^2). \end{aligned} \quad (3.16)$$

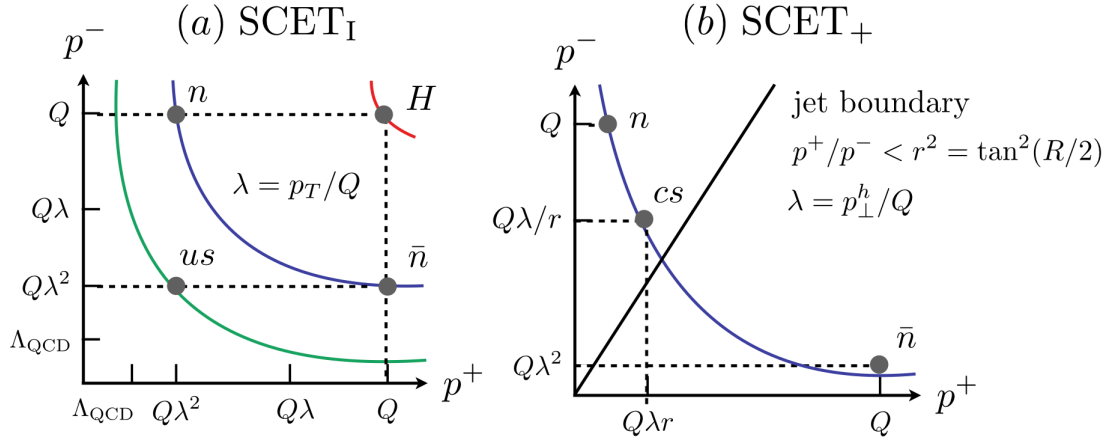


FIGURE 3.6: Modes of SCET<sub>I</sub> (a) and SCET<sub>+</sub> (b) plotted on curves of constant virtuality  $p^2$  of the hard, collinear, collinear-soft, and ultra-soft modes. The relevant power counting parameter  $\lambda$  is shown in each case. In (b), the diagonal line represents a line of constant rapidity representing the boundary of a jet of radius parameter  $R$ .

Here, the convention is  $p^\mu \sim (p^+, p^-, \mathbf{p}_\perp)$  and  $\lambda \equiv p_T/Q \ll 1$  is our power counting parameter. **Collinear** modes are particles that have scaling  $p_c^+ \ll p_c^\perp \ll p_c^-$  in hemisphere (a) or  $p_c^- \ll p_c^\perp \ll p_c^+$  in hemisphere (b). **Ultra-soft** modes, denoted  $p_{us}$ , scale homogeneously in their  $(+, -, \perp)$  components such that they can interact with collinear modes in both jets without changing the scaling of either one. Fig. 3.6(a) illustrates these modes on curves of constant virtuality  $p^2$ . The  $n$  and  $\bar{n}$ -collinear modes live on the same invariant mass curve but are separated in rapidity, which in light-cone coordinates can be expressed as  $y = 1/2 \log(p^+/p^-)$ . The ultra-soft mode lives at a different virtuality, as shown in the figure.

Processes with this particular set of modes are described by a version of SCET called SCET<sub>I</sub>. Different processes may require different sets of modes depending on the specifics of the kinematics. There are many different versions of SCET, but this work focuses on two in particular: SCET<sub>I</sub> and SCET<sub>+</sub>. SCET<sub>I</sub> generally describes  $N$  jet processes where the jets are well-separated and will be used to study jets where the angularity is measured in Section 4.4. SCET<sub>+</sub> was developed in Refs. [98, 99],

originally to study jets that are close together in rapidities. We will utilize SCET<sub>+</sub> to study jet substructure observables that depend on the angle of particles with respect to a jet's axis in Section 4.5. In this case, since the collinear and soft modes both scale as  $\mathcal{O}(\lambda)$  in the  $\mathbf{p}_\perp$  components, certain soft energy scale particles will play an important role in describing the substructure of the jet. SCET<sub>+</sub> thus includes an additional **collinear-soft** mode which has a collinear scaling with respect to a soft energy scale. These modes are illustrated in Fig. 3.6(b), which shows the rapidity regions within and outside of a jet of radius  $R$ . The collinear and collinear-soft modes live on the same invariant mass hyperbola and the collinear-soft mode scales as

$$p_{cs}^\mu \sim p_\perp^h(r, 1/r, 1) \sim Q(\lambda r, \lambda/r, \lambda). \quad (3.17)$$

Here,  $r \equiv \tan(R/2)$  for a jet of radius  $R$  and the power counting parameter is  $\lambda = p_\perp^h/Q$ , where  $p_\perp^h$  is the magnitude of the transverse momentum 3-vector of a given hadron with respect to the jet axis. The scaling with  $r$  reflects the sensitivity of the collinear-soft mode to the boundary of the jet and can be derived by considering that particles within the jet must satisfy  $p^+/p^- < r^2$  and  $p^+p^- \sim p_\perp^2$ .

#### 3.4.4 Label Momentum Formalism

The power counting of the fields in SCET is manifest in the **label momentum formalism**. In SCET<sub>I</sub>, QCD quark fields are split into collinear and ultra-soft pieces using  $q^\mu(x) = q_n^\mu(x) + q_{us}^\mu(x)$  where  $q^\mu$  is a QCD quark field and  $q_n^\mu, q_{us}^\mu$  are SCET collinear and ultra-soft quark fields, respectively. We get manifest power counting by adopting a formalism where momenta are written as

$$p^\mu = p_\ell^\mu + p_r^\mu \quad \text{where} \quad p_\ell^\mu \sim Q(0, 1, \lambda), \quad p_r^\mu \sim Q(\lambda^2, \lambda^2, \lambda^2). \quad (3.18)$$

Here,  $p_l$  is the **label** momentum which is defined as  $p_n^\mu = \bar{n} \cdot p_n \frac{n^\mu}{2} + p_\perp^\mu$  where  $\bar{n} \cdot p_n$  contains the  $\mathcal{O}(1)$  part and  $p_\perp^\mu$  contains the  $\mathcal{O}(\lambda)$  part of the light-cone momentum.

The  $p_r$  term is called the **residual** momentum and contains the  $\mathcal{O}(\lambda^2)$  components of the light-cone momentum. This can be visualized as a grid where label momenta are described in a discrete way as the centers of each grid box and residual momenta represent  $\mathcal{O}(\lambda^2)$  fluctuations within each box. Working in momentum space where the fields are expressed (via Fourier transform) as  $\tilde{q}_n(p) = \int d^4x e^{ip \cdot x} q_n(x)$ , the label momentum formalism dictates that

$$\tilde{q}_n(p) \rightarrow \tilde{q}_{n,p_\ell}(p_r), \quad (3.19)$$

where integrals over momenta are now expressed as

$$\int d^4p \rightarrow \sum_{p_\ell \neq 0} \int d^4p_r. \quad (3.20)$$

Note that the  $p_\ell = 0$  bin is excluded in order to avoid double counting, since it will be accounted for when considering ultra-soft modes.<sup>2</sup> Conservation of momentum is now enforced separately over label and residual momenta via

$$\int \frac{d^4x}{(2\pi)^4} e^{i(p_\ell - q_\ell) \cdot x} e^{i(p_r - q_r) \cdot x} = \delta_{p_\ell, q_\ell} \delta^4(p_r - q_r). \quad (3.21)$$

Using a Fourier transform we write our total collinear quark field as the sum/integral over label and residual momenta contributions as follows

$$\begin{aligned} q_n(x) &= \int \frac{d^4p}{(2\pi)^4} e^{-ip \cdot x} \tilde{q}_n(p) = \sum_{p_\ell \neq 0} \int \frac{d^4p_r}{(2\pi)^4} e^{-ip_\ell \cdot x} e^{-ip_r \cdot x} \tilde{q}_{n,p_\ell}(p_r) \\ &= \left( \sum_{p_\ell \neq 0} e^{-ip_\ell \cdot x} \right) \left( \int \frac{d^4p_r}{(2\pi)^4} e^{-ip_r \cdot x} \right) \tilde{q}_{n,p_\ell}(p_r) \\ &= \sum_{p_\ell \neq 0} e^{-ip_\ell \cdot x} q_{n,p_\ell}(x). \end{aligned} \quad (3.22)$$

---

<sup>2</sup> In calculations of amplitudes, these modes will initially be included for simplicity of integration and later removed using a zero-bin subtraction technique introduced in Ref. [100].

This notation also dictates that derivatives  $\partial^\mu$  extract  $\mathcal{O}(\lambda^2)$  fluctuations such that

$$i\partial_\mu q_{n,p_\ell}(x) \sim \lambda^2 q_{n,p_\ell}(x),$$

since the quark (or gluon) field is only a function of residual momenta. It is then also convenient to define label momentum operators as

$$\mathcal{P}^\mu \equiv \frac{n^\mu}{2} \bar{n} \cdot \mathcal{P} + \mathcal{P}_\perp^\mu, \quad \text{with} \quad (3.23)$$

$$\mathcal{P}^\mu q_{n,p_\ell}(x) \equiv p_\ell^\mu q_{n,p_\ell}(x).$$

By introducing this label operator  $\mathcal{P}^\mu$ , the ordinary derivative  $\partial^\mu$  has effectively been replaced by  $i\partial^\mu q_{n,p_\ell}(x) \rightarrow (\mathcal{P}^\mu + i\partial^\mu)q_{n,p_\ell}(x)$ . The fields we will actually use in SCET will be the collinear limits of QCD fields in the label formalism. We can separate the large and small collinear projections of the quark fields  $q_{n,p_\ell}$  along the light-cone directions using

$$q_{n,p_\ell} = \frac{\not{n}\not{\bar{n}}}{4} q_{n,p_\ell} + \frac{\not{\bar{n}}\not{n}}{4} q_{n,p_\ell} \equiv \xi_{n,p_\ell} + \phi_{n,p_\ell}. \quad (3.24)$$

Using the corresponding equations of motion, the small-component fields  $\phi_{n,p_\ell}$  of this collinear limit can be removed from the theory at the level of the Lagrangian.

### 3.4.5 Leading-Order SCET Lagrangian

At leading order in the power counting parameter  $\lambda$ , the SCET Lagrangian can be written as [91]

$$\mathcal{L}_{\text{SCET}} = \mathcal{L}_{\xi_n} + \mathcal{L}_{A_n} + \mathcal{L}_{us}, \quad (3.25)$$

where the collinear quark Lagrangian piece  $\mathcal{L}_{\xi_n}$  is

$$\mathcal{L}_{\xi_n} = \bar{\xi}_n(x) \left( in \cdot D + i\not{D}_{n\perp} W_n(x) \frac{1}{i\bar{n} \cdot \mathcal{P}} W_n^\dagger(x) i\not{D}_{n\perp} \right) \not{\bar{n}} \xi_n(x). \quad (3.26)$$

In this expression, the covariant derivatives  $D^\mu$  and  $D_n^\mu$  are given by

$$D^\mu = \partial^\mu - igA_n^\mu - igA_{us}^\mu \quad \text{and} \quad iD_n^\mu = \mathcal{P}^\mu + gA_n^\mu, \quad (3.27)$$

and  $W_n$  is a Wilson line that is built from collinear gluon fields

$$W_n(x) = \sum_{\text{perms}} \exp \left[ -g \frac{1}{\bar{n} \cdot \mathcal{P}} \bar{n} \cdot A_n(x) \right]. \quad (3.28)$$

The collinear gluon part of the Lagrangian  $\mathcal{L}_{A_n}$  is given by

$$\begin{aligned} \mathcal{L}_{A_n} = & \frac{1}{2g^2} \text{Tr} \left\{ \left[ i\mathcal{D}^\mu + gA_n^\mu, i\mathcal{D}^\nu + gA_n^\nu \right]^2 + 2 \text{Tr} \left\{ \bar{c}_n \left[ i\mathcal{D}_\mu, [i\mathcal{D}^\mu + gA_n^\mu, c_n] \right] \right\} \right. \\ & \left. + \tau_n \text{Tr} \left\{ \left[ i\mathcal{D}_\mu, A_n^\mu \right] \right\} \right\}. \end{aligned} \quad (3.29)$$

Here,  $\tau_n$  is a gauge fixing parameter for the collinear gluon field  $A_n^\mu$ ,  $c_n$  and  $\bar{c}_n$  are ghost fields in the collinear limit, and the  $\mathcal{D}^\mu$  covariant derivative is defined as

$$i\mathcal{D}^\mu = \mathcal{P}^\mu + in \cdot D \frac{\bar{n}^\mu}{2}. \quad (3.30)$$

The ultra-soft Lagrangian,  $\mathcal{L}_{us}$ , then takes the form of the full QCD Lagrangian for massless ultra-soft quark, gluon, and ghost fields with gauge fixing parameter  $\tau_{us}$ . In this leading order SCET Lagrangian, the only coupling between collinear and ultra-soft modes comes from the covariant derivatives. When discussing factorization of jet cross-sections, we will perform a field redefinition to completely decouple these modes.

The separation of the gauge field  $A^\mu$  into collinear and ultra-soft pieces requires enforcing two separate gauge symmetries. This is the reason for the two gauge fixing parameters  $\tau_n, \tau_{us}$  above. Additionally, there is freedom in how the light-cone basis of  $n, \bar{n}, \dots$  is chosen based on the constraint that  $n^2 = \bar{n}^2 = 0$  and  $n \cdot \bar{n} = 2$ . The freedom to re-define the axes (as well as the fields) is a re-parameterization invariance (RPI) of SCET [101]. These symmetries are discussed briefly in Appendix B.

#### 3.4.6 Factorization in SCET

SCET factorization offers an elegant way to separate perturbatively calculable short-distance physics from non-perturbative long-distance physics. At leading order in the

power counting parameter  $\lambda$ , it also allows for a complete decoupling of collinear and ultra-soft degrees of freedom, providing a framework for organizing the perturbative resummation of large logarithms. As mentioned earlier, one important application of SCET factorization is to calculations of cross-sections in which event-shapes or jet substructure observables are measured.

In this section, we outline how the cross-section for  $e^+e^- \rightarrow \gamma^* \rightarrow q\bar{q}g \rightarrow 3$  jets factorizes when a generic jet substructure observable  $\tau$  is measured. These  $\tau$  can be, for example, the angularity  $\tau_a$  of a jet. Here, we leave  $\tau$  generic in order to emphasize the wide applicability of this factorization theorem. This process will take a cross-section dependent upon logarithms of ratios of several widely separated physical scales and factorize it into functions that are each dependent upon a single physical scale. These logarithms can then be resummed using the corresponding RGEs detailed in Appendix C.

Following the convention of Ref. [1], we can write down the differential cross-section for  $e^+e^- \rightarrow 3$  jets in QCD at center of mass energy  $Q$  as a function of the jet 3-momenta  $\mathbf{p}_{1,2,3}$  and where the generic jet substructure observable  $\tau^{(1)}$  of jet 1 is measured as

$$\begin{aligned} \frac{d\sigma}{d\tau^1 d^3\mathbf{p}_{1,2,3}} &= \frac{1}{2Q^2} \sum_X |\mathcal{M}(e^+e^- \rightarrow \gamma^* \rightarrow q\bar{q}g)|^2 (2\pi)^4 \delta^{(4)}(Q - p_X) \\ &\times \delta_{N(\mathcal{J}(X)),3} \delta(\tau^{(1)} - \tau(\mathcal{J}(X))) \times \prod_{j=1,2,3} \delta^{(3)}(\mathbf{p}_j - \mathbf{p}(J_j(\mathcal{J}(X)))). \end{aligned} \quad (3.31)$$

The partonic matrix element is then given by

$$|\mathcal{M}(e^+e^- \rightarrow \gamma^* \rightarrow q\bar{q}g)|^2 = |\langle X | j^\mu(0) | 0 \rangle L_\mu|^2 \quad \text{with} \quad j^\mu = \sum_f \bar{q}_f \gamma^\mu q_f, \quad (3.32)$$

where the sum is over flavors  $f$ , a sum over colors is implied, and  $L_\mu$  is the leptonic part of the amplitude. In the above expression,  $\mathcal{J}(X)$  is a jet algorithm acting on the final hadronic state  $|X\rangle$ ,  $N(\mathcal{J}(X))$  is the number of jets found by the algorithm,

$\tau(\mathcal{J}(X))$  measures the shape  $\tau$  of a jet, and  $\mathbf{p}(J_j(\mathcal{J}(X)))$  is the momentum of the jet  $J_j$ .

In order to work in the SCET formalism, we must match the QCD current,  $j^\mu(x)$ , onto SCET operators. Three-jet operators in SCET can be built from quark jet and gluon jet fields, which are defined as collinear quarks/gluons multiplied by collinear Wilson lines

$$\chi_n \equiv W_n^\dagger \xi_n \quad \text{and} \quad B_n^\perp \equiv \frac{1}{g} W_n^\dagger (\mathcal{P}^\perp + A_n^\perp) W_n. \quad (3.33)$$

By writing the momentum conserving delta function  $\delta^{(4)}(Q - p_X)$  as an integral, the matching condition can be written as

$$j^\mu(x) = \sum_{n_{1,2,3}} \sum_{p_{1,2,3}} e^{i(p_1 - p_2 + p_3) \cdot x} C_{\alpha\beta\nu}^\mu(n_{1,2,3}; p_{1,2,3}) \bar{\chi}_{n_1, p_1}^\alpha (g B_{n_3, p_3}^{\perp\nu}) \chi_{n_2, p_2}^\beta(x), \quad (3.34)$$

where  $n_i$  are the light-cone directions and  $p_i$  are label momenta along these directions. Sums over the Lorentz index  $\nu$ , Dirac spinor indices  $\alpha, \beta$  as well as implicit color and flavor indices are all implied. In this schematic derivation of factorization, we will suppress these indices going forward for convenience of notation. The matching coefficients  $C(n_{1,2,3}; p_{1,2,3})$  have been calculated for this process in Ref. [102].

The first step in factorizing the cross-section is to decouple the collinear and ultra-soft degrees of freedom in SCET. This can be done by using the Bauer-Pirjol-Stewart (BPS) field re-definitions from Ref. [91]

$$\begin{aligned} \chi_n(x) &= Y_n^\dagger(x) \chi_n^{(0)}(x) \\ \bar{\chi}_n(x) &= \bar{\chi}_n^{(0)} Y_n(x) \\ A_n^\mu(x) &= Y_n(x) A_n^{(0)}(x) Y_n^\dagger(x) \end{aligned} \quad (3.35)$$

where  $Y_n(x)$  is an ultra-soft Wilson line expressed as a path-ordered exponential of the ultra-soft gauge field

$$Y_n(x) = \mathbb{P} \exp \left[ ig \int_0^\infty ds n \cdot A_{us}(x + sn) \right]. \quad (3.36)$$

By putting these re-definitions into SCET Lagrangian, covariant derivatives (which contain the coupling of collinear/ultra-soft modes) are effectively replaced by ordinary derivatives such as  $\bar{\chi}_n(in \cdot D)\chi = \bar{\chi}^{(0)}(in \cdot \partial)\chi^{(0)}$ . In each of these expressions, the (0) notation denotes that the field has been completely decoupled from ultra-soft modes at the level of the Lagrangian. Moving forward, we drop this notation and assume collinear and ultra-soft modes are decoupled.

Having factorized the fields, we next factorize the matrix elements by performing the sum over the final states,  $|X\rangle$ . This must be done carefully, since the measurements of the number, momenta, and shape of the jets all depend on  $X$  through the jet-algorithm  $\mathcal{J}(X)$ . Once this sum is performed, the matrix elements will be expressible as vacuum expectation values. By factorizing the vacuum, the expression can then be re-organized into matrix elements of fields that have the same scaling. Refs. [96, 97, 103, 104] developed a clever formalism for recasting restrictions on the final state such as  $\mathcal{J}(X)$  as operators. This allows measurements of quantities such as  $N(\mathcal{J}(X))$  to become eigenvalues of operators that act on the state  $|X\rangle$ . Ref. [1] used these results to develop similar techniques for jet substructure measurements such as the angularity. The method uses an operator that measures the flow of 4-momentum along a particular direction  $n_i$  and is defined in terms of the energy-momentum tensor  $T_{\mu\nu}$  and thus in terms of fields in QCD/SCET. The restrictions on the final state  $|X\rangle$  can then take the form of operators

$$\begin{aligned}
\text{Number of Jets} &\rightarrow \delta_{N(\hat{\mathcal{J}}),3}, \\
\text{Jet Momenta} &\rightarrow \delta^{(3)}(\mathbf{p}_j - \hat{\mathbf{p}}(J_j(\hat{\mathcal{J}}))), \\
\text{Substructure Measurement} &\rightarrow \delta(\tau^{(1)} - \hat{\tau}^{(1)}). \tag{3.37}
\end{aligned}$$

Since the collinear and ultra-soft modes have been decoupled at the level of the Lagrangian, the energy-momentum tensor can also be split into  $T^{\mu\nu} \rightarrow T_{n_1, n_2, n_3}^{\mu\nu} + T_{us}^{\mu\nu}$ . Ref. [1] showed that, when combined with a few additional constraints, this

allows us to separate the restrictions on the final state  $|X\rangle$  into restrictions on purely collinear states  $|X_n\rangle$  and ultra-soft states,  $|X_{us}\rangle$ . The momenta  $\hat{\mathbf{p}}(\mathcal{J}(X))$  of the jets must receive negligible contributions from ultra-soft particles and thus the jet momenta should be built purely from the label momenta of collinear states  $|X_n\rangle$ . All radiation outside of the jets should then have ultra-soft scaling. This can be enforced using a cutoff  $\Lambda$ , which scales as a residual momentum, on the out-of-jet radiation. Additionally, each of the jets must be well-separated and cannot overlap. This allows one to separate the Kronecker delta  $\delta_{N(\hat{\mathcal{J}}),3}$  into 4 conditions which impose a one-jet restriction in each collinear direction  $n_i$  and a zero-jet restriction on all surrounding ultra-soft momenta. The separation of jets is parameterized by

$$t_{ij} = \frac{\tan(\theta_{ij}/2)}{\tan(R/2)}, \quad (3.38)$$

where  $\theta_{ij}$  is the polar angle between two jets and  $R$  is the jet size parameter. Jets are said to be well-separated if  $t_{ij} \gg 1$ . For a 3 jet final state in the Mercedes-Benz configuration, where  $\theta_{ij} = 2\pi/3$  for  $R = 0.7$  (a common  $R$  at hadron colliders), Ref. [1] showed that  $t_{ij} = 0.04 \ll 1$  and that for any  $\theta_{ij} > 2R$  that  $t_{ij} > 2$ .

With the condition of well-separated jets satisfied and writing the jet momentum measurements in terms of energies and directions, the measurement functions for the momenta and jet-shape can be factorized according to

$$\delta^{(3)}(\mathbf{p}_j - \hat{\mathbf{p}}(J_j(\hat{\mathcal{J}}))) \rightarrow \prod_{j=1,2,3} \delta(E_j - \omega_j/2) \delta^{(2)}(\Omega_j - \mathbf{n}_j), \quad (3.39)$$

$$\delta(\tau^{(1)} - \hat{\tau}^{(1)}) \rightarrow \int d\tau_J d\tau_{us} \delta(\tau^{(1)} - \tau_J - \tau_{us}) \delta(\tau_J - \hat{\tau}^{n_1}) \delta(\tau_{us} - \hat{\tau}^{us}), \quad (3.40)$$

where  $\omega_i \equiv \bar{n}_i \cdot p_i \sim 2E_i$  is a short-hand for the label momenta and  $E_i$  is the energy of the  $i$ th jet. The sum of the  $\omega_i$  over directions is the center-of-mass energy  $Q$ . The total substructure measurement has been factorized into contributions from collinear  $\tau_J = \hat{\tau}^{n_1}$  and ultra-soft  $\tau_{us} = \hat{\tau}^{us}$  particles inside the  $\hat{n}_1$  jet.

The cross-section, which we now write as differential in the substructure variable  $\tau^{(1)}$ , the jet energies  $E_{1,2,3}$ , and the jet directions (solid angles)  $\Omega_{1,2,3}$ , can then be written as

$$\begin{aligned}
\frac{d\sigma}{d\tau^{(1)}dE_{1,2,3}d^2\Omega_{1,2,3}} &= \frac{1}{6Q^2} \sum_{n_{1,2,3}} \sum_{\omega_{1,2,3}} L^2 |C^\mu(n_{1,2,3}; \omega_{1,2,3})|^2 \int d^4x e^{i(Q - \sum_{j=1,2,3} \omega_j n_j/2) \cdot x} \\
&\int d\tau_J d\tau_{us} \delta(\tau^{(1)} - \tau_J - \tau_{us}) \times \prod_{j=1,2,3} \delta(E_j - \omega_j/2) \delta^{(2)}(\Omega_j - \mathbf{n}_j) \\
&\times \langle 0 | \chi_{n_1, \omega_1}(x) \delta_{N(\hat{\mathcal{J}}), 1} \delta(\tau_J - \hat{\tau}^{n_1}) \bar{\chi}_{n_1, \omega_1}(0) | 0 \rangle \\
&\times \langle 0 | \bar{\chi}_{n_2, -\omega_2}(x) \delta_{N(\hat{\mathcal{J}}), 1} \chi_{n_2, -\omega_2}(0) | 0 \rangle \\
&\times \langle 0 | (gB_{n_3, \omega_3}^\perp)(x) \delta_{N(\hat{\mathcal{J}}), 1} (gB_{n_3, \omega_3}^\perp)(0) | 0 \rangle \\
&\times \langle 0 | \bar{Y}_{n_2}^\dagger Y_{n_3}^\dagger T^A \bar{Y}_{n_3}^\dagger Y_{n_1}^\dagger(x) \delta_{N(\hat{\mathcal{J}}), 0} \delta(\tau_{us} - \hat{\tau}^{us}) Y_{n_1} \bar{Y}_{n_3} T^B Y_{n_3} \bar{Y}_{n_2}(0) | 0 \rangle, \tag{3.41}
\end{aligned}$$

where again the explicit Lorentz, Dirac spinor, and color indices have been suppressed for notational convenience.

While Eq. (3.41) is, notationally, quite involved, its interpretation is simple. The key feature of this expression is that all of the fields, operators, and states have been completely factorized. Each matrix element is a product of only  $n_i$ -collinear or only ultra-soft fields with measurements of the substructure being applied only to ultra-soft and  $n_1$ -collinear parts of the expression. The matrix elements can be used to define functions that individually govern physics in the hard,  $n_i$ -collinear, or ultra-soft regimes. These functions will be a quark jet function  $J_{n_1, \omega_1}(\tau_J, n_1 \cdot k_1)$ , anti-quark jet function  $J_{n_2, \omega_2}(n_2 \cdot k_2)$ , a gluon jet function  $J_{n_3, \omega_3}(n_3 \cdot k_3)$ , and an ultra-soft function  $S(\tau_{us}, r)$ , where  $k_i$  are residual momenta. As shown in Ref. [1] (see also Ref. [96]) the  $n_1$ -collinear quark jet function is defined as

$$\int \frac{d^4k_1}{(2\pi)^4} e^{-ik_1 \cdot x} J_{n_1, \omega_1}(\tau_J, n_1 \cdot k_1) \left( \frac{\not{x}}{2} \right) = \langle 0 | \chi_{n_1, \omega_1}(x) \delta_{N(\hat{\mathcal{J}}), 1} \delta(\tau_J - \hat{\tau}^{n_1}) \bar{\chi}_{n_1, \omega_1}(0) | 0 \rangle, \tag{3.42}$$

where similar functions can be defined for the  $n_2$ -collinear antiquark jet and  $n_3$ -collinear gluon jet. The ultra-soft function can be defined as

$$\int \frac{d^4 r}{(2\pi)^4} e^{-ir \cdot x} S(\tau_{us}, r) = \frac{1}{N_C C_F} \text{Tr} \langle 0 | \bar{Y}_{n_2}^\dagger Y_{n_3}^\dagger T^A \bar{Y}_{n_3}^\dagger Y_{n_1}^\dagger(x) \delta_{N(\hat{J}),0} \delta(\tau_{us} - \hat{\tau}^{us}) \\ \times Y_{n_1} \bar{Y}_{n_3} T^B Y_{n_3} \bar{Y}_{n_2}(0) | 0 \rangle,$$

where  $r$  is a residual momenta. These momenta can ultimately be absorbed into their respective label momenta using RPI in SCET. Additionally, hard-scale physics is completely encapsulated by the matching coefficients  $C(n_{1,2,3}, \omega_{1,2,3})$ . Inserting these definitions into Eq. (3.41), the cross-section can be written as

$$\frac{1}{\sigma_0} \frac{d\sigma}{d\tau^{(1)} dE_{1,2,3}} = H(Q, \mu_H) \times J_{n_1}(\tau_J, \mu_{J_1}) \otimes J_{n_2}(\mu_{J_2}) \otimes J_{n_3}(\mu_{J_3}) \otimes S(\tau_{us}, \mu_{us}), \quad (3.43)$$

where  $\sigma_0$  is the Born cross-section,  $H = 1 + \mathcal{O}(\alpha_s)$  is a hard function calculated using the matching coefficients  $C(n_i, p_i)$ ,  $\otimes$  represents convolutions in  $\tau_J$  and  $\tau_{us}$ , and the directions  $\Omega_i$  have been integrated over. Each piece of this factorization theorem is a function of logarithms of a different physical scale that are minimized by the choice of renormalization scale  $\mu = \mu_H, \mu_{J_1}, \mu_{J_2}, \mu_{J_3}, \mu_{us}$ , respectively. Dependencies on other quantities such as momenta have been suppressed.

In order to calculate a cross-section for a particular jet substructure observable, we calculate the hard, jet, and ultra-soft functions individually in perturbation theory. The true power of the factorization then lies in the application of RG techniques. Each function runs with the scale  $\mu$  and has a corresponding RGE (i.e. RGEs for hard, jet, and soft functions). By evaluating each function at its characteristic scale and then evolving using the RGEs to a common scale  $\mu$ , the logarithms of these scales are resummed to all orders in  $\alpha_s$ .

Ref. [1] used this factorization theorem to resum logarithms of the scales that are functions of the angularity  $\tau_a$ . It can, however, be applied to any jet substructure

observable  $\tau$  that can be recast as an operator on  $|X\rangle$  using the momentum flow operator concept discussed above.<sup>3</sup> In a fixed order QCD calculation of this process, the logarithms of the angularity would not be so cleanly organized and any one choice of  $\mu$  would not minimize all of the logarithms.

---

<sup>3</sup> The characteristic scale of, for example, the jet where the angularity was measured was  $\mu_J^{\text{meas}} = \omega\tau_a^{1/(2-a)}$ .

## Fragmenting Jet Functions: Introduction & Developments

### 4.1 Introduction

In Chapter 2, we introduced how quarkonia such as the  $J/\psi$  are studied using NRQCD. While NRQCD has been used to accurately calculate the  $p_T$  dependence of quarkonium production cross-sections, the theory has repeatedly failed to predict their polarization. In Chapter 3, we outlined how SCET can be used to make high-precision calculations of jet processes. This chapter builds a connection between Chapters 2 and 3 in order to study quarkonia that are produced within jets. This connection will be provided by Fragmenting Jet Functions (FJF). Originally defined in Ref. [105], FJFs offer a way to study the formation of hadrons within jets where the substructure of the jets is measured. In 2014, Ref. [12] calculated the FJFs for the leading-power NRQCD production mechanisms for  $J/\psi$  described in Chapter 2. They found that FJFs could discriminate between the different  $J/\psi$  production mechanisms, opening the door for a new class of observables with which to study quarkonium production.

In this chapter, we will examine the FJF formalism, beginning with a brief review of fragmentation as described by FFs in QCD. We will explain the operator definitions of the FJF in terms of FFs and jet functions in the language of SCET. The rest of the chapter will then be dedicated to developing the FJF formalism for the purposes of studying quarkonia within jets beyond what was done in Ref. [12]. We will extend FJFs to several different jet substructure observables which will, in Chapter 5, be applied to  $J/\psi$  production. This chapter presents a number of results previously published by the author and collaborators in [36–38].

#### 4.1.1 Fragmentation Functions

FFs can be broadly defined as dimensionless functions that describe the distribution of a certain type of particle in the final state. In perturbative calculations, we focus on partonic FFs,  $D_i^h(z, \mu)$ , which give the number density of the hadron  $h$  that have a fraction  $z$  of the energy of the fragmenting parton  $i$ . Although the FF describes non-perturbative physics, at high COM energies, Ref. [35] proved that to all orders in  $\alpha_s$ , we can factorize the cross-section of  $e^+e^- \rightarrow h + X$  into pieces that describe contributions from individual partons

$$\frac{1}{\sigma_0} \frac{d\sigma(e^+e^- \rightarrow h + X)}{dz} = \sum_{i=g,u,\bar{u},d,\dots} \int_z^1 \frac{dx}{x} \frac{d\hat{\sigma}_i(e^+e^- \rightarrow i + X)}{dx} D_i^h(z/x, \mu), \quad (4.1)$$

which holds at leading power in  $\Lambda_{\text{QCD}}/Q$  where  $Q$  the center of mass energy. FFs are the final state cousins of the more familiar PDFs,  $f_{i/h}(z, \mu)$ . Where, for PDFs,  $z$  represented the fraction of a hadron’s momentum carried by a particular parton, for FFs, it represents the fraction of a parton’s energy carried by the final state hadron. Like PDFs, FFs exhibit scaling violation and are thus written as functions of  $\mu$ , the renormalization scale, which we define in the  $\overline{MS}$  subtraction scheme throughout this work. In Eq. 4.1,  $x$  is the energy fraction carried by the

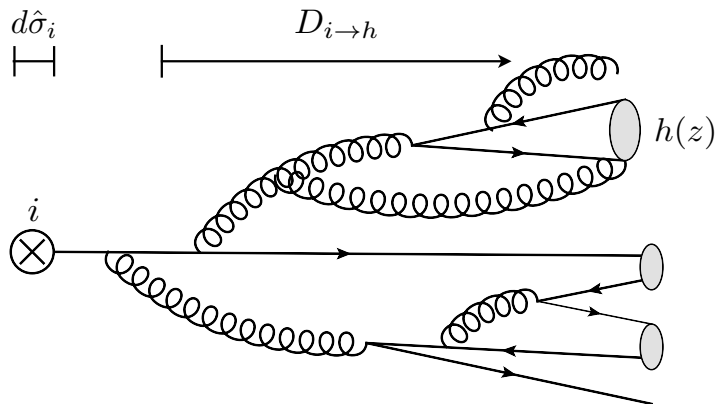


FIGURE 4.1: The information encoded in the fragmentation function as defined in Eq. (4.1) where the  $d\hat{\sigma}_i$  describes the short-distance partonic process and the right hand side of the diagram, encoded by the  $D_{i\rightarrow h}$ , describes the non-perturbative hadronization of the parton.

hadron  $h$  of the parent parton and  $z = 2E_h/Q$  represents the energy fraction carried by the hadron in the COM frame. Note that at LO, where this process is essentially  $e^+e^- \rightarrow q\bar{q}$ ,  $z = x$ . At higher orders in  $\alpha_s$ , we will have generally that  $x \geq z$  since some of the initiating parton's energy will be carried off by additional emitted radiation. In Eq. 4.1 the coefficients  $d\hat{\sigma}_i$  are perturbatively calculable and describe the short-distance (high-energy) partonic process. The FFs then describe the long-distance (low-energy) non-perturbative hadronization of partons  $i = g, u, \dots$  into a specific hadron  $h$  as illustrated in Fig. 4.1.

#### 4.1.2 Fragmentation with a Cut on Thrust

Experimentalists studying fragmentation often make additional measurements/cuts on the final state hadrons in an event. One such example is described in Ref. [31], where experimentalists working on the Belle collaboration studied light-quark fragmentation. In order to eliminate events from their data where hadrons were produced from the decays of  $B$ -mesons, they focused their studies on dijet final-state configurations. One way of requiring that the final state particles in accepted events be in

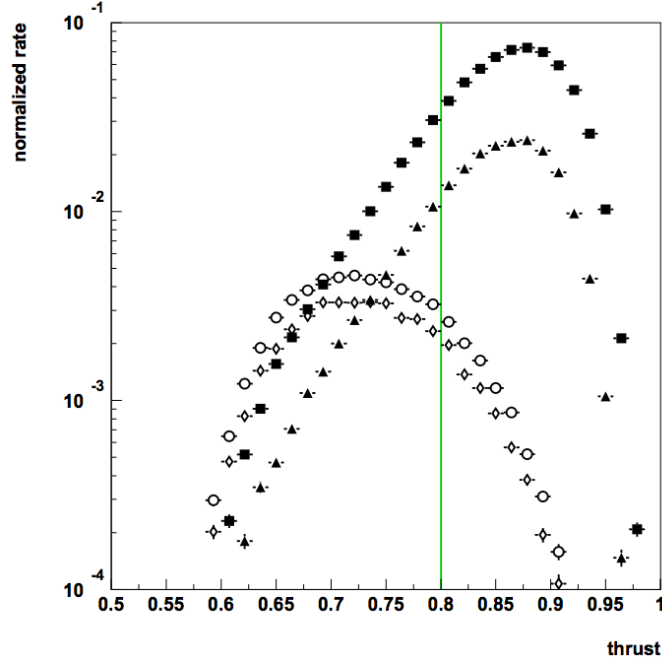


FIGURE 4.2: This plot [31] shows simulated results from Pythia for thrust distributions for selected 2-pion pairs at the  $\Upsilon(4S)$  resonance of  $\sqrt{s} = 10.58$  GeV. Shown are  $e^+e^- \rightarrow B^+B^-$  (open diamonds),  $e^+e^- \rightarrow B^0\bar{B}^0$  (open circles),  $e^+e^- \rightarrow c\bar{c}$  events (full triangles), and  $e^+e^- \rightarrow q\bar{q}$  for light-quarks  $q \in u, d, s$  (full squares). The plot is normalized to the total number of events in all channels and the vertical green line shows the thrust cut  $T > 0.8$ .

a dijet configuration is by making a cut on thrust  $\tau$  (see discussion in Chapter 3). The KEKB accelerator, an asymmetric  $e^+e^-$  collider at Belle, has a center-of-mass energy of 10.58 GeV, corresponding to the  $\Upsilon(4S)$  resonance. At this energy, the collider often produces  $B$  mesons nearly at rest in the CM frame, meaning that events containing  $B$ 's will generally not have a dijet-like configuration where  $\tau \sim 0$ . As shown in Fig. 4.2, a simple cut on the thrust of  $\tau < 0.2$  ( $T > 0.8$ ) for pion pairs removed 98% of the  $B$  data. The measurement of thrust and many other event and jet shape observables can be incredibly effective at reducing backgrounds and probing the mechanism of fragmentation. Fragmentation with a cut on thrust has been studied in this context using SCET in, for example, Ref. [106].

FFs are insufficient for studying the formation of hadrons where event shapes or

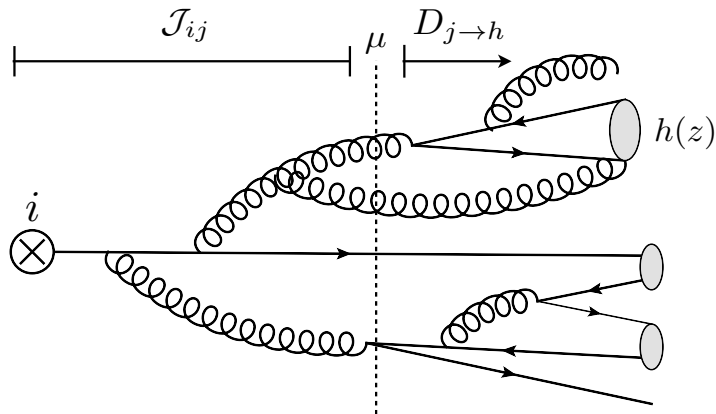


FIGURE 4.3: The information encoded in the fragmenting jet function as originally defined for measured jet invariant mass  $\mathcal{G}(s, z, \mu)$ . A parton  $i$  perturbatively splits off quarks/gluons and becomes a jet of invariant mass  $s$ . The initial splittings are large angle/high virtuality and are described perturbatively by the  $\mathcal{J}_{ij}(s, z, \mu)$ . At lower parton virtualities, the non-perturbative effects become important, at which point the emissions are described by the FFs,  $D_{i \rightarrow h}(z/x, \mu)$ .

jet substructure observables have been measured. This motivated the development of FJFs, which were originally defined in Ref. [105] to describe hadrons in jets where the invariant mass  $s$  of the jet is measured. Using basic kinematics, cuts on thrust can be shown to restrict the invariant masses of jets. In Chapter 5 we will study how FJFs allow us to place restrictions on the substructure of a jet that contains a  $J/\psi$  in order to probe the underlying mechanism of its production.

## 4.2 Basic Properties of the FJF

### 4.2.1 Origin of the FJF

FJFs, denoted by  $\mathcal{G}_i^h(s, z, \mu)$ , possess features of both FFs and jet functions  $J_i(s, \mu)$ . They describe the probability that a parton  $i$  fragments into a jet with invariant mass  $s$  that contains a hadron  $h$  carrying a fraction  $z$  of the jet's momentum. Fig. 4.3 gives a diagrammatic representation of the information encoded by the FJF. As discussed in Chapter 3, for processes containing a well-separated hierarchy of energy scales,

SCET provides factorization theorems of cross-sections and decay rates into hard, collinear, and soft modes. These cross-sections have the following schematic form

$$d\sigma = H \times S \otimes J(\otimes J) \otimes \dots, \quad (4.2)$$

where  $H$  is a hard function,  $\otimes$  represents convolution,  $S$  a soft-function describing inter-jet soft-scale radiation, and  $J$  are jet functions describing radiation collinear to different jet directions. It was shown in Ref. [105] that a factorization theorem for a jet production cross-section can be made into a factorization theorem for a jet with an identified hadron,  $h$ , using the following replacement rule

$$J_i(s, \mu) \rightarrow \frac{1}{2(2\pi)^3} \mathcal{G}_i^h(s, z, \mu) dz, \quad (4.3)$$

where  $J_i(s, \mu)$  is the jet function for a jet with a measured invariant mass  $s$  that is initiated by a parton  $i$  at the renormalization scale  $\mu$ . The FJF introduces an additional dependence on the fraction  $z$  of the jet energy carried by the hadron. We note that the FJFs (like jet functions) also carry an implicit dependence on the underlying choice of a jet algorithm and thus the cone size parameter  $R$ . When constraining the jet invariant mass it was shown in Ref. [105] that at leading power in  $\Lambda_{QCD}^2/s \ll 1$ , the FJF can be matched onto standard FFs,  $D_i^h$ , as follows

$$\mathcal{G}_i^h(s, z, \mu) = \sum_j \int_z^1 \frac{dx}{x} \mathcal{J}_{ij}(s, x, \mu) D_j^h(z/x, \mu) + \mathcal{O}(\Lambda_{QCD}^2/s). \quad (4.4)$$

Here, the coefficients  $\mathcal{J}_{ij}(s, z, \mu)$  are perturbatively calculable matching coefficients that describe the short-distance production of collinear radiation that ultimately forms a jet of invariant mass  $s$ . The  $D_j^h(z, \mu)$  then describe the non-perturbative (long-distance) hadronization of the parton  $j = g, u, \bar{u}, d, \dots$  into the hadron  $h$ .

### 4.2.2 Sum Rules

The relationship between FFs, FJFs, and jet functions naturally provides a non-trivial cross-check of calculations of the FJFs. Basic rules of probability dictate that

$$1 = \sum_h \int_0^1 dz z D_i^h(z). \quad (4.5)$$

From this and combinatorial arguments needed when summing over all possible hadrons  $h$ , Ref. [105] derived a sum rule for the  $\mathcal{J}_{ij}$  coefficients

$$J_i(s, \mu) = \frac{1}{2(2\pi)^3} \sum_j \int_0^1 dz z \mathcal{J}_{ij}(s, z, \mu), \quad (4.6)$$

such that the sum reproduces the jet function  $J_i(s, \mu)$ .

### 4.2.3 FJFs in the Literature

FJFs also give us an alternative method of measuring FFs, which are usually extracted from inclusive hadron production cross-sections in  $e^+e^- \rightarrow h + X$ . Most importantly, FJFs provide a new way of extracting gluon FFs [107, 108], which are not well-constrained by  $e^+e^-$ . These FFs will be of particular interest to us when applying the FJF formalism to quarkonium production.

The matching coefficients  $\mathcal{J}_{ij}(s, z, \mu)$  were calculated at one-loop order in Ref. [2] where they were used in the calculation of a cross-section resummed to next-to-next-to-leading-logarithmic (NNLL) accuracy for  $e^+e^- \rightarrow \pi^+ X$  at the  $\Upsilon(4S)$  resonance. FJFs can be defined for a number of other scenarios. FJFs that depend on the total energy of a jet were defined and calculated in Ref. [109] and a joint resummation of logarithms of the jet-cone size  $R$  and so-called *threshold logarithms* of  $1 - z$  was introduced. FJFs for heavy quark fragmentation were developed in Ref. [110]. More recently, so-called semi-inclusive FJFs were developed in Ref. [111]. FFs in the

context of jet production have been studied extensively using other similar methods such as jet fragmentation functions (JFF) in Ref. [108] and fragmentation functions to a jet (FFJ) in Ref. [112].

### 4.3 Operator Definitions of FJFs

The operator definition of FJFs can be derived from the QCD definition of a FF. As discussed in Ref. [2] the bare (un-renormalized) quark FF can be expressed in QCD as

$$D_q^{h,\text{bare}}(z) = \frac{1}{z} \int d^2 p_h^\perp \int \frac{dy^+ d^2 y_\perp}{2(2\pi)^3} e^{ik^- y^+ / 2} \sum_X \frac{1}{2N_c} \times \text{Tr} \left[ \frac{\bar{n}}{2} \langle 0 | \psi(y^+, 0, y_\perp) | Xh \rangle \langle Xh | \bar{\psi}(0) | 0 \rangle \right]. \quad (4.7)$$

Here, the initial quark with momentum  $k^\mu$  fragments into a hadron  $h$  with momentum  $p_h^\mu$ . We work in a frame where  $\vec{k}_\perp = 0$ ,  $p_h^- = zk^-$ , and the component  $p_h^+ = (p_{h\perp}^2 + m_h^2)/p_h^-$ . In this equation,  $\psi(\bar{\psi})$  represent quark (anti-quark) field operators, the factor  $1/(2N_c)$  for  $N_c = 3$  colors provides an average over the spin and color of the parton  $k$ . The state  $|Xh\rangle$  describes a hadron  $h$  and any other particles  $X$ . Taking the collinear limit and writing the expression in terms of fields in SCET we can write the un-renormalized FF as [105]

$$D_q^{h,\text{bare}}(x) = \frac{1}{z} \int d^2 p_h^\perp \sum_X \frac{1}{2N_c} \times \text{Tr} \left[ \frac{\bar{n}}{2} \delta(p_{Xh,r}^-) \delta^{(2)}(p_{Xh,r}^\perp) \langle 0 | [\delta_{\omega,\mathcal{P}} \delta_{0,\mathcal{P}_\perp} \chi_n(0)] | Xh \rangle \langle Xh | \bar{\chi}_n(0) | 0 \rangle \right], \quad (4.8)$$

where  $p_{Xh}^\mu = p_X^\mu + p_h^\mu$  and the quark fields have been replaced by gauge invariant  $n$ -collinear quark-jet fields  $\chi_n$  (see Eq. (3.33)). The FF in SCET notation is closely

related to the operator definition of FJF. The quark FJF as given in Ref. [105] as

$$\begin{aligned} \mathcal{G}_q^h(s, z) &= \int d^4 y e^{-ik^+ y^- / 2} \int dp_h^+ \sum_X \frac{1}{4N_c} \\ &\times \text{Tr} \left[ \frac{\bar{n}}{2} \langle 0 | [\delta_{\omega, \mathcal{P}} \delta_{0, \mathcal{P}_\perp} \chi_n(y)] | Xh \rangle \langle Xh | \bar{\chi}_n(0) | 0 \rangle \right], \end{aligned} \quad (4.9)$$

where the argument of  $\chi_n(y)$  is associated with residual momenta. By carrying out integrals over  $\bar{y}^\perp$  and  $y^+$ , we can write the FJF in a form comparable with the FF in Eq. (4.7)

$$\begin{aligned} \mathcal{G}_q^h(s, z) &= \frac{2(2\pi)^3}{\omega z} \int \frac{dy^-}{4\pi} e^{-iy^-(k^+ - p_{Xh}^+)/2} \int d^2 p_h^\perp \sum_X \frac{1}{2N_c} \\ &\times \text{Tr} \left[ \frac{\bar{n}}{2} \delta(p_{Xh, r}^-) \delta^{(2)}(p_{Xh, r}^\perp) \langle 0 | [\delta_{\omega, \mathcal{P}} \delta_{0, \mathcal{P}_\perp} \chi_n(0)] | Xh \rangle \langle Xh | \bar{\chi}_n(0) | 0 \rangle \right], \end{aligned} \quad (4.10)$$

where  $\omega \equiv k^-$ . This form allows us to see that the integral over  $y^-$  represents the measurement or restriction of the jet's invariant mass  $s$  via the delta function

$$\delta(\omega(k^+ - p_{Xh}^+)), \quad (4.11)$$

where

$$s = \left( \sum_i p_i^\mu \right)^2 = (k^\mu)^2 = k^+ k^- - \mathbf{k}_\perp^2 = \omega k^+. \quad (4.12)$$

At leading order, one can (cf. Eqs. (2.15, 2.23)) of Ref. [2]) show that the bare FFs can be reduced to

$$\begin{aligned} D_q^{q(0)}(z) &= D_g^g(z) = \delta(1 - z) \\ D_q^{g(0)}(z) &= D_g^q(z) = 0, \end{aligned} \quad (4.13)$$

where (0) will be used to denote the leading order piece and (1) the next-to-leading order contribution. The corresponding bare FJFs then can be written as

$$\begin{aligned} \mathcal{G}_q^{q(0)}(s, z) &= \mathcal{G}_g^{g(0)}(s, z) = 2(2\pi)^3 \delta(s) \delta(1 - z) \\ \mathcal{G}_q^{g(0)}(z) &= \mathcal{G}_g^{q(0)}(z) = 0. \end{aligned} \quad (4.14)$$

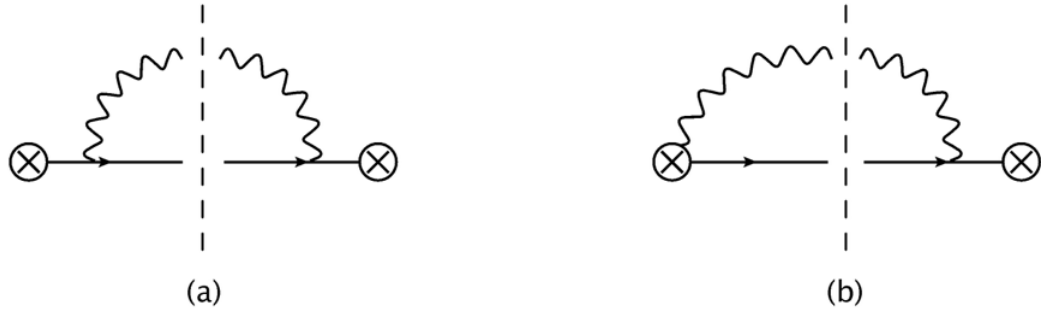


FIGURE 4.4: Feynman diagrams that give non-scaleless contributions to the quark FJF at NLO in  $\alpha_s$ . Diagram (b) also has a mirror image that is not explicitly shown.

To calculate the matching coefficients (and ultimately the FJFs) at NLO requires the evaluation of the diagrams shown in Figs. 4.4 and 4.5. The matching coeffi-

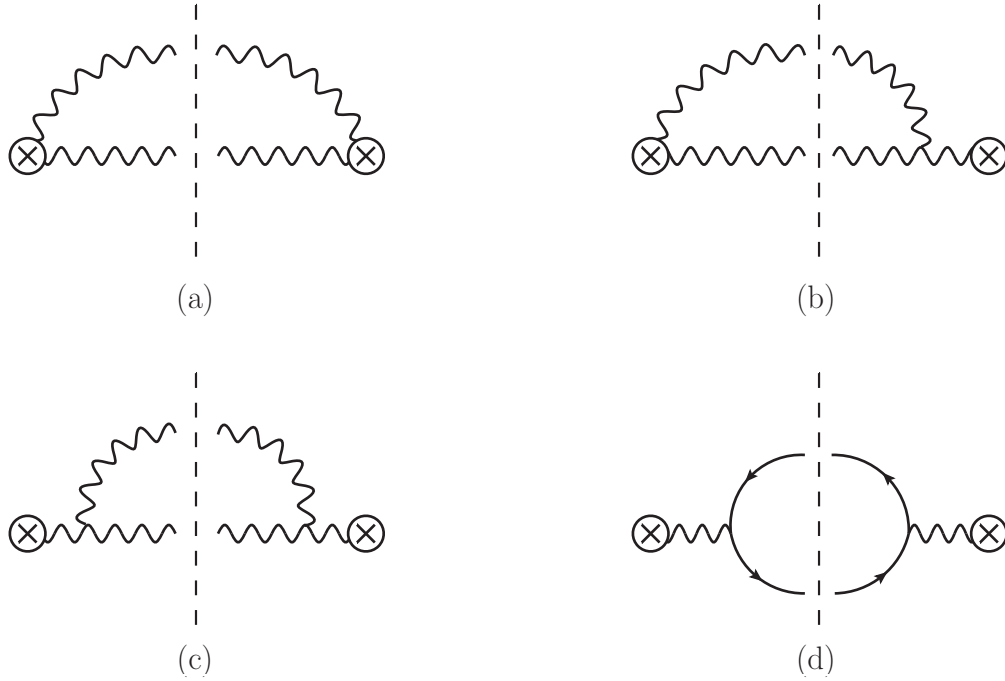


FIGURE 4.5: Non-scaleless diagrams that contribute to the gluon FJF at NLO. Again, diagram (b) has a mirror image that is not explicitly drawn above.

icients  $\mathcal{J}_{ij}(s, z, \mu)$  and the corresponding FJFs are calculated at NLO for measured jet invariant mass in Ref. [2]. We will calculate these  $\mathcal{J}_{ij}$  coefficients at NLO as functions of several other jet-substructure observables, including the angularity  $\tau_a$  in

Section 4.4 and the transverse momentum of a hadron relative to the jet-direction in Section 4.5.

#### 4.3.1 Calculating Renormalized FFs & FJFs at One-loop.

At one-loop order, the expressions for  $D_i^h(z, \mu)$  and  $\mathcal{G}_i^h(s, z, \mu)$  contain divergences and must be renormalized. According to Ref. [35], the FFs are renormalized via

$$D_i^{h,\text{bare}}(z) = \sum_j \int_z^1 \frac{dx}{x} Z_{ij}^D(z/x, \mu) D_j^h(x, \mu), \quad (4.15)$$

where  $\mu$  is, again, the renormalization scale and the sum over  $j$  runs over partons. The renormalization group equations for these FFs are the DGLAP equations where

$$\frac{d}{d \log(\mu)} D_i^h(z, \mu) = \sum_j \int_z^1 \frac{dx}{x} \gamma_{ij}^D(z/x, \mu) D_j^h(x, \mu) \quad (4.16)$$

where the anomalous dimension is calculated using

$$\gamma_{ij}^D(z, \mu) = - \int_z^1 \frac{dx}{x} (Z^D)^{-1}_{ik}(z/x, \mu) \frac{d}{d \log(\mu)} Z_{kj}^D(x, \mu). \quad (4.17)$$

These anomalous dimensions will, ultimately, be calculated in terms of the QCD splitting functions  $P_{ij}(z)$ . How we renormalize the FJFs will depend on whether or not the FJF is a function of the substructure of the jet. The RGEs for **measured**, (where the substructure of the jet is probed) and **unmeasured** (where only the radius  $R$  and energy  $E$  of the jet is known) functions are both described in detail in Appendix C. Working at  $\mathcal{O}(\alpha_s)$ , the renormalization procedure for FJFs yields that the perturbative matching will essentially reduce to (for the case where the invariant mass is probed<sup>1</sup>)

$$\underline{\mathcal{G}_i^{j(1)}(s, z, \mu) = 2(2\pi)^3 \delta(s) D_i^{j(1)}(z, \mu) + \mathcal{J}_{ij}^{(1)}(s, z, \mu)}. \quad (4.18)$$

<sup>1</sup> Note that this procedure will hold regardless of the measurement or lack of measurement. One simply has to replace  $s$  with, as we will show  $\tau_a, \mathbf{p}_\perp, E_{jet}$ , etc.

### 4.3.2 Anomalous Dimensions of the FJF

At this point, we make note of an interesting fact about the nature of the anomalous dimensions of FJFs. Consider the factorization theorem of a jet cross-section where the replacement rule in Eq. (4.3) has been used to study jets with an identified hadron

$$d\sigma = H \otimes S \otimes J_1 \otimes J_2 \quad \rightarrow \quad d\sigma = H \otimes S \otimes J_1 \otimes \mathcal{G}_2. \quad (4.19)$$

In order for our observable to make sense, the anomalous dimensions of each piece of the factorization theorem must have the following consistency relation

$$\gamma_H + \gamma_S + \gamma_{J_1} + \gamma_{J_2} = 0 \quad \rightarrow \quad \gamma_H + \gamma_S + \gamma_{J_1} + \gamma_{\mathcal{G}_2} = 0. \quad (4.20)$$

This implies that

$$\implies \gamma_{J_2} = \gamma_{\mathcal{G}_2} = -(\gamma_H + \gamma_S + \gamma_{J_1}), \quad (4.21)$$

which provides us with a powerful statement: FJFs evolve in  $\mu$  exactly as ordinary jet functions. This will ultimately provide yet another non-trivial check on whether our FJFs are consistent with jet functions calculated in the literature.

## 4.4 Angularity Dependent FJFs

### 4.4.1 Angularity in Light-Cone Coordinates

The most natural generalization of the FJFs for measured jet invariant mass  $s$  is to FJFs where the angularity  $\tau_a$  is measured. Recall from our discussion in Chapter 3 that angularities are a well-developed jet-substructure observable first introduced in Ref. [85] and studied within the context of SCET factorization in Ref. [1]. In light-cone coordinates, angularities can be calculated using

$$\tau_a = \frac{1}{\omega} \sum_i (p_i^+)^{1-a/2} (p_i^-)^{a/2}, \quad (4.22)$$

where the sum runs over all of the particles  $i$  in a given jet and  $\omega = \sum_i p_i^-$  represents the large light-like momentum of that jet. Angularities are a generalization of the jet invariant mass squared. We can see this by setting  $a = 0$  and using that  $k^+ = s/\omega$

$$\tau_0 = \frac{\sum_i p_i^+}{\sum_i p_i^-} = \frac{k^+}{\omega} = \frac{s}{\omega^2}. \quad (4.23)$$

In this section we will first extend the calculation of Ref. [2] to FJFs where the angularity of the jet is probed. We will adopt terminology consistent with Ref. [1] and refer to functions that depend on  $\tau_a$  as measured functions and functions that do not depend on  $\tau_a$  as unmeasured. Since this is a one-loop perturbative calculation, we will consider final states with at most 2 particles. This means we will be calculating  $1 \rightarrow 2$  splittings of partons  $j = g, q, \bar{q}$  into other partons (c.f. Fig. 4.6).

After defining the angularity dependent FJF,  $\mathcal{G}(\tau_a, z, \mu)$ , we will calculate the matching coefficients,  $\mathcal{J}_{ij}(\tau_a, z, \mu)$ , and perform a cross-check of the results by verifying that the sum rule in Eq. (4.6) still holds when generalizing  $s \rightarrow \tau_a$ . These matching coefficients can then be convolved with FFs from the literature in order to calculate the angularity FJF. In Chapter 5, we will study the  $z$  and  $\tau_a$  dependence of a cross-section for jets that contain a  $B$  meson or  $J/\psi$  in  $e^+e^-$  annihilation using our calculations of the  $\mathcal{G}(\tau_a, z, \mu)$ , a phenomenological  $B$ -meson FF, and the leading-power NRQCD FFs.

#### 4.4.2 Defining the Angularity FJF

In Ref. [2], it was shown that the measurement in the definition of the FJF restricts the invariant mass squared of the jet via the following delta function

$$\delta(\omega(k^+ - l^+ - p^+)) = \delta(s - \omega(l^+ + p^+)), \quad (4.24)$$

where again,  $k^\mu$  is the initial parton's momentum and  $l^\mu$  and  $p^\mu$  represent the momenta of the partons carrying large lightcone components  $l^- = (1 - z)k^-$  and

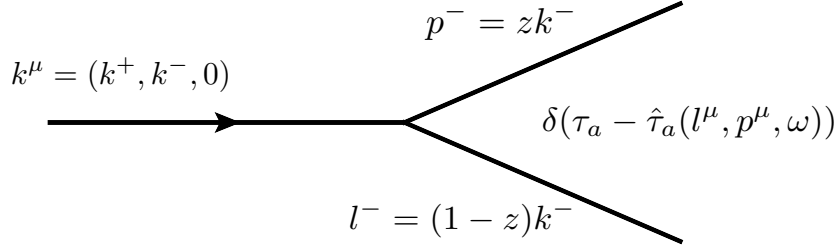


FIGURE 4.6: We consider  $1 \rightarrow 2$  splittings at NLO with the momenta shown. A delta function then provides the measurement of the invariant mass, angularity, etc.

$p^- = zk^-$  of the parent's momentum, respectively. We can generalize this measurement function from  $s \rightarrow \tau_a$  and write down the operator definition of the FJF where the angularity of the measured jet is restricted

$$\mathcal{G}_i^h(\tau_a, z, \mu) = \int \frac{dk^+ dp_h^+}{2\pi} \int d^4y e^{-ik^+y^-/2} \sum_X \frac{1}{4N_C} \times \text{Tr} \left[ \frac{\not{y}}{2} \langle 0 | \chi_{n,\omega}(y) \delta(\tau_a - \hat{\tau}_a) | Xh \rangle \langle Xh | \bar{\chi}_{n,\omega}(0) | 0 \rangle \right]$$

where at this order  $\mathcal{O}(\alpha_s)$  the measurement operator  $\hat{\tau}_a$  is expressed as

$$\delta(\tau_a - ((l^+)^{1-a/2} (l^-)^{a/2} - (p^+)^{1-a/2} (p^-)^{a/2}) / \omega). \quad (4.25)$$

To calculate  $\mathcal{G}_i^h(\tau_a, z, \mu)$  to  $\mathcal{O}(\alpha_s)$  we evaluate the diagrams shown in Figs. 4.4 and 4.5 for the quark and gluon contributions respectively. We note that it can be shown in pure dimensional regularization that at one-loop the FF can be expressed as

$$D_i^j(z) = \delta_{ij} \delta(1-z) + T_{ij} \frac{\alpha_s}{2\pi} P_{ij}(z) \left( \frac{1}{\epsilon_{UV}} - \frac{1}{\epsilon_{IR}} \right), \quad (4.26)$$

where  $T_{ij}$  is a matrix of  $SU(3)$  color factors with  $T_{qq} = C_F$ ,  $T_{gg} = C_A$ ,  $T_{qg} = C_F$ ,  $T_{gq} = T_R$  and  $P_{ij}(z)$  are QCD splitting functions defined in Eq. (2.7). For these

functions, we adopt the following convention

$$\begin{aligned}
\bar{P}_{qq}(z) &= P_{qq}(z) - \bar{\gamma}_q \delta(1-z) = \frac{1+x^2}{(1-x)_+}, \\
\bar{P}_{gq}(z) &= P_{gq}(z) = \frac{1+(1-z)^2}{z}, \\
\bar{P}_{qg}(z) &= P_{qg}(z) = z^2 + (1-z)^2, \\
\bar{P}_{gg}(z) &= P_{gg}(z) - \bar{\gamma}_g \delta(1-z) = \frac{2(1-x+x^2)^2}{x(1-x)_+},
\end{aligned} \tag{4.27}$$

where  $\bar{\gamma}_q = 3/2$  and  $\bar{\gamma}_g = \beta_0/(2C_A)$ . It can easily be verified that the  $1/\epsilon_{IR}$  poles in the calculation of the FJF cancel (as they must) with those in the calculation of the FFs for values of the angularity parameter  $a < 1$ . This justifies

$$\mathcal{G}_i^h(\tau_a, z, \mu) = \sum_j \int_z^1 \frac{dx}{x} \mathcal{J}_{ij}(\tau_a, x, \mu) D_{j \rightarrow h}\left(\frac{z}{x}, \mu\right), \tag{4.28}$$

up to power corrections that are functions of the angularity. This is, of course, the analog of Eq. (4.3) for FJFs that depend on the angularities. The cancellation of IR divergences in the matching also allows us to perform the perturbative calculations of the  $\mathcal{J}_{ij}(\tau_a, z, \mu)$  in pure dimensional regularization while setting all scaleless integrals to zero and interpreting  $1/\epsilon$  poles as ultraviolet divergences.

#### 4.4.3 One-Loop Calculation of Matching Coefficients

With the  $\mathcal{J}_{ij}$  free of IR divergences and scaleless integrals safely set to 0 in pure dimensional regularization, the quark FJF can be calculated by evaluating diagrams (a) and (b) of Fig. 4.4. Diagram (a) of Fig. 4.4 yields

$$\begin{aligned}
&\frac{C_F \alpha_s}{2\pi} \frac{(4\pi\mu^2)^\epsilon (1-\epsilon)}{\Gamma[1-\epsilon]} \frac{1-z}{1-a/2} \omega^{2a\epsilon/(2-a)} (1-z)^{-2(1-a)\epsilon/(2-a)} \\
&\quad \times \left( 1 + \frac{(1-z)^{1-a}}{z^{1-a}} \right)^{2\epsilon/(2-a)} \frac{1}{s_a^{1+2\epsilon/(2-a)}}, \tag{4.29}
\end{aligned}$$

and diagram (b) yields

$$\frac{C_F \alpha_s}{2\pi} \frac{2z}{1-a/2} \frac{(4\pi\mu^2)^\epsilon}{\Gamma[1-\epsilon]} \omega^{2a\epsilon/(2-a)} \frac{1}{(1-z)^{1+2(1-a)\epsilon/(2-a)}} \times \left( 1 + \frac{(1-z)^{1-a}}{z^{1-a}} \right)^{2\epsilon/(2-a)} \frac{1}{s_a^{1+2\epsilon/(2-a)}}, \quad (4.30)$$

where  $s_a = \omega^2 \tau_a$ . These expressions contain singularities at  $\tau_a \rightarrow 0$  in (a) and (b) and  $z \rightarrow 1$  in (b), but these are regulated in dimensional regularization. By employing plus-distribution identities of the form

$$\frac{1}{(1-z)^{1+\epsilon}} = -\frac{1}{\epsilon} \delta(1-z) + \left( \frac{1}{1-z} \right)_+ - \epsilon \left( \frac{\ln(1-z)}{1-z} \right)_+ + \dots, \quad (4.31)$$

for the singularities in  $z$  and  $\tau_a$  the divergent pieces of the above expression can be written (expanding in  $\epsilon$ ) as

$$\frac{C_F \alpha_s}{2\pi} \left( \delta(s_a) \delta(1-z) \left[ \frac{2-a}{1-a} \frac{1}{\epsilon^2} + \frac{2-a}{1-a} \frac{1}{\epsilon} \ln \left( \frac{\mu^2}{\omega^2} \right) + \frac{3}{2\epsilon} \right] - \frac{1}{1-a} \frac{2}{\epsilon} \delta(1-z) \frac{1}{\omega^2} \left[ \frac{1}{\tau_a} \right]_+ - \delta(s_a) \frac{1}{\epsilon} P_{qq}(z) \right), \quad (4.32)$$

where  $P_{qq}$  is the quark-quark splitting function as defined in Eq. (4.27). As expected, the first four terms of this expression are UV poles that match the UV poles for the jet function for measured angularities (multiplied by  $\delta(1-z)$ ) shown in Eq. (3.37) of Ref. [1]. The final term  $\delta(s_a) P_{qq}(z)/\epsilon$  is also expected from NLO perturbative calculations of the FFs in Ref. [2]. Thus, the divergences of our angularity FJF appear to have the correct structure. Note that in Eq. (4.32) above we rescaled the renormalization scale  $\mu^2 \rightarrow e^{\gamma_E} \mu^2 / 4\pi$  in accordance with the  $\overline{MS}$  subtraction

scheme. We can write the finite pieces of the matching coefficients as

$$\begin{aligned}
\frac{1}{\omega^2} \frac{\mathcal{J}_{qq}(\tau_a, z, \mu)}{2(2\pi)^3} &= \frac{C_F \alpha_s}{2\pi} \frac{1}{\omega^2} \left\{ \delta(\tau_a) \delta(1-z) \frac{2-a}{1-a} \left( -\frac{\pi^2}{12} + \frac{1}{2} \ln^2 \left( \frac{\mu^2}{\omega^2} \right) \right) \right. \\
&+ \delta(\tau_a) \left( 1-z - \left[ \ln \left( \frac{\mu^2}{\omega^2} \right) + \frac{1}{1-a/2} \ln \left( 1 + \frac{(1-z)^{1-a}}{z^{1-a}} \right) \right] \frac{1+z^2}{(1-z)_+} \right. \\
&+ \left. \frac{1-a}{1-a/2} (1+z^2) \left( \frac{\ln(1-z)}{1-z} \right)_+ \right) \\
&+ \left[ \frac{1}{\tau_a} \right]_+ \left( \frac{1}{1-a/2} \frac{1+z^2}{(1-z)_+} - \delta(1-z) \frac{2}{1-a} \ln \left( \frac{\mu^2}{\omega^2} \right) \right) \\
&\left. + \frac{2\delta(1-z)}{(1-a)(1-a/2)} \left[ \frac{\ln \tau_a}{\tau_a} \right]_+ \right\}. \tag{4.33}
\end{aligned}$$

In the limit  $a \rightarrow 0$  this becomes

$$\begin{aligned}
\frac{1}{\omega^2} \frac{\mathcal{J}_{qq}(\tau_0, z, \mu)}{2(2\pi)^3} &= \frac{C_F \alpha_s}{2\pi} \left\{ \delta(s) \delta(1-z) \left( -\frac{\pi^2}{6} + \ln^2 \left( \frac{\mu^2}{\omega^2} \right) \right) \right. \\
&+ \delta(s) \left( 1-z - \ln \left( \frac{\mu^2}{\omega^2} \right) \frac{1+z^2}{(1-z)_+} + \ln z P_{qq}(z) + (1+z^2) \left( \frac{\ln(1-z)}{1-z} \right)_+ \right) \\
&\left. + \frac{1}{\omega^2} \left[ \frac{1}{\tau_0} \right]_+ \left( \frac{1+z^2}{(1-z)_+} - 2\delta(1-z) \ln \left( \frac{\mu^2}{\omega^2} \right) \right) + 2\delta(1-z) \frac{1}{\omega^2} \left[ \frac{\ln \tau_0}{\tau_0} \right]_+ \right\}, \tag{4.34}
\end{aligned}$$

where we have used  $\delta(\tau_0)/\omega^2 = \delta(s)$ . Using the following distributional identities

$$\begin{aligned}
\frac{1}{\omega^2} \left[ \frac{1}{\tau_0} \right]_+ &= \frac{1}{\omega^2} \left[ \frac{\omega^2}{s} \right]_+ = \frac{1}{\mu^2} \left[ \frac{\mu^2}{s} \right]_+ + \ln \left( \frac{\mu^2}{\omega^2} \right) \delta(s), \\
\frac{1}{\omega^2} \left[ \frac{\ln \tau_0}{\tau_0} \right]_+ &= \frac{1}{\omega^2} \left[ \frac{\ln(s/\omega^2)}{s/\omega^2} \right]_+ = \frac{1}{\mu^2} \left[ \frac{\ln(s/\mu^2)}{s/\mu^2} \right]_+ + \frac{\ln(\mu^2/\omega^2)}{\mu^2} \left[ \frac{\mu^2}{s} \right]_+ \\
&+ \frac{1}{2} \ln \left( \frac{\mu^2}{\omega^2} \right) \delta(s), \tag{4.35}
\end{aligned}$$

which are readily verified by integrating both sides over  $s$ , we find that taking  $a \rightarrow 0$  limit yields the finite terms

$$\begin{aligned} \frac{\mathcal{J}_{qq}(s, z, \mu)}{2(2\pi)^3} &= \frac{C_F\alpha_s}{2\pi} \left\{ \delta(s) \left( 1 - z + \ln z P_{qq}(z) + (1 + z^2) \left( \frac{\ln(1-z)}{1-z} \right)_+ - \frac{\pi^2}{6} \delta(1-z) \right) \right. \\ &\left. + \frac{1}{\mu^2} \left[ \frac{\mu^2}{s} \right]_+ \frac{1+z^2}{(1-z)_+} + 2\delta(1-z) \frac{1}{\mu^2} \left[ \frac{\ln(s/\mu^2)}{s/\mu^2} \right]_+ \right\}, \end{aligned} \quad (4.36)$$

which agrees with the calculation in Eq. (2.32) of Ref. [2] for measured jet mass. The matching coefficient  $\mathcal{J}_{gg}(\tau_a, z, \mu)$  is closely related to  $\mathcal{J}_{qq}(\tau_a, z, \mu)$  by substituting  $z \rightarrow 1-z$ . This simplifies the calculation of the FJF since when convolving  $\mathcal{J}_{gg}(\tau_a, x, \mu)$  with FFs, the integral over  $x$  in Eq. (4.28) no longer hits a pole as  $z \rightarrow 0$ . Thus, the  $1/(1-z)^{1+\epsilon}$  pole we regulated in  $\mathcal{J}_{qq}(\tau_a, z, \mu)$  can be replaced with the identity

$$\frac{1}{z^{1+\epsilon}} = \frac{1}{z} - \epsilon \frac{\ln z}{z} + O(\epsilon^2). \quad (4.37)$$

Thus,  $\mathcal{J}_{gg}(\tau_a, z, \mu)$  is found from  $\mathcal{J}_{qq}(\tau_a, z, \mu)$  by taking  $z \rightarrow 1-z$  and simply dropping  $\delta(z)$  and plus-function terms which yields

$$\frac{1}{\omega^2} \frac{\mathcal{J}_{gg}^{div}(\tau_a, z, \mu)}{2(2\pi)^3} = -\frac{1}{\omega^2} \frac{C_F\alpha_s}{2\pi} \frac{1}{\epsilon} \delta(\tau_a) P_{gq}(z), \quad (4.38)$$

for the divergent terms where  $P_{gq}$  is given in Eq. (4.27). The finite pieces are then

$$\begin{aligned} \frac{1}{\omega^2} \frac{\mathcal{J}_{gg}(\tau_a, z, \mu)}{2(2\pi)^3} &= \frac{C_F\alpha_s}{2\pi} \frac{1}{\omega^2} \left\{ \delta(\tau_a) \left( z + \left[ \frac{1}{1-a/2} \ln \left( \frac{z^{1-a}(1-z)^{1-a}}{z^{1-a} + (1-z)^{1-a}} \right) \right. \right. \right. \\ &\left. \left. - \ln \left( \frac{\mu^2}{\omega^2} \right) \right] P_{gq}(z) \right) + \frac{1}{1-a/2} \left[ \frac{1}{\tau_a} \right]_+ P_{gq}(z) \right\}. \end{aligned} \quad (4.39)$$

Once again, these reproduce the matching coefficients of Ref. [2] in the  $a \rightarrow 0$  limit. We calculate  $\mathcal{J}_{gg}(\tau_a, z, \mu)$  using the diagrams in Fig. 4.5. This yields the following

divergent terms

$$\begin{aligned} \frac{1}{\omega^2} \frac{\mathcal{J}_{gg}^{div}(\tau_a, z, \mu)}{2(2\pi)^3} &= \frac{C_A \alpha_s}{2\pi} \frac{1}{\omega^2} \left\{ \delta(\tau_a) \delta(1-z) \left[ \frac{2-a}{1-a} \frac{1}{\epsilon^2} + \frac{2-a}{1-a} \frac{1}{\epsilon} \ln \left( \frac{\mu^2}{\omega^2} \right) + \frac{\beta_0}{2C_A} \frac{1}{\epsilon} \right] \right. \\ &\quad \left. - \frac{1}{1-a} \frac{2}{\epsilon} \delta(1-z) \left[ \frac{1}{\tau_a} \right]_+ \right\} - \frac{\alpha_s}{2\pi} \frac{1}{\omega^2} \delta(\tau_a) \frac{1}{\epsilon} P_{gg}(z). \end{aligned} \quad (4.40)$$

The finite terms of  $\mathcal{J}_{gg}(\tau_a, z, \mu)$  are then

$$\begin{aligned} \frac{1}{\omega^2} \frac{\mathcal{J}_{gg}(\tau_a, z, \mu)}{2(2\pi)^3} &= \frac{C_A \alpha_s}{2\pi} \frac{1}{\omega^2} \left\{ \delta(\tau_a) \delta(1-z) \frac{2-a}{1-a} \left( -\frac{\pi^2}{12} + \frac{1}{2} \ln^2 \left( \frac{\mu^2}{\omega^2} \right) \right) \right. \\ &\quad + \delta(\tau_a) \left( -P_{gg}(z) \left[ \ln \left( \frac{\mu^2}{\omega^2} \right) + \frac{1}{1-a/2} \ln \left( 1 + \frac{(1-z)^{1-a}}{z^{1-a}} \right) \right] \right. \\ &\quad + \frac{1-a}{1-a/2} \frac{2(1-z+z^2)^2}{z} \left( \frac{\ln(1-z)}{1-z} \right)_+ \left. \right) \\ &\quad + \left[ \frac{1}{\tau_a} \right]_+ \left( \frac{1}{1-a/2} P_{gg}(z) - \delta(1-z) \frac{2}{1-a} \ln \left( \frac{\mu^2}{\omega^2} \right) \right) \\ &\quad \left. + \frac{2\delta(1-z)}{(1-a)(1-a/2)} \left[ \frac{\ln \tau_a}{\tau_a} \right]_+ \right\}. \end{aligned} \quad (4.41)$$

In the limit  $a \rightarrow 0$ , this expression reduces to  $\mathcal{J}_{gg}^{(1)}(s, z, \mu)$  found in Eq. (2.33) of Ref. [2].

Finally, the divergent terms of  $\mathcal{J}_{gq}(\tau_a, z, \mu)$  are

$$\frac{1}{\omega^2} \frac{\mathcal{J}_{gq}^{div}(\tau_a, z, \mu)}{2(2\pi)^3} = -\frac{1}{\omega^2} \frac{\alpha_s T_R}{2\pi} \frac{1}{\epsilon} \delta(\tau_a) P_{qg}(z), \quad (4.42)$$

and the finite terms are

$$\begin{aligned} \frac{1}{\omega^2} \frac{\mathcal{J}_{gq}(\tau_a, z, \mu)}{2(2\pi)^3} &= \frac{\alpha_s T_R}{2\pi} \frac{1}{\omega^2} \left\{ \frac{1}{1-a/2} \left[ \frac{1}{\tau_a} \right]_+ P_{qg}(z) + \delta(\tau_a) 2z(1-z) \right. \\ &\quad \left. + \delta(\tau_a) P_{qg}(z) \left[ \frac{1}{1-a/2} \ln \left( \frac{z^{1-a}(1-z)^{1-a}}{z^{1-a} + (1-z)^{1-a}} \right) - \ln \left( \frac{\mu^2}{\omega^2} \right) \right] \right\}, \end{aligned} \quad (4.43)$$

where  $P_{qq}$  is given in Eq. (4.27) and the expression reduces to  $\mathcal{J}_{gq}^{(1)}(s, z, \mu)$  of Ref. [2] as  $a \rightarrow 0$ .

#### 4.4.4 Summary of Perturbative Results

We can parameterize our perturbative results for  $\mathcal{J}_{ij}(\tau_a, z, \mu)$  as

$$\frac{\mathcal{J}_{ij}(\tau_a, z, \mu)}{2(2\pi)^3} = \delta_{ij}\delta(1-z)\delta(\tau_a) \quad (4.44)$$

$$+ T_{ij} \frac{\alpha_s}{2\pi} \left[ c_0^{ij}(z, \mu)\delta(\tau_a) + c_1^{ij}(z, \mu) \left( \frac{1}{\tau_a} \right)_+ + c_2 \delta_{ij}\delta(1-z) \left( \frac{\ln \tau_a}{\tau_a} \right)_+ \right], \quad (4.45)$$

where the coefficients are given by

$$\begin{aligned} c_0^{ij}(z, \mu) &= \frac{1-a/2}{1-a} \delta_{ij}\delta(1-z) \left[ \ln^2 \frac{\mu^2}{\omega^2} - \frac{\pi^2}{6} \right] + c^{ij}(z) \\ &\quad - \bar{P}_{ji} \left[ \ln \frac{\mu^2}{\omega^2} + \frac{1}{1-a/2} \ln \left( 1 + \left( \frac{1-z}{z} \right)^{1-a} \right) + (\delta_{ij} - 1) \frac{1-a}{1-a/2} \ln(1-z) \right], \\ c_1^{ij}(z, \mu) &= -\frac{2}{1-a} \delta_{ij}\delta(1-z) \ln \frac{\mu^2}{\omega^2} + \frac{1-a}{1-a/2} \bar{P}_{ij}, \\ c_2 &= \frac{2}{(1-a)(1-a/2)}, \end{aligned} \quad (4.46)$$

with

$$\begin{aligned} c^{qq}(z) &= 1-z + \frac{1-a}{1-a/2} (1+z^2) \left( \frac{\ln(1-z)}{1-z} \right)_+, \\ c^{gg}(z) &= \frac{1-a}{1-a/2} \frac{2(1-z+z^2)^2}{z} \left( \frac{\ln(1-z)}{1-z} \right)_+, \\ c^{qg}(z) &= z, \\ c^{gq}(z) &= 2z(1-z), \end{aligned} \quad (4.47)$$

Having already discussed how our results for  $\mathcal{J}_{ij}(\tau_a, z, \mu)$  satisfy

$$\lim_{a \rightarrow 0} \mathcal{J}_{ij}(\tau_a, z, \mu) = \omega^2 \mathcal{J}_{ij}(s, z, \mu), \quad (4.48)$$

where  $\mathcal{J}_{ij}(s, z, \mu)$  are the matching coefficients for measured jet invariant mass found in Ref. [2], we can perform one additional consistency check of our results by verifying that

$$J_i(\tau_a, \mu) = \frac{1}{2(2\pi)^3} \sum_j \int_0^1 dz z \mathcal{J}_{ij}(\tau_a, z, \mu). \quad (4.49)$$

This describes the sum-rule relating the  $\mathcal{J}_{ij}(\tau_a, z, \mu)$  and  $J_i(\tau_a, \mu)$ , the jet functions for measured jets as calculated in Ref. [1]. We begin by checking the quark jet case where we see that

$$J_q(\tau_a) = \frac{1}{2(2\pi)^3} \sum_j \int_0^1 dz z \mathcal{J}_{qj}(\tau_a, z) \quad (4.50)$$

$$= \frac{1}{2(2\pi)^3} \int_0^1 dz z (\mathcal{J}_{qq}(\tau_a, z) + \mathcal{J}_{qg}(\tau_a, z)) \quad (4.51)$$

$$= \frac{1}{2(2\pi)^3} \int_0^1 dz z (\mathcal{J}_{qq}(\tau_a, z) + \mathcal{J}_{qq}(\tau_a, 1-z)) \quad (4.52)$$

$$= \frac{1}{2(2\pi)^3} \int_0^1 dz \mathcal{J}_{qq}(\tau_a, z). \quad (4.53)$$

Note that the last line is obtained by taking  $z \rightarrow 1-z$  in the second term of the second-to-last line. Putting Eq. (4.33) into this integral, we recover the  $J_q(\tau_a)$  calculated in Eq. (3.35) of Ref. [113].

For gluon jets we find that

$$\begin{aligned} J_g(\tau_a) &= \frac{1}{2(2\pi)^3} \int_0^1 dz z (\mathcal{J}_{gg}(\tau_a, z) + \mathcal{J}_{gq}(\tau_a, z)) \\ &= \frac{1}{2(2\pi)^3} \int_0^1 dz \frac{\mathcal{J}_{gg}(\tau_a, z) + \mathcal{J}_{gq}(\tau_a, z)}{2}, \end{aligned} \quad (4.54)$$

where in the second line we used that  $\mathcal{J}_{gg}(\tau_a, z)$  and  $\mathcal{J}_{gq}(\tau_a, z)$  are both symmetric under  $z \rightarrow 1-z$ . To verify the sum rule in these cases, we backtrack the calculation of  $\mathcal{J}_{gg}$  and  $\mathcal{J}_{gq}$  to their  $d$ -dimensional expressions before taking the expansion in

$\epsilon = (4 - d)/2$ . We then find

$$\begin{aligned} \frac{1}{\omega^2} \frac{\mathcal{J}_{gg}(\tau_a, z, \mu)}{2(2\pi)^3} &= \frac{1}{\omega^2} \left( \frac{4\pi\mu^2}{\omega^2} \right)^\epsilon \frac{C_A\alpha_s}{2\pi} \frac{1}{\Gamma[1-\epsilon]} \frac{1}{1-a/2} (z^{a-1} + (1-z)^{a-1})^{\frac{2\epsilon}{2-a}} \\ &\times \left( \frac{1}{\tau_a} \right)^{1+\frac{2\epsilon}{1-a}} \left( \frac{2z}{1-z} + \frac{2(1-z)}{z} + 2z(1-z) \right) \\ \frac{1}{\omega^2} \frac{\mathcal{J}_{gq}(\tau_a, z, \mu)}{2(2\pi)^3} &= \frac{1}{\omega^2} \left( \frac{4\pi\mu^2}{\omega^2} \right)^\epsilon \frac{T_R\alpha_s}{2\pi} \frac{1}{\Gamma[1-\epsilon]} \frac{1}{1-a/2} (z^{a-1} + (1-z)^{a-1})^{\frac{2\epsilon}{2-a}} \\ &\times \left( \frac{1}{\tau_a} \right)^{1+\frac{2\epsilon}{1-a}} \left( 1 - \frac{2}{1-\epsilon} z(1-z) \right). \end{aligned}$$

By then putting these two expressions into Eq. (4.54), we recover the integral expression for the  $d$ -dimensional  $J_g(\tau_a)$  found in Eq. (4.22) of Ref. [1]. Our perturbative results for  $\mathcal{J}_{ij}(\tau_a, z, \mu)$  are independent of  $R$ , the jet size parameter. These effects could be explicitly included in our calculations using a Heaviside- $\Theta$  function to impose the phase space constraints required by a given jet algorithm. However, Ref. [1] showed that terms dependent on the jet-algorithm for cone and  $k_T$ -type algorithms are suppressed by powers of  $\tau_a/R^2$ . In our study where  $\tau_a \sim 10^{-3}$  and  $R \sim 0.5$ , these terms are negligible. This suppression makes sense physically, since for very small  $\tau_a$  the particles in a jet lie essentially all along the jet axis.

## 4.5 Transverse Momentum Dependent FJFs (TMDFJF)

### 4.5.1 TMDs & Collinear-Soft Modes

Our next goal is to extend FJFs to transverse momentum dependent (TMD) observables. TMDs have seen extensive recent developments in EFT literature such as Refs. [114–122] and they offer promising new techniques for studying jet substructure and hadron production. In SCET, TMD parton distribution functions (TMDPDF) have been applied to the study of Higgs production at small transverse momentum at the LHC [122–127].

In this section, after motivating the definition of the transverse momentum dependent fragmenting jet function (TMDFJF), the matching coefficients  $\mathcal{J}_{ij}(\mathbf{p}_\perp, z, \mu)$  for these TMDFJFs onto FFs are calculated. TMDFJFs will be dependent on the jet energy  $E_J = \omega/2$ , the fraction  $z$  of the jet's momentum carried by the identified hadron, and the transverse momentum  $\mathbf{p}_\perp^h$  of the identified hadron relative to the jet initiating parton.<sup>2</sup>

The key difference between the definitions of the TMDFJF and the angularity FJF arises when we identify the relevant momentum modes. As we discussed in Section 3.4.3, an additional collinear-soft mode must be included when studying TMDFJFs because the scaling of the transverse components of soft and collinear modes are of the same order. This mode describes soft energy modes that are collinear to the direction of a jet. First introduced in Ref. [98] and further studied in works such as Ref. [99] this collinear-soft mode has the following scaling

$$\begin{aligned} \text{collinear-soft: } p_{cs}^\mu &\sim \omega(\lambda r, \lambda/r, \lambda), & \lambda &= p_\perp/\omega \\ \text{collinear: } p_n^\mu &\sim \omega(\lambda^2, 1, \lambda), \end{aligned} \tag{4.55}$$

where  $r \equiv \tan(R/2)$  for jet cone size  $R$ . These new collinear-soft modes can be systematically included using the SCET<sub>+</sub> formalism, whose modes are illustrated in Fig. 3.6. Originally constructed to study jets that are close together, SCET<sub>+</sub> is one of several extensions of SCET that have additional hierarchies of well-separated energy scales and layered phase space regions [98, 99, 120, 128]. As we did for angularity FJFs in Section 4.4, we will extend the definition of FJFs to a different observable (in this case the transverse momentum  $\mathbf{p}_\perp$ ) and calculate the the matching coefficients onto FFs at one-loop. The TMDFJF will then be applied to quarkonium production in Chapter 5.

---

<sup>2</sup> In the context of this work, the direction of the jet initiating parton will always correspond to the direction of the jet axis.

### 4.5.2 Definition & Factorization

In the following sections we will perturbatively calculate the matching coefficients  $\mathcal{J}_{ij}(\mathbf{p}_\perp^h, z, \mu)$  to one-loop order. In order to properly connect the TMDFJF with definitions of TMD Fragmentation Functions (TMDFFs) in the literature, let us first re-write the FF from Eq. (4.8) using the delta function identity

$$\delta_{\omega, p_t^-} \delta(p_r^-) = \delta(\omega - p^-). \quad (4.56)$$

We can then write the quark FF as

$$D_q^h(z, \mu) = \frac{1}{z} \sum_X \frac{1}{2N_c} \delta(\omega - p_X^- - p_h^-) \text{Tr} \left[ \frac{\not{h}}{2} \langle 0 | \psi(0) | Xh \rangle \langle Xh | \bar{\psi}(0) | 0 \rangle \right] \Big|_{\mathbf{p}_\perp^X = -\mathbf{p}_\perp^h}, \quad (4.57)$$

where  $\psi(x)$  is a QCD quark field. As defined in Ref. [129], the TMDFF can be given by

$$D_q^h(\mathbf{p}_\perp^h, z, \mu) = \frac{1}{z} \int \frac{d^2 x_\perp}{(2\pi)^2} \sum_X \frac{1}{2N_c} \delta(\omega - p_X^- - p_h^-) \times \text{Tr} \left[ \frac{\not{h}}{2} \langle 0 | \psi(0, 0, x_\perp) | Xh \rangle \langle Xh | \bar{\psi}(0) | 0 \rangle \right], \quad (4.58)$$

where it is related to the traditional FFs by

$$\int d^2 \mathbf{p}_\perp^h D_q^h(\mathbf{p}_\perp^h, z, \mu) = D_q^h(z, \mu). \quad (4.59)$$

In this expression,  $\mathbf{p}_\perp^h$  is the transverse momentum of the hadron  $h$  with respect to the direction of the original fragmenting quark. We will enforce that the axis of the jet coincides with the direction of the jet initiating parton. In the context of TMDs, we assume that all out-of-jet radiation has ultra-soft scaling. All soft-scaling radiation will be inside the jet radius. We note that the TMDFF can also be defined for measurements of the transverse momentum with respect to other axes such as

the winner-take-all axis [130]. Taking the collinear limit of Eq.(4.58) and matching onto SCET fields yields an operator definition of the quark TMDFJF

$$\begin{aligned} \mathcal{G}_q^h(\mathbf{p}_\perp, z, \mu) &= \frac{1}{z} \sum_X \frac{1}{2N_c} \delta(p_{Xh;r}) \delta^{(2)}(\mathbf{p}_\perp + \mathbf{p}_\perp^X) \\ &\times \text{Tr} \left[ \frac{\not{n}}{2} \langle 0 | \delta_{\omega, \bar{\mathcal{P}}} \chi_n^{(0)}(0) | Xh \rangle \langle Xh | \bar{\chi}_n^{(0)}(0) | 0 \rangle \right], \end{aligned} \quad (4.60)$$

where we define  $z \equiv E_h/E_J$  and  $|Xh\rangle$  to represent a collinear final state hadron  $h$  and any other particles  $X$  that are within a jet. In Eqs. (4.57) and (4.58), the states  $|Xh\rangle$  were completely inclusive states. Once again, the index (0) indicates that the field has been decoupled from the ultra-soft modes through BPS field redefinitions<sup>3</sup> as shown in Eq. (3.35). In Section 4.6, we show that the the expression for the TMDFJF given in Eq.(4.60) is closely related to the FJF introduced in Ref. [105] and in Eq.(4.9) above.

Because we are measuring the  $\mathbf{p}_\perp^h$ , the TMDFJF must include collinear-soft (csoft) modes in addition to collinear modes. As discussed in Ref. [128], these contributions can be made explicit by performing a matching of our TMDFJF onto SCET<sub>+</sub> fields

$$\begin{aligned} \mathcal{G}_q^h(\mathbf{p}_\perp, z, \mu) &= C_+^\dagger(\mu) C_+(\mu) \frac{1}{z} \sum_X \frac{1}{2N_c} \delta(p_{Xh;r}) \delta^{(2)}(\mathbf{p}_\perp + \mathbf{p}_\perp^X) \\ &\times \text{Tr} \left[ \frac{\not{n}}{2} \langle 0 | \delta_{\omega, \bar{\mathcal{P}}} V_n^\dagger{}^{(0)}(0) \chi_n^{(0)}(0) | Xh \rangle \langle Xh | \bar{\chi}_n^{(0)}(0) V_n^{(0)}(0) | 0 \rangle \right], \end{aligned} \quad (4.61)$$

where

$$V_n^{(0)}(x) = \sum_{\text{perm}} \exp \left( \frac{-g}{\bar{n} \cdot \mathcal{P}} \bar{n} \cdot A_{n,cs}^{(0)}(x) \right), \quad (4.62)$$

are Wilson lines of csoft fields and  $C_+(\mu)$  are matching coefficients from the matching of SCET<sub>I</sub>  $\rightarrow$  SCET<sub>+</sub>. We now perform a second field-redefinition (analogous to

<sup>3</sup> While previously we dropped the (0), we leave them in explicitly here for the moment. They will subsequently be dropped after a further field re-definition is performed when we re-factorize (i.e. perform an additional factorization of) our TMDFJF.

the BPS redefinitions used above) as done in Ref. [98]. This procedure completely decouples purely collinear fields  $A_n^{(0)}$  and  $\chi_n^{(0)}$  from csoft gluons from the csoft gluons via

$$\begin{aligned} \mathcal{G}_q^h(\mathbf{p}_\perp, z, \mu) &= C_+^\dagger(\mu)C_+(\mu)\frac{1}{z}\sum_X\frac{1}{2N_c}\delta(p_{\bar{X}h;r}^-)\delta^{(2)}(\mathbf{p}_\perp+\mathbf{p}_\perp^X) \\ &\times \text{Tr}\left[\frac{\not{n}}{2}\langle 0|\delta_{\omega,\bar{p}}V_n^\dagger{}^{(0)}(0)U_n^{(0)}(0)\chi_n^{(0,0)}(0)|Xh\rangle\langle Xh|\bar{\chi}_n^{(0,0)}(0)U_n^\dagger{}^{(0)}(0)V_n^{(0)}(0)|0\rangle\right], \end{aligned} \quad (4.63)$$

where the Wilson line  $U_n(x)$  is defined as

$$U_n^\dagger{}^{(0)}(x)=\mathbb{P}\exp\left(ig\int_0^\infty ds n\cdot A_{n,cs}^{(0)}(ns+x)\right). \quad (4.64)$$

In these equations, the superscript  $(0,0)$  denotes that a field has been decoupled from both ultra-soft and csoft modes. Now that collinear, csoft, and ultra-soft operators have been factorized, we can perform a similar factorization of the states

$$|Xh\rangle\rightarrow|X_nh\rangle|X_{cs}\rangle, \quad (4.65)$$

where  $X_n$  are collinear particles, and  $X_{cs}$  are csoft particles. We also separate

$$\sum_X\rightarrow\sum_{X_n}\sum_{X_{cs}}, \quad (4.66)$$

$$\delta^{(2)}(\mathbf{p}_\perp+\mathbf{p}_\perp^X)\rightarrow\delta^{(2)}(\mathbf{p}_\perp+\mathbf{p}_\perp^{X_n}+\mathbf{p}_\perp^{X_{cs}}). \quad (4.67)$$

This allows us to factorize the TMDFJF into

$$\mathcal{G}_q^h(\mathbf{p}_\perp, z, \mu)=H_+(\mu)\times\left[\mathcal{D}_q^h\otimes_\perp S_C\right](\mathbf{p}_\perp, z, \mu), \quad (4.68)$$

where  $H_+$  is proportional to the square of the matching coefficient and  $\mathcal{D}_q^h$  and  $S_C$  are the purely collinear and csoft functions, respectively, of SCET $_+$ . They are given by

$$H_+(\mu)=(2\pi)^2N_c C_+^\dagger(\mu)C_+(\mu), \quad (4.69)$$

$$\mathcal{D}_q^h(\mathbf{p}_\perp^{\mathcal{D}}, z) \equiv \frac{1}{z} \sum_{X_n} \frac{1}{2N_c} \delta(p_{Xh;r}^-) \delta^{(2)}(p_{Xh;r}^\perp) \text{Tr} \left[ \frac{\not{h}}{2} \langle 0 | \delta_{\omega, \bar{\mathcal{P}}} \chi_n(0) \delta^{(2)}(\mathcal{P}_\perp^{X_n} + \mathbf{p}_\perp^{\mathcal{D}}) | X_n h \rangle \right. \\ \left. \times \langle X_n h | \bar{\chi}_n(0) | 0 \rangle \right], \quad (4.70)$$

$$S_C(\mathbf{p}_\perp^S) \equiv \frac{1}{N_c} \sum_{X_{cs}} \text{Tr} \left[ \langle 0 | V_n^\dagger(0) U_n(0) \delta^{(2)}(\mathcal{P}_\perp + \mathbf{p}_\perp^S) | X_{cs} \rangle \langle X_{cs} | U_n^\dagger(0) V_n(0) | 0 \rangle \right]. \quad (4.71)$$

Note that the trace is taken over both Dirac and color indices in  $\mathcal{D}_q^h(\mathbf{p}_\perp^{\mathcal{D}}, z)$ , but over color indices only in  $S_C(\mathbf{p}_\perp^S)$ . Now that our expressions are completely factorized and collinear/csoft/ultra-soft modes are clearly distinguishable, we drop the (0) and (0, 0) for notational convenience. Let us define the notation  $\otimes_\perp$  to represent a convolution in perpendicular components

$$\mathcal{D}_q^h \otimes_\perp S_C(\mathbf{p}_\perp) = \int \frac{d^2 \mathbf{p}'_\perp}{(2\pi)^2} \mathcal{D}_q^h(\mathbf{p}_\perp - \mathbf{p}'_\perp) S_C(\mathbf{p}'_\perp). \quad (4.72)$$

This procedure also holds for gluon FJFs

$$\mathcal{D}_g^h(\mathbf{p}_\perp, z, \mu) = -g_{\mu\nu} \frac{1}{z} \sum_X \frac{\omega}{(d-2)(N_c^2-1)} \delta(p_{Xh;r}^-) \delta^{(2)}(\mathbf{p}_\perp + \mathbf{p}_\perp^X) \\ \times \langle 0 | \delta_{\omega, \bar{\mathcal{P}}} \mathcal{B}_{n,\perp}^{\nu,a}(0) \delta^{(2)}(\mathcal{P}_\perp^{X_n} + \mathbf{p}_\perp^{\mathcal{D}}) | X h \rangle \langle X h | \mathcal{B}_{n,\perp}^{\mu,a}(0) | 0 \rangle, \quad (4.73)$$

where  $iD_{n\perp} = \mathcal{P}_{n\perp}^\mu + gA_{n\perp}^\mu$  is the standard  $\perp$ -collinear covariant derivative in SCET and

$$\mathcal{B}_{n,\perp}^\mu(y) = \frac{1}{g} [W_n^\dagger(y) iD_{n\perp} W_n(y)], \quad (4.74)$$

is the collinear gluon jet field. In these completely factorized expressions,  $\mathcal{D}_i^h$  contains all of the information about the identified hadron  $h$  while  $S_C$  and  $H_+$  depend only on the initial parton  $i$ . Having identified the purely collinear piece  $\mathcal{D}_i^h$ , in the limit  $\mathbf{p}_\perp \gg \Lambda_{\text{QCD}}$ , we can (in analogy with the purely collinear angularity FJF) further factorize  $\mathcal{D}_i^h$  into the traditional FFs and perturbatively calculable matching coefficients that,

this case, depend on  $\mathbf{p}_\perp$  but do not depend on the identity of the hadron  $h$ ,

$$\mathcal{D}_i^h(\mathbf{p}_\perp, z, \mu, \nu) = \int_z^1 \frac{dx}{x} \mathcal{J}_{ij}(\mathbf{p}_\perp, x, \mu, \nu) D_j^h\left(\frac{z}{x}, \mu\right) + \mathcal{O}\left(\frac{\Lambda_{QCD}^2}{|\mathbf{p}_\perp|^2}\right). \quad (4.75)$$

Note that this expression depends on a parameter  $\nu$ , which is a dimensionful scale analogous to  $\mu$  that will be defined in the next section.

#### 4.5.3 Perturbative Calculation of TMD Matching Coefficients

The calculation of the matching coefficients  $\mathcal{J}_{ij}$  at one-loop will once again require the evaluation of the diagrams shown in 4.4 and 4.5 for the quark and gluon TMD-FJFs, respectively. We note that these coefficients are directly related to the  $\mathcal{I}_{ij}$  in Refs. [120, 122] (through the substitution  $\mathcal{I}_{ij} \rightarrow \mathcal{J}_{ji}$ ), which were matching coefficients between TMDPDFs and standard PDFs.<sup>4</sup> In order to regulate rapidity divergences that arise when measuring  $\mathbf{p}_\perp^h$  with respect to the jet-axis, we use the rapidity regulator formalism developed in SCET in Refs. [122, 134]. This is done by first modifying the collinear and collinear-soft Wilson lines

$$\begin{aligned} W_n &= \sum_{\text{perms}} \exp\left(-\frac{g w^2}{\bar{n} \cdot \mathcal{P}} \frac{|\bar{n} \cdot \mathcal{P}_g|^{-\eta}}{\nu^{-\eta}} \bar{n} \cdot A_n\right) \\ V_n &= \sum_{\text{perms}} \exp\left(-\frac{g w}{\bar{n} \cdot \mathcal{P}} \frac{|\bar{n} \cdot \mathcal{P}_g|^{-\eta/2}}{\nu^{-\eta/2}} \bar{n} \cdot A_{n,cs}\right), \end{aligned} \quad (4.76)$$

with similar modifications being made to  $U_n$ . Here we use a regulator  $\eta$ , a book-keeping parameter  $w$  (which we will ultimately set to 1.), and a new dimensional parameter  $\nu$ .<sup>5</sup> The dependence of our results on  $\nu$  should, of course, cancel amongst

<sup>4</sup> We also note that there exists a more general analogy between the relationship of FJFs to FFs and the relationship of so-called *beam functions* to PDFs. Beam functions are the subject of current research in SCET and have been studied in a variety of works including Refs. [120, 122, 131–133].

<sup>5</sup> Note that this formalism is similar to dimensional regularization (DR), with  $\eta$ ,  $w$ , and  $\nu$  playing the roles of the parameter  $\epsilon$ , coupling  $g_s$ , and scale  $\mu$  in DR. In this case, however,  $w$  is not a real coupling but merely a calculational tool.

the terms in our factorization theorem. This will be demonstrated in Chapter 5. For the quark-quark case we find for the purely collinear piece

$$\begin{aligned}
\mathcal{D}_q^{q,\text{bare},(1)}(\mathbf{p}_\perp, z, \mu, \nu) &= \frac{\alpha_s w^2 C_F}{\pi} \frac{e^{\gamma_E \epsilon}}{\Gamma(1-\epsilon)} \left(\frac{\nu}{\omega}\right)^\eta \frac{1}{2\pi\mu^2} \left(\frac{\mu^2}{\mathbf{p}_\perp^2}\right)^{1+\epsilon} \\
&\times \left\{ 2z \left(\frac{1}{1-z}\right)^{1+\eta} + (1-\epsilon)(1-z) \right\} \\
&= \frac{\alpha_s w^2 C_F}{\pi} \left\{ \left[ -\frac{2}{\eta} \left(-\frac{1}{2\epsilon} \delta^{(2)}(\mathbf{p}_\perp) + \mathcal{L}_0(\mathbf{p}_\perp^2, \mu^2)\right) \right. \right. \\
&+ \frac{1}{2\epsilon} \left( \ln\left(\frac{\nu^2}{\omega^2}\right) + \frac{3}{2} \right) \delta^{(2)}(\mathbf{p}_\perp) \left. \right] \delta(1-z) - \frac{1}{2\epsilon} P_{qq}(z) \delta^{(2)}(\mathbf{p}_\perp) \\
&+ \left( -\delta(1-z) \ln\left(\frac{\nu^2}{\omega^2}\right) + \bar{P}_{qq}(z) \right) \mathcal{L}_0(\mathbf{p}_\perp^2, \mu^2) + c_{qq}(z) \delta^{(2)}(\mathbf{p}_\perp) \left. \right\} \\
&+ \mathcal{O}(\eta, \epsilon),
\end{aligned}$$

where  $c_{qq}(z) = (1-z)/2$ , the superscript (1) indicates an  $O(\alpha_s)$  contribution, and quantities are renormalized unless notated as bare. We write plus functions in the following form

$$\mathcal{L}_n(\mathbf{p}_\perp^2, \mu^2) = \frac{1}{2\pi\mu^2} \mathcal{L}_n\left(\frac{\mathbf{p}_\perp^2}{\mu^2}\right) = \frac{1}{2\pi\mu^2} \left(\frac{\mu^2}{\mathbf{p}_\perp^2} \ln^n(\mu^2/\mathbf{p}_\perp^2)\right)_+. \quad (4.77)$$

The matching coefficient is then calculated using

$$\mathcal{J}_{qq}^{(1)}(\mathbf{p}_\perp, z, \mu) = \mathcal{D}_q^{q,(1)}(\mathbf{p}_\perp, z, \mu) - D_q^{q,(1)}(z, \mu) \delta^{(2)}(\mathbf{p}_\perp), \quad (4.78)$$

where

$$D_q^{q,(1)}(z) = -\frac{\alpha_s C_F}{\pi} P_{qq}(z) \frac{1}{2\epsilon}, \quad (4.79)$$

and where we interpret the  $1/\epsilon$  pole as being IR in origin. The matching coefficient is given by

$$\begin{aligned}
\mathcal{J}_{qq}(\mathbf{p}_\perp, z, \mu, \nu) &= \delta^{(2)}(\mathbf{p}_\perp) \delta(1-z) \\
&+ \frac{\alpha_s C_F}{\pi} \left\{ \left( \delta(1-z) \ln\left(\frac{\omega^2}{\nu^2}\right) + \bar{P}_{qq}(z) \right) \mathcal{L}_0(\mathbf{p}_\perp^2, \mu^2) + c_{qq}(z) \delta^{(2)}(\mathbf{p}_\perp) \right\}. \quad (4.80)
\end{aligned}$$

Once again following the procedure of Sec. 4.4, the quark-gluon coefficient  $\mathcal{J}_{qg}$  is found by replacing  $z \rightarrow 1 - z$  and dropping all  $\delta(z)$  and plus-function prescriptions

$$\mathcal{J}_{qg}(\mathbf{p}_\perp, z, \mu, \nu) = \frac{\alpha_s C_F}{\pi} \left\{ \bar{P}_{gq}(z) \mathcal{L}_0(\mathbf{p}_\perp^2, \mu^2) + c_{qg}(z) \delta^{(2)}(\mathbf{p}_\perp) \right\}, \quad (4.81)$$

where  $c_{qg}(z) = c_{qq}(1 - z) = z/2$ . For the gluon-gluon case we find

$$\begin{aligned} \mathcal{D}_g^{g,\text{bare},(1)}(\mathbf{p}_\perp, z, \mu, \nu) &= \frac{\alpha_s C_A w^2}{\pi} \frac{e^{\epsilon\gamma_E}}{\Gamma(1 - \epsilon)} \left(\frac{\nu}{\omega}\right)^\eta \frac{1}{2\pi\mu^2} \left(\frac{\mu^2}{\mathbf{p}_\perp^2}\right)^{1+\epsilon} \\ &\times 2 \left[ \frac{z}{(1-z)^{1+\eta}} + \frac{(1-z)}{z} + z(1-z) \right]. \end{aligned} \quad (4.82)$$

Performing an expansion first in  $\eta \rightarrow 0$  and then in  $\epsilon \rightarrow 0$  yields

$$\begin{aligned} \mathcal{D}_g^{g,\text{bare},(1)}(\mathbf{p}_\perp, z, \mu, \nu) &= \frac{\alpha_s C_A w^2}{\pi} \left[ -\frac{1}{2\epsilon} \delta^{(2)}(\mathbf{p}_\perp) + \mathcal{L}_0(\mathbf{p}_\perp^2, \mu^2) \right] \\ &\times \left[ -\frac{2}{\eta} \delta(1-z) - \ln\left(\frac{\nu^2}{\omega^2}\right) \delta(1-z) + \bar{P}_{gg}(z) \right] \\ &= \frac{\alpha_s C_A w^2}{\pi} \left\{ \left[ -\frac{2}{\eta} \left( -\frac{1}{2\epsilon} \delta^{(2)}(\mathbf{p}_\perp) + \mathcal{L}_0(\mathbf{p}_\perp^2, \mu^2) \right) \right. \right. \\ &\quad \left. \left. + \frac{1}{2\epsilon} \left( \ln\left(\frac{\nu^2}{\omega^2}\right) + \frac{1}{2}\beta_0 \right) \delta^{(2)}(\mathbf{p}_\perp) \right] \delta(1-z) \right. \\ &\quad \left. - \frac{1}{2\epsilon} P_{gg}(z) \delta^{(2)}(\mathbf{p}_\perp) + \left( -\delta(1-z) \ln\left(\frac{\nu^2}{\omega^2}\right) + \bar{P}_{gg}(z) \right) \mathcal{L}_0(\mathbf{p}_\perp^2, \mu^2) \right\}. \end{aligned} \quad (4.83)$$

The corresponding FF is given by

$$D_g^g(z) = \delta(1-z) - \frac{\alpha_s C_A}{\pi} P_{gg}(z) \frac{1}{2\epsilon} + \mathcal{O}(\alpha_s^2), \quad (4.84)$$

where the  $1/\epsilon$  is an IR pole. This yields following for the matching coefficient

$$\mathcal{J}_{gg}(\mathbf{p}_\perp, z, \mu, \nu) = \delta^{(2)}(\mathbf{p}_\perp) \delta(1-z) + \frac{\alpha_s C_A}{\pi} \left( \delta(1-z) \ln\left(\frac{\omega^2}{\nu^2}\right) + \bar{P}_{gg}(z) \right) \mathcal{L}_0(\mathbf{p}_\perp^2, \mu^2). \quad (4.85)$$

Performing a similar calculation for the  $gq$  channel yields, for the purely collinear piece of the TMDFJF

$$\begin{aligned} \mathcal{D}_g^{q,\text{bare},(1)}(\mathbf{p}_\perp, z, \mu, \nu) &= \frac{\alpha_s T_F \omega^2}{\pi} \frac{e^{\epsilon\gamma_E}}{\Gamma(2-\epsilon)} \frac{1}{2\pi\mu^2} \left( \frac{\mu^2}{\mathbf{p}_\perp^2} \right)^{1+\epsilon} \times (\bar{P}_{qg}(z) - \epsilon) \\ &= \frac{\alpha_s T_F \omega^2}{\pi} \left\{ -\frac{1}{2\epsilon} \bar{P}_{qg}(z) \delta^{(2)}(\mathbf{p}_\perp) + \mathcal{L}_0(\mathbf{p}_\perp^2, \mu^2) \bar{P}_{qg}(z) + c_{gq}(z) \delta^{(2)}(\mathbf{p}_\perp) \right\}, \end{aligned} \quad (4.86)$$

where  $c_{gq}(z) = z(1-z)$ . Matching onto the FF given by

$$D_g^q(z) = -\frac{\alpha_s T_F}{\pi} P_{qg}(z) \frac{1}{2\epsilon} + \mathcal{O}(\alpha_s^2), \quad (4.87)$$

results in the following matching coefficient

$$\mathcal{J}_{gq}(\mathbf{p}_\perp, z, \mu, \nu) = \delta^{(2)}(\mathbf{p}_\perp) \delta(1-z) + \frac{\alpha_s T_F}{\pi} \left\{ \mathcal{L}_0(\mathbf{p}_\perp^2, \mu^2) \bar{P}_{qg}(z) + c_{gq}(z) \delta^{(2)}(\mathbf{p}_\perp) \right\}. \quad (4.88)$$

#### 4.5.4 Summary of Collinear Perturbative Results

The renormalized TMDFJF matching coefficients can be written generically as

$$\begin{aligned} \mathcal{J}_{ij}(\mathbf{p}_\perp, z, \mu, \nu) &= \delta_{ij} \delta(1-z) \delta^{(2)}(\mathbf{p}_\perp) \\ &+ \frac{\alpha_s T_{ij}}{\pi} \left\{ \left( \delta_{ij} \delta(1-z) \ln \left( \frac{\omega^2}{\nu^2} \right) + \bar{P}_{ji}(z) \right) \mathcal{L}_0(\mathbf{p}_\perp^2, \mu^2) + c_{ij}(z) \delta^{(2)}(\mathbf{p}_\perp) \right\}, \end{aligned} \quad (4.89)$$

with

$$c_{qq}(z) = \frac{1-z}{2}, \quad c_{qg}(z) = \frac{z}{2}, \quad c_{gg}(z) = 0, \quad c_{gq}(z) = z(1-z), \quad (4.90)$$

where  $T_{qq} = T_{qg} = C_F$ ,  $T_{gg} = C_A$ ,  $T_{gq} = T_F$ ,  $\bar{\gamma}_q = 3/2$  and  $\bar{\gamma}_g = \beta_0/(2C_A)$ . Writing the convolutions of the FFs with the matching coefficients in  $z$  we find for the purely

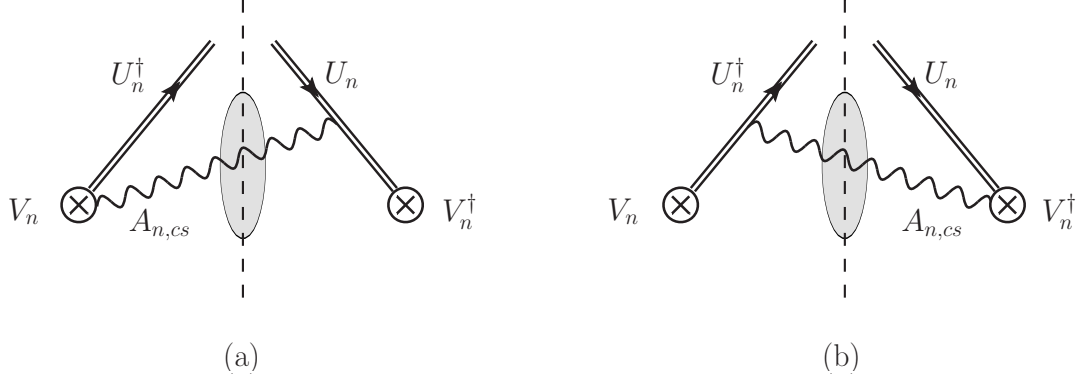


FIGURE 4.7: Real gluon emission diagrams that contribute to the collinear-soft function  $S_C^i(\mathbf{p}_\perp, z, \mu, \nu)$  at  $\mathcal{O}(\alpha_s)$ . The gluons passing through the shaded oval indicate they are contained within the phase-space of the jet.

collinear function

$$\begin{aligned} \mathcal{D}_i^h(\mathbf{p}_\perp^2, z, \mu, \nu) &= D_i^h(z, \mu) \delta^{(2)}(\mathbf{p}_\perp) + \frac{\alpha_s}{\pi} \left\{ \left[ T_{ii} D_i^h(z, \mu) \ln \left( \frac{\omega^2(1-z)^2}{\nu^2} \right) \right. \right. \\ &\quad \left. \left. + f_{P \otimes D}^{i/h}(z, \mu) \right] \mathcal{L}_0(\mathbf{p}_\perp^2, \mu^2) + f_{c \otimes D}^{i/h}(z, \mu) \delta^{(2)}(\mathbf{p}_\perp) \right\}, \quad (4.91) \end{aligned}$$

where

$$\begin{aligned} f_{P \otimes D}^{i/h}(z, \mu) &= \sum_j \left\{ \delta_{ij} T_{ii} \int_z^1 \frac{dx}{1-x} \left[ p_i(x) D_i^h \left( \frac{z}{x}, \mu \right) - 2 D_i^h(z, \mu) \right] \right. \\ &\quad \left. + (1 - \delta_{ij}) T_{ij} \int_z^1 \frac{dx}{x} P_{ji}(x) D_j^h \left( \frac{z}{x}, \mu \right) \right\}, \quad (4.92) \end{aligned}$$

with  $p_q(x) = (1+x^2)/x$ ,  $p_g(x) = 2(1-x+x^2)^2/x^2$  and

$$f_{c \otimes D}^{i/h}(z, \mu) = \sum_j T_{ij} \int_z^1 \frac{dx}{x} c_{ij}(x) D_j^h \left( \frac{z}{x}, \mu \right), \quad (4.93)$$

#### 4.5.5 Perturbative Calculation of Collinear-Soft Function

Calculating the collinear-soft function requires, at one-loop order, the evaluation of the diagrams shown in Fig. 4.7 where the real gluon is found in a jet defined by

a cone or  $k_T$ -type jet algorithm with jet-size parameter  $R$ . Similar soft functions were calculated for global soft radiation in Refs. [122] and [124] at NLO and NNLO, respectively in order to study the transverse momentum spectrum of Higgs decays. The two diagrams in Fig. 4.7 evaluate to the same expression and summing their contributions yields

$$S_C^{i,B(1)}(\mathbf{p}_\perp) = +g^2 w^2 \left( \frac{e^{\gamma_E} \mu^2}{4\pi} \right)^\epsilon \nu^\eta C_i \int \frac{dk^+ dk^- d^{d-2} k_\perp}{2(2\pi)^{d-1}} \quad (4.94)$$

$$\begin{aligned} & \times \frac{2}{k^+(k^-)^{1+\eta}} \delta(k^2) \delta^{(2)}(\mathbf{k}_\perp + \mathbf{p}_\perp) \Theta_{\text{alg}} \\ & = + \frac{\alpha_s w^2 C_i}{\pi} \frac{e^{\gamma_E \epsilon}}{\Gamma(1-\epsilon)} \left( \frac{\nu r}{\mu} \right)^\eta \frac{1}{\eta} \frac{1}{2\pi \mu^2} \left( \frac{\mu^2}{\mathbf{p}_\perp^2} \right)^{1+\epsilon+\eta/2}. \end{aligned} \quad (4.95)$$

Here,  $\Theta_{\text{alg}}$  represents the application of a jet-algorithm, a set of Heaviside-theta functions which restricts particles to be within the jet radius  $R$ . We also use  $r \equiv \tan(R/2)$ , and  $C_q = C_F$ ,  $C_g = C_A$ . Expanding in  $\eta$  and subsequently expanding in  $\epsilon$  we find

$$\begin{aligned} S_C^{i,B}(\mathbf{p}_\perp, \mu, \nu) &= \delta^{(2)}(\mathbf{p}_\perp) + \frac{\alpha_s w^2 C_i}{\pi} \left\{ \frac{2}{\eta} \left( -\frac{1}{2\epsilon} \delta^{(2)}(\mathbf{p}_\perp) + \mathcal{L}_0(\mathbf{p}_\perp^2, \mu^2) \right) \right. \\ &+ \delta^{(2)}(\mathbf{p}_\perp) \left( \frac{1}{2\epsilon^2} + \frac{1}{2\epsilon} \ln \left( \frac{\mu^2}{r^2 \nu^2} \right) \right) - \mathcal{L}_0(\mathbf{p}_\perp^2, \mu^2) \ln \left( \frac{\mu^2}{r^2 \nu^2} \right) + \mathcal{L}_1(\mathbf{p}_\perp^2, \mu^2) \\ &\left. - \frac{\pi^2}{24} \delta^{(2)}(\mathbf{p}_\perp) \right\}. \end{aligned} \quad (4.96)$$

Having expanded both the collinear and collinear-soft pieces in  $\eta$  and  $\epsilon$ , we can now set the bookkeeping parameter to  $\omega \rightarrow 1$  and calculate the  $\overline{MS}$  renormalized collinear-soft function

$$\begin{aligned} S_C^{i,R}(\mathbf{p}_\perp, \mu, \nu) &= \delta^{(2)}(\mathbf{p}_\perp) \\ &- \frac{\alpha_s C_i}{\pi} \left\{ \mathcal{L}_0(\mathbf{p}_\perp^2, \mu^2) \ln \left( \frac{\mu^2}{r^2 \nu^2} \right) - \mathcal{L}_1(\mathbf{p}_\perp^2, \mu^2) + \frac{\pi^2}{24} \delta^{(2)}(\mathbf{p}_\perp) \right\}. \end{aligned} \quad (4.97)$$

Using the regulators outlined above, contributions to  $S_C$  from virtual gluon emission diagrams (not shown) are scaleless integrals that can be set to zero and all divergences are interpreted as being UV in origin. <sup>6</sup>

Having now defined the TMDFJF and performed a NLO perturbative calculation of the matching coefficients  $\mathcal{J}_{ij}(\mathbf{p}_\perp, z, \mu, \nu)$  we will, in Section 5.4, resum the TMDFJF to NLL order. Using standard Renormalization Group (RG) and Rapidity Renormalization Group techniques to resum potentially large logarithms of the  $\mathbf{p}_\perp$ , we will perform a comparison of the TMDFJF with Monte Carlo events generated in Pythia.

## 4.6 Alternative Definition of TMDFJF

As an alternative to defining TMDFJFs from the definition of TMDFFs, we can derive the TMDFJFs from a factorized cross-section in SCET that is differential in the energy fraction,  $z$ , of the jet's energy carried by the identified hadron and the hadron's transverse momentum  $\mathbf{p}_\perp^h$  with respect to the jet's axis. Ref. [1] showed that the cross-section for  $e^+e^- \rightarrow$  dijets can be, for jet functions where a jet substructure observabled is not measured, factorized according to

$$d\sigma \sim d\sigma^{(0)} \times H_2(\mu) \times S_\Lambda(\mu) \times J_n^q(\omega, \mu) \times J_n^{\bar{q}}(\omega, \mu), \quad (4.98)$$

where  $d\sigma^{(0)}$  is the Born cross section,  $H_2(\mu)$  is the hard function found from a matching calculation of a 2-jet operator in QCD onto SCET operators, and  $J_n(\omega, \mu)$  is a jet function that describes radiation collinear to a jet direction  $\hat{n}$ . This jet (which will contain the identified hadron  $h$ ) carries energy  $E_J = \omega/2 = E_{\text{cm}}$  and we restrict the radiation found outside of the jet radius  $R$  to be ultra-soft  $E_{\text{out}} < \Lambda$ . The jet

---

<sup>6</sup> Although not shown here, we explicitly performed the calculations using an alternative set of regulators where the virtual diagrams are not scaleless. When using a gluon mass, rapidity regulator, and a dimensional regulator (where the virtual diagrams are not scaleless) IR divergences properly cancelled and the result was identical to that shown above.

function can be written as

$$J_n^q(\omega, \mu) = \int \frac{dk^+}{2\pi} \int d^4x \exp(ik^+x^-/2) \frac{1}{N_C} \text{Tr} \left[ \frac{\not{\eta}}{2} \langle 0 | \delta_{\omega, \bar{\mathcal{P}}} \delta_{0, \mathcal{P}_\perp} \chi_n(x) \bar{\chi}_n(0) | 0 \rangle \right]. \quad (4.99)$$

In order to study jets that contain identified hadrons, let us consider the following instantiation of the identity

$$\mathbf{1} = \sum_X |X\rangle \langle X| = \sum_X \sum_{h \in \mathcal{H}_i} \int \frac{dz d^2 \mathbf{p}_\perp^h}{2(2\pi)^3} |Xh(z, \mathbf{p}_\perp^h)\rangle \langle Xh(z, \mathbf{p}_\perp^h)|. \quad (4.100)$$

The states  $|Xh(z, \mathbf{p}_\perp^h)\rangle$  describe hadrons  $h$  and any other particles  $X$  where  $h$  carries an energy fraction  $z$  of the energy and has transverse momentum component  $\mathbf{p}_\perp^h$  with respect to the sum of the momenta of  $X$  and  $h$ . We then sum/integrate over  $z$ ,  $p_\perp$ , particles  $X$ , and identified hadrons  $h$  of species  $\mathcal{H}_i$  with the appropriate phase space and combinatorial factors. Putting this identity into the jet function we find

$$J_n^q(\omega, \mu) = \sum_{h \in \mathcal{H}_i} \int \frac{dz d^2 \mathbf{p}_\perp}{2(2\pi)^3} \int \frac{dk^+}{2\pi} \int d^4x \exp(ik^+x^-/2) \frac{1}{N_C} \times \sum_X \text{Tr} \left[ \frac{\not{\eta}}{2} \langle 0 | \delta_{\omega, \bar{\mathcal{P}}} \delta_{0, \mathcal{P}_\perp} \chi_n(x) |Xh(z, \mathbf{p}_\perp)\rangle \langle Xh(z, \mathbf{p}_\perp) | \bar{\chi}_n(0) | 0 \rangle \right]. \quad (4.101)$$

Performing the integration over  $x$  (the Fourier conjugate of the residual momenta) and  $k^+$  yields

$$J_n^q(\omega, \mu) = \sum_{h \in \mathcal{H}_i} \int zdz d^2 \mathbf{p}_\perp \mathcal{G}_{q/h}(\mathbf{p}_\perp, z, \mu). \quad (4.102)$$

If we put this expression into Eq.(4.98) we find that

$$d\sigma = \sum_{h \in \mathcal{H}_i} \int zdz d^2 \mathbf{p}_\perp d\sigma^{(0)} H_2(\mu) \times S_\Lambda(\mu) \times \mathcal{G}_{q/h}(\mathbf{p}_\perp, z, \mu) \times J_n^{\bar{q}}(\omega, \mu). \quad (4.103)$$

This implies that we can write the differential cross-section  $d\sigma^{i/h}/dzd^2\mathbf{p}_\perp$  for the specific identified hadron  $h$  as

$$\frac{d\sigma^{i/h}}{dzd^2\mathbf{p}_\perp} = d\sigma^{(0)} H_2(\mu) \times S_\Lambda(\mu) \times \mathcal{G}_{q/h}(\mathbf{p}_\perp, z, \mu) \times J_n^{\bar{q}}(\omega, \mu) + \mathcal{O}\left(\frac{\Lambda}{E_J}, \frac{\Lambda_{\text{QCD}}^2}{p_\perp^2}\right). \quad (4.104)$$

This shows that the replacement rule

$$\frac{d\sigma^{i/h}}{dzd^2\mathbf{p}_\perp} = d\sigma \left[ J^i(\omega, \mu) \rightarrow \mathcal{G}_{i/h}(\mathbf{p}_\perp, z, \mu) \right] \quad (4.105)$$

holds when the transverse momentum of the identified hadron is measured.

# Applications to Quarkonia in Jets with Comparisons to Monte Carlo & Data

## 5.1 Introduction

Jets and heavy flavor production are high priorities at modern collider experiments as they provide critical tests of our understanding of QCD. In this chapter we explore the application of the FJF formalism introduced and developed in Chapter 4 to the production of heavy mesons and quarkonia. Our goal is to understand whether we can gain a better understanding of quarkonium production by studying how  $J/\psi$  are produced inside jets where the substructure of that jet has been measured using FJFs. Since FJFs can be matched onto specific FFs, this approach offers an opportunity to use jet substructure techniques to better understand fragmentation.

In Chapter 2, we introduced NRQCD, the modern theory of quarkonium production. While the study of quarkonium is difficult because of the multiple disparate energy scales involved, we explained how NRQCD provides a formalism where the FFs for the  $J/\psi$  can be calculated perturbatively at the scale  $m_{J/\psi}$ . Ref. [12] calculated the FJFs for the  $J/\psi$  production mechanisms that, according to NRQCD,

should dominate at high transverse momenta. They showed that the dependence of these  $J/\psi$  FJFs on  $z$ , the fraction of a jet’s energy carried by the  $J/\psi$ , and that jet’s energy  $E$ , could discriminate between the different  $J/\psi$  production mechanisms. This insight showed that FJFs could be used to develop a powerful new set of observables for testing the theory of quarkonium production.

This chapter will be organized as follows. In Section 5.2, we will calculate a NLL’ resummed cross-section for  $e^+e^- \rightarrow b\bar{b} \rightarrow$  dijets where one of the  $b(\bar{b})$  subsequently fragments into a  $B$  meson and the angularity of the the jet containing that  $B$  is measured.<sup>1</sup> Using the  $\mathcal{J}_{ij}(\tau_a, z, \mu)$  calculated in Chapter 4 and a phenomenological  $B$ -meson FF extracted from  $e^+e^-$  data, we will study the  $z$  and  $\tau_a$  dependence of the cross-section. We will then compare our analytic results with Monte Carlo simulations from Madgraph [135] + PYTHIA [136] and Madgraph + Herwig [137]. In both cases, we find reasonable agreement in both the  $z$  and  $\tau_a$  distributions, giving support to the angularity FJF formalism for calculating the  $z$  distribution and jet substructure.

In Section 5.3, we will study  $J/\psi$  production in  $e^+e^- \rightarrow 3$  jets events, again comparing analytic results from a resummed cross-section containing an angularity FJF with Monte Carlo simulations from PYTHIA. While analytic and Monte Carlo predictions are largely consistent for the substructure, they predict fundamentally different  $z$  distributions. We discuss how this discrepancy is due to Pythia’s unphysical handling of quarkonia in its parton shower model and its inability to fragment gluons directly into quarkonia in its hadronization model. We describe a way to reconcile analytic and monte carlo predictions by modifying PYTHIA’s handling of the showering of quarkonium states to make its model more closely resemble the picture of quarkonium production described by NRQCD. What we call Gluon-

---

<sup>1</sup> NLL’ means that the cross-section is resummed using the anomalous dimensions required for NLL accuracy and one-loop corrections to the jet, soft, etc. functions are included.

Fragmentation-Improved-PYTHIA brings analytic and Monte Carlo predictions into agreement.

In Section 5.4, we will study the contributions of different NRQCD production mechanisms to the overall distributions of the transverse momentum and angle of a  $J/\psi$  relative to the axis of a jet. We will do this using TMDFJFs, the extension of the FJF to transverse momentum dependent measurements developed in Section 4.5. We will demonstrate that the TMDFJFs have discriminating power between the different NRQCD color-singlet and color-octet production mechanisms for  $J/\psi$ .

Finally, in Section 5.5 we analyze recent LHCb measurements of the distribution of  $z(J/\psi)$ , the fraction of the transverse momentum carried by a  $J/\psi$  within a jet. We compare the data to analytic calculations using two distinct approaches. The first approach utilizes the GFIP method where hard scattering processes in Madgraph are showered using Pythia and the resulting quark/gluon energy distributions are then convolved with leading order NRQCD FFs. The second approach uses the FJF formalism where the energy of the jet is measured and the FJF is resummed to NLL' accuracy. These two approaches give consistent results and agree with LHCb measurements much better than the default PYTHIA predictions of Ref. [138]. We perform these comparisons for three different extractions of the NRQCD LDMEs and show that the data favor extractions from exclusively high transverse momentum data. The results of Sections 5.2 and 5.3 show results previously published by the author and collaborators in Ref. [36]. Sections 5.4 and 5.5 show results from Ref. [37, 38] (also published by the author), respectively.

## 5.2 $b$ Quark to $B$ Meson Fragmentation in $e^+e^- \rightarrow$ Dijets

As a test of our angularity FJF formalism, we first study  $e^+e^- \rightarrow b\bar{b}$  dijet events, where the  $b(\bar{b})$  fragments into a jet that contains a  $B(\bar{B})$  meson. Ref. [1] showed that, in SCET, the cross-section for dijet events where the angularity  $\tau_a$  of one of

the jets is probed can be written as

$$\frac{1}{\sigma_0} \frac{d\sigma}{d\tau_a} = H_2(\mu) \times S^{\text{unmeas}}(\mu) \times J_{\bar{n}}^{(\bar{b})}(\mu) \times \left[ S^{\text{meas}}(\tau_a, \mu) \otimes J_n^{(b)}(\tau_a, \mu) \right], \quad (5.1)$$

where  $H_2(\mu)$  is the hard function,  $S^{\text{unmeas}}(\mu)$  and  $S^{\text{meas}}(\tau_a, \mu)$  are unmeasured and measured soft functions, respectively,  $J_{\bar{n}}^{(\bar{b})}(\mu)$  is the jet function containing the  $\bar{b}$  quark that is not dependent on the angularity (e.g. the unmeasured jet function) and  $J_n^{(b)}(\tau_a, \mu)$  is the  $\tau_a$ -dependent measured jet function containing the  $b$  quark. Note that we will not explicitly write the functional dependence of these functions on scales other than the renormalization scale  $\mu$  for notational convenience. At NLO the unmeasured,  $\tau_a$ -independent functions are written as

$$\begin{aligned} H_2(\mu) &= 1 - \frac{\alpha_s(\mu)C_F}{2\pi} \left[ 8 - \frac{7\pi^2}{6} + \ln^2 \frac{\mu^2}{\omega^2} + 3 \ln \frac{\mu^2}{\omega^2} \right], \\ S^{\text{unmeas}}(\mu) &= 1 + \frac{\alpha_s(\mu)C_F}{2\pi} \left[ \ln^2 \frac{\mu^2}{4\Lambda^2} - \ln^2 \frac{\mu^2}{4\Lambda^2 r^2} - \frac{\pi^2}{3} \right], \\ J_{\bar{n}}^{(\bar{b})}(\mu) &= 1 + \frac{\alpha_s(\mu)C_F}{2\pi} J_{\text{alg}}^q(\mu), \end{aligned} \quad (5.2)$$

where  $\Lambda$  is a veto on the energy that is not contained within the jets,  $r \equiv \tan(R/2)$  and  $J_{\text{alg}}^q(\mu)$  is a jet function that depends on the jet-algorithm. This dependence is given explicitly in Eq. (A.18) of Ref. [1] and must be included for unmeasured jets, where (c.f. Section 4.4) there is no suppression of these terms by powers of  $\tau_a$  as was the case for measured jet functions/FJFs. In the analysis below we will use a cone algorithm.<sup>2</sup> Eq. (5.1) can be made into a cross-section for a jet with an identified hadron using the replacement rule shown in Eq. (4.3) and the factorized form of the

---

<sup>2</sup> So-called *non-global* logarithms of ratios such as  $Q\tau_a/(2\Lambda r^2)$  do appear at NNLO in the fixed order calculation [99] however these logarithms are not needed at NLL' accuracy and are not considered here.

FJF introduced in Eq. (4.4) such that

$$\begin{aligned} \frac{1}{\sigma_0} \frac{d\sigma^{(b)}}{d\tau_a dz} &= H_2(\mu) \times S^{\text{unmeas}}(\mu) \times J_{\bar{n}}^{(b)}(\mu) \\ &\times \sum_j \left[ \left( S^{\text{meas}}(\tau_a, \mu) \otimes \frac{\mathcal{J}_{bj}^{(b)}(\tau_a, z, \mu)}{2(2\pi)^3} \right) \bullet D_{j \rightarrow B}(z) \right], \end{aligned} \quad (5.3)$$

where  $\bullet$  and  $\otimes$  define two different convolutions

$$G(z) \bullet F(z) = F(z) \bullet G(z) \equiv \int_z^1 \frac{dx}{x} F(x) G\left(\frac{z}{x}\right), \quad (5.4)$$

and

$$f(\tau) \otimes g(\tau) = \int d\tau' f(\tau - \tau') g(\tau'). \quad (5.5)$$

In order to perform a resummation of this cross-section to NLL' accuracy, we must

1. Evaluate each piece of the factorization theorem at its *characteristic* scale. This is the scale at which the potentially large logarithms in that function are minimized.
2. Solve the appropriate renormalization group (RG) equations and calculate anomalous dimensions for each function.
3. Write down the evolution kernels for each function in order to evolve each piece of the factorization theorem from its characteristic scale to a common scale  $\mu$ . We will choose this scale to be the scale of the hard interaction.

The convolution integrals outlined above must be performed over the angularity of the measured soft function,  $S^{\text{meas}}$ , the matching coefficients  $\mathcal{J}_{ij}$  and the evolution kernel  $\Pi$ . Following the RG techniques outlined in Appendix C, this process will involve a convolution over  $\delta$  and plus distributions, for which we use the plus-function

techniques developed in Appendix D. Using specifically Eqs. (D.6-D.7), we can write the cross-section in the following generic form

$$\begin{aligned}
d\sigma(\tau_a, z) &\equiv \frac{1}{\sigma_0} \frac{d\sigma^{(b)}}{d\tau_a dz} = H_2(\mu_H) \times S^{\text{runmeas}}(\mu_\Lambda) \times J_{\bar{n}}^{(\bar{b})}(\mu_{J_{\bar{n}}}) \times \\
&\times \sum_j \left\{ \left( \frac{\Theta(\tau_a)}{\tau_a^{1+\Omega}} \right) \left[ \delta_{bj} \delta(1-z) (1 + f_S(\tau_a, \mu_{S^{\text{meas}}})) + f_{\mathcal{J}}^{bj}(\tau_a, z, \mu_{J_n}) \right] \bullet \frac{D_{j \rightarrow B}(z, \mu_{J_n})}{2(2\pi)^3} \right. \\
&\quad \left. \times \Pi(\mu, \mu_H, \mu_\Lambda, \mu_{J_{\bar{n}}}, \mu_{J_n}, \mu_{S^{\text{meas}}}) \right\}_+,
\end{aligned} \tag{5.6}$$

where the plus-distribution is defined in Eq. (D.3).<sup>3</sup> We define

$$\Omega(\mu_{J_n}, \mu_{S^{\text{meas}}}) = \omega_{J_n}(\mu, \mu_{J_n}) + \omega_{S^{\text{meas}}}(\mu, \mu_{S^{\text{meas}}}), \tag{5.7}$$

where the functions  $\omega_{J_n}$  and  $\omega_{S^{\text{meas}}}$  are given in Appendix C. The expression  $f_S$  is [1]

$$f_S(\tau, \mu) = -\frac{\alpha_s(\mu) C_F}{\pi} \frac{1}{1-a} \left\{ \left[ \ln \frac{\mu \tan^{1-a} \frac{R}{2}}{\omega \tau} + H(-1-\Omega) \right]^2 + \frac{\pi^2}{6} - \psi^{(1)}(-\Omega) \right\}, \tag{5.8}$$

and  $f_{\mathcal{J}}^{ij}$  are written in terms of the coefficients  $c_0^{ij}$ ,  $c_1^{ij}$  and  $c_2$  defined the previous chapter in Eq. (4.46) as

$$\begin{aligned}
f_{\mathcal{J}}^{ij}(\tau, z, \mu) &= T_{ij} \frac{\alpha_s(\mu)}{2\pi} \left( c_0^{ij}(z, \mu) + c_1^{ij}(z, \mu) \left( \ln \tau - H(-1-\Omega) \right) \right. \\
&\quad \left. + c_2 \delta_{ij} \delta(1-z) \left( \frac{(\ln \tau - H(-1-\Omega))^2 + \pi^2/6 - \psi^{(1)}(-\Omega)}{2} \right) \right).
\end{aligned} \tag{5.9}$$

In the above expressions,  $\psi^{(1)}$  is the di-gamma function and  $H$  is the harmonic number. The evolution kernel  $\Pi$  is written in terms of  $K_F(\mu, \mu_0)$  and  $\omega_F(\mu, \mu_0)$  in

---

<sup>3</sup> The plus function symbol outside of the outer bracket indicates that the plus prescription is applied to all  $\tau_a$ -dependent quantities, including any implicit dependencies arising from any choice of characteristic scales  $\mu_F$ .

accordance with the formalism introduced in Appendix C,

$$\Pi(\mu, \mu_H, \mu_\Lambda, \mu_{J_{\bar{n}}}, \mu_{J_n}, \mu_{S^{\text{meas}}}) = \prod_{F=H, J_{\bar{n}}, S^{\text{unmeas}}} \exp(K_F(\mu, \mu_F)) \left(\frac{\mu_F}{m_F}\right)^{\omega_F(\mu, \mu_F)} \quad (5.10)$$

$$\times \frac{1}{\Gamma(-\Omega(\mu_{J_n}, \mu_{S^{\text{meas}}}))} \quad (5.11)$$

$$\times \prod_{F=J_n, S^{\text{meas}}} \exp(K_F(\mu, \mu_F) + \gamma_E \omega_F(\mu, \mu_F)) \left(\frac{\mu_F}{m_F}\right)^{j_F \omega_F(\mu, \mu_F)},$$

where  $\mu_F$ ,  $m_F$  and  $j_F$  are the characteristic scales of each function. We summarize our choice of these scales in Table 5.1.

The  $\bullet$  convolutions in the energy fraction,  $z$ , in the above expressions must be evaluated numerically. We use the phenomenological  $B$ -meson FF extracted from  $e^+e^-$  data in Ref. [139] for the FF of the  $b$  quark into a  $B$  meson

$$D_{b \rightarrow B}(z, \mu = m_b = 4.5 \text{ GeV}) \sim z^\alpha (1-z)^\beta \quad \text{with} \quad \alpha = 16.87, \beta = 2.628. \quad (5.12)$$

The parameters of this FF were determined using a fit to LEP data in Ref. [140] for the inclusive process  $e^+e^- \rightarrow B + X$  where  $\chi_{d.o.f.}^2 = 1.495$ .

We do not give errors on these FF parameters as Ref. [140] provided no errors associated with the extraction. We also neglect the contribution from other fragmenting partons for our  $e^+e^-$  collider studies as in Ref. [140]. At the LHC, gluon FJFs will play a prominent role since  $gg \rightarrow gg$  dijet events give a significant contributions to the production of jets containing heavy flavor [108]. As done in Ref. [12], these FFs are evolved using the associated DGLAP equations.

Fig. 5.1 shows the  $z$  distributions of  $d\sigma(\tau_0, z)$  for  $\tau_0 = (1.5, 2.0, 2.5) \times 10^{-3}$  from our resummed analytic calculation (green) and Monte Carlo simulations using Madgraph + PYTHIA (black) and Madgraph + Herwig (red). For each analytic and Monte Carlo distribution, the graphs are independently normalized such that the area is 1. For these fixed  $\tau_a$  plots we use a  $z$ -bin of  $\pm 0.1$ . Jets are reconstructed in

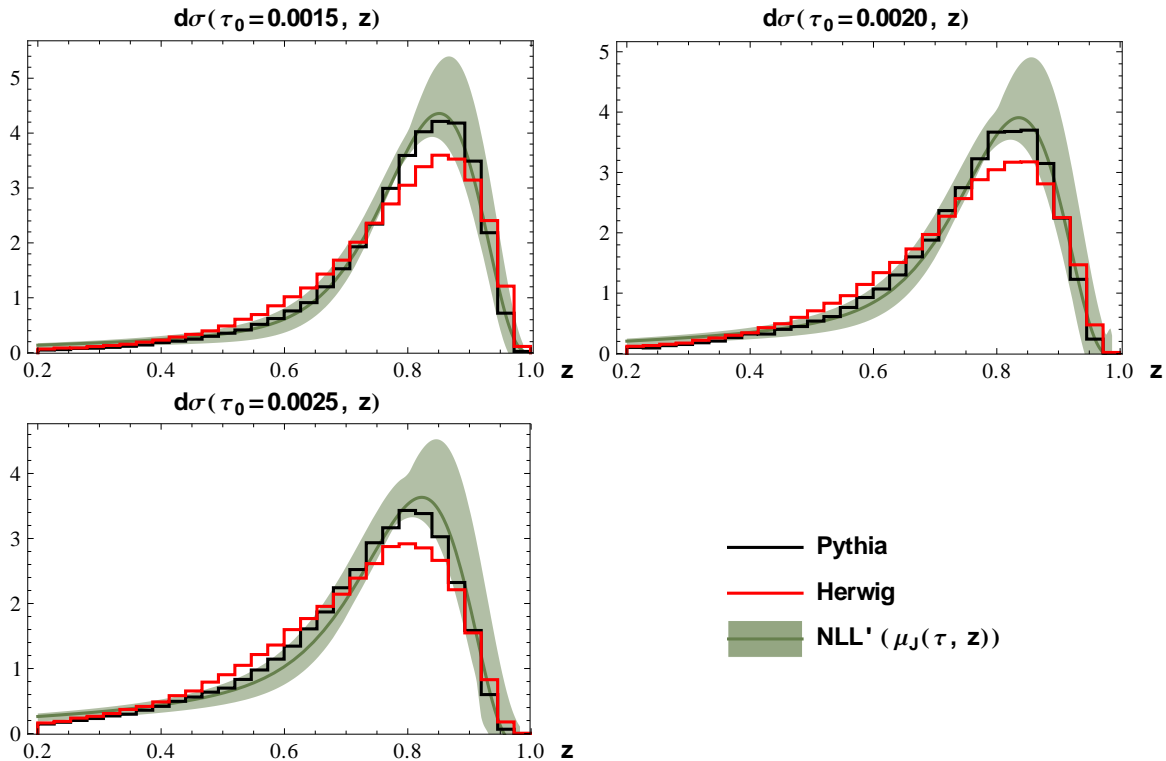


FIGURE 5.1: The  $z$  distributions for  $d\sigma(\tau_0, z)$  at  $\tau_0 = (1.5, 2.0, 2.5) \times 10^{-3}$  for analytic calculations with theoretical uncertainties (from varying the scale  $\mu$  up and down by a factor of 2) are shown in green. Monte Carlo simulations using Madgraph + PYTHIA and Madgraph + Herwig are shown as black and red lines, respectively.

PYTHIA using the Seedless-Infrared-Safe Cone (SISCONE) algorithm in the FastJets package [141] with jet-size parameter  $R = 0.6$ . We simulate  $e^+e^- \rightarrow$  dijet events at  $E_{cm} = 250$  GeV in which each jet has an energy of at least  $(E_{cm} - \Lambda)/2$  where  $\Lambda = 30$  GeV.<sup>4</sup>

The central line of the green curve in Fig. 5.1 corresponds to the analytic calculation with each piece of the factorization theorem evaluated at the characteristic scales listed in Table 5.2. The green band shows an estimate of theoretical uncertainty. For the unmeasured functions, this is calculated by varying the characteristic of these functions by  $\pm 50\%$ . For the measured functions, the uncertainty is cal-

<sup>4</sup> This is different than simply placing a cut  $\Lambda$  on energy outside the jets as we do in our analytic calculations. The difference between these two methods is an  $O(\alpha_s^2)$  effect in the soft function, and thus is beyond the scope of this NLO calculation.

Function ( $F$ )	$H_2$	$J_{\bar{n}}^b$	$S^{\text{unmeas}}$	$\mathcal{J}(\tau, z)$	$S^{\text{meas}}(\tau)$
Scale ( $\mu_F$ )	$E_{\text{cm}}$	$\omega_{\bar{n}} r$	$2\Lambda r^{1/2}$	$\omega_n \tau^{1/(2-a)} (1-z)^{(1-a)/(2-a)}$	$\omega_n \tau / r^{1-a}$
$m_F$	$\omega$	$w_{\bar{n}} r$	$2\Lambda r^{1/2}$	$\omega_n$	$\omega_n / r^{1-a}$
$j_F$	1	1	1	$2-a$	1

Table 5.1: The characteristic scales of each piece of the factorization theorem shown in Eq. (5.1). The scales minimize potentially large logarithms in each function.

culated using profile functions [83, 133, 142]. Profile functions provide a systematic way of introducing a scale variation that depends on the value of the angularity. This allows us to avoid poles in the  $\tau_a$  distributions by enforcing that angularity dependent scale freezes at the characteristic scale for high values of  $\tau_a$  (where the factorization theorem breaks down anyway) and at a fixed scale for small values of  $\tau_a$  (where we reach the non-perturbative regime). This method of estimating the theoretical uncertainty is used throughout this work. Additional details on these profile functions are provided in Appendix D. By using the following two plus-distribution integral identities

$$\int_z^1 \frac{dx}{x} \left( \frac{1}{1-x} \right)_+ f\left(\frac{z}{x}\right) = \int_z^1 dx \frac{1}{1-x} \left( \frac{1}{x} f\left(\frac{z}{x}\right) - f(z) \right) + f(z) \ln(1-z), \quad (5.13)$$

and

$$\int_z^1 \frac{dx}{x} \left( \frac{\ln(1-x)}{1-x} \right)_+ f\left(\frac{z}{x}\right) = \int_z^1 dx \frac{\ln(1-x)}{1-x} \left( \frac{1}{x} f\left(\frac{z}{x}\right) - f(z) \right) + f(z) \frac{1}{2} \ln^2(1-z), \quad (5.14)$$

we can re-write the convolutions of the  $D(z)$  with  $f_{\mathcal{J}}^{ij}(\tau, z, \mu)$  as

$$\begin{aligned} \frac{1}{T_{ij}} \frac{2\pi}{\alpha_s(\mu)} f_{\mathcal{J}}^{ij}(\tau, z, \mu) \bullet D(z) &= \delta_{ij} f_1(\tau, z, \mu) D(z) \\ &\quad - \int_z^1 dx f_2(\tau, x, \mu) \left( \frac{\bar{P}_{ji}(x)}{x} \circ D\left(\frac{z}{x}\right) \right) \\ &\quad + \int_z^1 dx \left[ c_{ij}(x) - \frac{1}{1-a/2} \ln \left( 1 + \left( \frac{1-x}{x} \right)^{1-a} \right) \frac{\bar{P}_{ji}(x)}{x} \right] \circ D\left(\frac{z}{x}\right), \end{aligned} \quad (5.15)$$

where

$$f_2(\tau, z, \mu) = 2 \ln \left( \frac{\mu}{\mu_J(\tau, z)} \right) + \frac{1}{1 - a/2} H(-1 - \Omega), \quad (5.16)$$

with

$$\mu_J(\tau, z) = \omega \tau^{1/(2-a)} (1 - z)^{(1-a)/(2-a)},$$

$$f_1(\tau, z, \mu) = \frac{1 - a/2}{1 - a} \left( f_2(\tau, z, \mu) \right)^2 + \frac{a(1 - a/4)}{(1 - a)(1 - a/2)} \frac{\pi^2}{6} - \frac{1}{(1 - a)(1 - a/2)} \psi^{(1)}(-\Omega), \quad (5.17)$$

$$\begin{aligned} c_{qq}(z) &= \frac{1 - z}{z}, \\ c_{gg}(z) &= 0, \\ c_{gq}(z) &= 2(1 - z), \\ c_{qg}(z) &= 1, \end{aligned}$$

and

$$\begin{aligned} f(x) \circ g(x) &= f(x)g(x), \\ [f(x)(h(x))_+] \circ g(x) &= h(x)[f(x)g(x) - f(1)g(1)]. \end{aligned}$$

Fig. 5.2 shows the differential cross section as a function of  $z$  for fixed  $\tau_0$  where the measured jet characteristic scale is chosen in two different ways

$$\text{(Orange Line)} \quad \rightarrow \quad \mu_J(\tau) = \mu_J(\tau, z = 0) = \omega \tau^{1/(2-a)} \quad (5.18)$$

$$\text{(Green Line)} \quad \rightarrow \quad \mu_J(\tau, z) = \omega \tau^{1/(2-a)} (1 - z)^{(1-a)/(2-a)} \quad (5.19)$$

where the orange plot is calculated with a scale independent of  $z$  and the green plot is calculated with the same characteristic scale choice as the green band in Fig. 5.1 that depends on  $z$ . Fig. 5.2 clearly shows that the choice of a  $z$  dependent scale  $\mu_J(\tau, z)$  gives smaller estimated errors near the peak of the  $z$  distribution.

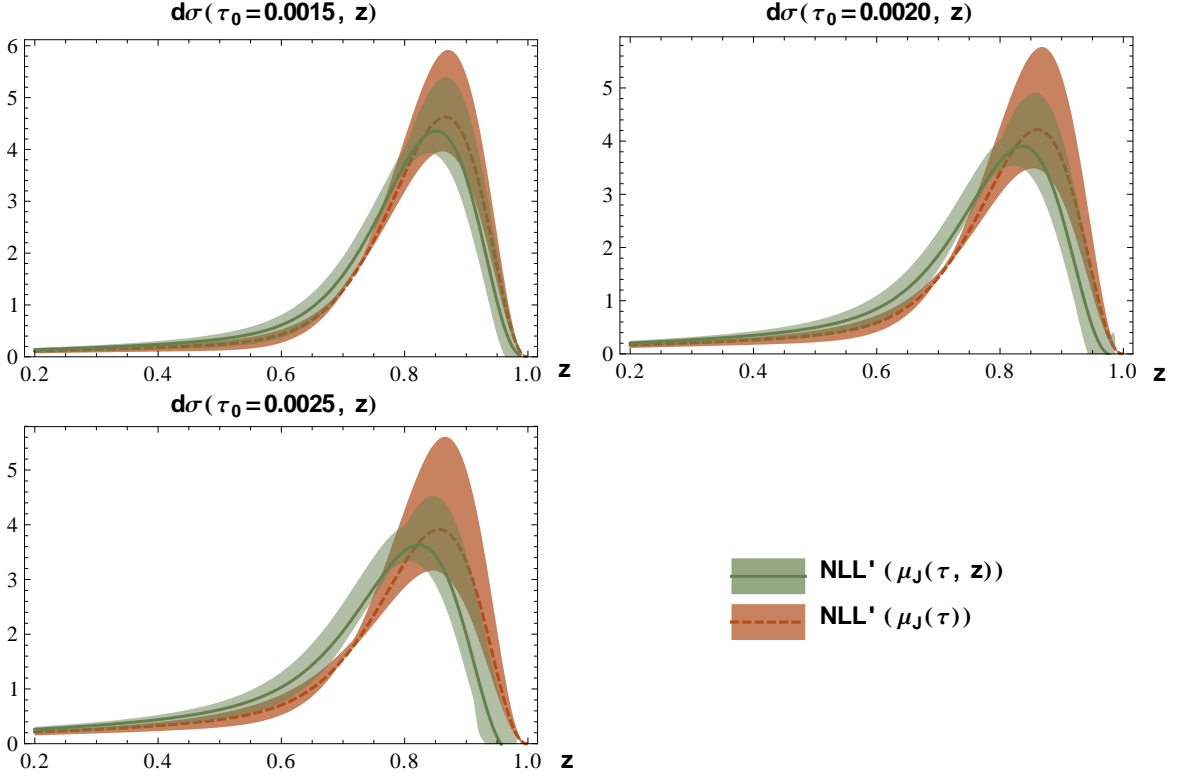


FIGURE 5.2: Analytic results for the  $z$  distributions of  $d\sigma(\tau_0, z)$  at  $\tau_0 = (1.5, 2.0, 2.5) \times 10^{-3}$ . The orange curve is calculated using characteristic scale for the measured jet function does not depend on  $z$  whereas the green curve uses a scale that does depend on  $z$  (as in Fig. 5.1).

In Fig. 5.3 we present the results for the  $\tau_0$  distributions of the differential cross section  $d\sigma(\tau_a, z)$  for  $z = 0.4, 0.6, \text{ and } 0.8$  where we use a  $\tau_a$  bin of  $\pm 2 \times 10^{-4}$ . The colors and normalizations are consistent with those used in Fig. 5.1. Notice that for high values of  $z$  the  $\tau_0$  distributions are shifted towards smaller values. This makes intuitive sense and was expected, since the majority of the energy of the jet in the  $z \rightarrow 1$  regime is carried by the B meson resulting in more narrow jets. Figs. 5.1 and 5.3 show that our results are consistent (within the uncertainty bands) with Monte Carlo simulations, whose uncertainty can be roughly estimated by taking the difference between the PYTHIA and Herwig predictions. Ultimately, this study of  $e^+e^- \rightarrow b\bar{b} \rightarrow \text{dijets}$  gives us confidence that NLL' resummed analytic calculations

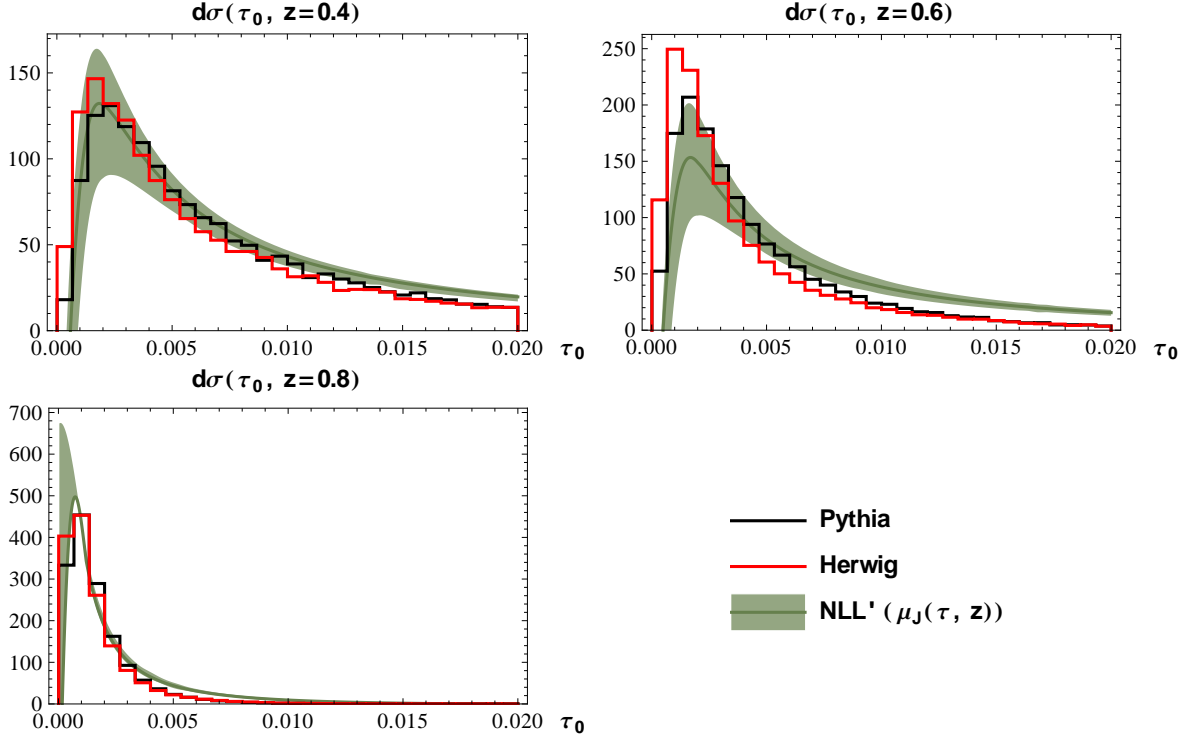


FIGURE 5.3: Angularity distributions of  $d\sigma(\tau_a, z)$  for  $a = 0$  at  $z = 0.4, 0.6, 0.8$ . Analytic results are shown as green bands. Monte Carlo results are shown as black lines for Madgraph + PYTHIA and red lines for Madgraph + Herwig.

using the FJF formalism can reliably be used to calculate both the substructure of a jet as well as the distribution of an identified hadron's energy fraction within that jet.

### 5.3 Gluon to $J/\psi$ Fragmentation in $e^+e^- \rightarrow 3$ Jets

In this section, will use the FJF formalism to calculate an NLL' resummed cross-section for  $e^+e^- \rightarrow 3$  jets where one of the jets, whose angularity is measured, contains a  $J/\psi$  produced via gluon fragmentation. We will compare these results with Monte Carlo predictions, discuss key discrepancies in the  $z$  distributions, and show how modifications to PYTHIA's method of producing  $J/\psi$  can bring its predictions of the  $z$  distributions into agreement with analytic predictions calculated using FJFs. In order to calculate a true physically observable quantity, we must include

contributions from all types of jets fragmenting to  $J/\psi$ . However, we expect gluon fragmentation mechanisms to dominate at high  $p_T$  at hadron colliders. It is theoretically possible to isolate gluon-initiated jets using jet substructure or  $B$ -tagging techniques in processes such as  $e^+e^- \rightarrow b\bar{b}g$ . The NLL' resummed cross-section for this process can be written as

$$\begin{aligned} \frac{1}{\sigma_0} \frac{d\sigma^{(g)}}{d\tau_a dz} &= H_3(\mu_H) \times S^{\text{unmeas}}(\mu_\Lambda) \times J_{n_1}^{(\bar{b})}(\mu_{J_{n_1}}) \times J_{n_2}^{(b)}(\mu_{J_{n_2}}) \\ &\times \sum_i \left\{ \left( \frac{\Theta(\tau_a)}{\tau_a^{1+\Omega}} \right) \left[ \delta_{gi} \delta(1-z)(1 + f_S(\tau_a, \mu_{S^{\text{meas}}})) + f_{\mathcal{J}}^{gi}(\tau_a, z, \mu_{J_{n_3}}) \right] \bullet \frac{D_{i \rightarrow J/\psi}(z, \mu_{J_{n_3}})}{2(2\pi)^3} \right. \\ &\quad \left. \times \Pi(\mu, \mu_H, \mu_\Lambda, \mu_{J_{n_1}}, \mu_{J_{n_2}}, \mu_{J_{n_3}}, \mu_{S^{\text{meas}}}) \right\}_+, \end{aligned} \quad (5.20)$$

where we define the exponent  $\Omega$  as

$$\Omega \equiv \Omega(\mu_{J_{n_3}}, \mu_{S^{\text{meas}}}) = \omega_{J_n}(\mu, \mu_{J_{n_3}}) + \omega_{S^{\text{meas}}}(\mu, \mu_{S^{\text{meas}}}), \quad (5.21)$$

and the  $b$ -quark initiated jets  $J_{n_1}^{(b)}$  and  $J_{n_2}^{(\bar{b})}$  are unmeasured. The  $f_S$  term is the same as Eq. (5.8) with the replacement  $C_F \rightarrow C_A$  and the  $f_{\mathcal{J}}^{ij}$  are written in terms of  $c_0^{ij}$ ,  $c_1^{ij}$  and  $c_2$  given in Eq. (4.46).  $\sigma_0$  is the Born cross section for the process  $e^+e^- \rightarrow b\bar{b}g$ . Our calculation will restrict the final state partons to be in the Mercedes-Benz configuration in which all three jets have approximately the same energy. We also require that the jets have energies large enough such that  $b$ -quark mass  $m_b$  can be neglected. The hard function piece  $H_3(\mu)$  takes the form  $1 + \mathcal{O}(\alpha_s)$  where we do not include the  $\mathcal{O}(\alpha_s)$  corections which come from the NLO virtual diagrams in  $e^+e^- \rightarrow b\bar{b}g$ . Omitting these corrections will affect the overall normalization of the cross-section, which will not be important for our discussion of the  $z$  and  $\tau_a$  distributions.

As discussed in Chapter 2, the FFs for  $J/\psi$  production can be calculated in NRQCD [60]. Refs. [9, 54, 143, 144] showed that FFs for the various  $J/\psi$  production

mechanisms can be calculated in terms of analytically calculable functions of  $\alpha_s(2m_c)$ ,  $z$ , and non-perturbative LDMEs to be obtained via fits to data. Recall that NRQCD dictates that  $J/\psi$  production consists of the perturbative creation of a  $c\bar{c}$  pair in a color and angular momentum state  $n = {}^{2S+1}L_J^{[1,8]}$  and the subsequent non-perturbative evolution of these  $c\bar{c}$  into physical, color-singlet  $J/\psi({}^3S_1^{[1]})$ . In the leading-power NRQCD approximation, the primary contributions to  $J/\psi$  production come from single parton fragmentation into color-singlet  ${}^3S_1^{[1]}$ , and color-octet  ${}^1S_0^{[8]}$ ,  ${}^3S_1^{[8]}$ , or  ${}^3P_J^{[8]}$  modes.

In Chapter 2, we discussed several different extractions of the LDMEs that have been performed in the literature. In this section, the LDMEs are taken to be the central values from the global fits performed in Refs. [14, 15], which are quoted in Table 2.1. Recall that, in NRQCD, color-octet mechanisms are suppressed by a factor of  $v^4$  relative to the color-singlet mechanism where  $v$  is the relative velocity of the  $c\bar{c}$  pair and has a typical value of  $v_c \sim 0.3$  [60].<sup>5</sup> This relative  $v^4$  suppression of the color-octet mechanisms is reflected in the numerical values of the LDMEs in Table 2.1. In the gluon FF to  $J/\psi$ , this relative  $v^4$  suppression is, however, compensated by powers of  $\alpha_s$  in the color-singlet channel. The leading color-octet contributions scale as  $O(\alpha_s^2)$  for the  ${}^1S_0^{(8)}$  and  ${}^3P_J^{(8)}$  channels and  $O(\alpha_s)$  in the  ${}^3S_1^{(8)}$  channel. The color-singlet contribution scales as  $O(\alpha_s^3)$ .

We will now calculate the gluon FJFs for each of the four production mechanisms mentioned above. Each FF will be evolved from the scale  $\mu = 2m_c$  to the characteristic scale of the measured jet  $\mu_{J_{n_3}}(\tau_a) = \omega\tau_a^{1/(2-a)}$  using the DGLAP evolution equations which are solved using Mellin transforms (as done in, for example, Appendix A of Ref. [12]). For most values of  $z$  considered in this section, a  $z$  dependent measured jet characteristic scale (as was used for  $B$  meson production in the

---

<sup>5</sup> The  ${}^3S_1^{[1]}$  scales as  $v^3$  and the octet mechanisms as  $v^7$ .

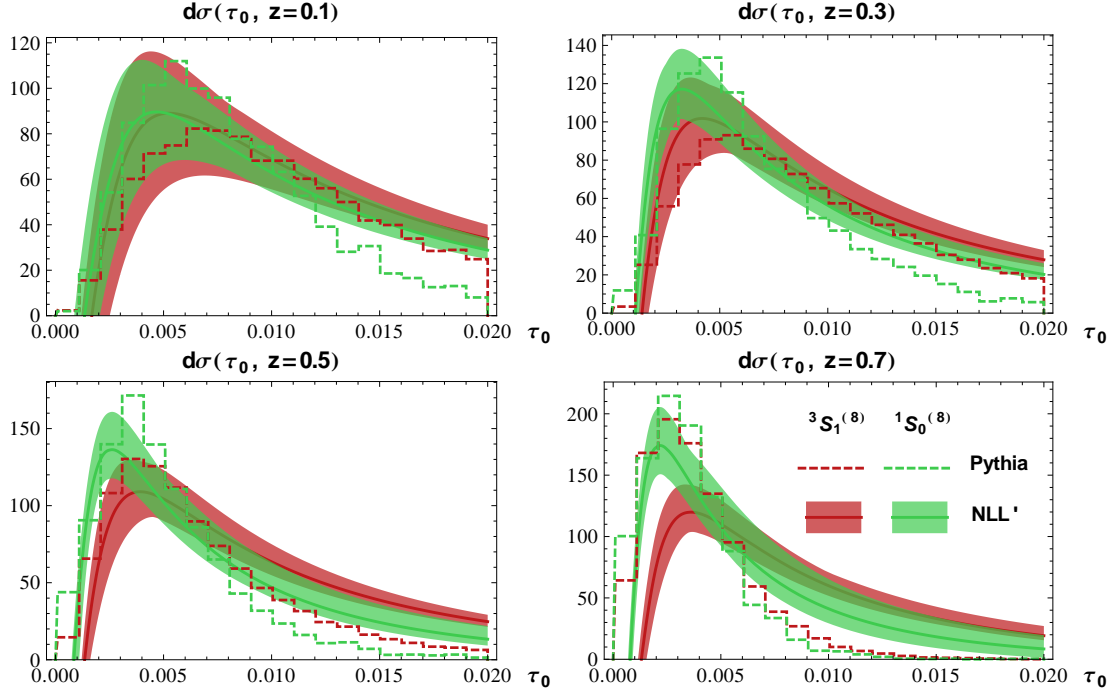


FIGURE 5.4: Angularity distributions of  $d\sigma(\tau_a, z)$  for  $a = 0$  at  $z = 0, 1, 0.3, 0.5, 0.7$ . Analytic calculations are shown as red (green) bands for the  ${}^3S_1^{(8)}$  ( ${}^1S_0^{(8)}$ ) production mechanisms. Results from Madgraph + PYTHIA are shown as red (green) dashed lines for the same mechanisms.

previous section) will not significantly improve scale-associated uncertainties. Since the  $z$  dependent scale also results in negative values for the  ${}^3P_J^{(8)}$  FF, we will not use such a scale choice in this section. After evolution, we perform the convolution  $[D \bullet f_{\mathcal{J}}](z)$  in  $z$  with the  $\mathcal{J}_{ij}$  matching coefficients derived in Chapter 4.

Fig. 5.4 shows the NLL' resummed analytic and simulated results from Madgraph + PYTHIA for the differential cross-section as a function of  $\tau_0$  for various fixed values of  $z$  for the  ${}^3S_1^{(8)}$  (red) and  ${}^1S_0^{(8)}$  (green) production mechanisms. We see fairly good agreement between analytic and Monte Carlo results in the peak regions at low  $z$  and notice some qualitative differences in the tail regions, especially for the  ${}^1S_0^{(8)}$  channel. At higher values of  $z$ , where the number of final state particles is smaller, differences in the  $\tau_0$  distributions can be attributed to PYTHIA's model of quarkonium production, which we will soon see is unrealistic. As  $z \rightarrow 0$ , we also

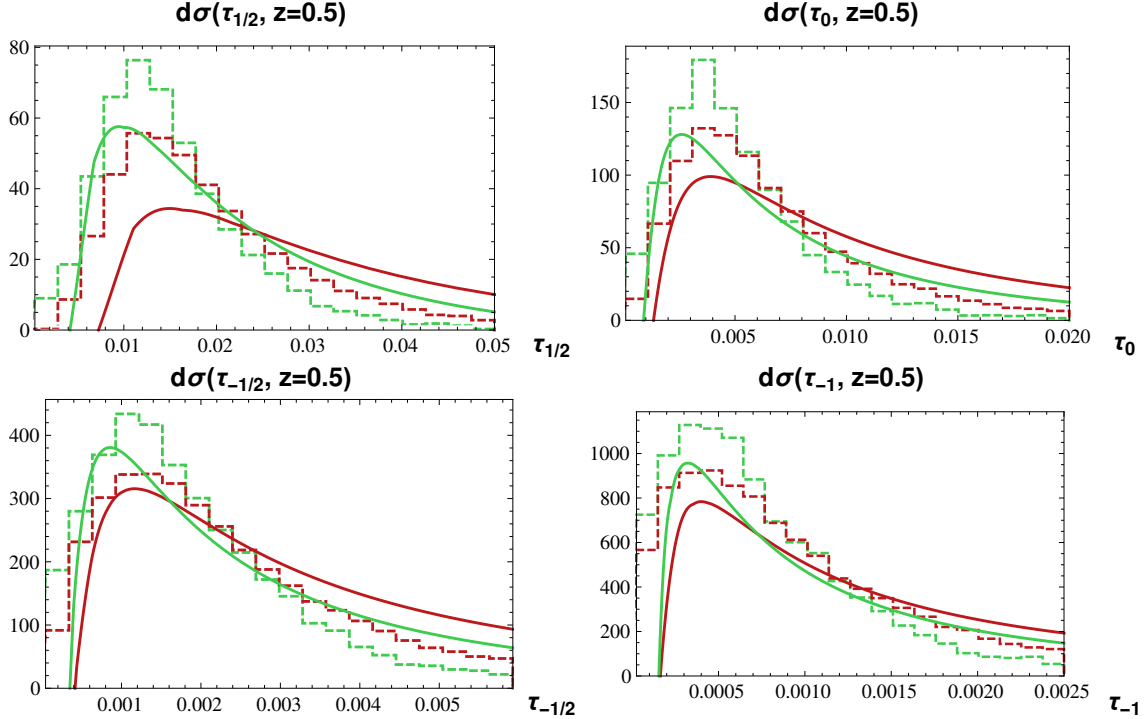


FIGURE 5.5: Angularity distributions of  $d\sigma(\tau_a, z)$  for  $a = +1/2, 0, -1/2, -1$  at  $z = 0.5$ . Analytic calculations are shown as red (green) solid lines for the  ${}^3S_1^{(8)}$  ( ${}^1S_0^{(8)}$ ) production mechanisms. Results from Madgraph + PYTHIA are shown as red (green) dashed lines for the same mechanisms.

see similar  $\tau_0$  dependence in the two analytic distributions. This suggests that at small  $z$ , the jet substructure is independent of the production mechanism. Thus, any attempts to use angularity distributions to extract the various LDMEs should focus on the range  $0.3 < z < 0.7$ .

Fig. 5.5 shows the  $\tau_0$  distributions for the  ${}^1S_0^{(8)}$  and  ${}^3S_1^{(8)}$  mechanisms for different values of the angularity parameter  $a = +1/2, 0, -1/2, -1$ , shown here without scale uncertainties so as reduce clutter in the plot. We see reasonably good agreement between analytic results and PYTHIA. As  $a$  is decreased, we also see less discrimination between the two production mechanisms. Any extraction of LDMEs using angularity should thus be done with larger values of  $a$ , for  $a < 1$  where SCET<sub>I</sub> factorization holds, with the caveat that the analytic results are less robust as  $a \rightarrow 1$  since power

corrections grow as  $1/(1 - a)$  [95].

In contrast to the angularity distributions, Fig. 5.8 shows that analytic and Monte Carlo calculations of the  $z$  distributions using Madgraph + PYTHIA yield strikingly different results, with the Monte Carlo yielding a much harder  $z$ -distribution. This discrepancy is due to PYTHIA utilizing an unphysical picture of quarkonium production that is in need of significant modifications. We will describe two approaches to simulating the production of  $J/\psi$  in jet events:

1. **Default Pythia** — Out-of-the-box implementation of MadOnia package of Madgraph. MadOnia generates color-singlet and color-octet  $c\bar{c}$  pairs such as  $e^+e^- \rightarrow b\bar{b}c\bar{c}[^3S_1^{(8)}]$  hard scale events using NRQCD FFs. These events are then showered and hadronized into multi-jet events containing  $J/\psi$  using PYTHIA’s default handling of onia states.
2. **Gluon Fragmentation Improved Pythia (GFIP)** — A modification of PYTHIA that takes hard scale partonic processes from Madgraph such as  $e^+e^- \rightarrow b\bar{b}g$ , uses PYTHIA’s parton shower to evolve the events down to where the gluon virtuality is  $2m_c$  and then convolves the resulting gluon energy distributions with NRQCD FFs by hand.

We will describe these two processes and their results below in detail. Additionally, Figs. 5.6 and 5.7 show diagrammatic representations of how each of these methods handles the showering/fragmentation of octet-onia states.

In the default PYTHIA approach, we first use Madgraph to generate  $e^+e^- \rightarrow b\bar{b}ggc\bar{c}[^3S_1^{(1)}]$ ,  $e^+e^- \rightarrow b\bar{b}gc\bar{c}[^1S_0^{(8)}]$ , and  $e^+e^- \rightarrow b\bar{b}c\bar{c}[^3S_1^{(8)}]$ . Madgraph offers flexibility and control over the selection and phase-space constraints of the hard-scale process, which makes it easier to use for generating hard processes than PYTHIA. We restrict our processes to diagrams in which a virtual photon couples to the  $b\bar{b}$ . This mandates that  $c\bar{c}$  pairs plus any additional gluons come from the decay of a

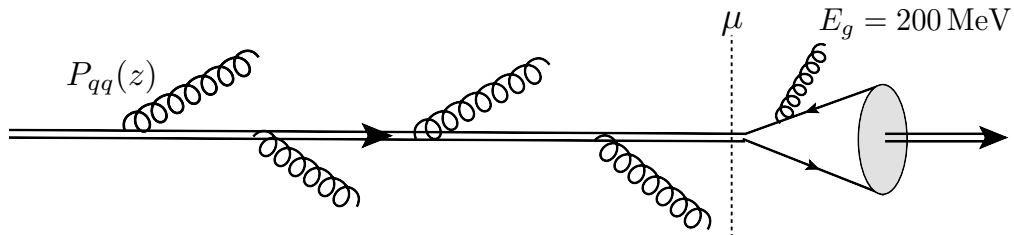


FIGURE 5.6: A diagrammatic representation of how default PYTHIA handles the showering of octet-onia states, via gluon emissions from a  $c\bar{c}$  state with probability  $2P_{qq}(z)$ . This creates an energy distribution that is, ultimately, much harder than analytic calculations due to the structure of  $P_{qq}$  splitting function.

virtual gluon. We did not simulate  ${}^3P_J^{(8)}$  channel events in  $e^+e^- \rightarrow b\bar{b}g \rightarrow b\bar{b}c\bar{c}g$  because IR divergences in the matrix elements require much longer running times to get the same number of events. We then shower and hadronize these hard processes using PYTHIA. Analysis is done using Rivet [145]. We require that after showering there are three jets in the event, two produced from the  $b$ -quarks and one from a gluon, which must also contain the  $J/\psi$ . We produce these three-jet events at  $E_{cm} = 250$  GeV in the Mercedes-Benz configuration by restricting jet energies via  $E_{jet} > (E_{cm} - \Lambda)/3$  with  $\Lambda = 30$  GeV, analogous to what was done in the previous section.

During PYTHIA's parton shower phase, color-singlet  $J/\psi$  do not radiate gluons. Thus, if one produces a  $J/\psi$  via the  ${}^3S_1^{[1]}$  intermediate  $c\bar{c}$  state within a jet, all surrounding in-jet radiation is due to the other colored particles in the event [136, 146]. This causes a large majority of these onia to have  $z \approx 1$ . PYTHIA allows the color-octet  $c\bar{c}$ , on the other hand, to emit gluons with a splitting function  $2P_{qq}(z)$ . Since  $P_{qq}(z)$  is peaked at  $z = 1$ , the color-octet  $c\bar{c}$  pair typically retains most of its energy after these emissions (c.f. Fig. 5.6). This showering model is quite different than the picture of a resummed analytic calculation.

In our NLL' calculation, the FF is calculated at the scale  $2m_c$ , then evolved up to the jet energy scale using the DGLAP equations. Since this is a gluon FF, the most important splitting kernel in this evolution is  $P_{gg}(z)$ . The resulting evolved FFs are not significantly changed if we use only this evolution kernel and ignore mixing with quarks. Thus our analytic calculation describes a highly energetic gluon produced in the hard process with virtuality of order the jet energy scale, which then showers by emitting gluons until one of the gluons, at a virtuality  $\sim 2m_c$ , hadronizes into the  $J/\psi$  (c.f. Fig. 5.7). Because  $P_{gg}(z)$  is peaked at both  $z = 0$  and  $z = 1$ , the  $z$  distribution of the  $J/\psi$  is much softer than the default PYTHIA prediction (c.f. the dashed colored lines in Fig. 5.8).

While PYTHIA allows the user to modify the color-factor in front of the splitting functions via “TimeShower:octetOniumColFac” parameter, the splitting function cannot be changed without fundamental programming changes to PYTHIA’s parton shower model. In an attempt to soften default PYTHIA’s  $z$  distributions, we changed this color-factor coefficient parameter in PYTHIA for a gluon radiating off a color-octet  $c\bar{c}$  pair from  $2P_{qq}$  to  $C_A P_{qq} = 3P_{qq}$ . While this resulted in a slighter softer  $z$  distribution than the default settings, it still described an unphysical evolution and was inconsistent with our analytic predictions.

We note that this change did not have significant impact on the  $\tau_a$  distributions. The  $\tau_a$  distribution predictions of PYTHIA are generally in better agreement with analytic predictions. The variable  $\tau_a$  depends on all of the hadrons in the jet and is therefore less sensitive to the behavior of the  $J/\psi$ . This is especially true when the  $J/\psi$  carries a small fraction of the jet energy (small  $z$ ), which can be seen in Fig. 5.4 where the analytic  $\tau_a$  distributions look similar for different color-octet mechanisms.

In an attempt to reconcile the analytic predictions with default PYTHIA’s  $z$  distributions, we developed a procedure for modifying PYTHIA called Gluon-Fragmentation-Improved PYTHIA (GFIP). GFIP aims to make PYTHIA’s picture of quarkonium

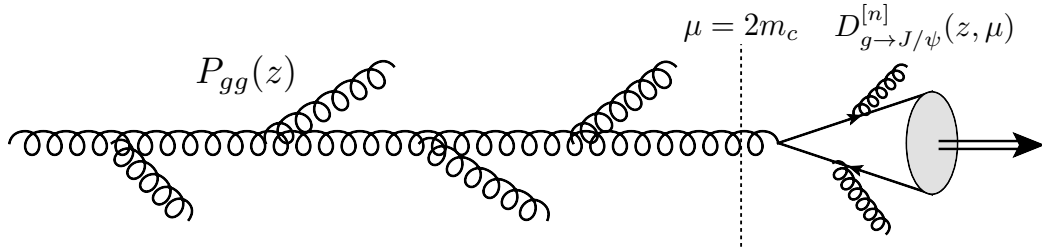


FIGURE 5.7: A diagrammatic representation of how gluon-fragmentation-improved-PYTHIA (GFIP) handles the showering and hadronization of quarkonium states, by mimicing our analytic picture of the evolution and fragmentation of a gluon. A hard-scale gluon is showered down by PYTHIA to the scale  $\sim 2m_c$ . The final state gluon energy distribution is then convolved with the leading-power NRQCD gluon FFs.

production fall more in line with the physical picture underlying our NLL' calculation. We generate  $e^+e^- \rightarrow b\bar{b}g$  events in Madgraph and allow PYTHIA to shower but not hadronize the events. The parton shower evolves the hard-scale partons from the jet-energy scale down to a scale where the typical invariant mass of a gluon is  $\sim 2m_c$ . GFIP then convolves the resulting gluon energy distribution with the NRQCD FFs calculated at this scale, which we expect will soften default PYTHIA's  $z$  distributions and bring them closer to our NLL' resummed predictions.

The lower cutoff scale in PYTHIA's parton shower is set by "TimeShower:pTmin," a parameter that sets the minimum virtuality of the particles in the shower before the hadronization phase is started. GFIP changes "TimeShower:pTmin" from the default value of  $p_T^{\min} = 0.4$  GeV to  $p_T^{\min} = 1.6$  GeV which can be shown to correspond to a virtuality of roughly  $2m_c$ . This comes from the basic kinematics of the parton shower where one can show that in a basic  $a \rightarrow bc$  splitting that  $(p_T^{\min})^2 \sim z(1-z)m^2$  where  $m$  is the mass of the fragmenting parton  $a$  and  $p_{\perp}$  is the magnitude of the transverse momentum of  $b, c$ . GFIP then obtains a  $z$  distribution for the gluons by randomly choosing a gluon from the gluon initiated jet and numerically convolving

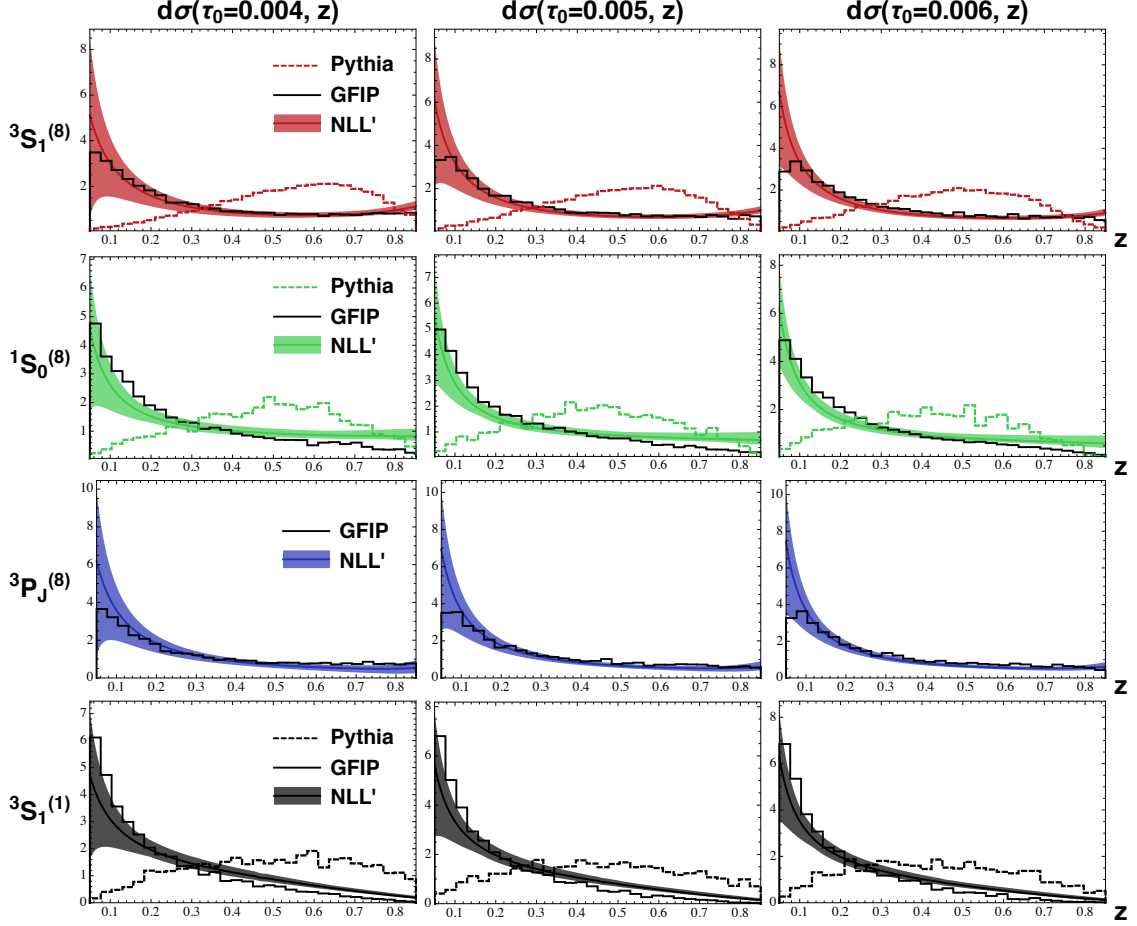


FIGURE 5.8:  $z$  distributions of  $d\sigma(\tau_a, z)$  for NLL' analytic calculations (colored bands), PYTHIA (colored dashed lines), and GFIP (solid black lines) for fixed values of  $\tau_0 = (4, 5, 6) \times 10^{-3}$ .

this  $z$  distribution with the analytic expressions for the NRQCD FFs. As illustrated in Fig. 5.7, GFIP's picture of gluon evolution/fragmentation is much closer to that of our analytic calculations using FJFs. The black curves in Fig. 5.8 show that  $z$  distributions from GFIP are consistent with our resummed analytic calculations.

It is also interesting to note that PYTHIA treats radiation off of octet  $c\bar{c}$  pairs the same regardless of the quantum numbers of the intermediate  $c\bar{c}$  state. In contrast, GFIP, like our analytic calculation gives different results for all three channels by applying the FFs at the end of the parton shower phase. GFIP can also be applied to all four NRQCD production mechanisms including the  ${}^3P_J^{(8)}$  channel as conver-

gence issues are absent in this process. As a check of our results, we also tested a procedure analagous to GFIP for the two-jet events with  $B$  mesons discussed in the previous section. We showered  $e^+e^- \rightarrow b\bar{b}$  produced in Madgraph using PYTHIA with hadronization turned off. We then convolved the resulting  $b$  quark distribution with the phenomenological FF (see Section 5.2) at the scale  $2m_b$  and found results for  $B$  mesons that are consistent with our earlier analytic calculations.

While GFIP is far from a proper modification of PYTHIA, as we can see from Fig. 5.8, it shows us that implementing gluon fragmentation (which is not included in PYTHIA) yields encouraging similarities to our NLL' resummed calculation using the FJF formalism. The modifications provide excellent motivation to continue the development of the FJF formalism for studying  $J/\psi$  production in jets. Additionally, GFIP suggests that fundamental changes in how PYTHIA treats heavy quarkonia are needed and that these changes will yield Monte Carlo predictions in-line with NRQCD.

A proper modification of PYTHIA of this type is important since GFIP can only be used to calculate the  $z$  distribution. Because hadronization is applied only to gluons fragmenting into  $J/\psi$  and PYTHIA's hadronization module is turned off, GFIP cannot reproduce the angularity distributions discussed above. Additionally, there are other jet substructure observables such as the transverse momentum of the  $J/\psi$  relative to the jet axis that should, in light of the analysis of this work, be able to discriminate between NRQCD production mechanisms. Other observables such as n-subjettines [86], are most easily calculated numerically using Monte Carlo and a properly implemented model of quarkonium production using NRQCD FFs will be needed.

## 5.4 Applications of the TMDFJF to Quarkonium Production

In this section, we continue to explore applying the FJF formalism to the production of heavy quarkonia within jets. Having had success comparing angularity-dependent FJFs with the GFIP predictions, we now will investigate whether TMDFJFs (see Section 4.5) can provide discriminating power between different the  $J/\psi$  production mechanisms in NRQCD. Again, we focus on  $J/\psi$  produced within jets initiated by fragmenting gluons, although our results can be generalized to other quarkonia. Building upon the formalism introduced in Section 4.5, we first discuss the resummation of potentially large logarithms in the TMDFJF via the use of RG and rapidity renormalization group (RRG) techniques. Note that we will, in this section, not be computing a full cross-section, but simply the TMDFJF resummed to NLL' accuracy while assuming that out-of-jet radiation has ultra-soft scaling. However, as our goal is to study the  $\mathbf{p}_\perp$  and  $z$  distributions the  $J/\psi$  in a jet, this should be sufficient.

Each of the diagrams in the perturbative calculation of the collinear  $\mathcal{J}_{ij}$  and collinear-soft  $S_C$  pieces discussed in Section 4.5 suffer from infra-red (IR), ultra-violet (UV) and rapidity divergences (RD) which are addressed as follows

- **IR Divergences** — IR divergences in the collinear-soft function cancel when summing over all diagrams. In the matching coefficients  $\mathcal{J}_{ij}$ , IR divergences cancel in the matching of the purely collinear piece  $\mathcal{D}_i^h$  of the TMDFJF onto the standard FFs,  $D_i^h$ .
- **UV + Rapidity Divergences** — These are regulated using a dimensional regulator and a rapidity regulator in accordance with the techniques developed in Refs. [122, 134]. Poles from UV and rapidity divergences are removed by renormalization, where we introduce the dimensionful scales  $\mu$  (for UV divergences) and  $\nu$  (for rapidity divergences), each of which has their own set of

evolution equations (RGEs for  $\mu$  and RRGs for  $\nu$ ).

For TMD functions, bare and renormalized quantities are related through the following convolution with the renormalization function  $Z$  (where functions are renormalized unless notated as bare)

$$F^{\text{bare}}(\mathbf{p}_\perp) = Z_F(\mathbf{p}_\perp, \mu, \nu) \otimes_\perp F(\mathbf{p}_\perp, \mu, \nu), \quad (5.22)$$

where the function  $F$  will be either  $\mathcal{D}_i^h$  or  $S_C^i$  and  $\otimes_\perp$  denotes a convolution in transverse components as defined in Eq. (4.72). This function satisfies the following RG and RRG equations respectively

$$\begin{aligned} \frac{d}{d \ln \mu} F(\mathbf{p}_\perp, \mu, \nu) &= \gamma_\mu^F(\mu, \nu) \times F(\mathbf{p}_\perp, \mu, \nu) \\ \frac{d}{d \ln \nu} F(\mathbf{p}_\perp, \mu, \nu) &= \gamma_\nu^F(\mathbf{p}_\perp, \mu, \nu) \otimes_\perp (\mathbf{p}_\perp, \mu, \nu), \end{aligned} \quad (5.23)$$

where  $\gamma_\mu^F$  and  $\gamma_\nu^F$  are the anomalous dimensions associated with RGEs and RRGs, respectively. These anomalous dimensions are defined via

$$\begin{aligned} \left[ (2\pi)^2 \delta^{(2)}(\mathbf{p}_\perp) \right] \times \gamma_\mu^F(\mu, \nu) &= -Z_F^{-1}(\mathbf{p}_\perp, \mu, \nu) \otimes_\perp \frac{d}{d \ln \mu} Z_F(\mathbf{p}_\perp, \mu, \nu) \\ \gamma_\nu^F(\mathbf{p}_\perp, \mu, \nu) &= -Z_F^{-1}(\mathbf{p}_\perp, \mu, \nu) \otimes_\perp \frac{d}{d \ln \nu} Z_F(\mathbf{p}_\perp, \mu, \nu). \end{aligned} \quad (5.24)$$

We find that the renormalization function for the purely collinear piece at  $\mathcal{O}(\alpha_s)$  is

$$\begin{aligned} Z^{\mathcal{D}}(\mathbf{p}_\perp, \mu, \nu) &= (2\pi)^2 \delta^{(2)}(\mathbf{p}_\perp) + (4\pi) \alpha_s w^2 C_F \left\{ -\frac{2}{\eta} \left( -\frac{1}{2\epsilon} \delta^{(2)}(\mathbf{p}_\perp) + \mathcal{L}_0(\mathbf{p}_\perp^2, \mu^2) \right) \right. \\ &\quad \left. + \frac{1}{2\epsilon} \left( \ln \left( \frac{\nu^2}{\omega^2} \right) + \bar{\gamma}_i \right) \delta^{(2)}(\mathbf{p}_\perp) \right\} \end{aligned} \quad (5.25)$$

where  $\bar{\gamma}$  is defined in Eq. (4.90). For the collinear-soft piece we find

$$\begin{aligned} Z^{S_C}(\mathbf{p}_\perp, \mu, \nu) &= (2\pi)^2 \delta^{(2)}(\mathbf{p}_\perp) + (4\pi) \alpha_s w^2 C_F \left\{ +\frac{2}{\eta} \left( -\frac{1}{2\epsilon} \delta^{(2)}(\mathbf{p}_\perp) + \mathcal{L}_0(\mathbf{p}_\perp^2, \mu^2) \right) \right. \\ &\quad \left. + \frac{1}{2\epsilon} \left( \ln \left( \frac{\mu^2}{r^2 \nu^2} \right) + \frac{1}{\epsilon} \right) \delta^{(2)}(\mathbf{p}_\perp) \right\} \end{aligned} \quad (5.26)$$

Using the definitions of Eq. (5.24), the anomalous dimensions in  $\mu$  are

$$\gamma_\mu^{\mathcal{D}}(\nu) = \frac{\alpha_s C_i}{\pi} \left( \ln \left( \frac{\nu^2}{\omega^2} \right) + \bar{\gamma}_i \right) \quad \text{and} \quad \gamma_\mu^{SC}(\nu) = \frac{\alpha_s C_i}{\pi} \ln \left( \frac{\mu^2}{r^2 \nu^2} \right). \quad (5.27)$$

In calculating the  $\gamma_\nu$ , the bookkeeping parameter  $w$  plays a role analogous to the coupling  $g$  in the  $\gamma_\mu$  anomalous dimensions<sup>6</sup> and has the property

$$\nu \frac{\partial}{\partial \nu} w = -\frac{\eta}{2} w, \quad (5.28)$$

thus yielding

$$\gamma_\nu^{\mathcal{D}}(p_\perp, \mu) = -(8\pi) \alpha_s C_i \mathcal{L}_0(\mathbf{p}_\perp, \mu^2) \quad (5.29)$$

$$\gamma_\nu^{SC}(p_\perp, \mu) = +(8\pi) \alpha_s C_i \mathcal{L}_0(\mathbf{p}_\perp, \mu^2). \quad (5.30)$$

We can show that the anomalous dimensions satisfy

$$\gamma_\mu^{\mathcal{D}}(\nu) + \gamma_\mu^{SC}(\nu) = \gamma_\mu^J = \frac{\alpha_s C_i}{\pi} \left( \ln \left( \frac{\mu^2}{r^2 \omega^2} \right) + \bar{\gamma}_i \right), \quad (5.31)$$

where  $\gamma_J$  is the anomalous dimension of the unmeasured quark jet function [1] and

$$\gamma_\nu^{\mathcal{D}}(\mathbf{p}_\perp, \mu) + \gamma_\nu^S(\mathbf{p}_\perp, \mu) = 0, \quad (5.32)$$

both of which must be satisfied for our TMDFJFs to be consistent with the corresponding jet functions. In order to resum our results to NLL' accuracy, we evolve the purely collinear and collinear-soft pieces from their characteristic scales to common scales in  $\mu$  and  $\nu$  using the RG and RRG respectively. To perform the evolution, we first take the Fourier transforms of both the RG and RRG equations as done in Ref. [122]. We then perform the evolution using the RG and RRG in this transformed space before finally performing the inverse Fourier transform in order to write the

---

<sup>6</sup> It is not, however a real coupling, but merely a calculational tool used to ensure that the total  $\gamma_\nu$  is independent of  $\nu$ .

resummed TMDFJF in momentum space. We first evolve our collinear-soft function in  $\nu$ -space, choosing the common scale to be  $\nu = \nu_{\mathcal{D}}$ , the characteristic  $\nu$  scale of the purely collinear part of the TMDFJF (which as shown below  $\nu_{\mathcal{D}} = 2 \exp(-\gamma_E)/b$ ). We then evolve both functions in  $\mu$ -space to the common scale  $\mu = \omega r$ .<sup>7</sup>

In order to ultimately make our plots easier to interpret, we study the quantity  $\mathcal{G}_i^h(p_{\perp}, z, \mu)$  which is related to the TMDFJF  $\mathcal{G}_i^h(\mathbf{p}_{\perp}, z, \mu)$  by a change of variables from vector transverse momenta ( $\mathbf{p}_{\perp}$ ) to the amplitude ( $p_{\perp} = |\mathbf{p}_{\perp}|$ ). Performing the evolutions described above we find,

$$\begin{aligned} \mathcal{G}_i^h(p_{\perp}, z, \mu) &= (2\pi)^2 p_{\perp} \int_0^{\infty} db b J_0(bp_{\perp}) \mathcal{U}_{S_C}(\mu, \mu_{S_C}, m_{S_C}) \mathcal{U}_{\mathcal{D}}(\mu, \mu_{\mathcal{D}}, 1) \\ &\times \mathcal{V}_{S_C}(b, \mu_{S_C}, \nu_{\mathcal{D}}, \nu_{S_C}) \mathcal{FT} \left[ \mathcal{D}_{i/h}(\mathbf{p}_{\perp}, z, \mu_{\mathcal{D}}, \nu_{\mathcal{D}}) \otimes_{\perp} S_C^i(\mathbf{p}_{\perp}, \mu_{S_C}, \nu_{S_C}) \right], \end{aligned} \quad (5.33)$$

where  $\mathbf{b}$  with  $b = |\mathbf{b}|$  is the Fourier conjugate variable of  $\mathbf{p}_{\perp}$ ,  $J_0$  is a Bessel function of the first kind and where

$$\mathcal{U}_F(\mu, \mu_0, m_F) = \exp(K_F(\mu, \mu_0)) \left( \frac{\mu_0}{m_F} \right)^{\omega_F(\mu, \mu_0)}, \quad (5.34)$$

$$\text{and } \mathcal{V}_F(b, \mu, \nu, \nu_0) = \left( \frac{\mu}{\mu_C(b)} \right)^{\eta_F(\mu, \nu, \nu_0)} \quad \text{where } \mu_C(b) = 2 \exp(-\gamma_E)/b, \quad (5.35)$$

are the evolution kernels for RG and RRG evolution, respectively.

The purely collinear term  $\mathcal{D}_i^h$  in Eq.(5.33) is then a convolution of the perturbatively calculated short distance coefficients and the standard fFF evaluated at their characteristic scale (in the case of NRQCD FFs this will again be  $2m_c$ ) and evolved to the characteristic scale of the purely collinear term in momentum space,  $\mu = p_{\perp}$ . Since the FFs are not dependent on the transverse momentum (and thus not the Fourier conjugate  $b$ ), their form is fixed in the evaluation of the  $b$  integral in

---

<sup>7</sup> Notice that  $S_C$  and  $\mathcal{D}$  have the same characteristic renormalization scale  $\mu_{S_C} = \mu_{\mathcal{D}} \equiv \mu_C$ .

Eq.(5.33). The scales  $\mu_F$ ,  $\nu_F$  and  $m_F$  for each of the functions discussed above are given in Table 5.2. Again, additional details on RG and RRG evolution are provided in Appendix C. In order to apply the TMDFJFs to quarkonium production, we will

Function ( $F$ )	RG scale ( $\mu_F$ )	RRG scale ( $\nu_F$ )	$m_F$
$\mathcal{D}_{i/h}$	$\mu_C(b)$	$\omega$	n.a.
$S_C^i$	$\mu_C(b)$	$\mu_C(b)/r$	$\nu r$

Table 5.2: Characteristic scales of the different functions in the factorization theorem.

once again use the NRQCD FFs for the  ${}^3S_1^{[1]}$ ,  ${}^3S_1^{[8]}$ ,  ${}^1S_0^{[8]}$ , and  ${}^3P_J^{[8]}$  production mechanisms of  $J/\psi$ . Our goal is to see if the  $z$  and  $p_\perp$  dependence of the TMDFJF can discriminate between these different mechanisms.

The TMDFJFs as a function of  $p_\perp$  for fixed  $z = 0.3, 0.5, 0.7$ , and  $0.9$  and jets of energies  $E_J = 100$  GeV and  $E_J = 500$  GeV are shown Figs. 5.9 and 5.10, respectively. In order to make it easier to view all distributions simultaneously, we have rescaled the  ${}^3S_1^{[8]}$ ,  ${}^1S_0^{[8]}$ ,  ${}^3P_J^{[8]}$ , and  ${}^3S_1^{[1]}$  distributions, by factors of  $10^6$ ,  $10^6$ ,  $3.0 \times 10^5$  and  $4.0 \times 10^5$ , respectively in the eight plots shown in Figs. 5.9 and 5.10. Theoretical uncertainties are calculated by varying the RRG and RG scales  $\nu_{S_C}$ ,  $\nu_{\mathcal{D}}$ , and  $\mu$  by a factor of 2 and 1/2. The dashed central lines in these plots show the choice of  $\nu = \nu_{\mathcal{D}} = \omega$  and  $\mu = \omega r$ . Note that while these plots show a range of  $0 < p_\perp < 20$  GeV, it is important that to keep in mind that our calculations are only reliable for  $p_\perp \geq 2m_c = 3$  GeV.

Figs. 5.9 and 5.10 demonstrate that the TMDFJF does in fact provide discriminating power between the four production mechanisms. For  $z = 0.3$ , all four distributions look similar for both  $E_J = 100$  GeV and 500 GeV. The distributions peak at roughly the same location and they have same slope for large  $p_\perp$ . For  $z \geq 0.5$ , the color-singlet  ${}^3S_1^{[1]}$  mechanism and the color-octet  ${}^1S_0^{[8]}$  mechanism peak at lower values of  $p_\perp$  and fall more steeply with  $p_\perp$  than the  ${}^3S_1^{[8]}$  and  ${}^3P_J^{[8]}$  mechanisms.

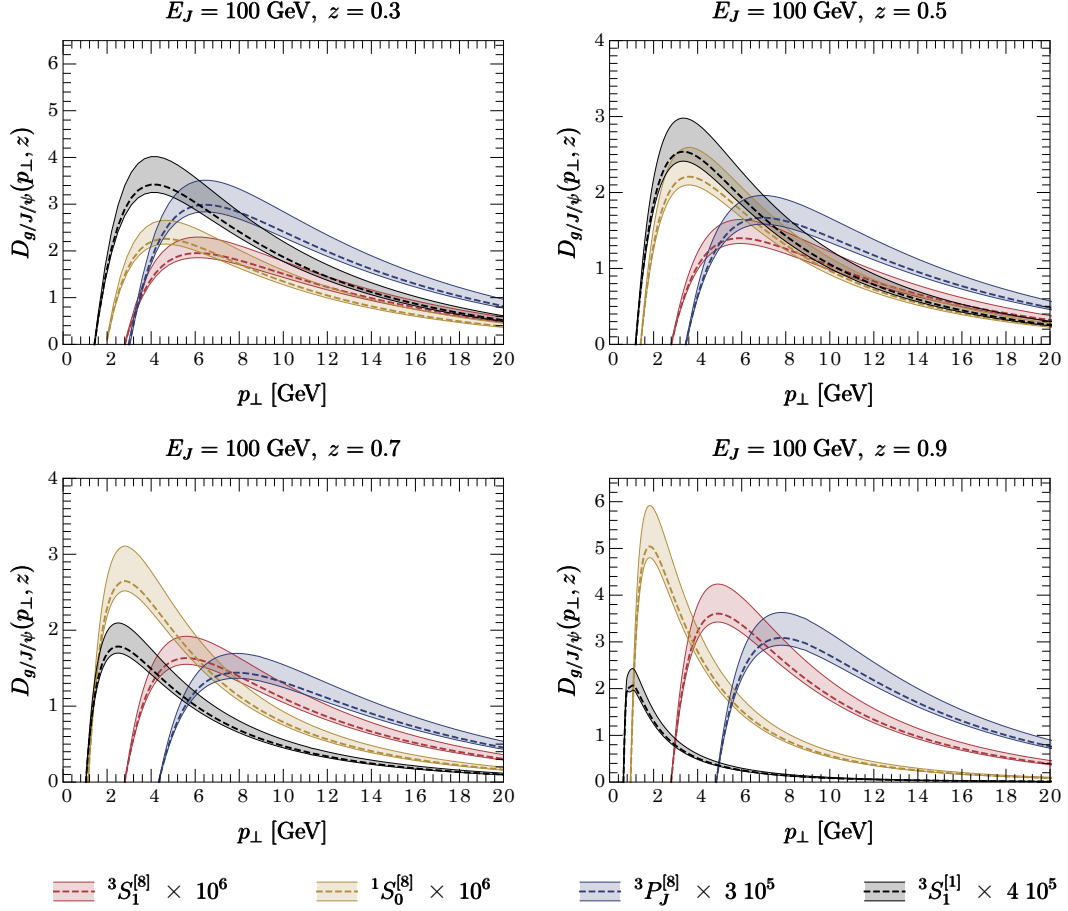


FIGURE 5.9: The TMDFJF as a function of the  $p_{\perp}$  of the  $J/\psi$  for the  ${}^3S_1^{[1]}$ ,  ${}^3S_1^{[8]}$ ,  ${}^1S_0^{[8]}$ ,  ${}^3P_J^{[8]}$  production mechanisms for jet energies  $E_J = 100$  GeV. Theoretical uncertainties are calculated by varying the renormalization scales by factors of  $1/2$  and  $2$ .

The  ${}^3P_J^{[8]}$  gives a slightly harder  $p_{\perp}$  distribution than  ${}^3S_1^{[8]}$  and both are significantly harder than the other mechanisms.<sup>8</sup>

In addition to the  $p_{\perp}$  distribution for fixed  $z$ , it is also interesting to study  $z$  distribution of the TMDFJF for different fixed values  $p_{\perp}$  (in the perturbative regime).

Fig. 5.11 shows the TMDFJF as a function of  $z$  for  $p_{\perp} = 10$  GeV for jets with energy

<sup>8</sup> We note that while the peak regions in the  $p_{\perp}$  distribution for the  ${}^3S_1^{[8]}$  and  ${}^3P_J^{[8]}$  distributions are at larger values of  $p_{\perp} \sim 6 - 8$  GeV where perturbation theory is reliable, the  ${}^3S_1^{[1]}$  and  ${}^1S_0^{[8]}$  peak regions occur at very low  $p_{\perp}$  where perturbation theory is not reliable. In this region, non-perturbative effects are likely to be important and could affect the shape of the distributions. We are interested in examining this problem in future work.

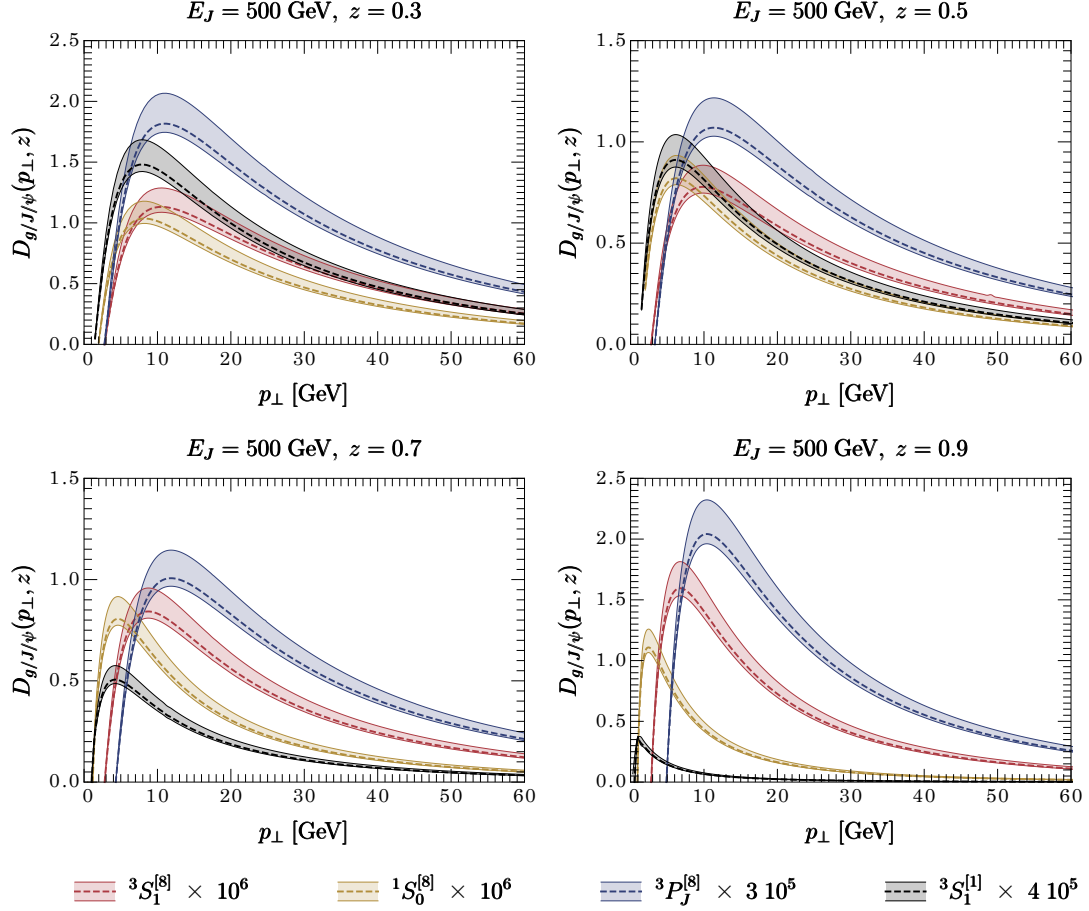


FIGURE 5.10: The TMDFJF as a function of the  $p_{\perp}$  of the  $J/\psi$  for the  ${}^3S_1^{[1]}$ ,  ${}^3S_1^{[8]}$ ,  ${}^1S_0^{[8]}$ ,  ${}^3P_J^{[8]}$  production mechanisms where the jet energies  $E_J = 500 \text{ GeV}$ . Theoretical uncertainties are calculated by varying the renormalization scales by factors of  $1/2$  and  $2$ .

$E_J = 100$  and  $500 \text{ GeV}$ . Large logarithms and non-perturbative effects will, of course, affect these distributions in the  $z \rightarrow 0$  and  $z \rightarrow 1$  limits. However, our calculations should be reliable for intermediate values of  $z$ . We notice that while for  $z < 0.5$  the distributions have similar shapes, in the range  $0.5 < z < 0.9$ , the shapes of all four mechanisms are different. This observation is consistent with our study of angularity FJFs, where there was also more differentiation between production mechanisms at higher values of  $z$ . Ultimately, the  $z$  dependence of the TMDFJF for fixed  $p_{\perp}$  can also be used to differentiate between the NRQCD production mechanisms.

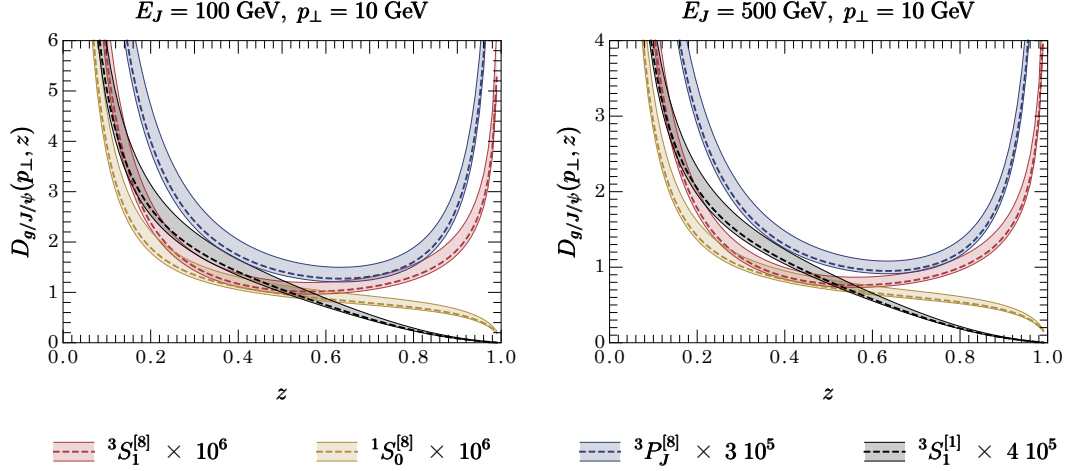


FIGURE 5.11: The TMDFJF as a function of the  $z$  of the  $J/\psi$  for the  ${}^3S_1^{[1]}$ ,  ${}^3S_1^{[8]}$ ,  ${}^1S_0^{[8]}$ ,  ${}^3P_J^{[8]}$  production mechanisms, with  $p_{\perp} = 10$  GeV for  $E_J = 100$  and 500 GeV. Theoretical uncertainties are calculated by varying the renormalization scales by factors of 1/2 and 2.

In addition to studying the transverse momentum distribution, we can use the TMDFJF formalism to calculate the angle  $\theta$  at which  $J/\psi$  are produced relative to the jet axis. The average production angle for the  $J/\psi$  can be written as

$$\langle\theta\rangle(z) = \frac{\int \theta d\theta (d\sigma/d\theta dz)}{\int d\theta (d\sigma/d\theta dz)}. \quad (5.36)$$

By using the small angle approximation, we can write down a cross-section differential in  $z$  and the average angle  $\theta$  via

$$\frac{d\sigma}{d\theta dz} = \int dp_{\perp} \delta\left(\theta - \frac{2p_{\perp}}{z\omega}\right) \frac{d\sigma}{dp_{\perp} dz}. \quad (5.37)$$

Substituting this into Eq. (5.36) yields an equation for the average angle in terms of the differential cross sections in  $p_{\perp}$  and  $z$

$$\langle\theta\rangle(z) = \frac{2 \int dp_{\perp} p_{\perp} (d\sigma/dp_{\perp} dz)}{z\omega \int dp_{\perp} (d\sigma/dp_{\perp} dz)}. \quad (5.38)$$

In SCET, the cross-section  $d\sigma/d\theta dz$  can be factorized into hard, collinear, and soft pieces. However, the quotient in Eq. (5.38) will not, in general, allow for the cancel-

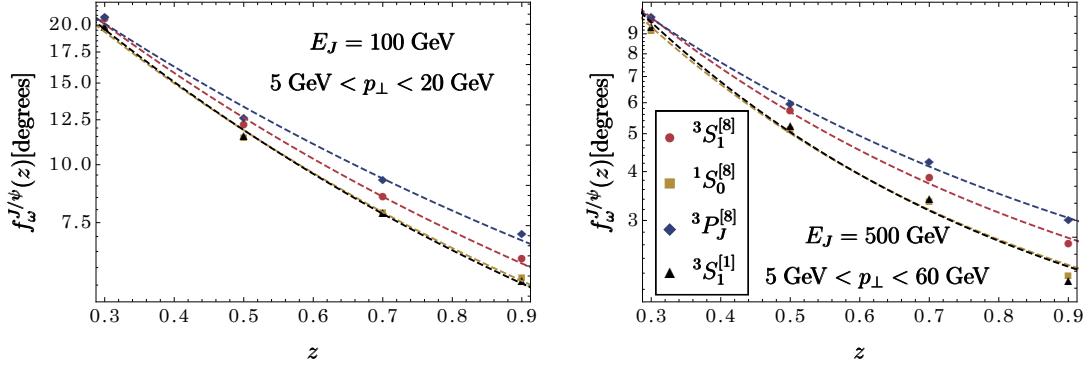


FIGURE 5.12: The quantity  $f_{\omega}^{J/\psi}(z)$  (as defined in the text) as a function of  $z$  relative to the jet axis for each NRQCD production mechanism where the jet has  $E_J = \omega/2 = 100$  GeV (left) and 500 GeV (right). The  $J/\psi$  is restricted to have  $p_{\perp} \in [5, 20]$  GeV in the 100 GeV jet and  $p_{\perp} \in [5, 60]$  GeV in the 500 GeV jet.

lation of the non-collinear functions because one must sum over the fragmentation of different partons in the numerator and denominator. However, if we focus on studying the gluon fragmentation channel (which as we have discussed is the leading contribution), the Eq. (5.38) can be written as the quotient

$$\langle \theta \rangle(z) \sim \frac{2 \int dp_{\perp} p_{\perp} \mathcal{G}_g^h(p_{\perp}, z, \mu)}{z\omega \int dp_{\perp} \mathcal{G}_g^h(p_{\perp}, z, \mu)} \equiv f_{\omega}^h(z), \quad (5.39)$$

where  $\mathcal{G}_g^h(p_{\perp}, z, \mu)$  is the gluon TMDFJF.

Fig. 5.12 shows the function  $f_{\omega}^{J/\psi}(z)$  for fixed  $z = 0.3, 0.5, 0.7$ , and  $0.9$  where  $\omega = 2E_J = 200$  GeV and 1 TeV for  $J/\psi$  in jets with  $p_{\perp} \in [5, 20]$  GeV and  $p_{\perp} \in [5, 60]$  GeV, respectively. The renormalization scale is again set to  $\mu = \omega r$ . The colored dashed lines show the results of a fit to the function,  $C_0 \exp(-z C_1)$ . The results of the fit for  $C_0$  and  $C_1$  are shown in Table 5.3 for each production mechanism at both jet energies. Note that the typical angles are small enough to justify the use of the small-angle approximation in Eq. (5.37).

Again we see that differences between the various NRQCD mechanisms become more pronounced as  $z$  increases. This shows that the average angle does in fact

$E_J = 100 \text{ GeV}$			$E_J = 500 \text{ GeV}$		
$^{2S+1}L_J^{[1,8]}$	$C_0$	$C_1$	$^{2S+1}L_J^{[1,8]}$	$C_0$	$C_1$
$^3S_1^{[1]}$	3.92	0.92	$^3S_1^{[1]}$	3.75	1.68
$^3S_1^{[8]}$	3.86	0.84	$^3S_1^{[8]}$	3.48	1.39
$^1S_0^{[8]}$	3.88	0.90	$^1S_0^{[8]}$	3.66	1.64
$^3P_J^{[8]}$	3.75	0.74	$^3P_J^{[8]}$	3.28	1.20

Table 5.3: Results of fits of the function  $\log(f_\omega(z))$  shown in Fig. 5.12 to the function  $C_0 \exp(-z C_1)$ .

discriminate between the different octet mechanisms. In particular, the slope on the log plot on the right side of Fig. 5.12, which is determined by the parameter  $C_1$  in Table 5.3, differs by as much as 20% between the various NRQCD mechanisms for  $E_J = 100 \text{ GeV}$  and as much as 40% for  $E_J = 500 \text{ GeV}$ . Note, however, that  $^1S_0^{[8]}$  and  $^3S_1^{[1]}$  give very similar predictions for this observable.

## 5.5 FJF/PYTHIA Predictions vs. LHCb Data on $J/\psi$ Production

In early 2017, the LHCb collaboration published the first study of  $J/\psi$  produced within jets in a collider experiment [32]. They found that the distribution of the fraction  $z(J/\psi)$  of the jet's transverse momentum carried by the  $J/\psi$  strongly disagree with predictions from PYTHIA. As shown in Fig. 5.13, LHCb saw a stark contrast between data and predictions from PYTHIA, which showed a much harder distribution in  $z$ . Based on the discussion presented in Section 5.3, we know that this PYTHIA distribution is unphysical due to the way in which onia are created and showered. In this section, we use versions of the GFIP and FJF formalisms to make two different improved theoretical predictions of the  $z(J/\psi)$  distribution and discuss the implications of the comparisons between NRQCD and LHCb results.

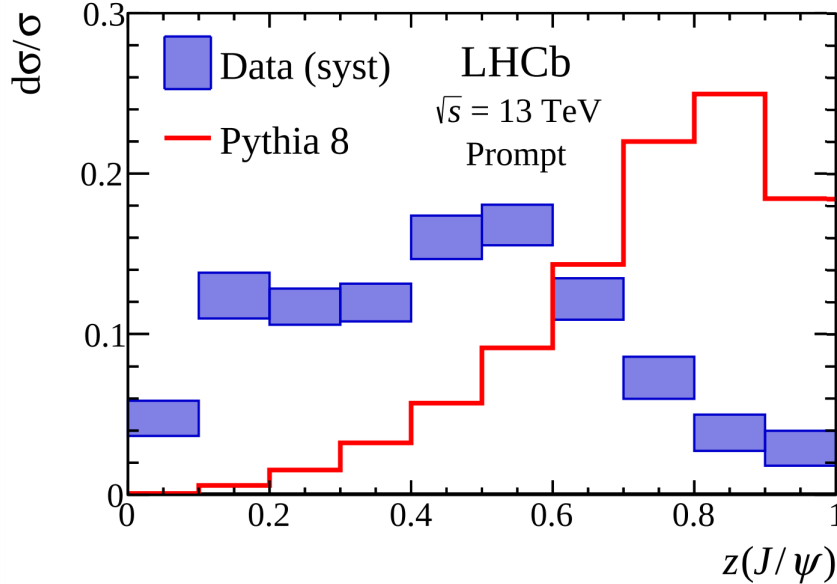


FIGURE 5.13: Differential cross section for prompt  $J/\psi$  production within jets as a function of  $z(J/\psi)$ , the fraction of the jet’s transverse momentum carried by the  $J/\psi$  produced within it as shown in Ref. [32]. The distribution is normalized such that the total sum of the bin heights is 1. The plot also shows a leading-order NRQCD-based prediction from PYTHIA as well as a breakdown of the PYTHIA contributions into single and double parton scattering contributions.

### 5.5.1 Method 1: GFIP for LHCb

We first generate events in Madgraph corresponding to hard-scale processes for charm quarks and gluons in  $pp$  collisions at  $\sqrt{s} = 13$  GeV. In general, we neglect contributions to  $J/\psi$  production from non-charm quarks as they are suppressed, either due to soft gluon emission or by  $\alpha_s$  evaluated at a large energy scale. We generate events using the constraints of the the LHCb analysis, where jets are required to have pseudorapidity  $2.5 < \eta < 4.0$ ,  $R = 0.5$ , and  $p_T > 20$  GeV. PYTHIA is then used to shower the event down to a scale where the final state particles have a virtuality of  $\sim 2m_c$ , but its hadronization module is turned off. We use the anti-kT algorithm with  $R = 0.5$  to reconstruct jets out of the final state partons, restricting charm quarks and gluons that will be hadronized to be within the jet.

The  $z$  distributions resulting from this shower are shown in Fig. 5.14. As men-

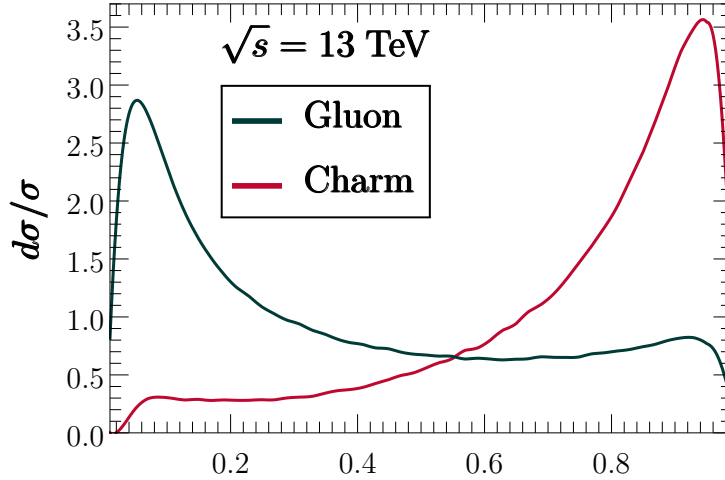


FIGURE 5.14: PYTHIA predictions for  $c$  quark and gluon  $z$  distributions (where  $z$  is the fraction of the energy of the parton initiating the jet) after showering to the scale  $2m_c$ .

tioned in Section 5.3, the  $z$  distribution of the charm (which showers using the  $P_{qq}$  splitting function) is peaked near  $z = 1$  while the gluon  $z$  distribution (which showers using the  $P_{gg}$  splitting function) is much softer and peaked near  $z = 0$ .  $J/\psi$  are typically studied experimentally through their decays to dimuons (e.g.  $J/\psi \rightarrow \mu^+\mu^-$ ). LHCb requires that both muons have  $2.0 < \eta < 4.5$ ,  $p > 5$  GeV, and  $p_T > 0.5$  GeV. This cut suppresses contributions from low  $z$  particles and thus enhances the contribution from  $c$  quark initiated jets, which then dominate at high  $z$ . We convolve the  $p_T$  distribution for the gluons with the NRQCD FFs for the  $^3S_1^{[1]}$ ,  $^3S_1^{[8]}$ ,  $^1S_0^{[8]}$  and  $^3P_J^{[8]}$  production mechanisms. For the case of charm quark fragmentation, color-singlet and color-octet FFs start at the same order in  $\alpha_s$ , so the relative  $v^4$  is no longer compensated for as it was for the gluon LDMEs. We thus restrict our analysis for charm quarks to the  $^3S_1^{[1]}$  channel.

After convolving with the FFs, we implement the muon cuts by first assuming the  $J/\psi$  are roughly unpolarized. This yields an isotropic angular distribution of the  $\mu^+, \mu^-$  in the rest frame of the  $J/\psi$ . After boosting these muons back to the

	$\langle \mathcal{O}^{J/\psi}(^3S_1^{[1]}) \rangle$ $\times \text{GeV}^3$	$\langle \mathcal{O}^{J/\psi}(^3S_1^{[8]}) \rangle$ $\times 10^{-2} \text{GeV}^3$	$\langle \mathcal{O}^{J/\psi}(^1S_0^{[8]}) \rangle$ $\times 10^{-2} \text{GeV}^3$	$\langle \mathcal{O}^{J/\psi}(^3P_0^{[8]}) \rangle / m_c^2$ $\times 10^{-2} \text{GeV}^3$
B & K [14, 15]	$1.32 \pm 0.20$	$0.224 \pm 0.59$	$4.97 \pm 0.44$	$-0.72 \pm 0.88$
Chao, et al. [18]	$1.16 \pm 0.20$	$0.30 \pm 0.12$	$8.9 \pm 0.98$	$0.56 \pm 0.21$
Bodwin et al. [22]	$1.32 \pm 0.20$	$1.1 \pm 1.0$	$9.9 \pm 2.2$	$0.49 \pm 0.44$

Table 5.4: We consider three sets of LDMEs for NRQCD production mechanisms, listed here in units of  $\text{GeV}^3$ .

lab frame, we apply the LHCb cuts mentioned above. In order to combine different production mechanisms, we give each a weight calculated via

$$r(i, n) = \frac{d\hat{\sigma}(pp \rightarrow i + X) \int_0^1 dz D_{i \rightarrow J/\psi}^n(z)}{d\hat{\sigma}(pp \rightarrow c + X) \int_0^1 dz D_{c \rightarrow J/\psi}^{3S_1^{[1]}}(z)}. \quad (5.40)$$

where  $i$  is the initiating parton,  $n$  represents the quantum numbers of the intermediate  $c\bar{c}$ , and the FFs  $D_{i \rightarrow J/\psi}^n(z)$  are again calculated at the scale  $2m_c$ . We note that  $D_{i \rightarrow J/\psi}^n(z) \propto \langle \mathcal{O}^{J/\psi}(n) \rangle$  which means that LDMEs from different fits will enter the ratios through the FFs at  $2m_c$ . For the LDMEs, we use the 3 sets extracted in Refs. [14, 15, 18, 22] whose values are shown in Table 5.4.

The LHCb data is normalized such that the sum of the heights of the bins is 1. Due to potentially large corrections that may occur at  $z \rightarrow 0$  and  $z \rightarrow 1$ , we will compare our GFIP and FJF methods with LHCb data in the range  $0.1 < z < 0.9$ , fixing the normalizations of our distributions to the sum of the data in only these bins accordingly. The results of this application of GFIP are shown in grey in Fig. 5.15. As we will discuss further below, they compare quite favorably to the LHCb data.

### 5.5.2 Method 2: FJF for LHCb

In addition to the GFIP method, we also make an analytic calculation of the  $z(J/\psi)$  distribution using FJFs for jets where the energy  $E$  and radius  $R$  of the jet are measured combined with hard events generated by Madgraph. In previous sections

we used a factorization for  $J/\psi$  production in jets of the form

$$d\sigma[e^+e^- \rightarrow \text{jets}, h] = H \otimes S \otimes J(\otimes J) \otimes \mathcal{G}^h \quad (5.41)$$

Resumming such a cross-section involved evaluating each function at its characteristic scale and then evolving it to a common scale  $\mu$  using its corresponding RGE. In the present case, we resum logarithms of  $m_{J/\psi}/E_J$  in the FJF by simply using the LO DGLAP equations to evolve the FF from  $2m_c$  to the jet energy scale,  $E_J$ . We allow Madgraph to calculate the remaining terms in the factorization theorem to LO in perturbation theory and do not perform NLL' resummation for the remaining terms in Eq. (5.41). Since the  $z(J/\psi)$  dependence of the cross-section is controlled primarily by the FJF, these other pieces will affect only the overall normalization.

We next combine the energy distribution of hard partons from Madgraph with the FJFs for  $R = 0.5$  jets reconstructed using the anti-kT algorithm to generate a  $z(J/\psi)$  distribution for each of the five production mechanisms. The LHCb muon cuts are implemented by using the GFIP results to calculate the probabilities for any given  $z$  that a  $\mu^+\mu^-$  will survive the cuts. Taking this probability into account and weighting the contributions of each NRQCD production mechanism according to Eq. (5.40) for each of the LDME sets shown in Table 5.4, we find the distribution shown in red in Fig. 5.15.

### 5.5.3 Comments on Uncertainties

For both methods, uncertainties are calculated using the uncertainties quoted in the LDME values of Refs. [14, 15, 18, 22]. For the extraction in Ref. [22], the errors take into account an error correlation matrix provided in Ref. [147]. The authors of Ref. [18] also observed that a fixed relationship between the  ${}^3S_1^{[8]}$  and  ${}^3P_J^{[8]}$  LDMEs must be enforced in order for  $J/\psi$  to be unpolarized. When taken into account in calculating the LDME value uncertainties, this constraint significantly reduces the

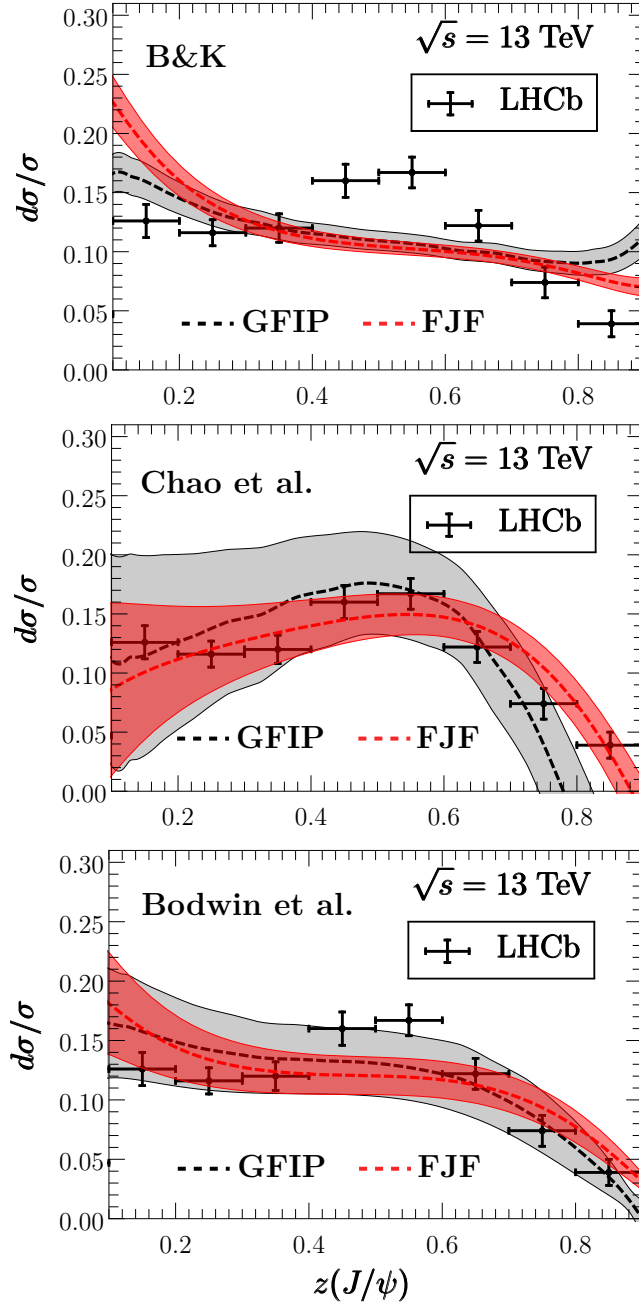


FIGURE 5.15: Predicted  $z(J/\psi)$  distribution using GFIP (gray) and FJF (red) for the three choices of LDME in Table 5.4 and the LHCb measurements of  $z(J/\psi)$ .

error bands relative to simply adding each of the errors on the LDMEs in quadrature.

In the absence of a complete factorization theorem, it is difficult to reliably esti-

mate theoretical uncertainties. For example, when calculating errors from variations of the renormalization scale, the  $\mu$  dependence would normally be cancelled between the hard, jet, and soft functions in the factorization theorem, but the soft functions have not been calculated. However, because of the way we have fixed the normalization to match the LHCb plots, these scale variations, which would simply affect the overall normalization and not the shapes of the  $z(J/\psi)$  distributions, will not affect the uncertainty.

We also note that our FJF method is more appropriate for  $n$ -jet cross sections like Eq. (5.41) than for the inclusive case. However, inclusive FJFs [111, 112, 148, 149] differ by a contribution from out-of-jet soft radiation that is suppressed by powers of  $\alpha_s$  as well as  $\Lambda/p_T^{\text{jet}}$ , where  $\Lambda$  is the scale of out-of-jet soft radiation (see the discussion following Eq. (4.15) of Ref. [1]). These power corrections will be small for jet radius  $R \sim \mathcal{O}(1)$ . Additionally, since our GFIP method uses PYTHIA (which generates the final state radiation in an inclusive manner) and gives similar results to the FJF method, this confirms our expectation that the FJF method is correct up to power corrections.

Other uncertainties such as underlying event and double parton scattering contributions should ideally be accounted for, especially as  $z \rightarrow 0$ . However, it is unclear how these should be estimated.

#### 5.5.4 Comparisons of GFIP, FJFs, & Data

For all three extractions of the LDMEs, Methods 1 and 2 both yield results that are much closer to the LHCb data than the default PYTHIA predictions of Ref. [32]. This provides support for the picture of quarkonium production we first described in Section 5.3. The data also seem to favor the LDMEs from the fits of Refs. [18, 22] over the global fits Ref. [14, 15]. To understand this, consider that LHCb measurement in Fig. 5.13 steadily decreases as  $z(J/\psi) \rightarrow 1$ . This behavior is characteristic of the

${}^3S_1^{[1]}$  and  ${}^1S_0^{[8]}$  FJFs whereas the  ${}^3S_1^{[8]}$  and  ${}^3P_J^{[8]}$  FJFs diverge as  $z \rightarrow 1$ . Thus, the cancellation of the  ${}^3S_1^{[8]}$  and  ${}^3P_J^{[8]}$  mechanisms enforced in the fits of [18, 22], which results in the  ${}^1S_0^{[8]}$  mechanism dominating production at high  $z$ , allows our results to better match the data in this region. Refs. [18, 22] also showed that the cancellation is critical to ensuring that the  $J/\psi$  are unpolarized at high- $p_T$ . This cancellation is not enforced in the global fits, which is why the distribution begins to turn upwards as  $z \rightarrow 1$ .

The success of this analysis will help motivate further measurements of the  $J/\psi$  in jets. It would be interesting to see comparisons of these analytic methods with measurements of  $J/\psi$  in jets at central rapidities as well as a measurement of the  $J/\psi$  polarization as a function of  $z(J/\psi)$ . Considering the large uncertainties shown the second plot of Fig. 5.15, this study also motivates a combined fit of the LDMEs to data of both LHCb and the high  $p_T$  data used in Ref. [18].

# 6

## Conclusions

In this work we have explored a novel way to probe the production of quarkonia. We used the FJF formalism to study the production of  $J/\psi$  in jets at high transverse momentum in a search for a better way to extract the  $J/\psi$  LDMEs at  $e^+e^-$  and  $pp$  colliders. After outlining the basic ideas of QCD, EFTs, and resummation in Chapter 1, we surveyed the development of quarkonium production theory from the earliest models such as the CSM to the modern theory, NRQCD, in Chapter 2. We motivated the need for further study of quarkonium production by discussing the  $J/\psi$  polarization puzzle, one of the most important remaining questions in SM physics.

Chapter 3 explained the essential ideas of jet physics, including how they are studied both analytically and experimentally. We introduced jet substructure observables and the basic formalism of SCET. We also schematically outlined how SCET provides factorization theorems for jet production cross-sections, allowing for high-precision resummed calculations of many jet processes.

Chapter 4 introduced the formalism of FJFs and extended their definition to jets where the angularity  $\tau_a$  is measured. It also extended FJFs to TMD distributions, allowing us to study the transverse momentum  $p_{\perp}^h$  and angle  $\theta$  of a hadron relative to

the axis of the jet. For both the angularity FJFs and TMDFJFs, we calculated the matching coefficients onto FFs at one-loop. For the TMDFJFs we also calculated the collinear-soft functions which describe in-jet radiation with a soft energy but collinear scaling at one-loop.

In Chapter 5, the theoretical developments of Chapter 4 were applied to the study of heavy mesons and quarkonia. The one-loop calculations of the matching coefficients performed in Chapter 4 were used along with RG techniques to calculate NLL' resummed cross-sections for  $B$  meson production in  $e^+e^- \rightarrow$  dijet events and  $J/\psi$  production in  $e^+e^- \rightarrow$  3 jets. These analytic calculations were compared with predictions from PYTHIA (and Herwig for  $B$  mesons) simulations. While good agreement was found in the  $B$  meson case, PYTHIA produced  $z$  (the fraction of the jet energy carried by the  $J/\psi$ ) distributions that were much harder than our NLL' analytic predictions. This disagreement was due to the unphysical manner in which quarkonium fragmentation is treated in PYTHIA. The differences between Monte Carlo and our analytic calculations were resolved through the development of the GFIP approach. GFIP took hard processes produced in Madgraph, showered them to the scale  $2m_c$  using PYTHIA and convolved the resulting gluon energy distribution with NRQCD FFs. This represents a more physical approach that reflects the picture of quarkonium production described by NRQCD. The authors of PYTHIA are now working to implement gluon fragmentation modes of quarkonium production.

Chapter 5 also demonstrated that the TMDFJF can, especially at high values of  $z$  where the  $J/\psi$  carries a large fraction of the jet's energy, discriminate between different color-octet  $J/\psi$  production mechanisms. This was done through an NLL' resummed calculation of the TMDFJF using the NRQCD LDMEs for  $J/\psi$ . This resummation required a careful implementation of both RG and RRG techniques in order to resum the UV and rapidity divergences present in calculations of TMD observables.

Finally, we used a combination of Madgraph, PYTHIA, and NRQCD FFs combined with RG evolved  $J/\psi$  FJFs (where the energy of the jet was measured but a jet substructure observable was not) to make predictions of the  $z(J/\psi)$  distributions at LHCb and compared them with recent data. We also compared results of our GFIP method for the  $z(J/\psi)$  distributions with the LHCb data. In both cases, we showed that our results agree far better with data than the default PYTHIA predictions performed in Ref. [32]. We also showed that the data are better described by LDMEs extracted from fits to larger  $p_T$  data than by the LDMEs extracted from global fits of  $J/\psi$  production.

These results demonstrate a need for continued study of identified hadrons within jets as a way of probing fragmentation. While we focused our study on quarkonium production, the FJF formalism can be used to study the production of any hadron for which FFs are available. A robust extraction of the NRQCD color-octet LDMEs, which should be universal, would help improve our understanding of quarkonium production. A proper understanding of the production of  $J/\psi$  would solve the polarization puzzle, a long-outstanding problem in perturbative QCD. Within the SCET community, the ability of jet substructure techniques to provide a new way of probing hadron production is a compelling idea that could be applied to other SM and BSM problems. SCET-related EFT techniques have been applied to heavy dark matter annihilation in Ref. [150], and jet-substructure techniques have been applied to searches for potential dark matter candidates in Refs. [151, 152].

# Appendix A

## Velocity Scaling in NRQCD

In this Appendix, we follow the steps of Ref. [33] in order to discuss NRQCD power counting in more detail and give estimations of the values of parameters such as  $\alpha_s$  and  $v$ . We derive the scaling in  $v$  of relevant operators in the NRQCD Lagrangian and show that, with a particular choice of gauge, the Lagrangian can be written in form where the power counting in  $v$  of the terms is manifest.

The velocity scaling rules of NRQCD can be derived from the self-consistency of the terms in the Lagrangian and basic qualitative features of quarkonia. Consider first the heavy-quark number operator  $\psi^\dagger\psi$ . In a quarkonium state  $\mathcal{Q}$ , the expectation value of this operator should be 1

$$\langle \mathcal{Q} | \int d^3x \psi^\dagger\psi | \mathcal{Q} \rangle \approx 1 \quad \text{where} \quad \langle \mathcal{Q} | \mathcal{Q} \rangle = 1. \quad (\text{A.1})$$

Since the dimensions of the volume element  $[d^3x] \sim 1/(Mv)^3$  (since the approx. width of the quarkonium state  $\sim Mv$ ), we know that  $[\psi] \sim (Mv)^{3/2}$ . Since the expectation value of the kinetic energy should scale as  $\sim Mv^2$

$$\langle \mathcal{Q} | \int dx \psi^\dagger \left( \frac{\mathbf{D}^2}{2M} \right) \psi | \mathcal{Q} \rangle \sim Mv^2 \implies [\mathbf{D}] \sim Mv. \quad (\text{A.2})$$

Operators	Estimate
$\psi$	$(Mv)^{3/2}$
$\chi$	$(Mv)^{3/2}$
$D_0$	$Mv^2$
$\mathbf{D}$	$Mv$
$g\mathbf{E}$	$M^2v^3$
$g\mathbf{B}$	$M^2v^4$
$gA_0$ (in Coulomb gauge)	$Mv^2$
$g\mathbf{A}$ (in Coulomb gauge)	$Mv^3$

FIGURE A.1: Relevant pieces of the NRQCD Lagrangian with estimates of their scaling in the power counting parameter  $v$  as seen in [33].

Since  $[D_0] \sim (\mathbf{D}^2/2M)$ , from the Lagrangian we know that  $[D_0] \sim Mv^2$ .

We now consider the scaling in  $v$  of the coupling  $\alpha_s$  using the potential model presented in Eq (2.2). Since  $\alpha_s$  is asymptotically free, we can say it depends on the scale as  $\alpha_s(1/R)$  where  $R$  is the size of the quarkonium. Since  $R \sim 1/Mv$ , by setting the potential and kinetic energy expressions equal

$$Mv^2 \sim -C_F \frac{\alpha_s(1/R)}{R} \sim -C_F \times Mv \times \alpha_s(Mv) \implies \alpha_s(Mv) \sim v. \quad (\text{A.3})$$

Knowing how the coupling scales with  $v$ , we can make estimates of both  $v$  and  $\alpha_s$  at the scales relevant to NRQCD namely  $M$ ,  $Mv$ ,  $Mv^2$ . The scale of radial and orbital angular momentum excitations of charmonium was said to be  $\sim Mv^2$ . The two lowest energy  $^3S_1$  state of charmonium, the  $J/\psi$  and  $\psi'$ , lie about 600 MeV apart in mass. The difference between the  $J/\psi$  and the  $\chi_{cJ}$ , the lowest  $^3P_J$  state of charmonium, is about 400 MeV. The average of these differences  $\sim 500$  GeV can be used as a reasonable estimate of the scale  $Mv^2$ . Using  $m_c = 1.5$  GeV as an estimate for the perturbative mass scale  $M$ , Ref. [33] made rough estimates of the various scales and the value of the coupling  $\alpha_s$  at these scales. These estimates are summarized in Fig. A.2.

The remainder of the velocity scaling rules for fields such as  $\mathbf{A}$ ,  $\mathbf{E}$ , ... can be

$M$	$Mv$	$Mv^2$	$\alpha_s(M)$	$\alpha_s(Mv)$	$\alpha_s(Mv^2)$
1.5 GeV	0.9 GeV	0.5 GeV	0.35	0.52	0.68

FIGURE A.2: Estimates of values of relevant scales in NRQCD for charmonium where  $v_{c\bar{c}} \sim 0.3$  as seen in [33].

estimated by fixing the gauge in  $\mathcal{L}_{\text{NRQCD}}$ . Ref. [153] showed that, in the Coulomb gauge  $\nabla \cdot \mathbf{A} = 0$ , the power counting of the Lagrangian in  $v$  becomes manifest if one re-scales the space-time coordinates  $\vec{x}$  and  $t$  by  $1/(Mv)$ , the heavy-quark fields by  $(Mv)^{3/2}$ , and the gauge field by  $Mv^{3/2}$ . The Lagrangian written explicitly in terms of the gauge field  $\mathbf{A}$  can be organized as

$$\mathcal{L}_{\text{NRQCD}} = \mathcal{L}_0 + \mathcal{L}_1 + \mathcal{L}_2 + \dots, \quad (\text{A.4})$$

where

$$\mathcal{L}_0 = \mathcal{L}_{\text{light}} + \psi^\dagger \left( i\partial_0 - gA_0 + \frac{\nabla^2}{2M} \right) \psi + \text{charge conjugate terms} \quad (\text{A.5})$$

$$\mathcal{L}_1 = -\frac{1}{M} \psi^\dagger (ig\mathbf{A} \cdot \nabla) \psi + \frac{c_4}{2M} \psi^\dagger (\nabla \times g\mathbf{A}) \cdot \boldsymbol{\sigma} \psi + \text{charge conjugate terms},$$

and

$$\begin{aligned} \mathcal{L}_2 = & -\frac{1}{2M} \psi^\dagger (g\mathbf{A})^2 \psi + \frac{c_1}{8M^3} \psi^\dagger (\nabla^2)^2 \psi \\ & + \frac{c_2}{8M^2} \psi^\dagger (-\nabla^2 gA_0) \psi - \frac{c_3}{4M^2} (\nabla gA_0) \times \nabla \cdot \boldsymbol{\sigma} \psi \\ & + \frac{c_4}{2M} \psi^\dagger (ig\mathbf{A} \times g\mathbf{A}) \cdot \boldsymbol{\sigma} \psi \\ & + \text{charge conjugate terms}. \end{aligned} \quad (\text{A.6})$$

Here,  $\mathcal{L}_0, \mathcal{L}_1, \mathcal{L}_2, \dots$  describe quarkonium energy levels suppressed by relative factors of  $v^0, v^1, v^2, \dots$ , respectively. Considering the Fock state expansion in Eq. (2.17), we see that the dominant state  $|Q\bar{Q}\rangle$  will receive its first corrections  $|Q\bar{Q}g\rangle$  from, for

example the interaction  $\psi^\dagger (ig\mathbf{A} \cdot \nabla)\psi$  in  $\mathcal{L}_1$ . A transition from a higher Fock state via this term describes the lowest chromo-electric transition.

# Appendix B

## Symmetries of Leading Order SCET Lagrangian

When deriving the form of operators in an EFT, symmetries play an important role in constraining their form. There are two particularly interesting symmetries of the SCET Lagrangian related to the choice of gauge and light-cone basis. With the decoupling of the gauge field into collinear and ultra-soft fields via the BPS field re-definitions, SCET comes with two separate gauge symmetries. Predictions of the theory are preserved under both collinear and ultra-soft gauge transformations, hence the inclusion above of two separate gauge fixing parameters  $\tau_n$  and  $\tau_{us}$ . Much more on the details of gauge symmetry in SCET can be found in Ref. [91].

Considerable freedom exists in our choice of the light-cone basis vectors  $n$  and  $\bar{n}$ . The conditions that  $n^2 = \bar{n}^2 = 0$  and  $n \cdot \bar{n} = 2$  are also satisfied when we perform the following transformations on the basis vectors

<b>RPI<sub>I</sub></b>	<b>RPI<sub>II</sub></b>	<b>RPI<sub>III</sub></b>
$n_\mu \rightarrow n_\mu + \Delta_\mu^\perp$	$n_\mu \rightarrow n_\mu$	$n_\mu \rightarrow e^\alpha n_\mu$
$\bar{n}_\mu \rightarrow \bar{n}_\mu$	$\bar{n}_\mu \rightarrow \bar{n}_\mu + \epsilon_\mu^\perp$	$\bar{n}_\mu \rightarrow e^{-\alpha} \bar{n}_\mu$
with $\Delta_\mu^\perp \sim \lambda^1$	with $\epsilon_\mu^\perp \sim \lambda^0$	with $\alpha \sim \lambda^0$ .

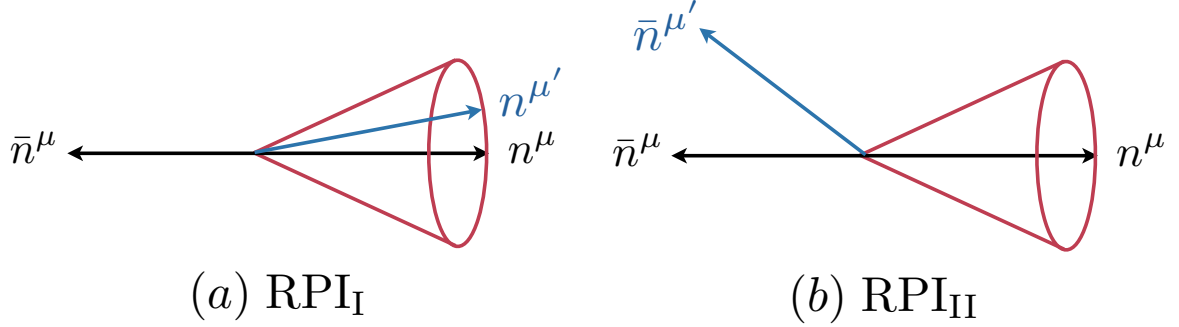


FIGURE B.1: Visualization of re-parameterizations of the of the light-cone directions  $n$  and  $\bar{n}$  via RPI<sub>I</sub> (a) and RPI<sub>II</sub> (b). Along with RPI<sub>III</sub>, which can be thought of as boosts, these transformations are an important symmetry of  $\mathcal{L}_{\text{SCET}}$

These are three types of so-called Re-parameterization Invariance (RPI) present in SCET [101, 154]. As shown in Fig. B.1, they can be visualized as changes in the directions of the basis vectors  $n$  and  $\bar{n}$  and, in the case of RPI<sub>III</sub>, boosts along the  $\hat{z}$ -direction. RPI is also manifest as an ambiguity of how we decompose label/residual momenta where, for example, we said  $n \cdot p \rightarrow n \cdot (p_l + p_r)$ . Proper SCET operators with collinear fields will always have the combination  $\mathcal{P}^\mu + i\partial^\mu$ , which is the combination needed to leave the theory invariant under transformations in how the label operator  $\mathcal{P}^\mu$  and the derivatives  $\partial^\mu$  extract the label/residual momenta

$$\mathcal{P}^\mu \rightarrow \mathcal{P}^\mu + \beta^\mu \quad \text{and} \quad i\partial^\mu \rightarrow i\partial^\mu - \beta^\mu. \quad (\text{B.1})$$

This means that the theory is invariant under the following transformation of, for example, the collinear quark fields

$$\xi_{n,p_\ell}(x) \rightarrow e^{i\beta(x)} \xi_{n,p_\ell+\beta}(x). \quad (\text{B.2})$$

RPI also requires other restrictions on the fields, light-cone directions, and Wilson lines not explicitly shown here.

# Appendix C

## Renormalization Group & Rapidity Renormalization Group Techniques

Here we outline the details of using Renormalization Group (RG) and Rapidity Renormalization Group (RRG) techniques to resum potentially large logarithms. We begin by discussing the tools needed to calculate resummed expressions for measured vs. unmeasured functions. Throughout this work we have referred to measured functions (such as measured jet and measured soft functions) as those that depend on a measurement of the substructure. In our case this meant measuring the angularity  $\tau_a$  of a jet containing an identified hadron. These expressions will be resummed using RGEs for measured functions, which we will describe below. For FJFs or other functions that depend on quantities such as the jet energy, the transverse momentum of the identified hadron with respect to the jet axis  $\mathbf{p}_\perp^h$ , etc., we utilize RGEs for unmeasured functions. We provide the tools (such as anomalous dimensions) necessary to resum expressions to next-to-leading-logarithmic (NLL) and next-to-leading-logarithmic prime (NLL') accuracy. NLL' resummation requires the same anomalous dimensions as NLL but implies that certain terms next-to-leading-order

(NLO) terms in the fixed order expansion in the coupling  $\alpha_s$  have been included. Recall that, for angularity FJFs, these terms were critical, as they provided the lowest order coupling of the  $z$  and  $\tau_a$  dependencies of the FJF.

## C.1 RGE for Unmeasured Functions

Functions  $F$  that do not depend on a substructure measurement are multiplicatively renormalized via

$$F^{\text{bare}} = Z_F(\mu)F(\mu) \quad (\text{C.1})$$

where functions such as  $F(\mu)$  are assumed to be renormalized quantities unless explicitly notated as bare. This class of functions satisfies the renormalization group equation (RGE) of the form

$$\mu \frac{d}{d\mu} F(\mu) = \gamma_\mu^F(\mu) F(\mu) \quad (\text{C.2})$$

where  $\gamma_\mu^F$  is the anomalous dimension for the evolution of the function  $F$  in  $\mu$  space. These are calculated in this case from the standard renormalization factor  $Z_F(\mu)$  via

$$\gamma_\mu^F(\mu) = -\frac{1}{Z_F(\mu)} \mu \frac{d}{d\mu} Z_F(\mu). \quad (\text{C.3})$$

This anomalous dimension for unmeasured quantities can ultimately be written in the following generic form

$$\gamma_\mu^F(\mu) = \Gamma^F[\alpha] \log \left( \frac{\mu^2}{m_F^2} \right) + \gamma_\mu^F[\alpha], \quad (\text{C.4})$$

where  $\mu_F$  is related to the characteristic scale of a particular function and the factors  $\Gamma_\mu^F[\alpha_s]$  and  $\gamma_\mu^F[\alpha_s]$  refer to the *cusp* and *non-cusp* parts respectively, of the total anomalous dimension. The cusp part  $\Gamma_\mu^F[\alpha_s]$  is proportional to the cusp anomalous dimension  $\Gamma_{\text{cusp}}$  and does not depend on function  $F(\mu)$  whereas the non-cusp part

$\gamma_\mu^F[\alpha_s]$  will need to be calculated explicitly for a given function. Both pieces have perturbative expansions in  $\alpha_s$

$$\Gamma^F[\alpha_s] = \sum_n \left(\frac{\alpha_s}{4\pi}\right)^{1+n} \Gamma_F^n \quad (\text{C.5})$$

$$\gamma_\mu^F[\alpha_s] = \sum_n \left(\frac{\alpha_s}{4\pi}\right)^{1+n} \gamma_F^n. \quad (\text{C.6})$$

where the cusp anomalous dimension has a similar expansion

$$\Gamma_{\text{cusp}}[\alpha_s] = \sum_n \left(\frac{\alpha_s}{4\pi}\right)^{1+n} \Gamma_{\text{cusp}}^n \quad (\text{C.7})$$

and the following two relations are needed to calculate a resummed function [155]

$$\Gamma^F[\alpha_s] = \left(\frac{\Gamma_F^0}{\Gamma_{\text{cusp}}^0} \Gamma_{\text{cusp}}[\alpha_s]\right) \quad \text{and} \quad \frac{\Gamma_{\text{cusp}}^1}{\Gamma_{\text{cusp}}^0} = \left(\frac{67}{9} - \frac{\pi^2}{3}\right) C_A - \frac{10N_f}{9}. \quad (\text{C.8})$$

The solution to the unmeasured RGE can be written as

$$F(\mu) = U_F(\mu, \mu_0) F(\mu_0) \quad (\text{C.9})$$

where  $U_F$  is an evolution kernel given by

$$U_F(\mu, \mu_0) = e^{K_F(\mu, \mu_0)} \left(\frac{\mu_0}{m_F}\right)^{\omega_F(\mu, \mu_0)}, \quad (\text{C.10})$$

where the pieces of the kernel are expressed as

$$K_F(\mu, \mu_0) = 2 \int_{\alpha(\mu)}^{\alpha(\mu_0)} \frac{d\alpha}{\beta(\alpha)} \Gamma_F(\alpha) \int_{\alpha(\mu_0)}^{\alpha} \frac{d\alpha'}{\beta(\alpha')} + \int_{\alpha(\mu)}^{\alpha(\mu_0)} \frac{d\alpha}{\beta(\alpha)} \gamma_F(\alpha), \quad (\text{C.11})$$

$$\omega_F(\mu, \mu_0) = 2 \int_{\alpha(\mu)}^{\alpha(\mu_0)} \frac{d\alpha}{\beta(\alpha)} \Gamma_F(\alpha), \quad (\text{C.12})$$

where resumming to NLL/NLL' accuracy requires calculating the cusp piece of the anomalous dimension to two-loop order and the non-cusp piece to one-loop order.

Fixed/Log Order	Matching	$\gamma_{H,J,S,\dots}$	$\Gamma_{\text{cusp}}$	$\beta[\alpha_s]$
LO	Tree	-	-	1-loop
NLO	1-loop	-	-	2-loop
LL	Tree	Tree	1-loop	1-loop
NLL	Tree	1-loop	2-loop	2-loop
NNLL	1-loop	2-loop	3-loop	3-loop

Table C.1: Orders of the matching calculation, non-cusp anomalous dimensions, cusp anomalous dimensions, and QCD  $\beta$ -function needed for various fixed order calculations and logarithmic resummation orders. Adapted from Refs. [1, 2].

At these orders the expressions  $K_F$  and  $\omega_F$  above are given by

$$K_F(\mu, \mu_0) = -\frac{\gamma_F^0}{2\beta_0} \ln r - \frac{2\pi\Gamma_F^0}{(\beta_0)^2} \left[ \frac{r-1+r \ln r}{\alpha_s(\mu)} + \left( \frac{\Gamma_c^1}{\Gamma_c^0} - \frac{\beta_1}{\beta_0} \right) \frac{1-r+\ln r}{4\pi} + \frac{\beta_1}{8\pi\beta_0} \ln^2 r \right], \quad (\text{C.13})$$

$$\omega_F(\mu, \mu_0) = -\frac{\Gamma_F^0}{j_F\beta_0} \left[ \ln r + \left( \frac{\Gamma_c^1}{\Gamma_c^0} - \frac{\beta_1}{\beta_0} \right) \frac{\alpha_s(\mu_0)}{4\pi} (r-1) \right], \quad (\text{C.14})$$

where  $r \equiv \alpha(\mu)/\alpha(\mu_0)$  and  $\beta_n$  are  $n$ -loop coefficients of the QCD  $\beta$ -function,

$$\beta(\alpha_s) = \mu \frac{d\alpha_s}{d\mu} = -2\alpha_s \sum_{n=0}^{\infty} \left( \frac{\alpha_s}{4\pi} \right)^{1+n} \beta_n, \quad (\text{C.15})$$

where the one-loop and two-loop coefficients (and the color factor  $T_R = 1/2$ ) are

$$\beta_0 = \frac{11C_A}{3} - \frac{2N_f}{3} \quad (\text{C.16})$$

$$\beta_1 = \frac{34C_A^2}{3} - \frac{10C_A N_f}{3} - 2C_F N_f, \quad (\text{C.17})$$

$$(\text{C.18})$$

where  $N_f$  is the number of quark flavors.

## C.2 RGE for Measured Functions

For measured jets (i.e. when we have probed the substructure) the RGE for objects such as  $S^{\text{meas}}$  and  $\mathcal{G}(\tau_a, z, \mu)$  is slightly more complicated. Since the function must be renormalized at a given measurement of  $\tau_a$  we have the following

$$F^{\text{bare}}(\tau_a) = \int d\tau'_a Z_F(\tau_a - \tau'_a, \mu) F(\tau'_a, \mu) = [\gamma_F(\mu) \otimes F(\mu)](\tau_a), \quad (\text{C.19})$$

where as shown in the text we use convolutions defined via

$$f(\tau_a) \otimes g(\tau_a) = \int d\tau'_a f(\tau_a - \tau'_a) g(\tau'_a), \quad (\text{C.20})$$

the RGE is then given by

$$\mu \frac{d}{d\mu} F(\tau_a, \mu) = [\gamma_F(\mu) \otimes F(\mu)](\tau_a), \quad (\text{C.21})$$

where the anomalous dimension is thus given by

$$\begin{aligned} \gamma_F(\tau_a, \mu) &= - \left[ Z_F^{-1}(\mu) \otimes \mu \frac{d}{d\mu} Z_F(\mu) \right] (\tau_a) \\ &= \Gamma_F(\alpha_s) \left( \ln \frac{\mu^2}{m_F^2} - \frac{2}{j_F} \left( \frac{\Theta(\tau_a)}{\tau_a} \right)_+ \right) + \gamma_F(\alpha_s) \delta(\tau_a), \end{aligned} \quad (\text{C.22})$$

whose solution is of the form

$$F(\tau_a, \mu) = \exp(K_F + \gamma_E \omega_F) \frac{1}{\Gamma(-\omega_F)} \left( \frac{\mu_0}{m_F} \right)^{j_F \omega_F} \left[ \left( \frac{\Theta(\tau_a)}{(\tau_a)^{1+\omega_F}} \right)_+ \otimes F(\tau_a, \mu_0) \right]. \quad (\text{C.23})$$

## C.3 RGE + RRGE for TMD Functions

For the RG evolution in the parameter  $\mu$ , the formalism for unmeasured functions above applies in a similar manner to  $\mathbf{p}_\perp$  dependent functions

$$\mu \frac{d}{d\mu} F^R(\mathbf{p}_\perp, \mu, \nu) = \gamma_\mu^F(\mu, \nu) \times F^R(\mathbf{p}_\perp, \mu, \nu), \quad (\text{C.24})$$

for the same set of anomalous dimensions given above. However, following the formalism of [122], our functions must also be evolved in the space of  $\nu$ , the dimensionful scale introduced when regulating rapidity divergences. The RRG equation in  $\mathbf{p}_\perp$  space is given by

$$\nu \frac{d}{d\nu} F(\mathbf{p}_\perp, \mu, \mu/\nu) = \gamma_\nu^F(\mathbf{p}_\perp, \mu, \nu) \otimes_\perp F(\mathbf{p}_\perp, \mu, \mu/\nu), \quad (\text{C.25})$$

where again we use the notation for convolution in transverse components given in Eq. (4.72) and where the anomalous dimension can be written in the following generic form,

$$\gamma_\nu^F(\mathbf{p}_\perp, \mu, \nu) = \Gamma_\nu^F[\alpha_s] \mathcal{L}_0(\mathbf{p}_\perp^2, \mu^2) + \gamma_\nu^F[\alpha_s] \delta^{(2)}(\mathbf{p}_\perp), \quad (\text{C.26})$$

where

$$\delta^{(2)}(\mathbf{p}_\perp) = \frac{1}{\pi} \delta(\mathbf{p}_\perp^2). \quad (\text{C.27})$$

The cusp and non-cusp parts of the anomalous dimension are listed in Table C.2. Taking the Fourier transform of Eq. (C.25) yields,

$$\frac{d}{d \ln \nu} \tilde{F}(b, \mu, \nu) = \tilde{\gamma}_\nu^F(b, \mu, \nu) \tilde{F}(b, \mu, \nu), \quad (\text{C.28})$$

where the Fourier conjugate of  $\mathbf{p}_\perp$  is  $\mathbf{b}$  where  $|\mathbf{b}| = b$  and using the form of the anomalous dimensions in Eq. (5.29,5.30) gives that,

$$\tilde{\gamma}_\nu^F(b, \mu, \nu) = -\frac{\Gamma_\nu^F[\alpha_s]}{(2\pi)^2} \ln \left( \frac{\mu}{\mu_C(b)} \right) + \frac{\gamma_\nu^F[\alpha_s]}{(2\pi)^2}, \quad (\text{C.29})$$

where  $\mu_C(b) = 2e^{-\gamma_E}/b$ . Integrating Eq. (C.28) yields

$$\tilde{F}(b, \mu, \nu) = \tilde{F}(b, \mu, \nu_0) \mathcal{V}_F(b, \mu, \nu, \nu_0), \quad (\text{C.30})$$

where

$$\mathcal{V}_F(b, \mu, \nu, \nu_0) = \exp \left[ G_F(\mu, \nu, \nu_0) \right] \left( \frac{\mu}{\mu_C} \right)^{\eta_F(\mu, \nu, \nu_0)}, \quad (\text{C.31})$$

with

$$G_F(\mu, \nu, \nu_0) = \frac{\gamma_\nu^F[\alpha_s]}{(2\pi)^2} \ln\left(\frac{\nu}{\nu_0}\right) \quad \text{and} \quad \eta_F(\mu, \nu, \nu_0) = -\frac{\Gamma_\nu^F[\alpha_s]}{(2\pi)^2} \ln\left(\frac{\nu}{\nu_0}\right). \quad (\text{C.32})$$

Function ( $F$ )	$\Gamma_\nu^F$	$\gamma_\nu^F$	$\Gamma_F^0$	$\gamma_F^0$
$\mathcal{D}_{i/h}$	$-(8\pi)\alpha_s C_i + \mathcal{O}(\alpha_s^2)$	$\mathcal{O}(\alpha_s^2)$	0	$4C_i(\ln(\nu^2/\omega^2) + \bar{\gamma}_i)$
$S_C^i$	$(8\pi)\alpha_s C_i + \mathcal{O}(\alpha_s^2)$	$\mathcal{O}(\alpha_s^2)$	$4C_i$	0

Table C.2: Values of the cusp and non-cusp parts of the anomalous dimensions for the collinear and collinear-soft functions.

# Appendix D

## Plus-functions and Profile Functions

In this appendix, we introduce and discuss the properties of plus-distributions and profile functions, both of which are used in the calculations of Chapters 4 and 5.

### D.1 Plus-Functions

Under integration, plus-functions give finite answers when convolved with smooth functions. For a sufficiently smooth function  $f(z)$ , one common use of plus-functions is for integrals appearing in QCD calculations that have the form

$$\int_0^1 dz \frac{f(z)}{(1-z)_+} \equiv \int_0^1 dz \frac{f(z) - f(1)}{1-z} \quad (\text{D.1})$$

and

$$\int_0^1 dz f(z) \left[ \frac{\log^n(1-z)}{(1-z)} \right]_+ \equiv \int_0^1 dz (f(z) - f(1)) \frac{\log^n(1-z)}{1-z}. \quad (\text{D.2})$$

These functions essentially behave as  $\frac{1}{(1-z)_+} = \frac{1}{1-z}$  and  $\left[ \frac{\log^n(1-z)}{(1-z)} \right]_+ = \frac{\log^n(1-z)}{(1-z)}$  for  $z \neq 1$ . For our calculations of angularity-dependent FJFs in Chapter 4, it is useful

to define them formally by

$$[f(\tau)]_+ \equiv \lim_{\beta \rightarrow 0} \frac{d}{d\tau} [\theta(\tau - \beta)F(\tau)] , \quad (\text{D.3})$$

where  $F(\tau)$  is defined via

$$F(\tau) \equiv \int_1^\tau d\tau' f(\tau') , \quad (\text{D.4})$$

which yields

$$\mathcal{L}\left\{ \left( \frac{1}{\tau^{1+\omega}} \right)_+ \right\} = s^\omega \Gamma(-\omega) . \quad (\text{D.5})$$

By taking the  $\tau' \rightarrow 0$  limit in Eq. (D.9), expanding in  $\omega_2$  on both sides and matching powers we find the following useful identities:

$$\int d\tau' \left[ \frac{\Theta(\tau - \tau')}{(\tau - \tau')^{1+\omega}} \right]_+ \delta(\tau') = \left[ \frac{\Theta(\tau)}{\tau^{1+\omega}} \right]_+ , \quad (\text{D.6})$$

$$\begin{aligned} \int d\tau' \left[ \frac{\Theta(\tau - \tau')}{(\tau - \tau')^{1+\omega}} \right]_+ \left[ \frac{\Theta(\tau')}{\tau'} \right]_+ &= \left[ \frac{\Theta(\tau)}{\tau^{1+\omega}} \right]_+ (\ln \tau - H(-1 - \omega)) , \\ \int d\tau' \left[ \frac{\Theta(\tau - \tau')}{(\tau - \tau')^{1+\omega}} \right]_+ \left[ \frac{\Theta(\tau') \ln \tau'}{\tau'} \right]_+ &= \left[ \frac{\Theta(\tau)}{\tau^{1+\omega}} \right]_+ \left[ \frac{(\ln \tau - H(-1 - \omega))^2}{2} \right. \\ &\quad \left. + \frac{\pi^2/2 - \psi^{(1)}(-\omega)}{2} \right] , \end{aligned} \quad (\text{D.7})$$

where we used the identity from [1]

$$\left[ \frac{\Theta(\tau)}{\tau^{1+\omega}} \right]_+ = -\frac{1}{\omega} \delta(\tau) + \sum_{n=0}^{\infty} (-\omega)^n \left[ \frac{\Theta(\tau) \ln^n \tau}{\tau} \right]_+ . \quad (\text{D.8})$$

We can also use Laplace transforms and the definition of a the plus function to show that

$$\int d\tau'' \left[ \frac{\Theta(\tau - \tau'')}{(\tau - \tau'')^{1+\omega_1}} \right]_+ \left[ \frac{\Theta(\tau'' - \tau')}{(\tau'' - \tau')^{1+\omega_2}} \right]_+ = \frac{\Gamma(-\omega_1)\Gamma(-\omega_2)}{\Gamma(-\omega_1 - \omega_2)} \left[ \frac{\Theta(\tau - \tau')}{(\tau - \tau')^{1+\omega_1+\omega_2}} \right]_+ . \quad (\text{D.9})$$

## D.2 Profile Functions

For the measured soft and measured jet functions for angularity FJFs, we perform the scale variations using so-called profile functions. Profile functions allow us to perform the scale variations of  $\mu$  in a way that depends on the the angularity  $\tau_a$ . They allow the variation to freeze at the characteristic scale for high values of  $\tau_a$  (where the factorization theorem begins to break down) and at a fixed scale for small values of  $\tau_a$  (where we reach the realm of non-perturbative physics). The profile function for the measured soft function,  $\mu_S^{PF}(\tau_0)$ , and the profile function for the measured jet function,  $\mu_J^{PF}(\tau_0)$ , are plotted in Fig. D.1 (for the case  $a = 0$ ). The analytic formulae for these functions are

$$\mu_S^{PF}(\tau_a) = \left[ 1 + \epsilon_S \frac{g(\tau_a)}{g(1)} \right] \times \begin{cases} \mu_{min} + \alpha \tau_a^\beta & 0 < \tau_a < \tau_{min} \\ \omega \tau_a / r^{(1-a)} & \tau_{min} \leq \tau_a \end{cases},$$

$$\mu_J^{PF}(\tau_a) = \left[ 1 + \epsilon_J \frac{g(\tau_a)}{g(1)} \right] \times \begin{cases} (\omega r)^{(1-a)/(2-a)} (\mu_{min} + \alpha \tau_a^\beta)^{1/(2-a)} & 0 < \tau_a < \tau_{min} \\ \omega \tau_a^{1/(2-a)} & \tau_{min} \leq \tau_a \end{cases},$$
(D.10)

where we have defined

$$g(\tau) = \frac{1}{\exp\left(1.26(\tau_{min} - \tau)/\tau_{min}\right) + 1},$$
(D.11)

and where  $\alpha$  and  $\beta$  are defined to be

$$\beta = \frac{\tau_{min}}{\tau_{min} - \mu_{min} r^{(1-a)}/\omega} \quad \text{and} \quad \alpha = \frac{\omega}{\beta \tau_{min}^{\beta-1} r^{(1-a)}}.$$
(D.12)

These choices for  $\alpha$  and  $\beta$  ensure that the profile functions and their first derivatives are continuous. We use the following values for the parameters

$$\begin{aligned} \tau_{min} &= 2\mu_{min} r^{1-a}/\omega \\ \mu_{min} &= 0.3 \text{ GeV}. \end{aligned}$$
(D.13)

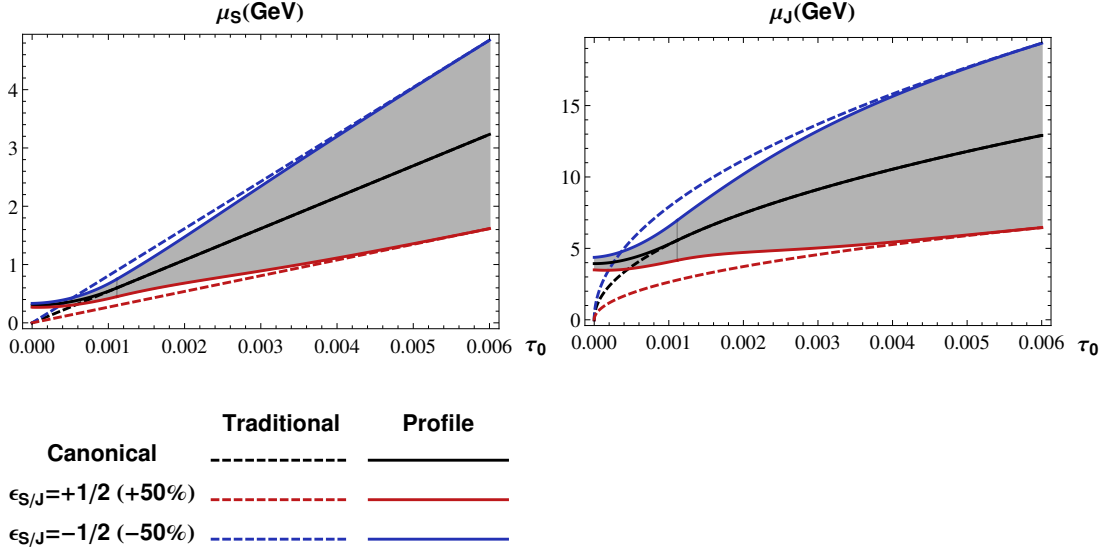


FIGURE D.1: Profile functions for  $\mu_S^{PF}(\tau_0)$  and  $\mu_J^{PF}(\tau_0)$ , the  $\tau_0$ -dependent renormalization scales that we use in the scale variations of our measured soft function and measured jet function. Also shown are traditional scale variations done by varying  $\mu$  by  $\pm 50\%$ .

We define our scale variations via

$$\begin{aligned}
 \epsilon_{S/J} = 1/2 &\quad \rightarrow \quad +50\% \text{ variation,} \\
 \epsilon_{S/J} = -1/2 &\quad \rightarrow \quad -50\% \text{ variation,} \\
 \epsilon_{S/J} = 0 &\quad \rightarrow \quad \text{Canonical scale,}
 \end{aligned}$$

and take the final scale variation bands as the envelope of the set of bands from the individual variations.

# Bibliography

- [1] S. D. Ellis, C. K. Vermilion, J. R. Walsh, A. Hornig and C. Lee, *Jet Shapes and Jet Algorithms in SCET*, *JHEP* **11** (2010) 101, [1001.0014].
- [2] A. Jain, M. Procura and W. J. Waalewijn, *Parton Fragmentation within an Identified Jet at NNLL*, *JHEP* **1105** (2011) 035, [1101.4953].
- [3] CMS collaboration, V. Khachatryan et al., *Measurement of the inclusive 3-jet production differential cross section in proton–proton collisions at 7 TeV and determination of the strong coupling constant in the TeV range*, *Eur. Phys. J.* **C75** (2015) 186, [1412.1633].
- [4] J. J. Aubert, U. Becker, P. J. Biggs, J. Burger, M. Chen, G. Everhart et al., *Experimental observation of a heavy particle  $j$* , *Phys. Rev. Lett.* **33** (Dec, 1974) 1404–1406.
- [5] PARTICLE DATA GROUP collaboration, C. Patrignani et al., *Review of Particle Physics*, *Chin. Phys.* **C40** (2016) 100001.
- [6] E. Braaten, M. A. Doncheski, S. Fleming and M. L. Mangano, *Fragmentation production of  $J/\psi$  and  $\psi'$  at the Tevatron*, *Phys. Lett.* **B333** (1994) 548–554, [hep-ph/9405407].
- [7] CDF COLLABORATION collaboration, F. Abe, H. Akimoto, A. Akopian, M. G. Albrow, S. R. Amendolia, D. Amidei et al.,  *$J/\psi$* , *Phys. Rev. Lett.* **79** (Jul, 1997) 572–577.
- [8] M. Kramer, 1, *Quarkonium production at high-energy colliders*, *Prog. Part. Nucl. Phys.* **47** (2001) 141–201, [hep-ph/0106120].
- [9] E. Braaten and S. Fleming, *Color octet fragmentation and the psi-prime surplus at the Tevatron*, *Phys. Rev. Lett.* **74** (1995) 3327–3330, [hep-ph/9411365].
- [10] E. Braaten, B. A. Kniehl and J. Lee, *Polarization of prompt  $J/\psi$  at the Tevatron*, *Phys. Rev.* **D62** (2000) 094005, [hep-ph/9911436].

- [11] CDF collaboration, T. Affolder et al., *Measurement of  $J/\psi$  and  $\psi(2S)$  polarization in  $p\bar{p}$  collisions at  $\sqrt{s} = 1.8$  TeV*, *Phys. Rev. Lett.* **85** (2000) 2886–2891, [hep-ex/0004027].
- [12] M. Baumgart, A. K. Leibovich, T. Mehen and I. Z. Rothstein, *Probing Quarkonium Production Mechanisms with Jet Substructure*, *JHEP* **11** (2014) 003, [1406.2295].
- [13] P. Faccioli, C. Lourenco, J. Seixas and H. K. Wohri, *Towards the experimental clarification of quarkonium polarization*, *Eur. Phys. J.* **C69** (2010) 657–673, [1006.2738].
- [14] M. Butenschoen and B. A. Kniehl, *World data of  $J/\psi$  production consolidate NRQCD at NLO*, *Phys. Rev.* **D84** (2011) 051501, [1105.0820].
- [15] M. Butenschoen and B. A. Kniehl, *Next-to-leading-order tests of NRQCD factorization with  $J/\psi$  yield and polarization*, *Mod. Phys. Lett.* **A28** (2013) 1350027, [1212.2037].
- [16] LHCb collaboration, R. Aaij et al., *Measurement of  $J/\psi$  polarization in  $pp$  collisions at  $\sqrt{s} = 7$  TeV*, *Eur. Phys. J.* **C73** (2013) 2631, [1307.6379].
- [17] B. Gong, L.-P. Wan, J.-X. Wang and H.-F. Zhang, *Polarization for Prompt  $J/\psi$  and  $\psi(2s)$  Production at the Tevatron and LHC*, *Phys. Rev. Lett.* **110** (2013) 042002, [1205.6682].
- [18] K.-T. Chao, Y.-Q. Ma, H.-S. Shao, K. Wang and Y.-J. Zhang,  *$J/\psi$  Polarization at Hadron Colliders in Nonrelativistic QCD*, *Phys. Rev. Lett.* **108** (2012) 242004, [1201.2675].
- [19] H.-S. Shao and K.-T. Chao, *Spin correlations in polarizations of  $P$ -wave charmonia  $\chi_{cJ}$  and impact on  $J/\psi$  polarization*, *Phys. Rev.* **D90** (2014) 014002, [1209.4610].
- [20] G. Aad, B. Abbott, J. Abdallah, A. Abdelalim, A. Abdesselam, O. Abidinov et al., *Measurement of the differential cross-sections of inclusive, prompt and non-prompt production in proton–proton collisions at*, *Nuclear Physics B* **850** (2011) 387 – 444.
- [21] S. Chatrchyan, V. Khachatryan, A. M. Sirunyan, A. Tumasyan, W. Adam, T. Bergauer et al.,  *$J/\psi$  and  $\psi(2s)$  production in  $pp$  collisions at  $\sqrt{s} = 7$  tev*, *Journal of High Energy Physics* **2012** (2012) 11.
- [22] G. T. Bodwin, H. S. Chung, U.-R. Kim and J. Lee, *Fragmentation contributions to  $J/\psi$  production at the Tevatron and the LHC*, *Phys. Rev. Lett.* **113** (2014) 022001, [1403.3612].

- [23] CDF collaboration, A. Abulencia et al., *Polarization of  $J/\psi$  and  $\psi_{2S}$  mesons produced in  $p\bar{p}$  collisions at  $\sqrt{s} = 1.96$ -TeV*, *Phys. Rev. Lett.* **99** (2007) 132001, [0704.0638].
- [24] CMS collaboration, S. Chatrchyan et al., *Measurement of the prompt  $J/\psi$  and  $\psi(2S)$  polarizations in  $pp$  collisions at  $\sqrt{s} = 7$  TeV*, *Phys. Lett.* **B727** (2013) 381–402, [1307.6070].
- [25] CDF COLLABORATION collaboration, T. Affolder, H. Akimoto, A. Akopian, M. G. Albrow, P. Amaral, S. R. Amendolia et al., *Measurement of  $J/\psi$  and  $\psi(2S)$  polarization in  $p\bar{p}$  collisions at  $\sqrt{s} = 1.8$ TeV*, *Phys. Rev. Lett.* **85** (Oct, 2000) 2886–2891.
- [26] CDF COLLABORATION collaboration, A. Abulencia, J. Adelman, T. Affolder, T. Akimoto, M. G. Albrow, S. Amerio et al., *Polarizations of  $j/\psi$  and  $\psi(2s)$  mesons produced in  $p\bar{p}$  collisions at  $\sqrt{s} = 1.96$  TeV*, *Phys. Rev. Lett.* **99** (Sep, 2007) 132001.
- [27] A. Ali and G. Kramer, *Jets and QCD: A Historical Review of the Discovery of the Quark and Gluon Jets and its Impact on QCD*, *Eur. Phys. J.* **H36** (2011) 245–326, [1012.2288].
- [28] TASSO collaboration, R. Brandelik et al., *Evidence for Planar Events in  $e+e-$  Annihilation at High-Energies*, *Phys. Lett.* **B86** (1979) 243–249.
- [29] G. P. Salam, *Towards Jetography*, *Eur. Phys. J.* **C67** (2010) 637–686, [0906.1833].
- [30] G. P. Salam and G. Soyez, *A Practical Seedless Infrared-Safe Cone jet algorithm*, *JHEP* **05** (2007) 086, [0704.0292].
- [31] BELLE collaboration, R. Seidl et al., *Measurement of Azimuthal Asymmetries in Inclusive Production of Hadron Pairs in  $e+e-$  Annihilation at  $s^{*(1/2)} = 10.58$ -GeV*, *Phys. Rev.* **D78** (2008) 032011, [0805.2975].
- [32] LHCb COLLABORATION collaboration, R. Aaij, B. Adeva, M. Adinolfi, Z. Ajaltouni, S. Akar, J. Albrecht et al., *Study of  $j/\psi$  production in jets*, *Phys. Rev. Lett.* **118** (May, 2017) 192001.
- [33] E. Braaten, *Introduction to the NRQCD factorization approach to heavy quarkonium*, in *3rd International Workshop on Particle Physics Phenomenology Taipei, Taiwan, November 14-17, 1996*, 1996. hep-ph/9702225.
- [34] N. Brambilla et al., *Heavy quarkonium: progress, puzzles, and opportunities*, *Eur. Phys. J.* **C71** (2011) 1534, [1010.5827].

- [35] J. C. Collins, D. E. Soper and G. F. Sterman, *Factorization of Hard Processes in QCD*, *Adv. Ser. Direct. High Energy Phys.* **5** (1989) 1–91, [hep-ph/0409313].
- [36] R. Bain, L. Dai, A. Hornig, A. K. Leibovich, Y. Makris and T. Mehen, *Analytic and Monte Carlo Studies of Jets with Heavy Mesons and Quarkonia*, *JHEP* **06** (2016) 121, [1603.06981].
- [37] R. Bain, Y. Makris and T. Mehen, *Transverse Momentum Dependent Fragmenting Jet Functions with Applications to Quarkonium Production*, *JHEP* **11** (2016) 144, [1610.06508].
- [38] R. Bain, L. Dai, A. Leibovich, Y. Makris and T. Mehen, *NRQCD Confronts LHCb Data on Quarkonium Production within Jets*, 1702.05525.
- [39] I. Z. Rothstein, *NRQCD: A Critical review*, hep-ph/9911276.
- [40] N. Brambilla, *NRQCD and Quarkonia*, *eConf* **C0610161** (2006) 004, [hep-ph/0702105].
- [41] J. E. Augustin, A. M. Boyarski, M. Breidenbach, F. Bulos, J. T. Dakin, G. J. Feldman et al., *Discovery of a narrow resonance in  $e^+e^-$  annihilation*, *Phys. Rev. Lett.* **33** (Dec, 1974) 1406–1408.
- [42] B. Björken and S. Glashow, *Elementary particles and  $su(4)$* , *Physics Letters* **11** (1964) 255 – 257.
- [43] S. L. Glashow, J. Iliopoulos and L. Maiani, *Weak interactions with lepton-hadron symmetry*, *Phys. Rev. D* **2** (Oct, 1970) 1285–1292.
- [44] PARTICLE DATA GROUP collaboration, e. a. Beringer, *Review of particle physics*, *Phys. Rev. D* **86** (Jul, 2012) 010001.
- [45] M. Gell-Mann, *A Schematic Model of Baryons and Mesons*, *Phys. Lett.* **8** (1964) 214–215.
- [46] G. Zweig, *An  $SU(3)$  model for strong interaction symmetry and its breaking. Version 1*, .
- [47] S. W. Herb, D. C. Hom, L. M. Lederman, J. C. Sens, H. D. Snyder, J. K. Yoh et al., *Observation of a dimuon resonance at 9.5 gev in 400-gev proton-nucleus collisions*, *Phys. Rev. Lett.* **39** (Aug, 1977) 252–255.
- [48] M. L. Perl, G. S. Abrams, A. M. Boyarski, M. Breidenbach, D. D. Briggs, F. Bulos et al., *Evidence for anomalous lepton production in  $e^+ - e^-$  annihilation*, *Phys. Rev. Lett.* **35** (Dec, 1975) 1489–1492.

- [49] R. D. Kephart, R. J. Engelmann, R. J. Fisk, M. L. Good, A. S. Ito, H. Jöstlein et al., *Measurement of the dihadron mass continuum in  $p$ - $be$  collisions and a search for narrow resonances*, *Phys. Rev. Lett.* **39** (Dec, 1977) 1440–1443.
- [50] G. Sterman and S. Weinberg, *Jets from quantum chromodynamics*, *Phys. Rev. Lett.* **39** (Dec, 1977) 1436–1439.
- [51] T. Appelquist, A. De Rújula, H. D. Politzer and S. L. Glashow, *Spectroscopy of the new mesons*, *Phys. Rev. Lett.* **34** (Feb, 1975) 365–369.
- [52] D. Ebert, R. N. Faustov and V. O. Galkin, *Properties of heavy quarkonia and  $B_c$  mesons in the relativistic quark model*, *Phys. Rev.* **D67** (2003) 014027, [[hep-ph/0210381](#)].
- [53] F. Halzen, F. Herzog, E. W. N. Glover and A. D. Martin,  $\frac{J}{\psi}$ , *Phys. Rev. D* **30** (Aug, 1984) 700–702.
- [54] E. Braaten and T. C. Yuan, *Gluon fragmentation into heavy quarkonium*, *Phys. Rev. Lett.* **71** (1993) 1673–1676, [[hep-ph/9303205](#)].
- [55] E. Braaten and T. C. Yuan, *Gluon fragmentation into  $P$  wave heavy quarkonium*, *Phys. Rev.* **D50** (1994) 3176–3180, [[hep-ph/9403401](#)].
- [56] G. Altarelli and G. Parisi, *Asymptotic Freedom in Parton Language*, *Nucl. Phys.* **B126** (1977) 298–318.
- [57] M. Cacciari and M. Greco,  *$J/\psi$  production via fragmentation at the Tevatron*, *Phys. Rev. Lett.* **73** (1994) 1586–1589, [[hep-ph/9405241](#)].
- [58] R. Barbieri, M. Caffo, R. Gatto and E. Remiddi, *Qcd corrections to  $p$  wave quarkonium decays*, *Nuclear Physics B* **192** (1981) 61 – 65.
- [59] R. Barbieri, R. Gatto and E. Remiddi, *Singular binding dependence in the hadronic widths of  $1^{++}$  and  $1^+$  heavy quark antiquark bound states*, *Physics Letters B* **61** (1976) 465 – 468.
- [60] G. T. Bodwin, E. Braaten and G. P. Lepage, *Rigorous QCD analysis of inclusive annihilation and production of heavy quarkonium*, *Phys. Rev.* **D51** (1995) 1125–1171, [[hep-ph/9407339](#)].
- [61] P. L. Cho and A. K. Leibovich, *Color octet quarkonia production*, *Phys. Rev.* **D53** (1996) 150–162, [[hep-ph/9505329](#)].
- [62] P. L. Cho and A. K. Leibovich, *Color octet quarkonia production. 2.*, *Phys. Rev.* **D53** (1996) 6203–6217, [[hep-ph/9511315](#)].

- [63] E. Braaten and Y.-Q. Chen, *Dimensional regularization in quarkonium calculations*, *Phys. Rev.* **D55** (1997) 2693–2707, [hep-ph/9610401].
- [64] Y.-Q. Ma, J.-W. Qiu and H. Zhang, *Heavy quarkonium fragmentation functions from a heavy quark pair. I. S wave*, *Phys. Rev.* **D89** (2014) 094029, [1311.7078].
- [65] K. Gottfried and J. D. Jackson, *On the Connection between production mechanism and decay of resonances at high-energies*, *Nuovo Cim.* **33** (1964) 309–330.
- [66] J. C. Collins and D. E. Soper, *Angular Distribution of Dileptons in High-Energy Hadron Collisions*, *Phys. Rev.* **D16** (1977) 2219.
- [67] P. L. Cho and M. B. Wise, *Spin symmetry predictions for heavy quarkonia alignment*, *Phys. Lett.* **B346** (1995) 129–136, [hep-ph/9411303].
- [68] G. T. Bodwin, H. S. Chung, D. Kang, J. Lee and C. Yu, *Improved determination of color-singlet nonrelativistic QCD matrix elements for S-wave charmonium*, *Phys. Rev.* **D77** (2008) 094017, [0710.0994].
- [69] G. Hanson, G. S. Abrams, A. M. Boyarski, M. Breidenbach, F. Bulos, W. Chinowsky et al., *Evidence for jet structure in hadron production by  $e^+e^-$  annihilation*, *Phys. Rev. Lett.* **35** (Dec, 1975) 1609–1612.
- [70] G. Hanson et al., *Hadron Production by  $e^+e^-$  Annihilation at Center-of-mass Energies Between 2.6-GeV and 7.8-GeV. Part 2. Jet Structure and Related Inclusive Distributions*, *Phys. Rev.* **D26** (1982) 991.
- [71] N. Cabibbo, G. Parisi and M. Testa, *Hadron Production in  $e^+e^-$  Collisions*, *Lett. Nuovo Cim.* **4S1** (1970) 35–39.
- [72] S. M. Berman, J. D. Bjorken and J. B. Kogut, *Inclusive processes at high transverse momentum*, *Phys. Rev. D* **4** (Dec, 1971) 3388–3418.
- [73] J. Ellis, M. K. Gaillard and G. G. Ross, *Search for gluons in  $e^+e^-$  annihilation*, *Nuclear Physics B* **111** (1976) 253 – 271.
- [74] D. P. Barber, U. Becker, H. Benda, A. Boehm, J. G. Branson, J. Bron et al., *Discovery of three-jet events and a test of quantum chromodynamics at petra*, *Phys. Rev. Lett.* **43** (Sep, 1979) 830–833.
- [75] PLUTO collaboration, C. Berger et al., *Evidence for Gluon Bremsstrahlung in  $e^+e^-$  Annihilations at High-Energies*, *Phys. Lett.* **B86** (1979) 418–425.
- [76] W. Bartel, T. Canzler, D. Cords, P. Dittmann, R. Eichler, R. Felst et al., *Observation of planar three-jet events in  $e^+e^-$  annihilation and evidence for gluon bremsstrahlung*, *Physics Letters B* **91** (1980) 142 – 147.

- [77] T. Becher and M. Neubert, *Factorization and NNLL Resummation for Higgs Production with a Jet Veto*, *JHEP* **07** (2012) 108, [1205.3806].
- [78] JADE collaboration, W. Bartel et al., *Experimental Studies on Multi-Jet Production in  $e^+ e^-$  Annihilation at PETRA Energies*, *Z. Phys.* **C33** (1986) 23.
- [79] S. Catani, Y. L. Dokshitzer, M. Olsson, G. Turnock and B. R. Webber, *New clustering algorithm for multi - jet cross-sections in  $e^+ e^-$  annihilation*, *Phys. Lett.* **B269** (1991) 432–438.
- [80] Y. L. Dokshitzer, G. D. Leder, S. Moretti and B. R. Webber, *Better jet clustering algorithms*, *JHEP* **08** (1997) 001, [hep-ph/9707323].
- [81] M. Cacciari, G. P. Salam and G. Soyez, *The anti- $k_t$  jet clustering algorithm*, *JHEP* **04** (2008) 063, [0802.1189].
- [82] E. Farhi, *Quantum chromodynamics test for jets*, *Phys. Rev. Lett.* **39** (Dec, 1977) 1587–1588.
- [83] R. Abbate, M. Fickinger, A. H. Hoang, V. Mateu and I. W. Stewart, *Thrust at  $N^3LL$  with Power Corrections and a Precision Global Fit for  $\alpha_s(m_Z)$* , *Phys.Rev.* **D83** (2011) 074021, [1006.3080].
- [84] S. D. Ellis, Z. Kunszt and D. E. Soper, *Jets at hadron colliders at order  $\alpha_s^3$ : A look inside*, *Phys. Rev. Lett.* **69** (1992) 3615–3618, [hep-ph/9208249].
- [85] C. F. Berger, T. Kucs and G. Sterman, *Event shape / energy flow correlations*, *Phys. Rev.* **D68** (2003) 014012, [hep-ph/0303051].
- [86] J. Thaler and K. Van Tilburg, *Identifying Boosted Objects with  $N$ -subjettiness*, *JHEP* **03** (2011) 015, [1011.2268].
- [87] J. Gallicchio and M. D. Schwartz, *Seeing in Color: Jet Superstructure*, *Phys. Rev. Lett.* **105** (2010) 022001, [1001.5027].
- [88] C. W. Bauer, S. Fleming and M. E. Luke, *Summing Sudakov logarithms in  $B \rightarrow X_s \gamma$  in effective field theory*, *Phys. Rev.* **D63** (2000) 014006, [hep-ph/0005275].
- [89] C. W. Bauer, S. Fleming, D. Pirjol and I. W. Stewart, *An effective field theory for collinear and soft gluons: Heavy to light decays*, *Phys. Rev.* **D63** (2001) 114020, [hep-ph/0011336].
- [90] C. W. Bauer and I. W. Stewart, *Invariant operators in collinear effective theory*, *Phys. Lett.* **B516** (2001) 134–142, [hep-ph/0107001].

- [91] C. W. Bauer, D. Pirjol and I. W. Stewart, *Soft collinear factorization in effective field theory*, *Phys. Rev.* **D65** (2002) 054022, [[hep-ph/0109045](#)].
- [92] I. Stewart, *8.851 effective field theory*, Massachusetts Institute of Technology: MIT OpenCourseWare, 2013.
- [93] C. W. Bauer, A. V. Manohar and M. B. Wise, *Enhanced nonperturbative effects in jet distributions*, *Phys. Rev. Lett.* **91** (2003) 122001, [[hep-ph/0212255](#)].
- [94] C. W. Bauer, C. Lee, A. V. Manohar and M. B. Wise, *Enhanced nonperturbative effects in Z decays to hadrons*, *Phys. Rev.* **D70** (2004) 034014, [[hep-ph/0309278](#)].
- [95] C. Lee and G. Sterman, *Momentum flow correlations from event shapes: Factorized soft gluons and Soft-Collinear Effective Theory*, *Phys. Rev.* **D75** (2007) 014022, [[hep-ph/0611061](#)].
- [96] C. W. Bauer, S. Fleming, C. Lee and G. Sterman, *Factorization of  $e^+e^-$  event shape distributions with hadronic final states in Soft Collinear Effective Theory*, *Phys. Rev.* **D78** (2008) 034027, [[0801.4569](#)].
- [97] C. W. Bauer, A. Hornig and F. J. Tackmann, *Factorization for generic jet production*, *Phys. Rev.* **D79** (2009) 114013, [[0808.2191](#)].
- [98] C. W. Bauer, F. J. Tackmann, J. R. Walsh and S. Zuberi, *Factorization and Resummation for Dijet Invariant Mass Spectra*, *Phys. Rev.* **D85** (2012) 074006, [[1106.6047](#)].
- [99] Y.-T. Chien, A. Hornig and C. Lee, *Soft-collinear mode for jet cross sections in soft collinear effective theory*, *Phys. Rev.* **D93** (2016) 014033, [[1509.04287](#)].
- [100] A. V. Manohar and I. W. Stewart, *The zero-bin and mode factorization in quantum field theory*, *Phys. Rev.* **D76** (2007) 074002, [[hep-ph/0605001](#)].
- [101] A. V. Manohar, T. Mehen, D. Pirjol and I. W. Stewart, *Reparameterization invariance for collinear operators*, *Phys. Lett.* **B539** (2002) 59–66, [[hep-ph/0204229](#)].
- [102] C. Marcantonini and I. W. Stewart, *Reparameterization invariant collinear operators*, *Phys. Rev.* **D79** (2009) 065028, [[0809.1093](#)].
- [103] M. Trott, *Jets in effective theory: Summing phase space logs*, *Phys. Rev.* **D75** (2007) 054011, [[hep-ph/0608300](#)].

- [104] A. V. Belitsky, G. P. Korchemsky and G. Sterman, *Energy flow in QCD and event shape functions*, *Phys. Lett.* **B515** (2001) 297–307, [[hep-ph/0106308](#)].
- [105] M. Procura and I. W. Stewart, *Quark Fragmentation within an Identified Jet*, *Phys.Rev.* **D81** (2010) 074009, [[0911.4980](#)].
- [106] A. Jain, M. Procura, B. Shotwell and W. J. Waalewijn, *Fragmentation with a Cut on Thrust: Predictions for B-factories*, *Phys. Rev.* **D87** (2013) 074013, [[1207.4788](#)].
- [107] T. Kaufmann, A. Mukherjee and W. Vogelsang, *Hadron Fragmentation Inside Jets in Hadronic Collisions*, *Phys. Rev.* **D92** (2015) 054015, [[1506.01415](#)].
- [108] Y.-T. Chien, Z.-B. Kang, F. Ringer, I. Vitev and H. Xing, *Jet fragmentation functions in proton-proton collisions using soft-collinear effective theory*, *JHEP* **05** (2016) 125, [[1512.06851](#)].
- [109] M. Procura and W. J. Waalewijn, *Fragmentation in Jets: Cone and Threshold Effects*, *Phys. Rev.* **D85** (2012) 114041, [[1111.6605](#)].
- [110] C. W. Bauer and E. Mereghetti, *Heavy Quark Fragmenting Jet Functions*, *JHEP* **04** (2014) 051, [[1312.5605](#)].
- [111] Z.-B. Kang, F. Ringer and I. Vitev, *Jet substructure using semi-inclusive jet functions in SCET*, *JHEP* **11** (2016) 155, [[1606.07063](#)].
- [112] L. Dai, C. Kim and A. K. Leibovich, *Fragmentation of a Jet with Small Radius*, *Phys. Rev.* **D94** (2016) 114023, [[1606.07411](#)].
- [113] A. Hornig, C. Lee and G. Ovanesyan, *Effective predictions of event shapes: Factorized, resummed, and gapped angularity distributions*, *JHEP* **05** (2009) 122, [[0901.3780](#)].
- [114] M. G. Echevarria, A. Idilbi and I. Scimemi, *Factorization Theorem For Drell-Yan At Low  $q_T$  And Transverse Momentum Distributions On-The-Light-Cone*, *JHEP* **07** (2012) 002, [[1111.4996](#)].
- [115] M. G. Echevarria, A. Idilbi, A. Schfer and I. Scimemi, *Model-Independent Evolution of Transverse Momentum Dependent Distribution Functions (TMDs) at NNLL*, *Eur. Phys. J.* **C73** (2013) 2636, [[1208.1281](#)].
- [116] M. G. Echevarria, A. Idilbi and I. Scimemi, *Unified treatment of the QCD evolution of all (un-)polarized transverse momentum dependent functions: Collins function as a study case*, *Phys. Rev.* **D90** (2014) 014003, [[1402.0869](#)].
- [117] M. G. Echevarria, I. Scimemi and A. Vladimirov, *Transverse momentum dependent fragmentation function at next-to-next-to-leading order*, *Phys. Rev.* **D93** (2016) 011502, [[1509.06392](#)].

- [118] M. G. Echevarria, I. Scimemi and A. Vladimirov, *Unpolarized Transverse Momentum Dependent Parton Distribution and Fragmentation Functions at next-to-next-to-leading order*, 1604.07869.
- [119] M. Anselmino, M. Boglione, J. O. Gonzalez Hernandez, S. Melis and A. Prokudin, *Unpolarised Transverse Momentum Dependent Distribution and Fragmentation Functions from SIDIS Multiplicities*, *JHEP* **04** (2014) 005, [1312.6261].
- [120] M. Procura, W. J. Waalewijn and L. Zeune, *Resummation of Double-Differential Cross Sections and Fully-Unintegrated Parton Distribution Functions*, *JHEP* **02** (2015) 117, [1410.6483].
- [121] B. U. Musch, P. Hagler, J. W. Negele and A. Schafer, *Exploring quark transverse momentum distributions with lattice QCD*, *Phys. Rev.* **D83** (2011) 094507, [1011.1213].
- [122] J.-Y. Chiu, A. Jain, D. Neill and I. Z. Rothstein, *A Formalism for the Systematic Treatment of Rapidity Logarithms in Quantum Field Theory*, *JHEP* **1205** (2012) 084, [1202.0814].
- [123] D. Neill, I. Z. Rothstein and V. Vaidya, *The Higgs Transverse Momentum Distribution at NNLL and its Theoretical Errors*, *JHEP* **12** (2015) 097, [1503.00005].
- [124] T. Lbbert, J. Oredsson and M. Stahlhofen, *Rapidity renormalized TMD soft and beam functions at two loops*, *JHEP* **03** (2016) 168, [1602.01829].
- [125] T. Becher, M. Neubert and D. Wilhelm, *Higgs-Boson Production at Small Transverse Momentum*, *JHEP* **05** (2013) 110, [1212.2621].
- [126] T. Becher, M. Neubert and D. Wilhelm, *Electroweak gauge-boson and Higgs production at Small  $q_T$ : Infrared safety from the collinear anomaly*, in *Proceedings, 20th International Workshop on Deep-Inelastic Scattering and Related Subjects (DIS 2012): Bonn, Germany, March 26-30, 2012*, pp. 721–724, 2012. DOI.
- [127] V. Ahrens, T. Becher, M. Neubert and L. L. Yang, *Renormalization-Group Improved Prediction for Higgs Production at Hadron Colliders*, *Eur. Phys. J.* **C62** (2009) 333–353, [0809.4283].
- [128] P. Pietrulewicz, F. J. Tackmann and W. J. Waalewijn, *Factorization and Resummation for Generic Hierarchies between Jets*, *JHEP* **08** (2016) 002, [1601.05088].
- [129] S. M. Aybat and T. C. Rogers, *TMD Parton Distribution and Fragmentation Functions with QCD Evolution*, *Phys. Rev.* **D83** (2011) 114042, [1101.5057].

- [130] D. Neill, I. Scimemi and W. J. Waalewijn, *Jet axes and universal transverse-momentum-dependent fragmentation*, *JHEP* **04** (2017) 020, [1612.04817].
- [131] S. Fleming, A. K. Leibovich and T. Mehen, *Resummation of Large Endpoint Corrections to Color-Octet  $J/\psi$  Photoproduction*, *Phys. Rev.* **D74** (2006) 114004, [hep-ph/0607121].
- [132] I. W. Stewart, F. J. Tackmann and W. J. Waalewijn, *Factorization at the LHC: From PDFs to Initial State Jets*, *Phys. Rev.* **D81** (2010) 094035, [0910.0467].
- [133] A. Hornig, Y. Makris and T. Mehen, *Jet Shapes in Dijet Events at the LHC in SCET*, 1601.01319.
- [134] J.-y. Chiu, A. Jain, D. Neill and I. Z. Rothstein, *The Rapidity Renormalization Group*, *Phys.Rev.Lett.* **108** (2012) 151601, [1104.0881].
- [135] J. Alwall, R. Frederix, S. Frixione, V. Hirschi, F. Maltoni, O. Mattelaer et al., *The automated computation of tree-level and next-to-leading order differential cross sections, and their matching to parton shower simulations*, *JHEP* **07** (2014) 079, [1405.0301].
- [136] T. Sjostrand, S. Mrenna and P. Z. Skands, *PYTHIA 6.4 Physics and Manual*, *JHEP* **05** (2006) 026, [hep-ph/0603175].
- [137] M. Bahr et al., *Herwig++ Physics and Manual*, *Eur. Phys. J.* **C58** (2008) 639–707, [0803.0883].
- [138] LHCb collaboration, R. Aaij et al., *Study of  $J/\psi$  production in jets*, 1701.05116.
- [139] V. G. Kartvelishvili and A. K. Likhoded, *Heavy Quark Fragmentation Into Mesons and Baryons*, *Sov. J. Nucl. Phys.* **29** (1979) 390.
- [140] B. A. Kniehl, G. Kramer, I. Schienbein and H. Spiesberger, *Finite-mass effects on inclusive  $B$  meson hadroproduction*, *Phys. Rev.* **D77** (2008) 014011, [0705.4392].
- [141] M. Cacciari, G. P. Salam and G. Soyez, *FastJet User Manual*, *Eur. Phys. J.* **C72** (2012) 1896, [1111.6097].
- [142] Z. Ligeti, I. W. Stewart and F. J. Tackmann, *Treating the  $b$  quark distribution function with reliable uncertainties*, *Phys. Rev.* **D78** (2008) 114014, [0807.1926].

- [143] E. Braaten, K.-m. Cheung and T. C. Yuan, *Z0 decay into charmonium via charm quark fragmentation*, *Phys. Rev.* **D48** (1993) 4230–4235, [[hep-ph/9302307](#)].
- [144] E. Braaten and Y.-Q. Chen, *Helicity decomposition for inclusive J / psi production*, *Phys. Rev.* **D54** (1996) 3216–3227, [[hep-ph/9604237](#)].
- [145] A. Buckley, J. Butterworth, L. Lonnblad, D. Grellscheid, H. Hoeth, J. Monk et al., *Rivet user manual*, *Comput. Phys. Commun.* **184** (2013) 2803–2819, [[1003.0694](#)].
- [146] *An Introduction to PYTHIA 8.2*, *Comput. Phys. Commun.* **191** (2015) 159–177, [[1410.3012](#)].
- [147] G. T. Bodwin *private communication* .
- [148] Z.-B. Kang, F. Ringer and I. Vitev, *Semi-inclusive jet cross sections within SCET*, 2016. [1609.07112](#).
- [149] L. Dai, C. Kim and A. K. Leibovich, *Fragmentation to a jet in the large z limit*, [1701.05660](#).
- [150] G. Ovanessian, T. R. Slatyer and I. W. Stewart, *Heavy Dark Matter Annihilation from Effective Field Theory*, *Phys. Rev. Lett.* **114** (2015) 211302, [[1409.8294](#)].
- [151] B. Bhattacharjee, S. Mukhopadhyay, M. M. Nojiri, Y. Sakaki and B. R. Webber, *Quark-gluon discrimination in the search for gluino pair production at the LHC*, *JHEP* **01** (2017) 044, [[1609.08781](#)].
- [152] CMS collaboration, V. Khachatryan et al., *Search for dark matter in proton-proton collisions at 8 TeV with missing transverse momentum and vector boson tagged jets*, *JHEP* **12** (2016) 083, [[1607.05764](#)].
- [153] M. E. Luke and A. V. Manohar, *Bound states and power counting in effective field theories*, *Phys. Rev.* **D55** (1997) 4129–4140, [[hep-ph/9610534](#)].
- [154] M. E. Luke and A. V. Manohar, *Reparametrization invariance constraints on heavy particle effective field theories*, *Phys. Lett.* **B286** (1992) 348–354, [[hep-ph/9205228](#)].
- [155] G. P. Korchemsky and A. V. Radyushkin, *Renormalization of the Wilson Loops Beyond the Leading Order*, *Nucl. Phys.* **B283** (1987) 342–364.

# Biography

Reginald Alexander Bain was born on January 14th, 1990 to Reginald F. Bain Jr. and Erin Keefe Bain in Evanston, IL. In 1991, he moved with his family to Columbia, SC where he spent his childhood and graduated from Irmo High School in 2008. After being offered a Carolina Scholarship, Bain elected to attend the University of South Carolina (USC), graduating summa cum laude and with honors from the South Carolina Honors College with a B.S. in Physics and Mathematics in 2012. At USC, Bain received a number of honors including the Barry M. Goldwater Scholarship in 2011 and a NSF Graduate Fellowship in 2012. He also received several university awards including the Nina and Frank Avignone Award in Physics for the top graduating physics major in 2012. In the fall of 2012, Bain began studying for his Ph.D. in physics at Duke as a Townes-Perkin-Elmer fellow. He received the Mary Creason Memorial Award for Undergraduate Teaching in 2013 and engaged in a number of teaching, professional development, and science communication initiatives during his time at Duke. These included co-founding ComSciCon-Triangle, an annual workshop for training graduate students in effective science communication practices. Bain has conducted research in theoretical nuclear physics, publishing several works on the production of quarkonium within jets at the LHC. With collaborators at Duke, Los Alamos, and the University of Pittsburgh, his work has helped develop analytical techniques for studying quarkonium production and has helped motivate recent measurements by experiments at the LHC.